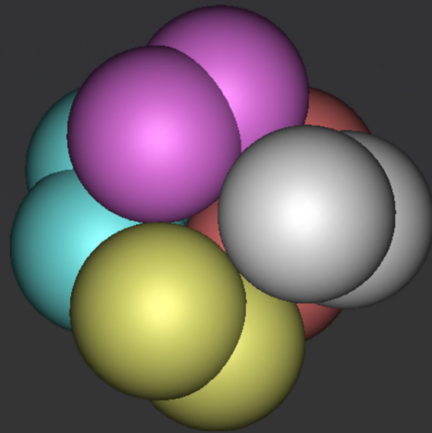
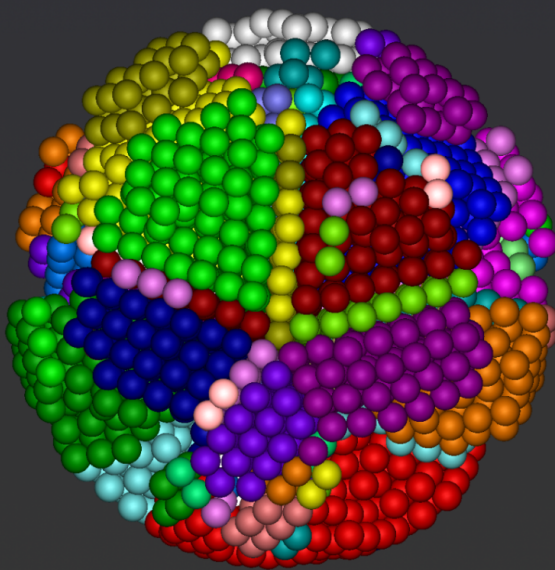
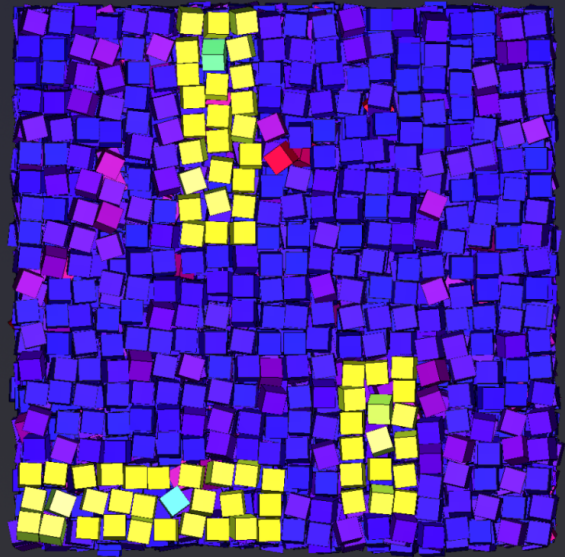
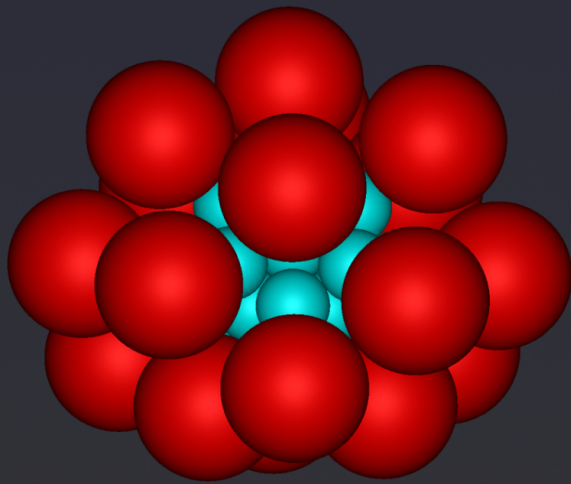


Clustering and self-assembly in colloidal systems



Frank Smallenburg

Clustering and self-assembly in colloidal systems

Cover: Snapshots of a colloidal micelle (top left), defects in a crystal of hard cubes (top right), a cluster of hard spheres compressed in spherical confinement (bottom left), and a cluster of five hard dumbbells compressed in spherical confinement (bottom right). These systems are discussed in Chapters 10, 5, 9, and 8, respectively.

Clustering and self-assembly in colloidal systems

Clustervorming en zelforganisatie in colloïdale systemen

(met een samenvatting in het Nederlands)

Proefschrift

ter verkrijging van de graad van doctor aan de Universiteit Utrecht op gezag van de rector magnificus, prof. dr. G.J. van der Zwaan ingevolge het besluit van het college voor promoties in het openbaar te verdedigen op maandag 9 januari 2012 des middags te 2.30 uur.

door

Frank Smalenburg

geboren op 1 juni 1983 te Castricum.

Promotor: Prof. dr. ir. M. Dijkstra

This research was supported by an NWO-Vici grant.

Contents

1	Introduction	1
1.1	Colloids	1
1.1.1	Colloidal phases	1
1.1.2	Colloidal interactions	2
1.2	Simulation methods	3
1.2.1	Monte Carlo	3
1.2.2	Event-driven molecular dynamics	5
1.3	Dipolar interactions induced by external fields	10
1.4	Outline of this thesis	12
2	Self-assembly of colloidal strings in a homogeneous external electric or magnetic field	13
2.1	Introduction	14
2.2	Model and simulation methods	15
2.3	Monodisperse systems	16
2.4	Bidisperse systems	18
2.4.1	Flame-like and ring-like clusters of small spheres	18
2.4.2	Alternating strings	21
2.5	Asymmetric dumbbells	22
2.6	Conclusions	27
2.7	Acknowledgements	28
2.8	Appendix: Experimental setup	28
3	Phase diagram of colloidal spheres in a biaxial electric or magnetic field	31
3.1	Introduction	32
3.2	Methods	33
3.3	Hard spheres in a biaxial field	37
3.4	Charged spheres in a biaxial field	39
3.5	Comparison with experiments	43
3.6	Conclusions	44
4	Colloidal cubes in an external electric or magnetic field	45
4.1	Introduction	46
4.2	Methods and model	46
4.3	Results	48
4.3.1	Phase diagram	48

4.3.2	Point-dipole approximation	51
4.4	Conclusions	52
4.5	Acknowledgements	53
5	Phase behavior and crystal vacancies in colloidal hard cubes	55
5.1	Introduction	56
5.2	Model and simulation methods	56
5.2.1	Overlap and collision detection	56
5.2.2	Free energy calculations	57
5.3	Order parameters and correlation functions	59
5.3.1	Positional order	60
5.3.2	Bond-orientational order	61
5.3.3	Orientational order	62
5.4	Results	63
5.5	Conclusions and discussion	71
5.6	Acknowledgements	72
6	Phase diagrams of colloidal spheres with a constant zeta-potential	73
6.1	Introduction	74
6.2	Model and theory	75
6.3	Effective charge and screening length	77
6.4	Effective interactions and phase diagrams	79
6.5	Summary and conclusions	85
6.6	Acknowledgements	85
7	Crystal nucleation in binary hard-sphere mixtures: The effect of the order parameter on the cluster composition	87
7.1	Introduction	88
7.2	Classical nucleation theory for multi-component systems	89
7.3	Free-energy barrier	94
7.4	Order parameter	95
7.5	A substitutional solid solution	98
7.6	An interstitial solid solution	103
7.7	Conclusions	107
7.8	Acknowledgements	109
8	Assembly of colloidal spheres and dumbbells through emulsion droplet evaporation	111
8.1	Introduction	112
8.2	Simulation Methods	113
8.3	Results	114
8.3.1	Spheres	114
8.3.2	Symmetric dumbbells	115
8.3.3	Asymmetric dumbbells	117
8.4	Conclusions	121
8.5	Acknowledgements	121

9	Crystallization of colloidal spheres in evaporating emulsion droplets	123
9.1	Introduction	124
9.2	Methods	124
9.3	Results	126
9.3.1	Colloidal hard spheres in a hard spherical cavity	126
9.3.2	Colloidal hard spheres in a spherical cavity with a repulsive wall-particle interaction	130
9.3.3	Colloidal hard spheres in a hard spherical cavity with repulsive particle-particle interactions	130
9.4	Conclusions	133
9.5	Acknowledgements	133
10	Colloidal micelles from asymmetric hard dumbbells	135
10.1	Introduction	135
10.2	Theory	136
10.2.1	Free-energy calculations	136
10.2.2	Critical micelle concentration	138
10.3	Model and methods	139
10.3.1	Interactions	139
10.3.2	Direct simulations	139
10.3.3	Grand-canonical Monte Carlo	139
10.3.4	Effective density	141
10.3.5	Experimental system	142
10.4	Results	143
10.4.1	Size ratio 0.76	143
10.4.2	Size ratio 0.5	149
10.4.3	Size ratio 0.3	149
10.5	Discussion	149
10.6	Conclusions	151
10.7	Acknowledgements	152
	References	153
	Summary	166
	Samenvatting	170
	Acknowledgements	174
	List of publications	176

Introduction

1.1 Colloids

Colloidal suspensions are systems that consist of microscopic particles dispersed in a solvent. These particles, or colloids, typically range from tens of nanometers to several micrometers in size. Both the particles and the solvent can be made out of a variety of materials. Many common colloidal suspensions consist of solid particles in a liquid solvent, such as blood or paint. However, it is also possible to create a colloidal suspension out of two immiscible liquids, with the particles being formed by small droplets of one liquid suspended in a continuous phase of the other. In this case, the suspension is called an emulsion. For example, butter, salad dressing and mayonnaise are emulsions where droplets of oil are suspended in a water-based solvent or vice versa. Alternatively, the colloidal particles can be small bubbles of gas suspended in a liquid medium, as in whipped cream or shaving cream. In smoke the solvent is a gas instead, containing either liquid or solid particles.

1.1.1 Colloidal phases

The main factor that distinguishes colloidal particles from other particles is not their size, but their dynamics: colloidal particles exhibit Brownian motion. When a particle is surrounded by either a liquid or gaseous solvent, thermal motion will cause the solvent particles to collide with it from all directions. If the particle is at rest with respect to the rest of the solvent, the direction of the net force exerted on it by the solvent is random at any instant of time, causing the particle to diffuse randomly through the solvent. This random motion was named after Robert Brown, who observed it in 1827 when he studied pollen grains suspended in water using a microscope,[1] and was only explained much later by Albert Einstein and William Sutherland in 1905.[2, 3] In principle, any object suspended in a gas or liquid will perform Brownian motion. However, typically Brownian forces are too weak to significantly affect particles larger than a few micrometers in diameter. Thus, unlike a system of larger particles (grains of sand, a box of marbles) which will generally remain motionless unless some external force is applied to it, colloidal systems are continually in motion. Given enough time, this random motion allows the colloids to explore all configurations available to them. As a result, after a sufficient

amount of equilibration time, colloidal particles can be expected to obey equilibrium statistical physics, and can spontaneously form gas, liquid and solid phases, analogous to those found in molecular systems. Combined with the fact that colloidal particles can often be observed in real space and real time using modern microscopy techniques, this makes them an ideal model system for the behavior of atoms and molecules. Additionally, in many cases the interactions between colloidal particles are relatively weak compared to the thermal energy. As a result, entropy often plays an important role in the phase behavior of colloids, stabilizing a range of liquid crystal phases, including nematic, smectic and cubatic phases, and plastic crystals.[4] By tuning the size of the colloids, it is possible to ensure that the interparticle distance in colloidal crystals and liquid crystals is on the order of the wavelength of visible light, opening up the possibility of a variety of electro-optical applications. [5–9] An example of the diffraction of light in a colloidal crystal can also be seen in nature as the beautiful colors in opals, which consist of silica spheres of a few hundred micrometers arranged on a close-packed lattice. [10]

1.1.2 Colloidal interactions

Since colloidal particles have a well-defined thermodynamic equilibrium, a variety of methods can be applied to predict their behavior either theoretically or with computer simulations, provided the interactions between the colloids are known. In the simplest case, colloids interact only via hard-core repulsions: in this case, each particle has a solid core that cannot deform or overlap with other particles, but the colloids do not attract or repel each other in any other way. For purely hard particles, the potential energy of the system is not affected at all by the positions of the particles, so any phase transition that occurs in such a system is purely driven by entropy. The first example of this, the crystallization of hard spheres, was demonstrated in 1957 by Wood and Jacobson [11] and Alder and Wainwright. [12] Experimentally, the same phase behavior was shown experimentally by Pusey and Van Meegen using suspensions of poly(methylmethacrylate) particles at different packing fractions. [13] Of course, colloidal particles need not be spherical. More recent synthesis techniques have allowed for the fabrication and study of colloids in a variety of shapes, including dumbbells, rods, platelets, polyhedral particles, superballs, and many more. Both simulations and experiments show that these anisotropic hard-core particles can self-assemble into a range of liquid crystal phases, such as nematic, smectic and cubatic phases, as well as a range of crystal and plastic crystal structures.[4] Similarly, binary systems of hard spheres have been predicted to form a wide variety of crystal structures, [14] and many more are likely to be accessible in mixtures of particles with other shapes.

Apart from their hard cores, colloidal particles can interact in a variety of ways. Examples include charges, electric or magnetic dipole moments, depletion attractions induced by other particles present in the solvent, and steric interactions resulting from polymer chains affixed to the particle surface. These interactions open up an additional range of phases accessible to colloidal particles, as well as the potential forming of finite clusters as a result of anisotropic attractions in “patchy particles”. [15, 16] In short, as experimental control over the interaction and shape of synthesized colloids improves, the variety of structures that can be formed in colloidal systems will only continue to increase.

Predicting what interactions lead to which structures is useful not only to increase our understanding of the physics driving these systems, but also to help determine what type of particle might be the most likely to yield specific desired structures. In this thesis, we will use computer simulations to study a number of models for colloidal systems that are currently experimentally realizable and, where possible, compare the predicted behavior with experimental results.

1.2 Simulation methods

In the majority of the chapters in this thesis, computer simulations are used to study the behavior of colloidal particles. The two main methods used are Monte Carlo (MC) simulations and Event-driven molecular dynamics (EDMD) simulations. While writing an EDMD simulation code is generally more involved than writing an MC code for the same system, the increase in speed can be significant, particularly for systems containing a large number of particles. For example, in chapter 5, where we calculate the equation of state in a system of 8000 cube-shaped particles using both MC and EDMD simulations, the EDMD simulations were seen to provide sufficiently accurate statistics roughly ten times faster. On the other hand, MC simulations can be adapted to a much larger variety of problems much more easily, such as systems with continuous interactions, simulation boxes with a variable box shape, and many biased sampling schemes.[17] In this thesis, both methods will be used, depending on the system under consideration and the quantities the simulations should measure. Below, we will give a brief overview of both methods.

1.2.1 Monte Carlo

Metropolis sampling Monte Carlo (MC) simulations are a commonly employed method to study the equilibrium behavior of many-body systems. Instead of following the dynamics of the system in a realistic way, a Monte Carlo simulation simply aims to sample the most relevant states of a system with sufficient accuracy to perform realistic measurements on the distribution of resulting configurations.

Consider a system of N particles, each interacting with other nearby particles via a pair potential $U_p(\mathbf{r})$ and confined to a volume V at temperature T . The probability of a state with a specific set of particle positions \mathbf{r}^N and momenta \mathbf{p}^N is simply proportional to the Boltzmann factor corresponding to the total energy U_{tot} of the system:

$$P(\mathbf{r}^N, \mathbf{p}^N) \propto \exp\left(-\beta U_{\text{tot}}(\mathbf{r}^N, \mathbf{p}^N)\right), \quad (1.1)$$

with $\beta = 1/k_B T$ and k_B Boltzmann's constant. Thus, the expectation value of a measurable quantity A in the system is then by the weighted average of A over all possible states in the system:

$$\langle A \rangle = \frac{\int d\mathbf{r}^N \int d\mathbf{p}^N A(\mathbf{r}^N, \mathbf{p}^N) P(\mathbf{r}^N, \mathbf{p}^N)}{\int d\mathbf{r}^N \int d\mathbf{p}^N P(\mathbf{r}^N, \mathbf{p}^N)}. \quad (1.2)$$

In most cases, the total energy of the system only depends on the momenta of the particles

via the kinetic energy $U_{\text{kin}}(\mathbf{p}^N)$. The total energy can then be written as:

$$U_{\text{tot}}(\mathbf{r}^N, \mathbf{p}^N) = U_{\text{pot}}(\mathbf{r}^N) + U_{\text{kin}}(\mathbf{p}^N) = \sum_{i=0}^N \sum_{j=i+1}^N U_p(\mathbf{r}_{ij}) + \sum_{i=0}^N \frac{\mathbf{p}_i^2}{2m_i}, \quad (1.3)$$

where m_i is the mass of particle i , \mathbf{r}_{ij} is the distance vector between particles i and j , and $U_{\text{pot}}(\mathbf{r}^N)$ is the total potential energy of the system. If the quantity of interest A is independent of the velocities of the particles, the integrals over the positions and momenta can be separated in both the numerator and denominator of Eq. 1.2, and the momentum integrals simply cancel:

$$\langle A \rangle = \frac{\int d\mathbf{r}^N A(\mathbf{r}^N) \exp(-\beta U_{\text{pot}}(\mathbf{r}^N))}{\int d\mathbf{r}^N \exp(-\beta U_{\text{pot}}(\mathbf{r}^N))}. \quad (1.4)$$

In practice, evaluating either of the integrals in this equation directly is impossible for systems with more than a few particles. However, the Metropolis scheme gives a way to calculate $\langle A \rangle$ by only sampling the most important regions of phase space. The strategy of this scheme is to generate a Markov chain of random configurations of the system in a way that follows the Boltzmann distribution, and then simply average A over the generated configurations. To do this, the simulation is initialized with one possible configuration with N particles in a volume V . Subsequently, a trial configuration is generated that is slightly different, for example by choosing one of the particles at random and displacing it by a small amount \mathbf{d} . To avoid biasing the simulation, we can choose the displacement vector uniformly from a cubic volume centered around 0. The trial move is accepted as the next configuration in the chain with a probability:

$$\text{acc}(o \rightarrow n) = \min(1, \exp[-\beta(U_{\text{pot}}(\mathbf{r}_n) - U_{\text{pot}}(\mathbf{r}_o))]), \quad (1.5)$$

where o and n denote the old and new configurations, respectively. If the trial move is rejected, the next configuration in the Markov chain is the same as the old configuration. Given enough time, this scheme will in principle lead to a chain of configurations that samples all of phase space, following the Boltzmann distribution. The thermodynamic average of the quantity of interest $\langle A \rangle$ can then be measured by averaging its value over a sufficiently large set of these configurations.

What we have described here is the most basic example of a Monte Carlo simulation in the canonical ensemble (at constant N, V , and T). There are a wide variety of ways to adapt this simulation method to a variety of systems and ensembles, and all of these involve the addition of new types of trial moves. For example, for the simulation of anisotropic particles moves have to be added that rotate the particle. To perform simulations at constant pressure, a move has to be included that changes the volume of the simulation box. Other possible moves include cluster moves, particle insertion and deletion, and swap moves that switch the positions of two particles. For a more detailed description of the Monte Carlo method, and the tricks and strategies that can be used in these simulations, see Ref. [17].

1.2.2 Event-driven molecular dynamics

In a Molecular Dynamics (MD) simulation, the dynamics of a system are taken explicitly into account: movement of the particles is based on Newton's Laws, which define the equations of motion for all particles in the system. While this does not mimic Brownian motion, this method provides a different way of sampling configurations according to the Boltzmann distribution. In normal (time-driven) Molecular Dynamics simulations, the equations of motion in the system are integrated in fixed time steps. Each time step, the velocities of the particles are changed based on the calculated forces acting on them, and their positions change as a result of these velocities. However, for such a scheme, the forces on the particles cannot be instantaneous, as they are between particles with discontinuous potentials. For example, the collision between two hard spheres happens at a specific point in time, and the force between the two particles is zero at every other instant. Thus, if a finite fixed time step is used for the simulation, such a collision would only be detected when the particles already overlap. In contrast, Event-driven molecular dynamics (EDMD) simulations predict the moment of collision explicitly ahead of time, so that it can be handled at the correct moment in the simulation.[18] In most cases, this method is applied to systems where the free motion of the particles, i.e. their movement in the time between collisions, is simple, and can be resolved without the need for numeric integration of the equations of motion. In practice, this corresponds to particles with interaction potentials that either are purely hard, or consist of a finite number of discontinuous energy levels (such as square wells). In these cases, the free motion of the particles simply corresponds to the linear motion of the center of mass of the particle, and (if the particles are anisotropic) a constant rotation with fixed angular momentum. In principle, continuous interactions can be approximated with a set of interfaces at small intervals, although each extra interface will slow down the simulation due to the increase in the number of interaction events.

In an EDMD simulation, time does not move forward in fixed intervals. Instead, future events such as particle collisions are predicted, and the simulation jumps from event to event, resolving them in chronological order. The simulation program maintains a list of all predicted future events, and events are added to and removed from this list whenever a collision occurs. Typically, a cell list (or neighbor list [19]) is used to determine which particle pairs are likely to collide in the near future: the simulation box is divided into a number of cells, such that only particles in neighboring cells can interact.[17, 18] As a result, events where a particle crosses from one cell to another are predicted and stored as well. Additional event types can correspond to e.g. the sampling of measurable quantities (such as the pressure) or the effects of a thermostat (often used in order to maintain a constant temperature in an interacting system).

Hard spheres

In this section, we will describe the implementation of an EDMD simulation of monodisperse hard spheres. For the purposes of EDMD, hard spheres are an ideal system: collisions between two particles can be detected analytically, making the simulation both simpler and faster. The prediction of the collision time for two identical hard spheres is very straightforward, as the particles perform simple linear motion between collisions. If

two particles are currently (at time $t = 0$) at a separation $\mathbf{r}_{ij} = \mathbf{r}_i - \mathbf{r}_j$, and have a relative velocity $\mathbf{v}_{ij} = \mathbf{v}_i - \mathbf{v}_j$, the square of the distance d between them is a simple quadratic function of time:

$$d(t)^2 = |\mathbf{r}_{ij} + \mathbf{v}_{ij}t|^2. \quad (1.6)$$

For spherical particles, a collision occurs when the center-to-center distance is equal to the particle diameter σ . Therefore, we are interested in the solution of the quadratic equation $d(t)^2 = \sigma^2$. If there are two roots to this equation, the particles are in contact between the first and second solution. The first root is given by:

$$t = \frac{-b - \sqrt{b^2 - v_{ij}^2(r_{ij}^2 - \sigma^2)}}{v_{ij}^2}, \quad (1.7)$$

with $b = \mathbf{r}_{ij} \cdot \mathbf{v}_{ij}$. When the particles collide, the velocities of both particles change by an equal but opposite amount:

$$\delta\mathbf{v}_i = -\delta\mathbf{v}_j = -b\mathbf{r}_{ij}/\sigma^2. \quad (1.8)$$

Here, we have assumed that the particles are perfectly frictionless, and that both energy and total momentum are conserved during the collision. With these equations, we can both predict and resolve collisions of two spheres. Similarly, predicting the next time a specific particle will cross over to the next cell is a matter of solving linear equations. With the ability to predict collisions and cell crossings, setting up a rough outline of the simulation is straightforward:

1. Initialize particle positions and velocities.
2. Predict and store next cell crossing for each particle.
3. Predict and store collisions between particles currently in neighboring cells.
4. Find the first predicted event, and move time forward to that moment.
5. In case of a cell crossing, update the cell list, and predict and store collisions of that particle with those in the new neighboring cells.
6. In case of a collision, update the particle velocities, delete all events related to both colliding particles, and predict and store new collisions for both.
7. In both cases, delete the old cell crossing event and predict the new cell crossing for the particle(s) involved in the event.
8. Repeat steps 4 through 7.

Note that to move time forward (step 4), there is no reason to update the positions of any particles that are not affected by the event that will now be resolved. Instead, we simply keep track of the last moment each particle was updated, and its position and velocity at that point, allowing us to calculate its position at any time it will be needed.

Whenever a collision (or other event) occurs, only the velocities of the particles involved change. As a result, any events previously predicted that do not involve those

particles remain unchanged. On the other hand, a particle has several predicted collisions associated with it at any time, which all need to be discarded whenever the velocity of the particle changes. While this may seem redundant, only keeping track of the *first* collision for each particle is impractical, because that prediction may never happen if the other colliding particle is deflected by a third particle before the collision occurs. To efficiently deal with the addition and deletion of events at every simulation step, we require a fast way to add and delete events from the event list. In addition, to be able to quickly find the first scheduled event for every step, the list should be time-ordered. As it turns out, the binary tree data structure can fulfill these requirements.[18] In this structure, each event node in the tree is linked to one 'parent' event and up to two 'children': one on the left, and one on the right (see Fig. 1.1). The left child event always takes place before the parent event, while the right child event happens at a later time than the parent. Thus, the first event in the tree is always on the far left, and can be found quickly by traversing the tree from the top, taking the left node down at every step until a node without a left child is reached. Similarly, when adding an event to the tree, the correct location for it can be found by starting from the top, and either choosing the left or right child at every step based on whether the new event will take place after or before the current node. As soon as an empty spot is found, the new event can be placed there. When deleting an event from the tree, any child events connected to it have to be relinked into the tree, taking care to maintain the chronological order of the nodes. Due to the structure of the event tree, any of these operations only affect a small part of the tree, and the time required to update the event tree is low, scaling with the logarithm of the total number of events.

In order to allow for quick removal of all events related to a specific particle, events are also connected via doubly-linked lists that join all events related to the same particle, as indicated by the colored arrows in Fig. 1.1. Because each event involves at most two particles, each event is linked into up to two of these lists. We use the cell crossing event related to each particle as the head of both linked lists. In other words, the cell crossing event for particle i is at the start of two linked lists: one for all events where particle i is the first particle involved (the solid lines in Fig. 1.1), and one for all events where particle i is the second particle involved (the dashed lines). The cell lists we employ consist of doubly linked lists as well. Table 1.1 summarizes the data stored for each particle and each event.

In an MD simulation, the temperature T is given by the average kinetic energy of the particles:

$$\sum_i \frac{1}{2} m \mathbf{v}_i^2 = \frac{3}{2} k_B T. \quad (1.9)$$

In a system of purely hard particles at constant volume, conservation of energy will ensure that the temperature is fixed. If particle interactions are present or the energy in the system is otherwise able to change, a thermostat can be used to keep the temperature constant. The simplest version of this is the Andersen thermostat, where at fixed intervals one or more particles are chosen at random and given a new random velocity drawn from a Boltzmann distribution of velocities corresponding to the desired temperature.

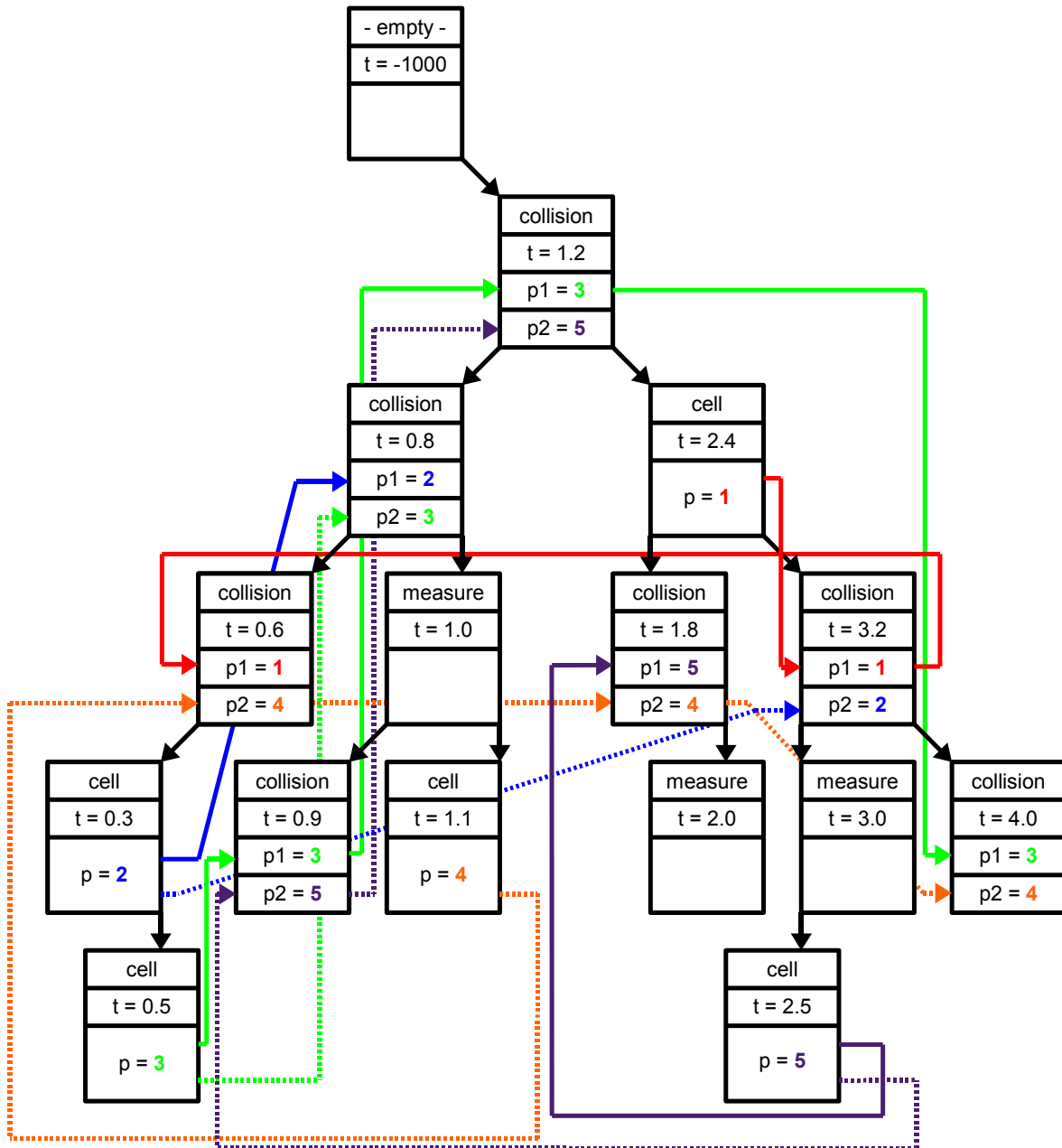


Figure 1.1: Illustration of the event tree structure for a small system. Each block represents an event: either a collision, cell crossing, or measurement. The root event at the top is empty, and only serves as a starting point for accessing the event tree. Left and right children of each event are represented by black arrows starting at the bottom left and right corner of the block, respectively. The colored arrows denote the linked lists linking events with the same particle as either the first (solid lines) or second (dashed lines) particle involved in an event, with different colors indicating different particles.

Particle	Event
Last update time t_{last}	Time of event
Position at t_{last}	First particle involved
Velocity at t_{last}	Second particle involved (if any)
Current cell	Parent event
Next particle in cell	Left child event
Previous particle in cell	Right child event
Cell crossing event	Next and previous event related to particle 1
	Next and previous event related to particle 2

Table 1.1: Data stored for each particle and event in a hard-sphere EDMD simulation.

If we choose our unit of length, energy and mass to be σ , $k_B T$ and m , respectively, the unit of time τ is given by:

$$\tau = \sqrt{m\sigma^2/k_B T}, \quad (1.10)$$

and roughly corresponds to the time an average freely moving particle takes to reach a distance of σ .

The pressure P in an EDMD simulation can be calculated from the total momentum transfer between particles, using the virial expression for the pressure, by averaging the sum of interparticle forces over all particle pairs over a time interval $[t_a, t_b]$:

$$P = \rho k_B T + \frac{1}{3V} \frac{\int_{t_a}^{t_b} \sum_{i < j} \mathbf{f}_{ij} \cdot \mathbf{r}_{ij}}{t_b - t_a}, \quad (1.11)$$

where $\rho = N/V$ is the number density in the system, \mathbf{f}_{ij} is the force between particles i and j and $\mathbf{r}_{ij} = \mathbf{r}_i - \mathbf{r}_j$ is the distance vector between them. In our case, the interparticle forces are given by delta peaks at the moments of collision, and for a single collision:

$$\mathbf{f}_{ij}(t) = \delta(t - t_{col}) \delta \mathbf{p}_i, \quad (1.12)$$

with t_{col} the time of collision, $\delta(t)$ the Dirac delta function, and $\delta \mathbf{p}_i$ the change in momentum for particle i . The pressure can then be written as:

$$P = \rho k_B T + \frac{1}{3V} \frac{\sum \delta \mathbf{p}_i \cdot \mathbf{r}_{ij}}{t_b - t_a}, \quad (1.13)$$

where the sum is taken over all collisions between particle pairs in the measured time interval, and i and j denote the two particles involved in each collision.

Anisotropic particles

Broadly, the same scheme that was described above can be followed for simulations of anisotropic particles as well. However, in addition to linear motion, particles now also rotate at a constant angular momentum while performing free motion. This extra movement makes predicting collisions analytically impossible in most cases. However, even

if collisions have to be predicted numerically, EDMD can still be an efficient simulation method.[20, 21]

To find the time of collision for two anisotropic particles, we define an overlap potential which can distinguish between overlapping and non-overlapping states. This overlap potential is a continuous function $f(\mathbf{r}_1, \mathbf{\Omega}_1, \mathbf{r}_2, \mathbf{\Omega}_2)$ of two particle positions \mathbf{r}_i and their orientations $\mathbf{\Omega}_i$, which is smaller than 0 if the two particles overlap, and larger than 0 if they are non-overlapping. Predicting a collision is then equivalent to solving the equation

$$f(\mathbf{r}_1(t), \mathbf{\Omega}_1(t), \mathbf{r}_2(t), \mathbf{\Omega}_2(t)) = 0, \quad (1.14)$$

where the dependencies of the particle positions and orientations on time are given by their free motion. Calculating the overlap potential for two particles is only required in the time intervals where their circumscribed spheres overlap (or in other words, when the center-to-center distance between them is smaller than their maximum interaction range). Collisions between circumscribed spheres of two particles can be predicted exactly as described above, and when such an event occurs the overlap potential f between the two particles and its time derivative are calculated on an evenly spaced grid of points in time. If an overlap is detected, numerical root-finding algorithms are used to determine the time of collision. If the derivative $\frac{df}{dt}$ changes sign from negative to positive, a grazing collision may have been missed, and the minimum of f is determined numerically and checked for a possible collision.

The only other major change required to simulate anisotropic particles is the resolution of predicted collisions. In the case of rigid non-spherical particles, the instantaneous force between the particles follows not only from conservation of energy and momentum, but also angular momentum. By again assuming that the particles are perfectly frictionless the forces can be chosen perpendicular to the colliding surfaces (or, in the case of a collision between two edges of sharp particles, perpendicular to both colliding edges). For a detailed description of the approach used for the prediction and resolution of collisions in the EDMD simulations employed in this thesis, see Ref. [20].

1.3 Dipolar interactions induced by external fields

One type of interaction that will be studied in several chapters in this thesis is a dipolar interaction induced by an external homogeneous electric field. In these systems, colloidal particles are suspended in a solvent with a different dielectric constant, and an electric field is applied to the sample using two electrodes. Due to the contrast in dielectric constant between the particles and the solvent, this induces a dipole moment in each particle in the direction of the field, leading to dipolar interactions between the particles. As a result, the particles tend to self-assemble into string-like clusters parallel to the electric field at low densities, and the crystal structures formed at higher packing fractions can be changed by the presence of dipolar interactions as well. These dipolar interactions can be induced with a magnetic field as well, if there is a difference between the magnetic susceptibility of the particles and that of the solvent.

To model the interactions between particles with induced dipole moments, we use the so-called point-dipole approximation: the dipole moment for each particle is assumed to

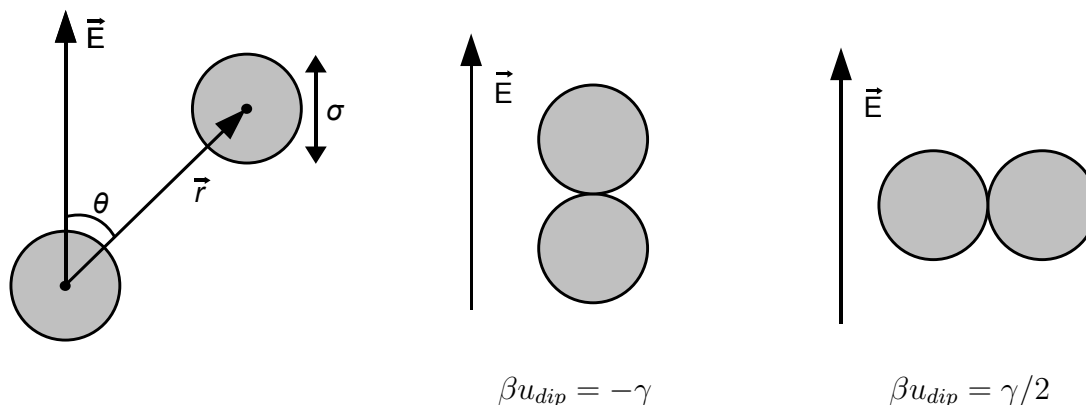


Figure 1.2: Illustration of the dipolar interaction in Eq. 1.15. The second and third picture show the configurations with the lowest and highest energy for two particles, respectively.

be concentrated in the center of the particle as a point dipole. This approximation ignores the fact that in reality, all of the material in each particle will be polarized to some degree, leading to higher-order multipole interactions at close range.[22] Additionally, the dipole moment of each particles is considered to be dominated by the external field. In reality, the field generated by the dipole moment in one particle can influence the polarization in another particle and vice versa, changing the strength and direction of the dipolar interactions. However, iteratively solving for the resulting polarizations of the colloids is too time-consuming to be practical in most simulations.

The interaction potential u_{dip} between two aligned point dipoles is given by:

$$\beta u_{dip}(r, \theta) = \frac{\gamma}{2} \left(\frac{\sigma}{r} \right)^3 (1 - 3 \cos^2 \theta), \quad (1.15)$$

where r is the distance between the two point dipoles, θ is the angle between the vector connecting the two particles and the direction of the dipole moments (and the external field), and σ is the unit of length in the system, usually chosen as the hard-core diameter of the particles. The prefactor γ determines the strength of the dipolar interactions, and in an experimental setup can be controlled by the strength of the external field. In the case of spherical particles with diameter σ in a local electric field \mathbf{E}_{loc} :

$$\gamma = \frac{(\epsilon_p - \epsilon_s)^2 \epsilon_s \pi \sigma^3 |\mathbf{E}_{loc}|^2}{(\epsilon_p + 2\epsilon_s)^2 8k_B T}, \quad (1.16)$$

where ϵ_p and ϵ_s denote the dielectric constant of the particle and the solvent, respectively.

As seen in Eq. 1.15, the dipolar interaction potential is proportional to r^{-3} . This slow decay can cause problems when simulating, as the potential energy of a particle in the system is strongly affected by the presence of particles far away. In order to deal with these long-range interactions, we make use of Ewald summations.[17, 23] In this technique, the calculation of the potential energy is split into a long-ranged part which is calculated in Fourier space, and a short-ranged part calculated in real space.

The phase behavior of monodisperse hard and soft spheres with aligned dipolar interactions has been shown to contain a string fluid, as well as hexagonally close-packed

(HCP), body-centered-tetragonal (BCT) and body-centered-orthogonal (BCO) crystal structures.[24–26] In this thesis, we will investigate the effects of external fields on several other systems including bidisperse spheres, asymmetric dumbbells, and cubes. In addition, we will study the phase behavior of spheres in a rapidly rotating (biaxial) electric field.

1.4 Outline of this thesis

In the rest of this thesis, we will study the self-assembly of a variety of systems. First, we investigate colloidal particles in external electric or magnetic field, where the induced dipole interactions are the main driving force behind the behavior of the system. In chapter 2 we look at the string-like clusters formed in these fields, and compare the results with both theory and experiments. In chapter 3 we study spherical particles in a biaxial field, leading to the formation of sheet-like structures. Chapter 4 describes the phase behavior of cube-shaped particles in an external field. In the next three chapters, we investigate bulk systems without external fields, starting with a more detailed study of the phase behavior of hard cubes in chapter 5. In chapter 6, we use a theoretical approach to predict the phase behavior of colloidal particles with a constant surface potential, and chapter 7 investigates the nucleation of a binary hard-sphere crystal phase. In the last three chapters we return to finite-sized clusters. Chapters 8 and 9 both study the structures formed by colloids compressed within an evaporating droplet, and in chapter 10 we examine colloidal micelles formed by asymmetric dumbbells with depletion interactions.

Self-assembly of colloidal strings in a homogeneous external electric or magnetic field

Colloidal particles with a dielectric constant (magnetic susceptibility) mismatch with the surrounding solvent acquire a dipole moment in a homogeneous external electric (magnetic) field. The resulting dipolar interactions lead to aggregation of the particles into string-like clusters. We use Monte Carlo simulations to investigate the structure of the self-assembled string-like aggregates in systems of both monodisperse and bidisperse dipolar hard spheres, as well as dipolar hard asymmetric dumbbells. For monodisperse systems, we show that the string length distributions in the dilute regime are in quantitative agreement with the predictions by the first-order thermodynamic perturbation theory of Wertheim. In bidisperse system, the particles aggregate in different types of clusters depending on the size ratio of the spheres. For highly asymmetric systems, the small spheres form ring-like and flame-like clusters around strings of large spheres, while for size ratios closer to 1, alternating strings of both large and small spheres are observed. For asymmetric dumbbells, we investigate both the effect of size ratio and dipole moment ratio, leading to a large variety of cluster shapes, including chiral clusters.

2.1 Introduction

The interactions of colloidal particles in a suspension can be tuned by the application of an oscillating external electric or magnetic field. Due to the contrast of the dielectric constant or magnetic susceptibility of the particles with that of the fluid, the particles obtain a dipole moment parallel to the field lines. At low field strengths, the resulting dipolar interactions between the colloids cause the particles to self-assemble into string-like structures along the field direction. These suspensions are called electro- (ER) or magneto (MR) rheological fluids, as their rheological properties can be tuned by external fields. [27, 28] These fluids can be used in a wide range of applications, e.g, hydraulic valves, brakes, clutches [27], displays [29], and bullet-proof army vests. For systems of monodisperse hard spheres with induced dipolar interactions, the phase diagram is well known from both experiments and simulations.[24–26, 30, 31] A stable string fluid exists at low field strengths and at low packing fractions, while at higher field strengths, a body-centered-tetragonal (bct) crystal structure is formed.

The string fluid can be compared to the formation of chain-like aggregates in ferromagnetic fluids, where the direction of the dipole moment of the particles is not fixed by an external field. The structure of these chains has been studied extensively, both for monodisperse and polydisperse systems.[32–36] In bidisperse or polydisperse systems, where the dipole moment scales with the particle volume, the larger particles dominate the formation of chains. Subsequently, the smaller particles can aggregate around these large-sphere structures, thereby hindering the formation of longer chains.[37] Previous studies showed that the size polydispersity greatly influences the electrorheological response, which can even be enhanced in an equimolar mixtures of large and small spheres.[38]

In highly asymmetric bidisperse systems of spheres with induced dipolar interactions, clustering leads to ring-like and flame-like clusters of small spheres around strings of large spheres. Mixtures of more similarly sized particles can form strings containing both types of spheres, sometimes regularly ordered. As the interactions causing these structures are induced by an external field, this provides a way of obtaining a variety of structures from spherical colloidal particles. A wider range of cluster shapes opens up if dipolar hard dumbbells are considered, with two spheres fused at a fixed distance. By tuning the size ratio and the ratio of dipole moments between the two parts of the dumbbell, a wide variety of structures can be formed. In earlier studies, various chiral structures were observed in similar systems, both experimentally [39] and in simulations.[40] More importantly, in a recent paper a new methodology has been presented to produce strings of various colloidal particles by applying electric fields, followed by thermal heating or seeded growth to make the strings permanent.[41] The authors also show that the length and even the flexibility of the beadchains can be controlled, and that the resulting systems can serve as colloidal analogues of charged and uncharged polymer chains with tunable flexibility. In this chapter, we use simulations to study the formation of strings in systems of aligned dipolar hard and charged spheres. In particular, we study the string length distributions for monodisperse systems, the formation of ringed and alternating strings in binary systems, and the structures formed in systems consisting of asymmetric dumbbells. In the case of binary systems, the field strengths needed to form binary strings are often so high that the string fluid phase is metastable with respect to a broad phase coexistence

between a dilute gas phase and a crystalline phase. However, due to the lower mobility of the larger strings compared to the single particles, the system can get kinetically trapped into a metastable fluid for long time scales at low packing fractions. As a result, one can study the resulting strings out of equilibrium in both experiments and simulations. We compare our results with preliminary experimental observations.

2.2 Model and simulation methods

We examine both hard and charged colloids in an electric field. For homogeneous particles of the same material, the dipole moment in an external field is proportional to its volume, leading to stronger dipole moments for larger particles. The dipole-dipole interaction for two particles with diameters σ_i and σ_j is given by:

$$\beta u_{dip}(r_{ij}, \theta_{ij}) = \frac{\gamma_{ij}}{2} \left(\frac{\sigma}{r_{ij}} \right)^3 (1 - 3 \cos^2 \theta_{ij}) \quad (2.1)$$

where $\mathbf{r}_{ij} = \mathbf{r}_i - \mathbf{r}_j$ is the center-of-mass distance vector between particles i and j , θ_{ij} the angle of \mathbf{r}_{ij} with the dipole moment (oriented along the z -axis), and $\beta = 1/k_B T$ with k_B Boltzmann's constant and T the temperature. We use the particle diameter σ as unit of length, which is chosen to be the diameter of the largest particle in the case of a binary mixture.

The factor γ_{ij} is determined by the strength of the electric field, which is chosen to be uniform along the z -axis:

$$\gamma_{ij} = \frac{\pi \sigma_i^3 \sigma_j^3 \alpha^2 \epsilon_s |\mathbf{E}_{loc}|^2}{8 k_B T \sigma^3}. \quad (2.2)$$

Here, $\alpha = (\epsilon_p - \epsilon_s)/(\epsilon_p + 2\epsilon_s)$ is the polarizability of the particles, ϵ_s the dielectric constant of the solvent, ϵ_p the dielectric constant of the particle, and \mathbf{E}_{loc} the local electric field. We define γ as the value of γ_{ij} for two particles of the largest size present in the system.

The hard-sphere interaction is given by:

$$\beta u_{hs}(r_{ij}) = \begin{cases} 0, & r_{ij} \geq \sigma_{ij} \\ \infty, & r_{ij} < \sigma_{ij} \end{cases}, \quad (2.3)$$

with $\sigma_{ij} = (\sigma_i + \sigma_j)/2$. In the case of charged spheres, a Yukawa potential is used to model the charge repulsions. For the interaction between particles of different sizes, we assume that the pair potential is given by the linear superposition approximation of the DLVO theory.[42, 43]

$$\beta u_Y(r_{ij}) = \begin{cases} \epsilon_{ij} \frac{\exp(-\kappa(r_{ij} - \sigma_{ij}))}{r_{ij}/\sigma}, & r_{ij} \geq \sigma_{ij} \\ \infty, & r_{ij} < \sigma_{ij} \end{cases} \quad (2.4)$$

$$\epsilon_{ij} = \frac{Z_i Z_j}{(1 + \kappa \sigma_i/2)(1 + \kappa \sigma_j/2)} \frac{\lambda_B}{\sigma}. \quad (2.5)$$

where Z_i is the charge of particle i , κ^{-1} is the Debye screening length, and $\lambda_B = e^2/4\pi\epsilon_0\epsilon_s k_B T$ is the Bjerrum length with e the elementary charge and ϵ_0 the vacuum permittivity.

We performed Monte Carlo (MC) simulations in the NVT ensemble, i.e. we fixed the number of particles N , the volume V and temperature T of the system. To handle the long-range dipolar interactions, we use Ewald summations with conducting boundary conditions.[17, 23] To improve equilibration and sampling speed in systems with strings, cluster moves were introduced to move particles residing in a cylindrical volume collectively. To maintain detailed balance, cluster moves that would change the number of particles present in this cylindrical volume were rejected.

Additionally, we perform simulations of hard dumbbells, which we model as two fused hard spheres interacting with the pair potential (2.1). Rotation moves were implemented to change the orientation of the dumbbells.

2.3 Monodisperse systems

We first investigate the string fluid regime for monodisperse dipolar hard spheres using NVT MC simulations of $N = 1200$ particles with diameter σ in a simulation box elongated along the field direction in order to accommodate long strings. We measured the probability distribution function $P(n)$ of string length n in the system for varying field strength γ . In Fig. 2.1 we plot $P(n)$ as a function of the number of particles n in a string for $\gamma = 5, 8, 9, 10$ and 11 , at a constant packing fraction $\eta = \pi\sigma^3 N/6V = 7.1 \cdot 10^{-4}$. Our simulation results are denoted by the symbols. We clearly observe that the lengths of the strings increase with both dipole strength γ and packing fraction η , leading to percolating strings at field strengths larger than $\gamma \simeq 10$. While two short strings repel each other when they are parallel to one another, sufficiently long strings attract, and the attraction increases as the strings become longer.[44] As a result, for high field strengths single strings are no longer stable, and thicker strings are formed. At even higher interaction strengths, the system forms crystalline domains with a bct structure. In experiments, strings were shown to self-assemble into metastable sheet-like structures before crystallizing.[45]

We compare our results with the first-order thermodynamic perturbation theory of Wertheim, which yields free energy predictions for associating fluids.[46–48] These free energy expressions can be used to predict the distribution of cluster sizes in equilibrium systems.[49] While the theory is more suitable for particles with short-ranged interactions, it can also be used to describe the formation of strings in a dipolar system.

To this end, we consider colloidal spheres with two binding sites in diametrically opposite positions. The first-order thermodynamic perturbation theory of Wertheim is based on the assumption that each binding site can only form one bond with another particle and that pairs of particles can only be single-bonded. These assumptions are satisfied in the string fluid regime for monodisperse dipolar spheres, assuming the packing fraction and field strength are low enough to ensure that all strings are well-separated. In this case, each particle can form a bond with at most two other particles. According to Wertheim theory the probability p_b that an arbitrary binding site is bonded can be determined from the chemical equilibrium between two non-bonded particles and a dimer cluster:

$$\frac{p_b}{(1 - p_b)^2} = \rho\Delta, \quad (2.6)$$

where Δ is calculated by integrating the Mayer function $f(\mathbf{r}) = \exp(-\beta u_{dip}(\mathbf{r})) - 1$ over

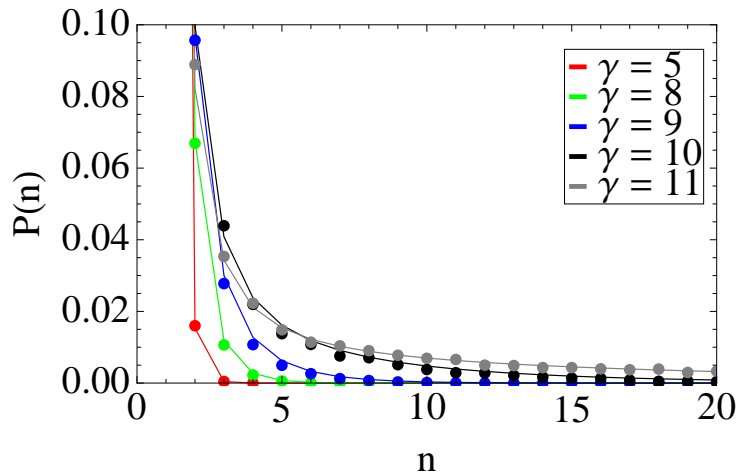


Figure 2.1: String length distribution $P(n)$ with n the number of spheres in a string for a fluid of dipolar hard spheres at packing fraction $\eta = 7.1 \cdot 10^{-4}$ and for various field strength γ as labeled. The symbols are obtained from simulations, the lines show the predictions from Wertheim theory.

the volume of a binding site:[46–48]

$$\Delta = \int_{site} d\mathbf{r} g(\mathbf{r}) f(\mathbf{r}) \quad (2.7)$$

$$\simeq 2\pi \int_{\theta=0}^{\theta_{max}} d\theta \int_{r=\sigma}^{r_{max}} dr f(r, \theta) r^2 \sin \theta, \quad (2.8)$$

with $g(r)$ the pair correlation function of a reference system at the same packing fraction. As the packing fractions for the studied string fluid systems are low, we use the ideal gas approximation $g(\mathbf{r}) \simeq 1$.

As the integral in Eq. 2.8 is over the volume of a single bonding site, θ_{max} is chosen to be the edge of this bonding site, where $u_{dip}(r, \theta) = 0$. The integral diverges logarithmically for $r \rightarrow \infty$, and therefore we have to choose a reasonable limit r_{max} for the distance at which particles can still be considered bonded. We have set $r_{max} = 2\sigma$.

In addition, the number density of monomers is $\rho_1 = \rho(1 - p_b)^2$, since for a monomer both sides are unbonded. Here we define $\rho = N/V$ as the particle number density. Similarly, the number density ρ_n of strings of length n is

$$\rho_n = \rho(1 - p_b)^2 p_b^{n-1}, \quad (2.9)$$

as the first and last particle in the chain have one unbonded site each. From Eq. 2.6, we can easily determine p_b once Δ is known. Using the bond probability p_b , we can determine the cluster size distribution $P(n)$:

$$P(n) = \frac{\rho_n}{\sum_{i=1}^{\infty} \rho_i} = (1 - p_b) p_b^{n-1}, \quad (2.10)$$

where $P(n)$ is the probability that a randomly selected string has a length of n , and $\sum_{i=1}^{\infty} \rho_i = \rho(1 - p_b)$, obtained by summing the geometric series over all chain lengths.

However, in our system there are correlations between nearby bonds, since the attractive potential of the dipoles extends beyond the distance of a single particle. As a result, a particle is more likely to be attached to longer strings. If we assume that neighboring particles in the string are at contact along the z -axis then the potential near the top of a string of length n is given by:

$$u(\mathbf{r}, n) = \sum_{i=0}^{n-1} u_{dip}(\mathbf{r} - i\hat{\mathbf{z}}). \quad (2.11)$$

This potential can then be used to calculate $\Delta(n)$ using Eq. 2.8 with the Mayer function corresponding to $u_n(\mathbf{r}, n)$. Subsequently, we can write a recursive relation for ρ_n :

$$\frac{\rho_n}{\rho_{n-1}\rho_1} = \Delta(n). \quad (2.12)$$

To calculate ρ_1 , we normalize this distribution using

$$\sum_{n=1}^{\infty} n\rho_n = \rho. \quad (2.13)$$

We plot the theoretical results (solid lines) along with the simulation results in Fig. 2.1. The theoretical predictions fit the simulation data for low packing fractions and field strengths very well, as shown in Figure 2.1. We obtain agreement between theory and simulations as long as the simulated strings do not cluster together or span the simulation box. As no fit parameters are required in the theory to match the simulation data, Wertheim theory allows a direct quantitative prediction of the distribution of string lengths in the dilute string fluid regime of hard dipolar spheres. In principle, it should also be straightforward to extend this theory to charged dipolar spheres, by adding a Yukawa repulsion in Eq. 2.8.

2.4 Bidisperse systems

2.4.1 Flame-like and ring-like clusters of small spheres

We now turn our attention to binary systems of large and small colloidal spheres with diameters σ_L and σ_S , respectively, with a large size asymmetry. The dipolar interactions as given by Eq. 2.1 and 2.2 are much stronger between the large particles than between the small particles. As a result, the formation of strings will be dominated by the clustering of the large particles. Additionally, the small particles may aggregate with the chains formed by the large particles. Due to the interactions between small and large particles, a circular attractive potential well arises for the small particles around the contact point of two large particles in the chain, and consequently the small particles can get trapped into this well.[33] Figure 2.2 shows a typical snapshot of the strings formed in a Monte Carlo simulation, as well as a confocal snapshot and a scanning electron microscopy picture of similar clusters in an experimental setup, all at size ratio $q = \sigma_S/\sigma_L = 0.25$. For details on the experimental setup, see the Appendix.

At size ratio $q = 0.25$, a maximum of 14 small particles can fit geometrically in this circular well in such a way that each small particle is in contact with both large spheres. At $q = 0.33$, only up to 10 particles fit in this well. However, the repulsive interactions between the small particles reduce the number of small particles per ring in the lowest energy state. We calculate the potential energy due to the dipolar interactions as a function of the number of small particles in the circular well around the contact point between two large spheres in a string of 2 and 15 large spheres. We plot the results for $q = 0.25$ (top panel) and 0.33 (bottom panel) in Figure 2.3. We clearly observe that for both size ratios the number of small particles in the lowest potential energy configuration increases for longer string lengths due to a stronger attractive potential around the contact points in a string. We like to mention here that entropic effects favor a lower number of particles per ring, as this allows for more free volume or entropy both inside and outside the cluster. In addition, we find from Fig. 2.3 that for a size ratio $q = 0.25$, the small particles get trapped in this well for $\gamma \simeq 50$ as the potential energy is $\sim 0.02k_B T$ per particle for string length 15. For such high fields, the string fluid of large particles is thermodynamically metastable with respect to a broad gas-solid transition. [26] In experiments, the large strings are partially stabilized by inhomogeneities in the external field, causing the strings to stay in local areas of high field strength and preventing them from clustering together. In standard MC simulations (without any (unphysical) cluster moves), the clustering of strings is inhibited as the mobility of the self-assembled strings is extremely low. Since the interactions with the small particles are much weaker, the small spheres can still sample phase space, and can reach equilibrium within the constraints given by the configuration of the larger particles.

Due to the dipolar interactions between the small and large spheres, the small spheres can also aggregate in a large potential well at the end of the chains (see the left side of Fig. 2.2). The resulting aggregate of small particles is wider near the string of large particles. In addition, the fluctuations of the cluster are more pronounced far from the strings, giving a flame-like shape to the cluster. Due to the larger and deeper potential well, a flame-like cluster will generally contain more small spheres than a ring-like cluster.

In order to study the structure of the binary strings, we performed MC simulations to study binary strings of dipolar hard spheres with a size ratio $q = 0.25$ and 0.33, both starting from a homogeneous random initial configuration, and from a configuration containing a single string of large spheres in a sea of small spheres. For the simulations starting from a random configuration, we used 100 large particles, and varied the number of small particles from 100 to 600. The overall packing fraction was well below 1% ($\eta_L = 0.002$), to keep the strings of large spheres from clustering. We indeed observe that the large particles self-assemble in linear strings parallel to the field direction and that small particles form ring-like and flame-like clusters around the strings of larger spheres. To determine the probability distribution of the number of small spheres in the ring-like clusters, we perform Monte Carlo simulations of a string of 15 large spheres at varying densities of small spheres. While the large spheres were allowed to move in the simulation, field strengths were always sufficiently high to prevent the string from breaking.

At the field strengths where the ring-like clusters are regularly seen, the flame-like clusters always appear as well. The presence of small particles near the ends of the strings of large spheres hinders the formation of long strings in the simulation, as it can take a

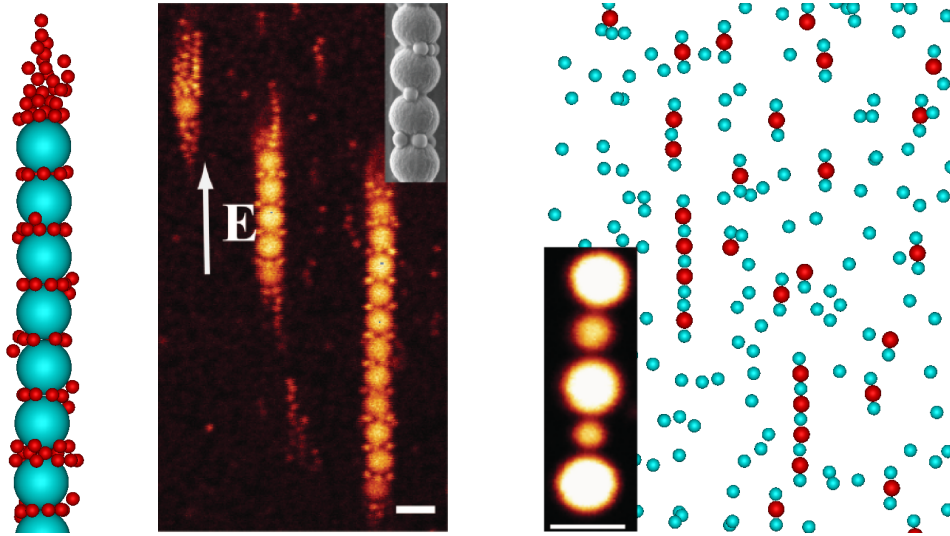


Figure 2.2: **Left:** Part of a snapshot of a typical configuration of a string of 15 large particles with rings of small particles, at size ratio $q = \sigma_S/\sigma_L = 0.25$. The field is along the vertical axis, and surrounding small particles have been removed. **Middle:** A confocal image and a scanning electron microscopy picture of an experimental system of strings with ring-like and flame-like clusters. The particles in the experiments are poly-(methylmetacrylate) (PMMA) spheres with diameters $\sigma_L = 2.4\mu\text{m}$ and $\sigma_S = 0.6\mu\text{m}$. The scalebar is $2\mu\text{m}$. **Right:** Typical snapshot of a bidisperse system of dipolar hard spheres at size ratio $\sigma_S/\sigma_L = 0.8$, with $N_S/N_L = 10$. Here, $\gamma = 102$, $\kappa\sigma_S = 1.0$, and $Z_S^2\lambda_B/\sigma_S = 100$. Most of the gaps between two large spheres contain exactly one small sphere. The field is along the vertical axis. The picture at the bottom left is a confocal image of a binary system of PMMA spheres with diameters $\sigma_L = 1.5\mu\text{m}$ and $\sigma_S = 1.05\mu\text{m}$.

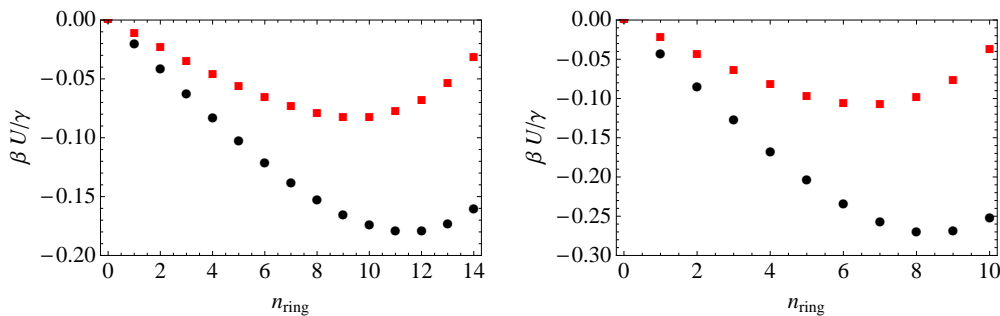


Figure 2.3: Potential energy of ring-like clusters of small dipolar hard spheres adsorbed near the contact point of two large dipolar hard spheres, in a string consisting of 2 large spheres (■) and 15 large spheres (●) as a function of the number of small spheres in the ring, i.e. n_{ring} . The size ratio between small and large spheres is $q = \sigma_S/\sigma_L = 0.25$ (left) and $q = 0.33$ (right). Interactions between the large particles are not included in the potential energy.

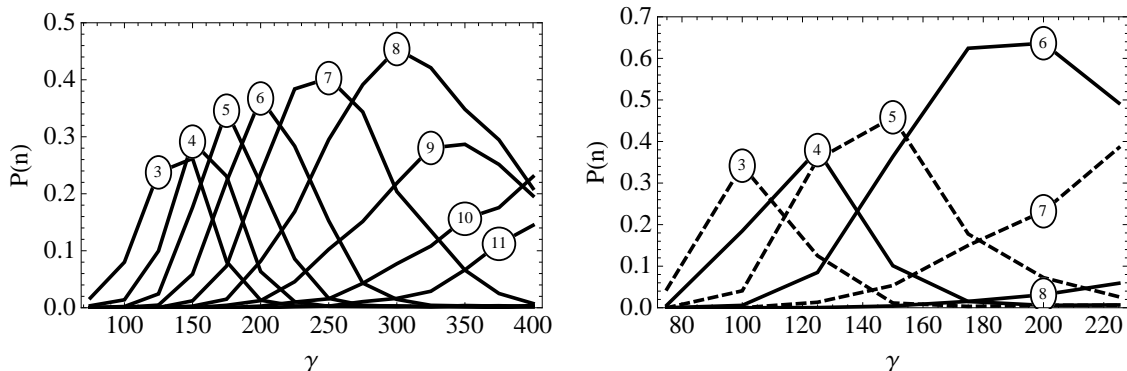


Figure 2.4: Probability distribution function $P(n)$ for a ring-like cluster of n small dipolar particles as a function of the field strength γ for a string of 15 large dipolar spheres, at small particle density $\eta_S = 1.9 \cdot 10^{-3}$. The size ratios are $q = 0.25$ (left) and $q = 0.33$ (right).

long time ($\gtrsim 10^5$ MC cycles) for the small particles to be pushed away from two merging strings. The ring-like clusters can be seen in a wide range of field strengths, and the occupancy of the ring rises as γ increases. Figure 2.4 shows the probability distribution of the ring sizes as determined from simulations at various field strengths, for size ratios of 0.25 and 0.33. The plots show a continuous increase of the number of small spheres per ring as a function of γ , as well as a preference over a large range of field strengths for 8 particles per ring at size ratio 0.25 and 6 at size ratio 0.33. It should be noted that the total number of small particles in the system is constant, and trapping many small particles in the ring-like and flame-like clusters decreases the density of free small particles. However, changing the density of small spheres did not change the probability distribution functions significantly.

For very high field strengths, we observe the formation of thicker ring-like clusters of small spheres around the contact point between two large spheres. Due to the weaker potential wells further away from the string, these thicker rings tend to be more disordered, and exchange small particles with the surrounding fluid at a faster rate.

2.4.2 Alternating strings

For less asymmetric systems, we observe the formation of binary strings that consist of alternating large and small particles. We studied the self-assembly of these strings for both hard and charged dipolar particles, using MC simulations of systems with several size ratios and a range of stoichiometries. The electrostatic repulsions are described by screened-Coulomb interactions (see Eq. 2.4), where the charge Z is chosen to be proportional to the surface area of the spheres. In all cases, the total packing fraction was below 1%. The simulations were performed in a rectangular box, elongated along the z -axis to allow for longer strings. All simulations are started from a random initial configuration. On the right in Fig. 2.2 we show a typical snapshot of the strings formed in a system of charged particles, together with a confocal image of a short alternating string taken from experiments.

The formation of alternating strings can be understood as the bond between a large and a small particle is significantly stronger than the bond between two small particles. In systems with many more small dipolar particles than large particles, the large particles will first bond with a small number of small ones on each side shortly after the field is turned on. These clusters will then join to form longer strings, with several interstitial small particles between the large ones. While in equilibrium the large particles are bonded in a string, the removal of the small particles is a slow process. The free energy barrier that these small particles have to overcome to escape the string is dependent on the number of small particles between two large spheres, and is highest for one small particle with two large neighbors.

For uncharged dipolar spheres, alternating strings were not observed with any regularity, as the potential energy differences are too small between configurations with one, two, or three small spheres in between two large ones. As a result, in sufficiently long simulations all interstitial small particles are removed from the strings, resulting in strings of large particles with small particles only at the ends.

Interestingly, simulations of charged particles show the self-assembly of alternating strings that remain stable on much longer time scales. Since the charge on each particle scales with the surface area, the bonds between the large spheres are relatively weaker, and hence configurations with more than one small particle between two large spheres in a string become less stable. While defects always appear, for inverse screening lengths on the order of σ_S and a size ratio of $\sigma_S/\sigma_L = 0.8$, the average number of small particles between two large spheres in a string can be tuned by the field strength. In order to study the field-strength dependence of the number of interstitial small spheres n_{IS} in between a pair of large spheres in a string, we determine the probability distribution $P(n_{IS})$ for varying γ .

Figure 2.5 shows the distribution of the number of small colloids between two large ones in the strings, for two different numbers of charges per colloid. The simulations consisted of $N_L = 50$ large and $N_S = 500$ small particles, at an overall packing fraction of $3.5 \cdot 10^{-3}$. Increasing the field strength increases the number of small particles per gap, as the stronger attractions hinder the escape of small particles from the strings. Interestingly, a large fraction of trimers, with one large particle sandwiched by two small particles, are also often seen in addition to the longer strings. While forming alternating strings is much easier with an added Yukawa repulsion, the formed configurations are still metastable states: if swap moves are introduced into the simulations, allowing a large and small particle to switch positions, the alternating strings rapidly change into strings consisting mainly of large spheres. However, without swap moves, these structures are stable even in long simulations, and the distribution of the number of small particles between two larger ones is approximately constant after equilibration, as shown in Fig. 2.6.

2.5 Asymmetric dumbbells

Finally, we investigate strings in a system of asymmetric hard dumbbells in an external electric field. Each dumbbell particle consists of a large and a small sphere, with diameters

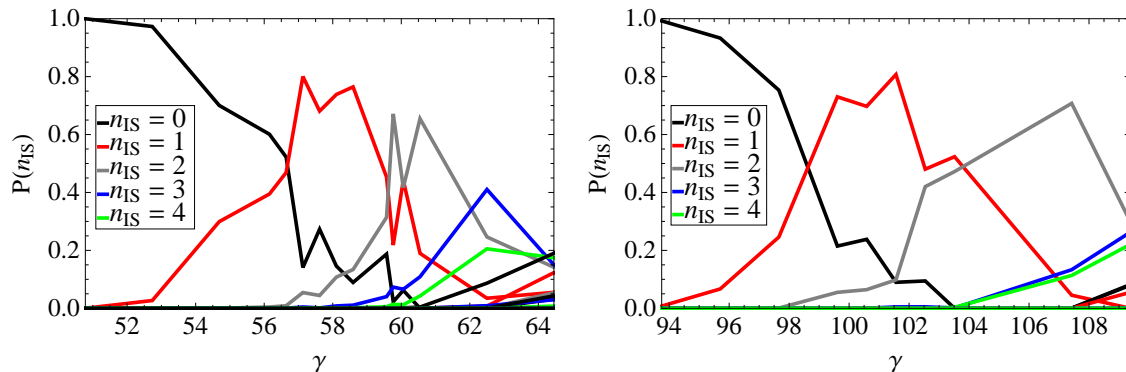


Figure 2.5: Probability distribution function $P(n_{IS})$ of the number n_{IS} of interstitial small dipolar particles between a pair of large dipolar spheres in a string, for $\kappa\sigma_S = 1.00$, $\eta_L = 6.3 \cdot 10^{-4}$, and $\eta_S = 2.9 \cdot 10^{-3}$, as a function of the field strength γ . The size ratio is $\sigma_S/\sigma_L = 0.8$. The particle charge for the left and right plot are given by $Z_S^2 \lambda_B / \sigma_S = 50$ and 100, respectively. The black circle indicates the state point where the snapshot in Fig. 2.2 was taken.

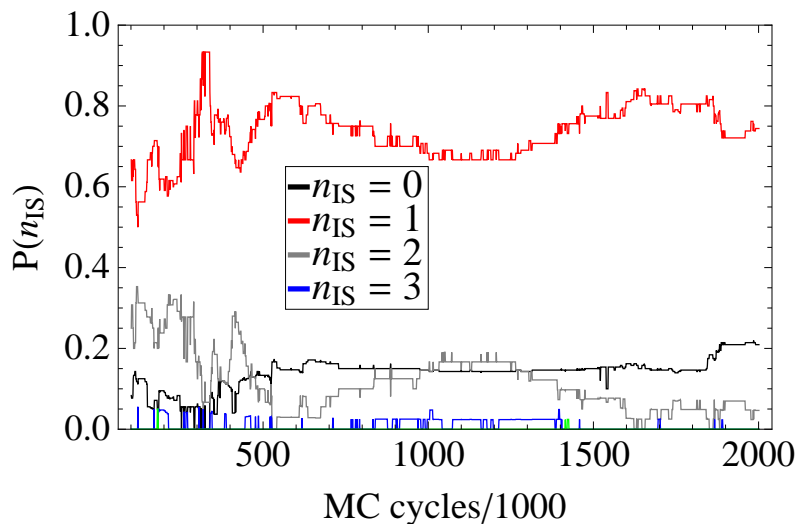


Figure 2.6: Time dependence of the probability distributions $P(n_{IS})$ shown in Fig. 2.5, showing how n_{IS} changes as a function of the number of MC cycles, where one MC cycle consists of $N_S + N_L$ trial moves of the particles. The same parameters were used as in Fig. 2.5, with $Z_S^2 \lambda_B / \sigma_S = 50$ and $\gamma = 58.6$.

σ_L and σ_S respectively, and a fixed separation distance $d \leq \sigma_{LS}$, where $\sigma_{LS} = (\sigma_L + \sigma_S)/2$. Each of the spheres contains a point dipole at its center that interacts with all others with interaction potential:

$$\beta u_{dip}(r_{ij}, \theta_{ij}) = \frac{\gamma p_i p_j}{2p_L^2} \left(\frac{\sigma}{r_{ij}} \right)^3 (1 - 3 \cos^2 \theta_{ij}). \quad (2.14)$$

Here, the dipole strength p_i for sphere i is determined by the size of the sphere, and is equal to either p_L or p_S for small and large spheres, respectively. The relative interaction strengths for the two types of spheres is therefore controlled by the ratio p_S/p_L , while the absolute interaction strength is determined by $\gamma = \gamma_{LL}$, as defined in Eq. 2.2.

Due to the interaction between the two spheres in a single dumbbell, a single particle favors an orientation aligned along the z-axis. Magnetic colloidal particles of this type have been seen to form chiral structures in experimental systems where the smaller part of the dumbbell acquires a much stronger dipole moment in the external magnetic field.[39] Recently, a variety of helical structures has been characterized as global potential minima for clusters of asymmetric dumbbells consisting of two Lennard-Jones particles and a point dipole directed across the axis between the spheres.[40]

Similar to systems of dipolar spheres, asymmetric dipolar dumbbells form strings at low field strengths and packing fractions, which grow in length and thickness as γ increases. We investigate the zero-temperature structure of these strings, and perform Monte Carlo simulations to study the behavior at finite temperatures.

We first consider hard dumbbells consisting of two adjacent hard spheres at separation distance $d = \sigma_{LS}$. The structure of a single string in the limit of strong fields (or zero temperature) mainly depends on the size ratio of the dumbbell σ_S/σ_L , and the ratio between the dipole moments of the two spheres p_S/p_L . By comparing the potential energy for a number of possible configurations, we can draw a phase diagram of the predicted structures as shown in Fig. 2.7. The candidate structures considered were head-to-toe and head-to-head strings, buckled strings, columnar structures, and helical structures. In the head-to-toe or head-to-head configuration, all spheres are centered on a straight line, with the dumbbells oriented all in the same direction or alternating between 'up' and 'down', respectively. The buckled strings consist of a central string of large spheres, with the smaller spheres pushed to either the side or the end of the string. When the dipole moment of the smaller spheres is sufficiently large, the central string consists of smaller spheres instead. For size ratio $\sigma_S/\sigma_L > 0.5$, the larger spheres arrange into two adjacent columns. For $\sigma_S/\sigma_L < 0.5$, the structure formed can either consist of two sets of these columns, or helical structures, strongly depending on the size ratio.

If the dipole moment of the spheres scales with the volume of the spheres, as would be the case if both parts are made out of the same material, the large particles will have the stronger dipole moment. The dashed line in Fig. 2.7 shows the structures formed in this case. Depending on the size ratio, the string only takes two shapes: aligned dumbbells in head-to-head orientations, or a string of large particles with the small particles all on the same side (except at the ends).

We wish to remark here that it is possible that we missed some structures, which can change the phase diagram. In particular, for highly asymmetric dumbbells where the dipole moment of the small sphere is large, the potential energies of helical and columnar

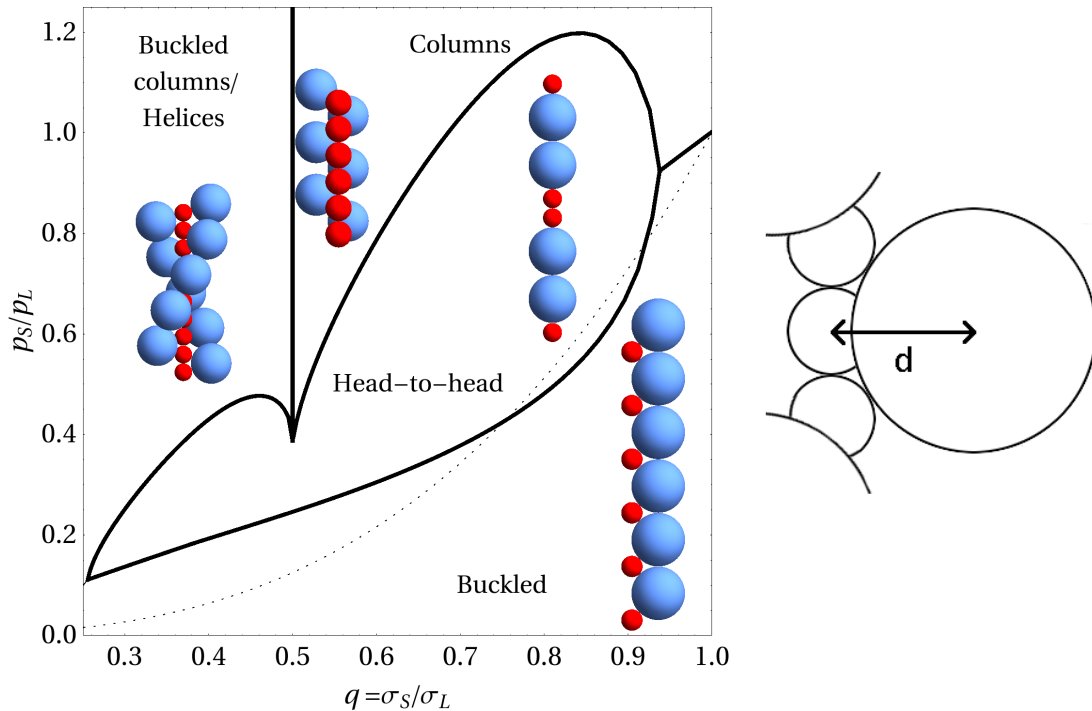


Figure 2.7: **Left:** Ground-state phase diagram for strings of 15 asymmetric dumbbells, as a function of size ratio q and dipole moment ratio p_S/p_L . The head-to-head configurations consist of alternating pairs of large and small spheres, while the buckled strings are strings of large particles with the small ones positioned at the contact points of two large particles. The columnar or helical structures consist of strings of small spheres with the large spheres arranged in multiple columns or in a helical structure. The dashed line illustrates dumbbells made out of one material. **Right:** Cartoon of three dumbbell particles arranged in a string, with d chosen such that the large part of the middle dumbbell touches the two small parts of its neighbours.

structures are close together. Since we only calculated the potential energies of a limited set of candidate cluster configurations, with highly regular orientations of the particles within the string, the possibility of more irregular structures being favored cannot be discounted. Therefore, the phase diagram shown in Fig. 2.7 is mainly a qualitative indication of the expected cluster shapes. However, the structures in the ground-state phase diagram agree qualitatively with structures seen in simulations using high field strengths.

The boundaries between the different structures shift slightly based on the length of the string, but the observed structures seen remain the same for longer strings. While changing center-of-mass distance d has some influence on the boundaries of these regimes, it does not seem to qualitatively change most of the self-assembled structures. However, changing d can strongly influence the columns and helices found at low size ratios with $p_L < p_S$.

To further investigate the possibility of helical strings, we performed simulations of highly asymmetric dumbbells, where the dipole moment of the small spheres was much

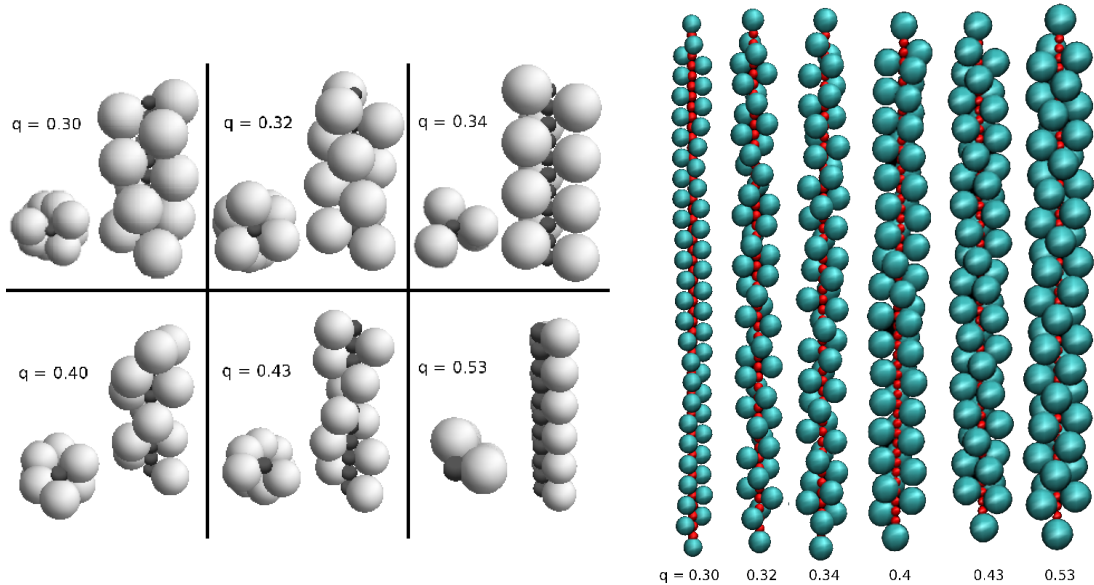


Figure 2.8: Left: Structures resulting from the energy calculations, at various size ratios. Here, $d = d_t + 0.01$, the same values as used in the simulations. The numbers indicate the size ratio. Both a side view and top view are shown for each size ratio. **Right:** Strings dipolar asymmetric dumbbells resulting from simulations starting with a string consisting of 50 particles, quenched to high field strengths, at various size ratios q as labeled and center-of-mass distance $d = d_t + 0.01$.

larger than that of the large spheres. For sufficiently high field strengths, the small spheres will form a string, with the large spheres sticking out to the sides. Depending on the size ratio, these large spheres can form either columns around the central string, or helical structures. These chiral structures appear due to the frustrations caused by hard-core interactions between the large spheres, which prevent them from lining up along the field direction. By constraining the large spheres to a narrow ring-like volume around their smaller partners, these frustrations cannot be compensated by small deviations parallel to the string. This restriction can be obtained by choosing the distance d between the two spheres of a dumbbell close to the minimum value d_t where the large particles touches the small spheres of nearby dumbbells in the string, as shown on the right in Fig. 2.7. For this case, the ground-state structures we obtained are shown on the left side of Fig. 2.8 for six different size ratios.

From the potential energy minimization, we find that at size ratios just above $\sigma_L/\sigma_s = 0.5$ the large form two columns close together and aligned parallel to the string. At slightly larger size ratios, this configuration would lead to overlaps, and each column becomes buckled. In this case, the two buckled columns tend to be on opposite sides of the string. For size ratio $q < 0.47$, the structure changes from columns to a double helix, decreasing in pitch length as q decreases. Close to a size ratio of $q = 0.33$, the structure crosses over to three vertical columns, turning into a triple helix once $q < 1/3$. For size ratios $q < 0.28$, the large spheres will overlap in any configuration. At this point, the string of

small particles will always be deformed.

We now perform MC simulations to investigate the formation of these structures. To this end, we first carried out a normal simulation at low field strength, to allow the dumbbell particles to form strings of sufficient length. Subsequently, we quenched these strings to high field strengths, which should then mostly affect the positions of the large spheres along these strings. These simulations were performed at low packing fractions $\eta \simeq 0.01$, with $N = 200$ dumbbell particles in the simulation box. For each size ratio, the distance d between spheres was chosen just above d_t to minimize fluctuations of the large spheres parallel to the string. Due to the high field strengths, the formation of the strings is a process far out of equilibrium. The resulting string length distribution is therefore not an equilibrium quantity that can be reliably measured from these simulations. Since we are mostly interested in the configurations of individual strings after quenching, these simulations can also be started from an initial configuration containing one long string. When quenching the system, the field strength is increased in small steps ($\Delta\gamma \simeq 1$) during the simulation, eventually freezing the system into a local energy minimum. At this point, we observe the resulting structures. Long strings form readily in systems with $q > 0.4$. For $q < 0.4$, the hard cores of the large spheres hamper the formation of strings of more than four or five dumbbells. More asymmetric size ratios will also hinder reconfigurations within the string, as the hard-core interactions severely limit the rotational freedom of the dumbbells. While chiral structures can be found in these simulations, defects and changes in the handedness are regularly seen, since both directions of chirality have equal probability.

On the right side of Fig. 2.8, we show snapshots from simulations starting from an initial configuration consisting of a straight string of 50 randomly oriented dumbbells. After quenching, we observe that structures are formed similar to the predicted ground-state structures, although defects in the structures exist in the structures resulting from simulations, as the system can get trapped in local energy minima during the quench. In these simulations, the dipole moment of the small spheres is 5 times that of the large spheres, which is large enough to prevent breaking or bending of the string. While the simulated strings show good agreement with the ground-state structures shown in Fig. 2.8, the spontaneous formation of regular chiral structures appears to be difficult. This may be a severe problem for experimentalists attempting to fabricate helical strings of asymmetric dumbbells by applying an external electric field. The difficulty can be explained by the fact that the energy costs involved in defects (which depend largely on next-nearest neighbor interactions) are small compared to the gain in entropy for additional disorder in the string. Additionally, the free energy barrier that has to be overcome to change the local direction of the chirality in a string is large, due to both hard-core interactions and attractive forces.

2.6 Conclusions

We investigated the self-assembly and structure of strings in systems of colloidal particles with dipole moments induced by an external field. For dilute fluids of monodisperse dipolar spheres dipoles, the distribution of string lengths can be effectively described

by a first order thermodynamic perturbation theory. This allows for a fast prediction of expected cluster sizes in string fluids, as long as strings do not cluster together. Potentially, this result could be used to obtain a rough estimate of the effective field strength in experimental systems if a string length distribution is known.

In binary systems, strings of large particles with both ring-like and flame-like clusters of small particles can be formed in highly asymmetric systems, where $q = \sigma_S/\sigma_L \ll 1$. In systems with a size ratio of $q = 0.8$ alternating strings can be formed instead. While these structures are not thermodynamically stable, they persist in simulations on very long timescales, and have been observed in experiments as well.

Asymmetric hard dumbbells can form a variety of structures in an electric field. When the particles are made out of a single material, the lowest-energy structures are head-to-head strings for nearly symmetric dumbbells, and buckled strings for more asymmetric particles. However, in the case where the dipole moment of the small spheres is sufficiently high, the lowest-energy structure consists of a string of small spheres, with the large spheres either positioned in multiple columns or in a helical structure around the string. It should be noted that defects are expected to be common in spontaneously formed clusters of dumbbells, due to the large free energy barriers involved in changing the chirality of the helical structure.

2.7 Acknowledgements

I would like to thank Rao Vutukuri for performing the experiments discussed in this chapter.

2.8 Appendix: Experimental setup

In the experimental setups shown in Fig. 2.2, the colloidal dispersion consisted of equal amounts (1.8 wt%) of small and large PMMA spheres in CHB. The polymethylmethacrylate (PMMA) particles were synthesized by dispersion polymerization, covalently labelled with the fluorescent dye 7-nitrobenzo-2-oxa-1, 3-diazol (NBD) or rhodamine isothiocyanate (RITC) and sterically stabilized with poly(12-hydroxystearic acid) [50]. We used both suspensions with a size ratio of 0.25 ($\sigma_L = 2.40\mu\text{m}$ and $\sigma_S = 0.60\mu\text{m}$) and size ratio 0.7 ($\sigma_L = 1.50\mu\text{m}$ and $\sigma_S = 1.05\mu\text{m}$). The particles were dispersed in a 3:1 wt/wt mixture of cyclohexyl bromide (Fluka) and cis-decalin (Sigma), saturated with tetrabutylammonium bromide (TBAB, Sigma). In this mixture, the particles were nearly density and refractive-index-matched, and they behaved like hard spheres [24]. All solvents were used as received without any further purification. The solutions were placed in sample cells with attached electrodes. After filling the cell with the colloidal suspension, we sealed at both ends with UV-curing optical adhesive (Norland no.68), and we studied particle dynamics by means of confocal laser scanning microscopy (Leica TCS SP2). An oscillating electric field was applied using a function generator (Agilent, Model 3312 OA) and a wide band voltage amplifier (Krohn-Hite, Model 7602M). Subsequently, the structures formed in the cell were permanently fixed using a thermal annealing method. The cell was then

carefully opened and dried on a scanning electron microscopy grid, and the remaining clusters were imaged with a scanning electron microscope (FEI, XL30FEG).

Phase diagram of colloidal spheres in a biaxial electric or magnetic field

Colloidal particles with a dielectric constant mismatch with the surrounding solvent in an external biaxial magnetic or electric field experience an “inverted” dipolar interaction. We determine the phase behavior of such a system using Helmholtz free energy calculations in Monte Carlo simulations for colloidal hard spheres as well as for charged hard spheres interacting with a repulsive Yukawa potential. The phase diagram of colloidal hard spheres with “inverted” dipolar interactions shows a gas-liquid transition, a hexagonal ABC stacked crystal phase, and a stretched hexagonal-close-packed (hcp) crystal. The phase diagram for charged spheres is very similar, but displays an additional layered-fluid phase. We compare our results with recent experimental observations.

3.1 Introduction

The phase behavior of colloidal particles in a suspension can be influenced by applying an oscillating external magnetic or electric field. If the magnetic susceptibility or dielectric constant of the colloidal particles differs from that of the solvent, the particles will acquire a dipole moment along an external uniaxial field, leading to dipolar interactions between the particles. In this way, the colloidal interactions can be tuned reversibly without having to modify the chemistry of the colloidal particles or the solvents involved. Hence, an external uniaxial electric or magnetic field leads to a greater control over the macroscopic phase behavior and structure of the colloidal system. The phase behavior of both hard and charged colloids with aligned dipolar interactions obtained by applying an external uniaxial field has been studied theoretically[51, 52] and experimentally[24, 25, 30, 31] extensively. In addition, the phase diagram of charged and uncharged dipolar hard spheres has been determined by free energy calculations using Monte-Carlo simulations.[26] In this work, it was shown that three new crystal structures, i.e., hexagonal-close-packed (hcp), body-centered-tetragonal (bct), and body-centered-orthorhombic (bco) phases, can be stabilized by applying an external uniaxial field. For completeness, we mention that the behavior of colloidal particles with permanent dipole moments in external fields [53–55] and in confinement [56, 57], has been widely investigated as well.

By applying multi-axial fields, more complicated anisotropic interactions can be induced, leading to the formation of more complex particle structures.[58] In this chapter, we determine the phase diagram of colloidal particles in an external biaxial electric or magnetic field, which can be obtained by rotating or randomly changing the field direction. Effectively, the particles have a rotating dipole moment in the plane of the rotating field. If the frequency of the rotating field is sufficiently high, the particles experience a rotationally or time averaged dipolar interaction, leading to a net attraction in the plane of the biaxial field, and a repulsion perpendicular to the field. The time-averaged dipolar interaction that the particles experience in a uniaxial field rotating in the xy -plane is just $-1/2$ times the dipolar interaction in a uniaxial field oriented in the z -direction, and can be regarded as a negative or “inverted” dipolar interaction. In contrast to the relatively simple dipolar interaction, the “inverted” dipolar interactions between the colloids give rise to a gas-liquid coexistence at low field strengths. At higher field strengths, large hexagonal sheets of particles form, eventually merging into a crystal phase.

Simulations of granular particles in various biaxial and multi-axial fields have been performed by Martin *et al.*,[58–61] with a focus on kinetics and non-equilibrium structures, as well as magnetic properties of the structures formed. The magnetic properties have also been compared to experimental results measured in systems of magnetic field-structured composites, formed by polymerizing the solvent while the particles are in the external field. [62] In a study of freely rotating permanent dipoles in a rotating field, Murashov and Patey showed the formation of sheet-like and layered structures for a range of angular velocities of the external field, using Molecular Dynamics and Brownian Dynamics simulations.[63] In these systems, the formation of layers highly depends on the moment of inertia of the dipoles and the frequency of the rotating field. More recently, colloidal systems in an external biaxial electric field have been investigated using confocal microscopy, [64] showing the formation of large hexagonal sheet-like structures, which were

made permanent by thermal annealing. The formation of these sheets in two-dimensional systems has also been studied experimentally [65] with the particles confined to an interface. In this chapter, we investigate using Monte Carlo simulations the equilibrium phase behavior of charged and uncharged colloidal hard spheres interacting with an “inverted” dipolar interaction. Additionally, we map out the phase diagrams for both systems using free energy calculations.

3.2 Methods

We perform Monte Carlo simulations in the canonical (NVT) and isothermal-isobaric (NPT) ensemble, where we fix the volume V and pressure P , respectively. In addition, we keep the number of particles N in the system fixed and the temperature T . We perform simulations of $N = 384 - 432$ particles. Larger systems were used for the layered-fluid phase and the low-density crystals to reduce finite-size effects. Finite size effects were checked by performing the same free energy calculation in a larger system ($N = 900$) at one point in each phase diagram. This caused the fluid-solid coexistence packing fractions to shift by less than 0.005 in both the charged and uncharged system, which remains within our statistical error bars.

Cluster moves were introduced to move or rotate clusters of particles at once in order to speed up equilibration of the layered-fluid phase. In the initial step of a cluster move, a random particle in the system is selected and taken as the center of the cluster. We construct a cylindrical volume around this particle with its symmetry axis aligned along the z -axis. The radius r_c and height h are selected randomly from a uniform distribution. For our simulations, we use $0 < r_c < \min(L_x, L_y)$ and $0 < h < \sigma$. All particles positioned with their center of mass in the cylinder are considered to be part of the cluster and are moved collectively. In the case of a rotation move, the particles are rotated around the central particle in the plane of the external field. In the case of a translation move, the particles are given the same random displacement $d\mathbf{r}$. The number of particles in the cluster volume is counted before and after the cluster move. If any new particles are present in the cluster volume after the move, moving the same cluster in reverse would also move these extra particles. As this would break detailed balance, any cluster moves where the number of particles in the chose cylinder around the central particle changes are rejected. Eventually, the translation or rotation is accepted or rejected based on the Boltzmann factor $\exp(-\beta(U_{new} - U_{old}))$.

In our model, we assume an external rotating electric or magnetic field in the xy -plane of our system. The colloidal particles experience an “inverted” dipolar interaction given by:

$$\beta u_{inv}(\mathbf{r}_{ij}) = -\frac{\gamma}{4} \left(\frac{\sigma}{r_{ij}} \right)^3 (1 - 3 \cos^2 \theta_{ij}), \quad (3.1)$$

where \mathbf{r}_{ij} is the center-of-mass distance vector between particles i and j , θ_{ij} denotes the angle that \mathbf{r}_{ij} forms with the z -axis, σ is the diameter of the particle, and $\beta = 1/k_B T$ with k_B Boltzmann’s constant. In the case of an external electric field \mathbf{E} , the dimensionless

prefactor γ in Eq. (3.1) is given by

$$\gamma = \frac{\pi\alpha^2\epsilon_s\sigma^3|\mathbf{E}|^2}{8k_B T} \quad (3.2)$$

where $\alpha = (\epsilon_p - \epsilon_s)/(\epsilon_p + 2\epsilon_s)$ is the dielectric contrast factor with $\epsilon_{p,s}$ the dielectric constants of the particles and the solvent, respectively. Similarly, in the case of an external magnetic field \mathbf{H} , γ is written as

$$\gamma = \frac{\pi\alpha^2\mu_s\sigma^3|\mathbf{H}|^2}{8k_B T} \quad (3.3)$$

where $\alpha = (\mu_p - \mu_s)/(\mu_p + 2\mu_s)$ and $\mu_{p,s}$ is the magnetic susceptibilities of the particles and the solvent, respectively. We note that for $\gamma = 1$, the maximum value of the pair potential, i.e. $0.5k_B T$, is reached, when two adjacent particles are aligned along the z -axis. The minimum value ($-0.25k_B T$) is obtained when both adjacent particles are in the xy -plane. In addition, the colloidal hard spheres interact with a hard-sphere potential given by

$$\beta u_{hs}(r_{ij}) = \begin{cases} 0, & r_{ij} \geq \sigma \\ \infty, & r_{ij} < \sigma \end{cases}, \quad (3.4)$$

while we use a repulsive hard-core Yukawa potential in the case of charged spheres

$$\beta u_Y(r_{ij}) = \begin{cases} \frac{\epsilon \exp[-\kappa(r_{ij} - \sigma)]}{r_{ij}/\sigma}, & r_{ij} \geq \sigma \\ \infty, & r_{ij} < \sigma \end{cases}, \quad (3.5)$$

where

$$\epsilon = \frac{Z^2}{(1 + \kappa\sigma/2)^2} \frac{\lambda_B}{\sigma} \quad (3.6)$$

is a constant prefactor depending on the colloidal charge number Z , Debye screening length κ^{-1} and Bjerrum length $\lambda_B = e^2/\epsilon_s k_B T$ with e the elementary charge. Eq. (3.5) is the pair potential given by the Derjaguin-Landau-Verwey-Overbeek theory for charged colloids.[42] We have neglected the Van der Waals attraction in Eq. (3.5) as we are interested in refractive index matched systems. The repulsion increases the distance between the layers of the crystal phase, and causes part of the liquid phase to form fluid-like layers.

The Ewald summation is employed to calculate the long-range dipolar interactions.[17, 23] The calculation of the “inverted” dipolar interactions using the Ewald summation method is largely identical to the method used for normal dipolar systems, with the exception of the term related to the boundary conditions. In this case, we assume conducting boundary conditions. We first note that the “inverted” dipolar interaction, which is formed by a time-averaged rotating dipolar interaction in the xy -plane, is identical to the averaged interaction induced by two perpendicular external uniaxial fields in the xy -plane. Hence, the total potential energy of the system is the average of two energy calculations. The correction factor can be derived by summing the effect of the boundary conditions on both of these calculations.

For non-conducting boundary conditions, the total potential energy of a specific configuration $\{\mathbf{r}^N\}$ of the “inverted” dipolar system U_{inv}^{nc} equals the average of the total potential energy of two dipolar systems with uniaxial fields in the x and y directions:

$$U_{inv}^{nc} = \frac{U_x^{nc} + U_y^{nc}}{2} = -\frac{1}{2}U_z^{nc}. \quad (3.7)$$

For normal dipolar interactions the difference between non-conducting and conducting boundary conditions is given by:[17]

$$U_{x,y,z}^{cond} = U_{x,y,z}^{nc} - \frac{2\pi}{3V}\mathbf{M} \cdot \mathbf{M}, \quad (3.8)$$

where U^{cond} is the interaction with conducting boundary condition and \mathbf{M} is the square of the total dipole moment of the system, with $\mathbf{M} \cdot \mathbf{M} = \gamma N^2/2$. Combining the difference in potential energy between conducting and non-conducting boundary conditions for the two dipolar systems with perpendicular uniaxial fields, yields:

$$U_{inv}^{cond} = \frac{U_x^{cond} + U_y^{cond}}{2} \quad (3.9)$$

$$= \frac{U_x^{nc} + U_y^{nc}}{2} - \frac{2\pi}{3V} \frac{\gamma N^2}{2} \quad (3.10)$$

$$= -\frac{1}{2}U_z^{nc} - \frac{2\pi}{3V} \frac{\gamma N^2}{2} \quad (3.11)$$

$$= -\frac{1}{2}U_z^{cond} - \frac{\pi}{V} \frac{\gamma N^2}{2}. \quad (3.12)$$

As a result, we can calculate the potential energy of a biaxial system with conducting boundary conditions U_{inv}^{cond} from the energy of the same configuration in a system with normal dipolar interactions by multiplying the energy by $-1/2$ and adding the above correction term $-\pi\gamma N^2/2V$.

The Helmholtz free energies of the ABC stacked crystals were calculated using the Einstein integration method.[17, 66] In addition, we calculate the Helmholtz free energy as a function of density by integrating the equation of state. We determine the coexisting densities with the fluid phase by employing the common tangent construction. At high densities, a coexistence between face-centered-cubic (fcc) and hexagonal-close-packed (hcp) crystal phases occurs. The free energy difference between these structures is on the order of $10^{-3}k_B T$, and therefore hard to measure with sufficient statistical accuracy using this method. Instead, we use the hard-sphere crystal as a reference state for both structures, and calculate the free energy as a function of the interaction strength by using a thermodynamic integration path consisting of a gradual increase in the field strength. For these crystals, only the free energy difference between hcp and fcc stacking is needed, which was linearly interpolated from literature values for this difference at coexistence and close packing [67]. Due to the narrow coexistence region, and a large estimated error in the free energy calculations, we only show one coexistence line between these high-density crystal phases. The estimated error in the coexistence field strength γ is on the order of 0.5. For the fluid phase, the hard-sphere fluid (using the equation of state by Speedy [68]) and ideal gas were used as reference states for the liquid and the gas, respectively.

For the free energy of the layered-fluid phase in the case of charged spheres, we use a method similar to the one employed by Bolhuis and Frenkel for the smectic phase of hard spherocylinders.[69] Via a thermodynamic integration path, we relate the free energy of the layered fluid in the system of charged spheres with inverted dipolar interactions to the free energy of a hard sphere fluid. This integration is done in two steps. We first couple the particles to their layers by applying an external sinusoidal potential while turning off the interactions. The resulting potential in the system depends on a switching coefficient λ :

$$U(\lambda) = \lambda U_{sin} + (1 - \lambda)U_{int}, \quad (3.13)$$

$$= \lambda \alpha \sum_{i=0}^N \sin(2\pi n_l z_i / L_z) + (1 - \lambda)U_{int}, \quad (3.14)$$

with U_{sin} and U_{int} the total energy in the system due to the external potential and the particle interactions, respectively. The factor α is the strength of the sinusoidal potential and is chosen such that the particles in the layer remain disordered for all $0 < \lambda < 1$. The number of layers n_l and the height of the box L_z are chosen such that they match the equilibrium layer spacing measured from independent NPT simulations. The free energy difference between $F_{inv} - F_{sin}$ the system with inverted dipolar interactions and the system with the sinusoidal potential is given by:

$$\beta(F_{inv} - F_{sin}) = \int_1^0 d\lambda \langle U_{sin} - U_{int} \rangle_\lambda - \ln V. \quad (3.15)$$

The resulting system consists of hard spheres confined to layers by the external potential. To allow equilibration of the density within the layers throughout the whole system, we use shifted boundary conditions, such that the fluid layers are interconnected at the edges of the simulation box. In our simulation, a particle that leaves the simulation box in the x -direction, does not only enter the simulation box at the opposite face, but is also shifted in the z -direction by one fluid layer, i.e., by L_z/n_l . The direction of the shift is determined by the direction in which the particle leaves the simulation box. In this way, the particles can diffuse throughout the whole system, as there is effectively one single layer, which allows for the relaxation of the density within each fluid layer. Of course, the energy calculations should also incorporate this shift. For the Yukawa interaction and the real space contribution of the Ewald sums, this can be done by simply calculating the energy from the relevant image particles. For the reciprocal space contribution of the Ewald summation, we use the fact that the system is still periodic along x , but with a period n_l times larger and with n_l times more particles. Since the contributions from these extra particles are the same as those in the original box, but multiplied by a complex factor, the energy calculation does not require significant extra computer time.

The free energy of the system of pure hard spheres in an external sinusoidal potential can be calculated in two ways. Turning off the potential, the system transforms gradually into an isotropic hard-sphere fluid, which can be used as a reference state. The free energy difference between the hard sphere fluid and hard spheres in an external sinusoidal potential can be calculated similar to Eq. 3.15, but without inverted dipolar interactions. Combining the two steps, the free energy of the layered fluid can then be calculated as:

$$\beta F_{inv} = \beta F_{HS} + \int_0^1 d\lambda \langle U_{sin} \rangle_\lambda^{HS} + \int_1^0 d\lambda \langle U_{sin} - U_{int} \rangle_\lambda,$$

with F_{HS} the free energy of a hard sphere fluid at the same density as the layered fluid, and with the first integral evaluated without inverted dipolar interactions. Alternatively, if the strength of the external sinusoidal potential is sufficiently high, the particles are strongly constrained to their layer and the system behaves effectively as a two-dimensional hard-disk fluid with additional harmonic vibrations perpendicular to the plane, for which one can calculate the free energy analytically. We checked that the free energies using both methods are equal within our statistical errorbars. However, since integrating to a hard sphere fluid uses a shorter integration path, the numerical errors in this method are smaller. Note that two integration paths are needed: in the first path, we switch off the inverted dipolar interactions, but we have to switch on an external sinusoidal potential to keep the symmetry of the fluid. In the second path, we turn off the sinusoidal potential to obtain a homogeneous fluid phase.

3.3 Hard spheres in a biaxial field

We plot the calculated phase diagram for hard spheres in a biaxial field in Fig. 3.1. In Fig. 3.2, we show snapshots of the system in various phases, as denoted by the crosses in the phase diagram (Fig. 3.1). At $\gamma = 0$, the well-known hard-sphere fluid-fcc (hexagonal ABC stacked) phase behavior is recovered. As opposed to the normal dipolar hard spheres,[26] we find at $\gamma \simeq 6$ a gas-liquid coexistence for this system. We note that well-inside the gas-liquid coexistence region, system-size spanning slabs of liquid and gas are formed, which are aligned in the plane of the rotating field. Moreover, the system can phase separate and/or change phase very easily. It is tempting to speculate that these observations are due to a strongly anisotropic gas-liquid interfacial tension, which is much lower for the plane parallel to the biaxial field than the orthogonal planes.

Additionally, we find two stable crystal structures in the phase diagram. At maximum packing the fcc crystal is favored for low field strengths due to the small free energy difference between fcc and hcp, where fcc is the most stable phase in the case of hard spheres ($\gamma = 0$). The orientation of the crystal phase with respect to the field has no effect on its energy when the crystal is not deformed, however, at non-zero field strengths, the crystal is compressed in the plane of the field and stretched in the perpendicular direction, leading to a difference in free energy between the possible orientations for the crystal. As a result, the stable structure consists of hexagonal sheets parallel to the field plane.

The lowest-energy structure of this system is a close-packed hcp crystal, with the hexagonal planes perpendicular to the plane of the rotating field. The energy per particle for this orientation ($-1.48138(1)\gamma kT$) is slightly lower than that of hcp with sheets oriented parallel to the field ($-1.48012(1)\gamma kT$) or that of fcc ($-1.48096(1)\gamma kT$, for any orientation). Evidently, the free energy difference between fcc and hcp is very small for the different orientations, and hcp is only stable in a small pocket at very high densities. At lower densities, the stable structure is fcc. We wish to remark here that the fcc and the hcp phases are not entirely symmetric, but are slightly stretched in the z -direction. Hence, the fcc phase is an ABC-stacked crystal of hexagonal sheets, oriented along the xy -plane, while in the hcp phase the hexagonal planes themselves are stretched. Stacking defects are likely to occur, since the free energy loss is only on the order of $10^{-3}kT\gamma$ per

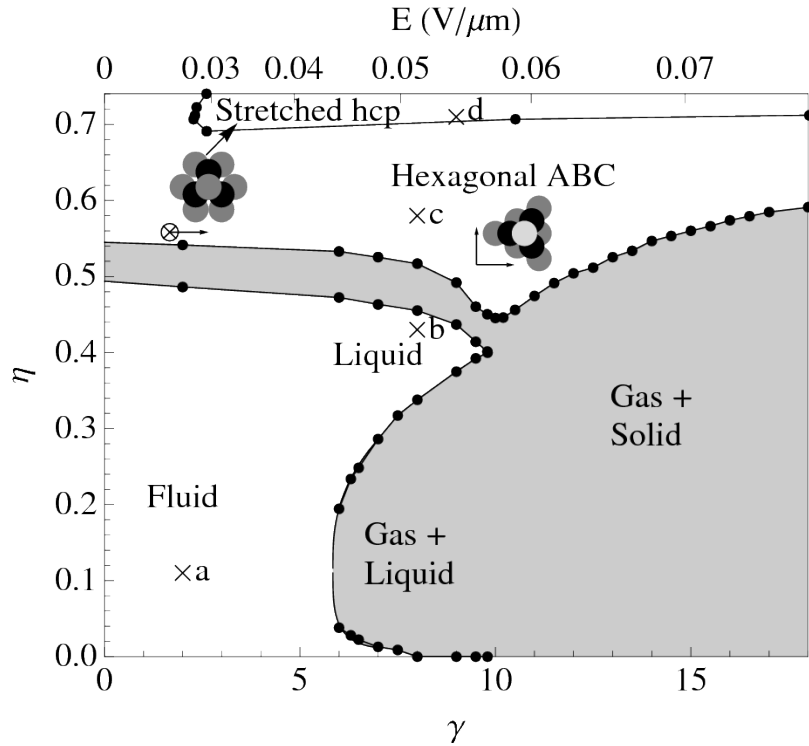


Figure 3.1: Phase diagram for hard spheres in an external biaxial electric or magnetic field in the dipole moment strength γ versus packing fraction η representation. The black circles denote the points where the phase boundaries were determined, while the gray areas denote the coexistence regions. The tielines that connect the coexisting phases are vertical. The hexagonal ABC stacked crystal phase can be regarded as an fcc crystal, which is stretched in the direction perpendicular to the field and is oriented with the hexagonal planes parallel to the plane of the biaxial field, as illustrated by the two perpendicular arrows indicating the plane of the field in the schematic picture. The stretched hcp is oriented with the hexagonal planes perpendicular to the biaxial field, as illustrated by the \otimes and arrow in the picture, with \otimes indicating the axis perpendicular to the page, and is slightly stretched in the direction perpendicular to the field. The top axis shows the electric field strength corresponding to the dipole moment strength γ , using the experimental values $\alpha = -0.22$, $\epsilon_s = 5.8\epsilon_0$, $\sigma = 2\mu\text{m}$, and $T = 300\text{K}$. [64] The crosses denote the points where the snapshots in Fig. 3.2 were taken.

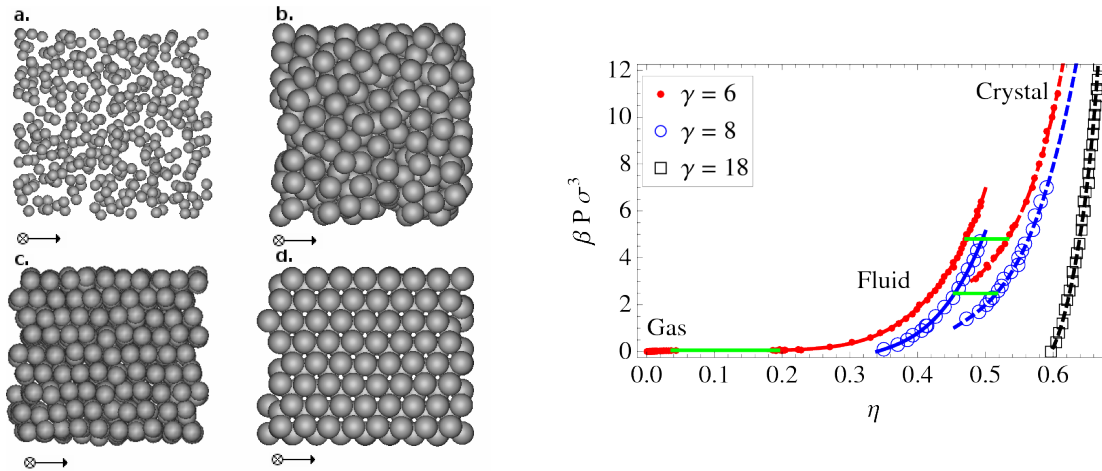


Figure 3.2: Left: Snapshots of typical simulation configurations for hard spheres with inverted dipolar interactions. The arrows indicate the two field directions, with \otimes indicating the axis perpendicular to the page. **a)** A low-density fluid at $\gamma = 2, \eta = 0.11$. **b)** A higher density fluid, with $\gamma = 8$ and $\eta = 0.43$. **c)** Crystalline ABC-stacked hexagonal layers of spheres at $\eta = 0.58$ and $\gamma = 8$. **d)** The stretched hcp crystal at $\gamma = 9, \eta = 0.71$. Note that the stretched hexagonal planes are perpendicular to the field plane.

Right: Equations of state for hard spheres with inverted dipolar interactions at field strengths $\gamma = 6, 8, 18$. The lines are fits through the data, using dashed lines for the crystals and solid lines for the fluids. The green horizontal lines show the coexistences. For $\gamma = 8$ and 18 the coexistences with a gas at near-zero pressure have been omitted.

particle at close packing, and becomes even lower at lower densities.

Solitary sheets or rafts can appear at high field strengths whenever there are insufficient particles in the simulation box to form a box-spanning sheet. However, if the fields are strong enough to form these structures, and there are multiple sheets in the box, they will join into a crystal if their orientation matches, showing that these structures are not stable on their own. Our phase diagram explains these findings as it displays indeed an enormous widening of the solid-gas transition for increasing γ . We note that the tielines that connect the coexisting phases are vertical in Fig. 3.1. Hence, the coexisting gas and solid phases becomes progressively more dilute and dense, respectively, upon increasing γ , yielding coexistence of a dense solid phase with a gas phase, which is extremely dilute.

Equations of state for the fluid and fcc phases at field strengths $\gamma = 6, 8, 18$ are shown on the right side of Fig. 3.2. For $\gamma = 6$, a gas, liquid and solid branch are shown, with the coexistences denoted by horizontal lines. For $\gamma = 8$, only the liquid and solid branch are shown, as the liquid coexists with a gas at near zero density. At $\gamma = 18$, we show only the fcc branch, which again coexists with an extremely dilute gas.

3.4 Charged spheres in a biaxial field

The colloidal particles that are used in experimental systems are often charged, due to ionisable groups on their surfaces, which dissociate when suspended in a solvent. The bare

Coulombic repulsions between the colloidal particles are then screened by the ions in the solvent, leading to a Yukawa or screened-Coulombic interaction.[42] In our simulations, we choose an inverse screening length of $\kappa\sigma = 10$, and surface charge $Z^2\lambda_B/\sigma = 450$. The phase diagram for charged spheres in an external biaxial field is shown in Fig. 3.3. In Fig. 3.4, we show the equations of state for three field strengths. For $\gamma = 10$, the fluid and crystal branch are shown. At $\gamma = 16$, the liquid and solid branch are shown, omitting the coexistence with a gas at near zero pressure. For $\gamma = 24$, we again show only the crystal branch, which also coexists with a gas at extremely low pressures.

At $\gamma = 0$, we find a fluid-fcc (hexagonal ABC) coexistence with coexisting packing fractions $\eta_{fluid} = 0.31$ and $\eta_{fcc} = 0.32$. Additionally, we again find a gas-liquid coexistence, which is shifted to much lower densities compared to that of hard spheres. Moreover, the coexisting liquid becomes inhomogeneous for field strengths $\gamma > 16$, and system-size spanning fluid-like layers are formed with their orientations aligned in the plane of the rotating field. Fig. 3.4c shows a typical configuration of a layered-fluid phase. The inhomogeneous structure of the fluid phase can be explained by the Yukawa repulsion between the particles, which not only increases the distances between the particles within each sheet, but also induces a repulsion between neighboring sheets. Particles can diffuse from one layer to another, but close to the triple point, this process slows down significantly. In addition, we also observe large fluctuations in the distances between adjacent sheets at low pressures, indicating a low free energy cost to create an interface between the gas and the layered-fluid phase. Consequently, at low densities the system can easily form small numbers of fluid layers, which are separated by a dilute gas phase. It is likely that the same would happen in experiments at low packing fractions, especially when the sheets are too large to move easily. At low field strengths, a stable homogeneous liquid exists in between the layered-fluid phase and the stable crystal phase, but disappears when $\gamma > 19$. The transition between the layered-fluid phase and the isotropic liquid appears to be continuous as no hysteresis can be seen in the equation of state, and the amplitude in the density profile of the layers changes continuously with field strength and density. Exemplarily, the left side of Fig. 3.5 displays the pair correlation function that measures the positional order in the direction perpendicular to the field for varying packing fractions. We indeed observe clearly that the amplitude decreases continuously with increasing packing fraction.

The lowest energy state of the system now depends on the field strength: at close packing and $\gamma > 5.9168(2)$, the dipolar interactions dominate the Yukawa interactions, and hcp is the ground state. At lower field strengths, the Yukawa interactions cause the system to favor the fcc phase. Due to the entropy difference for hard spheres between fcc and hcp ($0.0011(1)kT$ per particle at close packing [67]), the phase transition between the two structures appears at slightly higher field strength than $\gamma = 5.9168$, i.e., $\gamma = 8.4(4)$. We again note that the hexagonal planes of the fcc and hcp phase are parallel and perpendicular respectively to the plane of the biaxial field (xy -plane) and that both structures are stretched in the z -direction. Hence, the fcc phase is a hexagonal ABC stacked crystal phase, and the hcp is a slightly stretched hcp phase.

We also find that the coexistence region between a dilute gas phase and the ABC stacked crystal becomes wider upon increasing γ . However, the density of the crystal at coexistence is much lower than in the hard sphere case, mainly due to a larger distance

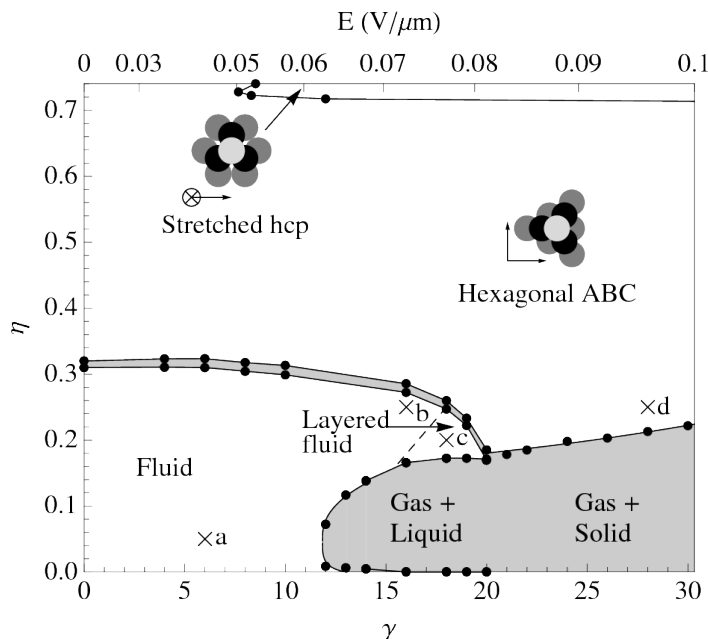


Figure 3.3: Same as Fig. 1, but for a system of charged spheres interacting with a Yukawa interaction. The inverse screening length $\kappa\sigma = 10$, and $\lambda_B Z^2/\sigma = 450$ ($\epsilon = 12.5$). The layered-fluid phase consists of system-spanning slabs of fluid aligned in the plane of the biaxial field. The crosses indicate the positions in the phase diagram where the snapshots in Fig. 3.4 were taken.

between adjacent sheets (as shown in Fig. 3.4d). As the distance between the sheets increases, the effect of the relative position and orientation between neighboring sheets on the potential energy reduces significantly, leading to a large amount of disorder in the position and orientation of the sheets. We observe that the distance between the sheets can fluctuate significantly during our simulations at low densities. However, the crystal is still the stable phase. In the bulk limit, the entropy gain from detaching a sheet from the crystal would be dominated by the energy cost to detach an infinite sheet of particles. Consequently, the fcc crystal will be the thermodynamically stable phase in the bulk limit. In finite systems, however, the sheets will be translationally and rotationally disordered. The translational disorder can be clearly seen to appear in simulations: when a crystal phase is used as the initial configuration, the layers of the crystal become disordered during simulations at low density. Rotational disorder does not emerge in crystals in a rectangular periodic box, but is expected to appear in experimental systems. At low pressures, the separations between the hexagonal sheets fluctuate substantially, resulting in large density fluctuations. It is likely that these fluctuations contribute to the disorder of the sheets as well.

On the right side of Fig. 3.5 we plot the difference in potential energy per particle $\beta\Delta U$ of various stackings of the hexagonal crystalline sheets in the crystal phase with ABC stacking, as a function of sheet distance Δz for $\gamma = 30$. In addition, we plot the contribution of the Yukawa interaction to this potential energy difference, denoted by the dashed lines, and we observe that the contribution from the dipolar interaction dominates

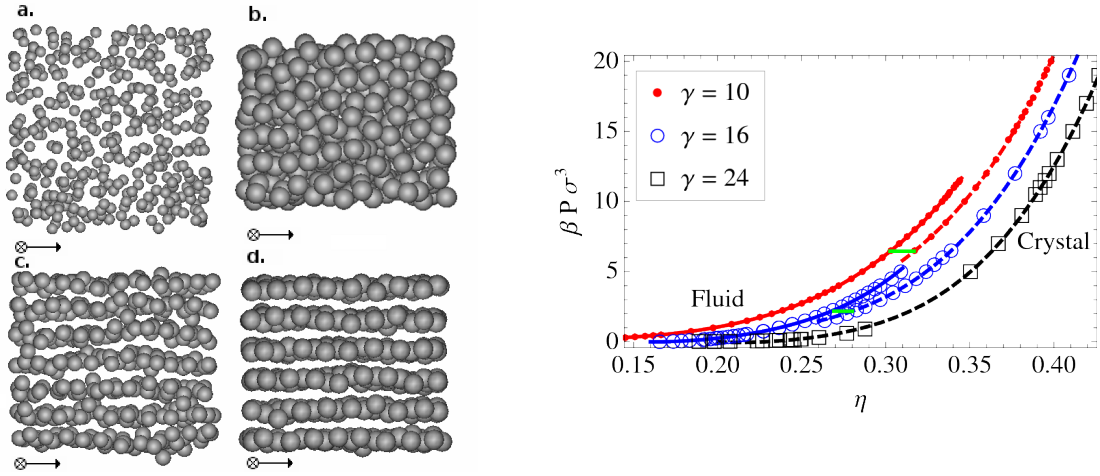


Figure 3.4: Left: Snapshots of typical simulation configurations for charged spheres with inverted dipolar interactions. The arrows indicate the two field directions, with \otimes indicating the axis perpendicular to the page. **a)** A low-density fluid at $\gamma = 6, \eta = 0.05$. **b)** A higher density fluid, just above the line in the phase diagram marking the crossover between the homogeneous and layered fluids ($\gamma = 16, \eta = 0.26$). **c)** Layered fluid at $\gamma = 18, \eta = 0.20$. **d)** Crystalline ABC-stacked hexagonal layers of charged spheres at $\eta = 0.32$ and $\gamma = 28$.

Right: Equations of state for charged spheres with inverted dipolar interactions at field strengths $\gamma = 10, 16, 24$. The lines are fits through the data, using dashed lines for the crystals and solid lines for the fluids. The green horizontal lines show the coexistences. Both the crystal at $\gamma = 24$ and the liquid at $\gamma = 16$ also coexist with an extremely dilute gas at near-zero density.

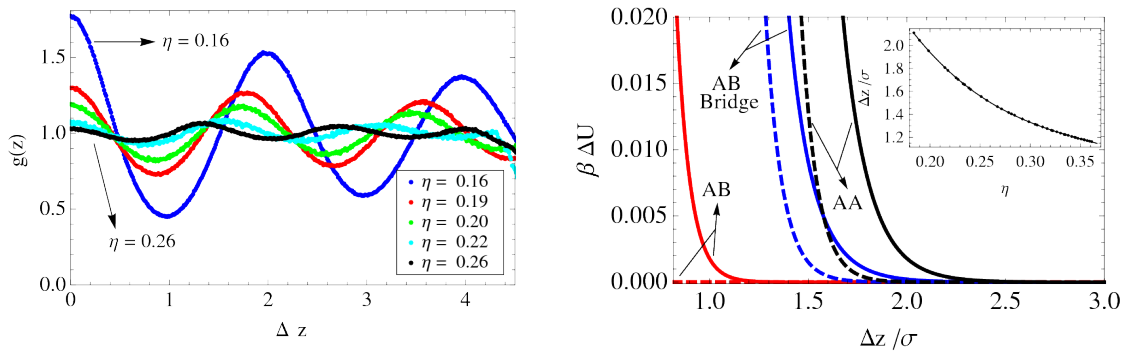


Figure 3.5: Left: Pair correlation function in the z -direction (perpendicular to the biaxial field) of the layered-fluid phase with dipole moment strength $\gamma = 17$ for varying packing fractions. The amplitude decreases with increasing η , as denoted by the labels.

Right: Difference in potential energy per particle $\Delta\beta U$ between a perfect crystal of ABC stacked hexagonal sheets and differently stacked sheets, at $\gamma = 30$ as a function of the center-to-center distance between the sheets Δz . From left to right, the red, blue and black solid lines denote the comparison with AB hollow-site stacking, AB bridge-site stacking, and AA stacking, respectively. The dashed lines represent the contributions from the Yukawa interactions to the total potential energy difference. The inset shows the sheet distance as a function of the packing fraction at $\gamma = 30$.

that of the Yukawa interaction close to coexistence. We find that the total difference in potential energy decreases exponentially with sheet distance. The potential differences are dominated by the dipolar repulsions from nearby particles in the adjacent layer. Hence, hollow-site stackings have the lowest potential energy, while the AA stacking corresponds to the highest one. In the inset, we plot typical sheet separations Δz for equilibrium ABC stacked crystals close to the coexistence density. In the inset, we plot typical sheet separations Δz for equilibrium ABC stacked crystals close to the coexistence density. We find that at a sheet distance of $\Delta z = 2.0\sigma$, the difference in potential energy per particle between ABC and AA stacking is only $0.002 k_B T$ per particle, while the difference compared with other stackings is even smaller. As a result, we expect large amounts of stacking disorder in any low-density crystal.

3.5 Comparison with experiments

Recently, colloidal systems in an external biaxial field have been studied experimentally by Leunissen *et al.*[64] In these experiments, a biaxial field was applied by using two perpendicular uniaxial electric fields and randomly changing the field direction. A system of colloids in suspension with large amounts of salt was used in order to approach the uncharged case. Field strengths were varied in a range approximately corresponding to $31 < \gamma < 170$, and the packing fraction was $\eta = 0.2$. The particles were seen to organize into large hexagonal sheets, with multiple domains, which generally did not merge into three-dimensional structures due to orientational disorder. However, close to the edge of the sample, where the orientation of the hexagonal structure was fixed by the wall, they observed an AB bridge-site stacking of the sheets, which is in contradiction with our bulk simulations. Even in the case of charged particles, where we find substantial disorder between the sheets, there is a clear preference for hollow-site stacking of the particles, as can be seen in Fig. 3.5 on the right-hand side. As our simulations do not take into account the effect of the walls, it seems likely that the electrodes in the experiments impose an orientation on the hexagonal planes. For systems of colloids in a uniaxial field, image charge effects have been shown to affect the orientation of sheet-like structures, leading to lines of particles parallel to the electrode. [45] This effect is likely to occur here as well. If the distance to the electrode is also the same for each sheet, the sheets can only move relative to their neighbors along the direction parallel to both the wall and one of the field directions. In this case, an AB bridge-site stacking would indeed be the lowest-energy state (the right side of Fig. 3.5 illustrates the potential energy difference between AB bridge-site stacking and AA stacking). Further from the wall, no stacking preference was clearly visible, which indeed agrees with the disorder seen in the simulations. In the experimental setup, the sheets are much larger than in the simulations, which slows down their motion considerably. In addition, the sheets can have multiple domains with different orientations, and can be attached to the walls or other sheets, further preventing equilibration.

3.6 Conclusions

In conclusion, we have calculated the phase diagrams for uncharged and charged hard spheres in an external biaxial electric or magnetic field. In both systems, the interaction included a hard-core interaction and an “inverted” dipolar interaction with its strength determined by the field strength γ . In the charged sphere case, a Yukawa repulsion was included as well, using $\kappa\sigma = 10.0$ and $\lambda_B Z^2/\sigma = 450$. The phase behavior as a function of the field strength and particle density shows a gas-liquid coexistence for both systems, as well as a number of crystal structures. All crystal structures found are distortions of the close-packed structures hcp and fcc, where the distortions are caused by a stretching of the crystal in the direction perpendicular to the plane of the biaxial field. Especially in the case of charged spheres, these deformation can be very strong, resulting in separations between layers of particles on the order of 2σ . While free energy considerations show that even at low densities the stable crystal structure is that of fcc, we expect a huge number of planar defects present in the crystal as the potential energy differences are small. In addition to these structures, the system of charged spheres exhibits a layered-fluid phase close to the triple point. These layers are internally disordered, but the density profiles show strong periodicity perpendicular to the plane of the rotating field.

Colloidal cubes in an external electric or magnetic field

Electric fields have proven to be a versatile tool for directing colloidal particles into 1D strings, 2D sheets and 3D crystal structures. When a suspension of colloidal particles is placed in an oscillating electric field, the contrast in dielectric constant between the particles and the solvent induces a dipole moment in each of the colloidal particles. The resulting dipole-dipole interactions can strongly influence the phase behavior of the system. In addition, most anisotropic particles can be aligned in electric fields. However, in the case of cubes the potential energy of a single cube-shaped particle in an electric field is independent of its orientation. As a result, single cubic particles do not align in such an external field. Alignment effects can still occur due to hard-core constraints when multiple particles cluster into a string or crystal phase. We investigate the phase behavior of cube-shaped colloidal particles in electric fields, using Monte Carlo simulations. In addition to string fluid and orientationally ordered BCT phases, we observe a columnar phase consisting of hexagonally ordered strings of rotationally disordered cubes. By simulating the system for a range of pressures and electrical field strengths, we map out an approximate phase diagram. Additionally, we study the effect of the point-dipole approximation on the alignment of cubes in string-like clusters.

4.1 Introduction

In the previous chapter, we studied the string-like clusters formed by spherical particles in an external electric or magnetic field. As shown there, external fields can strongly affect the behavior of colloidal particles. Due to the difference in dielectric constant between the colloids and the solvent, an external field induces a dipole moment in each colloid, leading to anisotropic dipole-dipole interactions. These interactions can lead to self-assembly into a variety of string-like clusters. In addition, the bulk phase behavior exhibits a body-centered tetragonal (BCT) and a hexagonally close-packed (HCP) crystal phase as well as the face-centered cubic (FCC) crystal that also appears in hard-sphere systems.[26] While we limited ourselves to spherical and dumbbell particles in the previous chapter, the same method can be used to induce dipolar interactions in colloidal particles of any shape. As seen in dumbbells, external electric fields can also be used to align anisotropic particles along the direction of the field. This technique is commonly used in liquid-crystal displays by changing the director of the nematic phase using an electric field.

Recently, methods to synthesize cubes on the micrometer [70, 71] and nanometer scale [72–74] have become available, generating interest in the phase behavior of cube-shaped particles. Several simulation studies have investigated the phase behavior of cubic and similar particles, resulting in phase diagrams for tetragonal parallelepipeds [75] and colloidal superballs [76], as well as for a range of polyhedral shapes with varying degrees of anisotropy.[77] A simulation study on cubes with fixed dipole moments that rotate along with the particle, as might be expected for semiconductor nanoparticles, showed that these can self-assemble into wires, sheets or ring-like structures depending on the orientations of the dipoles with respect to the cubes.[78]

In this chapter, we use Monte Carlo simulations to study the effect of external fields on the phase behavior of dielectric colloidal cubes. In contrast with most anisotropic particles, the orientation of a single cube is not affected by external electric fields: the symmetry of the particle causes its potential to be independent of its orientation. As a result, colloidal cubes can rotate freely in the electric field. However, the hard-core interactions between particles can lead to alignment when two or more particles are in close proximity, either due to a high packing fraction in the system, or as a result of the dipolar attractions induced by the external field. By observing the behavior of the system in Monte Carlo simulations, we find both partial alignment of the particles in the string fluid and columnar crystal phases, and complete alignment in the BCT and simple cubic crystal phases.

4.2 Methods and model

We model the colloidal cube-shaped particles as perfect hard cubes with edge length σ and one or more point dipoles inside each particle. The interactions thus consist of a dipolar interaction between the cubes and a hard-core repulsion that prevents particles from overlapping. In the case where each particle contains a single dipole, the dipolar

interaction potential between two particles i and j is given by:

$$\beta u_{dip}(r_{ij}, \theta_{ij}) = \frac{\gamma}{2} \left(\frac{\sigma}{r_{ij}} \right)^3 (1 - 3 \cos^2 \theta_{ij}), \quad (4.1)$$

where r_{ij} denotes the distance between the two particles and θ_{ij} the angle between the distance vector between the particles and the direction of the field. As in the previous chapter, the strength of the dipole interaction is given by the field strength γ : the interaction potential between two particles separated by a distance σ along the field direction is $-\gamma k_B T$. The long-range interactions were handled using Ewald summations.[17, 23] To detect overlaps between two cubes, we used a triangle tessellation scheme. [79] While a cube-specific algorithm based on the separating axis theorem would likely be more efficient, the difference is negligible compared to the computational cost of the Ewald summations used to calculate the potential energy.

In the simplest approximation, the dipole interactions are modeled by a single point dipole in the middle of each cube. In this model, rotations do not affect the dipolar pair interaction between two cubes, and rotational order can only emerge due to the hard-core interactions. However, it is not clear that the interaction between two cubes can be approximated with two point dipoles: due to the external field, the full volume of each colloidal cube will be polarized, resulting in a more complex interaction. While at large distances the interaction between two particles should behave as a simple dipole-dipole interaction, there will be short-range deviations from this behavior. To investigate this, we also studied cubes containing multiple dipoles arranged in a simple cubic lattice aligned with the orientation of the particle. Thus, if a particle at position \mathbf{r} contains n^3 point dipoles, the positions of these dipoles are given by:

$$\mathbf{r}_{ijk} = \mathbf{r} + (2i + 1 - n)\mathbf{a} + (2j + 1 - n)\mathbf{b} + (2k + 1 - n)\mathbf{c}, \quad (4.2)$$

where \mathbf{a} , \mathbf{b} and \mathbf{c} denote the three (mutually perpendicular) edge directions of the particle, and $1 \leq i, j, k \leq n$. Each point dipole interacts with all others via Eq. 4.1, with the interaction strength γ lowered by a factor n^3 to ensure that the interactions between particles at large distances are unchanged. Even with multiple point dipoles in each particle, the potential energy of a single particle is orientation independent. However, the particle pair interaction is now a function of both the relative position of the two particles and their individual orientations.

We investigate the phase behavior of this system by performing Monte Carlo simulations in the NPT ensemble, at a fixed number of particles $N = 512$, pressure P and temperature T . Simulations are performed in a series where the pressure is either increased or reduced slowly, leading to compression or expansion of the system. During the compression runs, the simulations start from an initial configuration in the fluid phase, and the pressure is increased in small steps, up to pressures well past the expected coexistence pressure. Expansion runs start from an initial configuration in one of the crystal phases likely to be stable for the field strength γ used in the simulations. Where needed, additional compression and decompression runs were performed using a different structure as the initial configuration. From the phase transitions observed in both runs, we determined the approximate phase boundaries of the system.

As the strings in the string fluid at high field strengths span the simulation box, it is likely that the phase behavior of the system in this regime is affected by finite size effects. To investigate this, the simulations for high field strengths ($\gamma \geq 12.5$) and low pressures ($P\sigma^3/k_B T < 1$) were performed in a system of $N = 1024$ particles as well. No significant shift in the phase behavior was observed.

To determine the transition from a simple cubic (sc) to a body-centered tetragonal (BCT) crystal structure, we performed simulations at constant pressure for a range of field strengths γ , starting from either of the two phases. Since the system can easily switch between these structures, no clear hysteresis was visible in these simulations, and determining the approximate phase boundary was straightforward.

4.3 Results

4.3.1 Phase diagram

An approximate phase diagram for colloidal hard cubes in an electric field is shown in Fig. 4.1 as a function of the field strength γ and the packing fraction η . For this phase diagram, the dipole interactions are modeled by a single point dipole in the middle of each particle. The phase behavior bears close resemblance to that of dipolar hard spheres [26], with the main difference being the added hexagonal string phase. In addition, the FCC crystal structure that is stable at low field strengths for spheres is replaced by a simple cubic (SC) crystal in the case of cube-shaped particles. As the simple cubic and BCT structures pack equally well for cubes ($\eta_{max} = 1$), the simple cubic structure only appears for a sufficiently low field strength.

As in the case of hard spheres in an external field, a string fluid appears for low field strengths and low packing fractions. Neighboring cubes in a string are aligned such that the touching faces of the two cubes are approximately parallel, as this allows the point dipoles to approach each other more closely. Because aligning the cubes along this direction carries an entropic cost, the field strengths required to form strings are slightly higher than those seen in the case of spheres. However, it should also be noted that the dipole moment induced by an external field in cube-shaped particles will be stronger than that of a sphere with diameter σ , due to its larger volume, provided the material of the particle is the same. Therefore, the same value of γ for spheres and cubes does not correspond to the same external field strength. Since the cubes only contain a single point dipole, rotations along the field axis do not influence the potential energy of the system. As a result, the cubes do not align all faces within a single string: there is only alignment in one direction. Hard-core interactions with neighboring strings or a wall could cause the particles to align in all three directions, but this was only observed in the body-centered-tetragonal crystal phase that appears at high packing fractions.

The maximum packing fraction for sharp cubes is $\eta = 1$. At this packing fraction, all cubes are aligned along the same three axes, but a limited amount of freedom remains for the positions of the particles. At $\eta = 1$, the lowest energy state is a body-centered tetragonal (BCT) structure. This structure can be seen as a further aggregation of strings of cubes onto a square lattice, with all the particles aligned. Each string is shifted along the field direction with respect to its four neighboring strings by a distance equal to

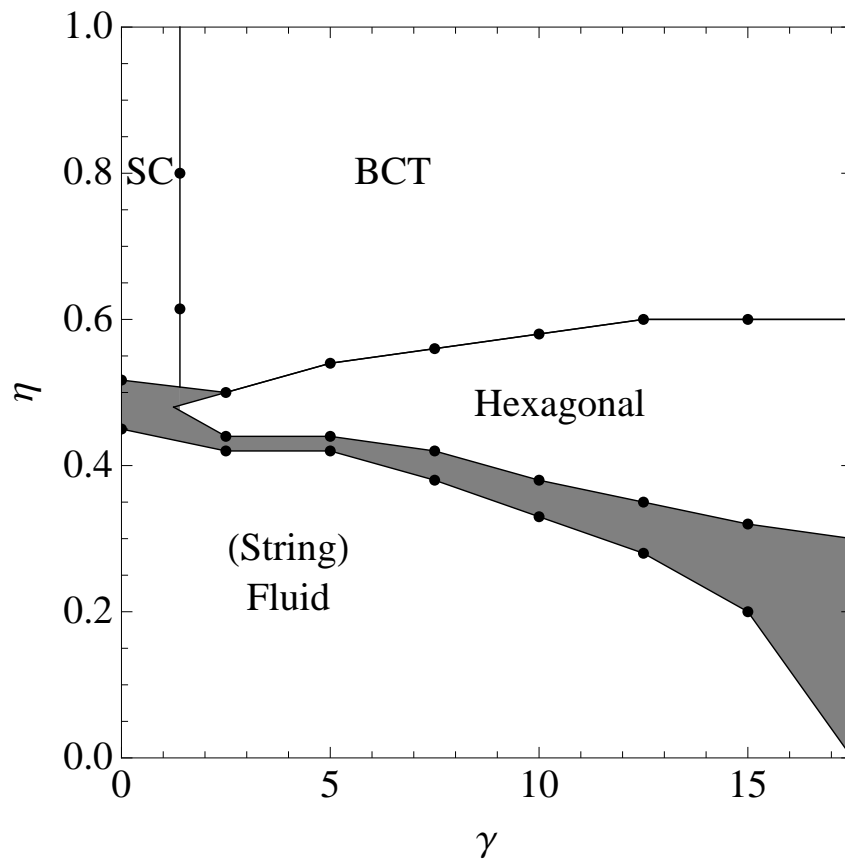


Figure 4.1: Approximate phase diagram for colloidal hard cubes in an external electric or magnetic field, as a function of the field strength γ and the packing fraction η . The black points indicate where phase boundaries were determined based on the phases found in MC simulations at constant pressure. The labels SC and BCT denote a simple cubic and body-centered tetragonal phase, respectively, while the hexagonal phase consists of strings of particles arranged on a hexagonal lattice.

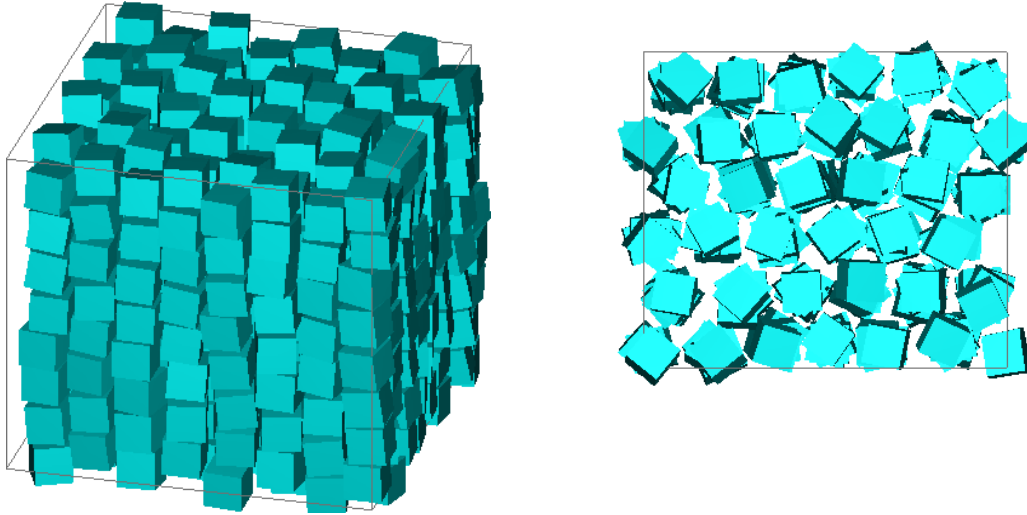


Figure 4.2: Left: Snapshot of the BCT phase, at $\gamma = 15$ and pressure $\beta P\sigma^3 = 4$ ($\eta = 0.64$). The external field points along the vertical direction. **Right:** Snapshot of the hexagonal phase, at $\gamma = 15$ and $\beta P\sigma^3 = 1$ ($\eta = 0.43$). The field direction is perpendicular to the plane of view.

half of the lattice spacing. A typical snapshot of this structure is shown in Fig. 4.2. This structure is readily seen to form at high field strengths, regardless of the starting configuration. However, for lower field strengths, the same starting configuration can also lead to a hexagonal ordering of strings, without alignment with respect to rotation along the field axis. In this case, the lowest energy state would likely have three of the six neighbors of each string shifted up by a third of the interparticle distance in a string, and the other three shifted down by the same amount, but this order is not clearly visible in the simulations so far. For an example, see Fig. 4.2. This configuration maximizes the distance between strings, allowing for larger orientational entropy at the cost of a lower potential energy. It might be interesting to note that an added Yukawa repulsion would likely further stabilize this phase, as this would increase the distance between the strings. In the limit of high field strengths, the hexagonal columnar phase is expected to vanish eventually: the BCT phase has a lower potential energy, and will coexist with a dilute gas at sufficiently high interaction strengths. Both the BCT phase and hexagonal phase were seen in experiments on neighborite cubes in an electric field as well, as shown in Fig. 4.3.[80] In the experimental snapshots of the hexagonal phase, the range of the positional order in the strings appears to be limited. In our simulations, the range of the hexagonal order in the system was always at least equal to the system size, but it can not be excluded that this may change for larger systems.

When the field strength $\gamma = 0$, the stable crystal phase is a simple cubic crystal (SC). At low but finite fields, this structure remains stable, but becomes slightly distorted: the lattice is compressed along the field direction, actually leading to a simple tetragonal lattice. As the distortions are small, this crystal is still labeled SC in Fig. 4.1.

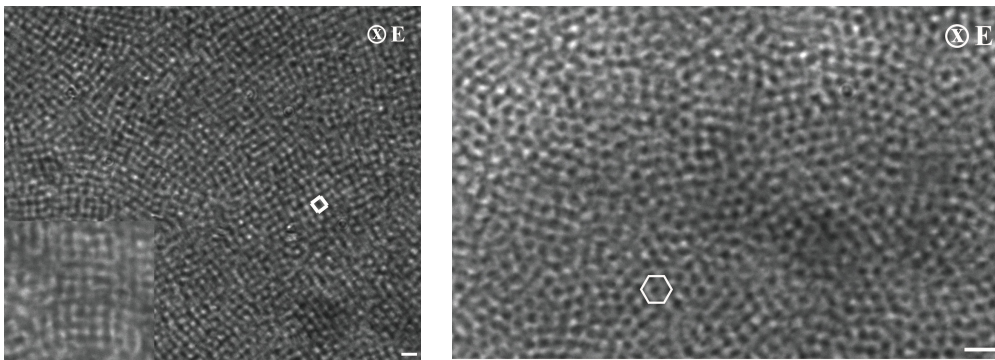


Figure 4.3: Experimental snapshots of a system of neighborite cubes.[80] In both snapshots, the field direction is perpendicular to the plane of view. **Left:** For high field strengths ($E_{rms} \simeq 0.12$ V/ μm), strings of particles order into domains with a square lattice, likely corresponding to a BCT structure. The scalebar is 4 μm . **Right:** At lower field strengths ($E_{rms} \simeq 0.08$ V/ μm), hexagonal domains are clearly visible. The scalebar is 3 μm .

4.3.2 Point-dipole approximation

In simulations of the string fluid, cubic particles in strings show orientational disorder: while the top and bottom faces of neighboring particles are aligned in order to minimize the distance between them, particles are free to rotate around the field axis. This can be understood from the way the interactions are modeled: since the potential in Eq. 4.1 only depends on the positions of the centers of the particles, there is no way for it to align the particles orientationally. In experiments performed on a dilute string fluid of cube-shaped particles in an external electric field, particles within the same string were seen to mostly align orientationally only at high field strengths (see chapter 7 of Ref. [81]). This suggests that weak aligning forces may exist as a result of the way the cube-shaped particles are polarized in the external field.

To investigate possible effects of different dipole moment distributions, we approximate the polarization of the cube with multiple dipoles evenly spread through the particle. To do this, we divide each cube into n^3 smaller cubes, and place a weaker dipole in the middle of each smaller cube, resulting in a simple cubic lattice. As the total number of dipoles quickly becomes hard to simulate directly, we only performed simulations for the case where each cube contains $n^3 = 2^3 = 8$ point dipoles, but performed energy calculations for cubes containing up to $n^3 = 7^3$ point dipoles.

It is interesting to note that even with multiple dipoles, a single particle in an external electric field still has a potential energy that is independent of the orientation. Thus, particles will not align in the electric field purely due to their polarization with this distribution of dipoles. Note that this is not true for all possible dipole distributions in the cube.

Secondly, if two cubes are placed on top of each other (as if they were in a string), the potential energy difference between different orientations turns out to be very small. For 8 dipoles in each cube, the difference between perfect alignment and the maximum misalignment (45°) is only around $0.04\gamma k_B T$. While this difference will induce alignment

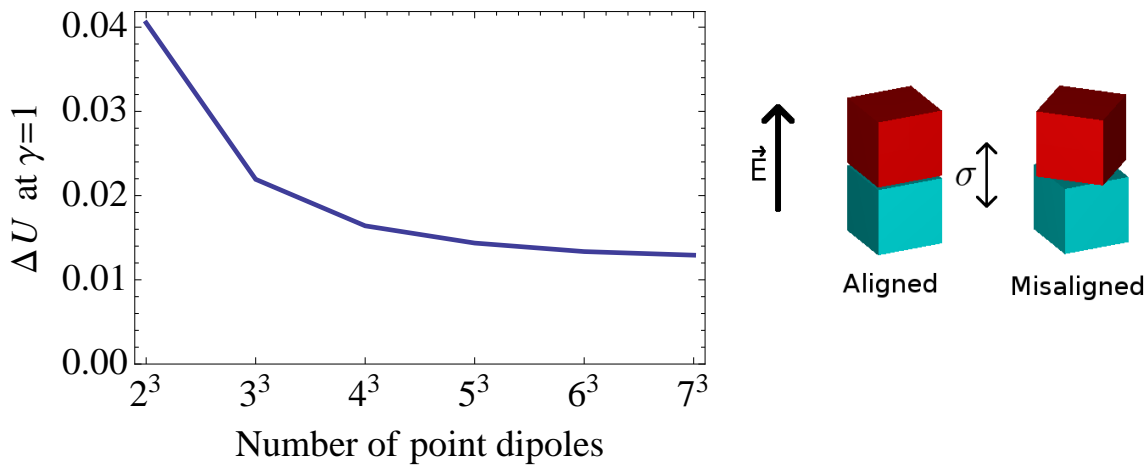


Figure 4.4: Energy difference ΔU between the most favorable (aligned) and least favorable (misaligned) orientations of two particles at distance σ along the z -axis, for different numbers of point dipoles per particle. A cartoon depicting the aligned and misaligned orientations is also shown

at very high field strengths, the effect will be small below $\gamma \simeq 25$. Moreover, for particles containing more than 8 point dipoles, the effect of rotations on the potential energy decreases with the number of dipoles (see Fig. 4.4). The energy difference appears to level off around $0.01k_B T$, which would indicate that field strengths over $\gamma \simeq 100$ would be needed to align particles with the electric field.

To check this, we performed simulations of cubes containing 8 point dipoles, and studied alignment of particles in a string as a function of the field strength. Neighboring particles were seen to align in strings at field strengths higher than $\gamma \simeq 30$, but for lower field strengths, no clear correlations in the orientations of neighboring particles were visible. Since the energy calculations show that the alignment effect decreases in strength on increasing the number of point dipoles per particle, we conclude that for a field strength lower than $\gamma = 30$, using multiple point dipoles per particle is not likely to significantly influence the aligning of cubes in the string fluid phase or hexagonal columnar phase.

4.4 Conclusions

In summary, we used Monte Carlo simulations in the NPT ensemble to study the phase behavior of hard colloidal cubes in an external electric or magnetic field. The resulting phase diagram contains BCT and SC crystal phases, a hexagonal columnar phase, and a string fluid phase. The dipolar interactions were modeled as point-dipole interactions. While the dipolar interactions between colloidal cubes may not be perfectly described by this approximation, spreading out the dipole moment of the particle over multiple evenly spaced points was shown to lead to only very small potential energy differences for the interaction strengths studied here. However, for sufficiently high field strengths, aligning forces may arise between cubes in close proximity, leading to alignment in all

three directions for particles that are part of the same string.

4.5 Acknowledgements

I would like to thank Rao Vutukuri for performing the experiments on cubes mentioned and shown in this chapter, and Joost de Graaf for supplying the overlap algorithm used in the Monte Carlo simulations. I would also like to thank Laura Filion for determining the coexistence densities for hard cubes and for useful discussions and Bas Kwaadgras for performing calculations on the polarization of cube-shaped particles in an external field.

Phase behavior and crystal vacancies in colloidal hard cubes

In this chapter we explore the phase behavior of colloidal hard cubes, using both Monte Carlo simulations and Event-Driven Molecular Dynamics simulations. In previous simulation studies, these particles were seen to not only form fluid and simple cubic crystal phases, but also an intermediate cubatic phase at packing fractions $0.52 < \eta < 0.57$. However, this cubatic phase still shows sign of significant positional order. We investigate the ordering in this intermediate phase more closely and map out the phase behavior of the hard-cube system using free energy calculations. Our simulations confirm that truly long-range positional order is destroyed in simulations starting from a simple cubic system with all lattice sites filled. However, spontaneous creation of extra layers in the crystal suggest that a higher concentration of vacancies in the crystal could stabilize the structure. We show that incorporating a sufficient number of vacancies in the crystal structure allows the system to retain its long-range order and to lower its pressure in comparison to the system without defects. The estimated equilibrium concentration of vacancies slightly above coexistence is on the order of 6.4%, orders of magnitude higher than the defect concentration in hard-sphere crystals.

5.1 Introduction

In recent years a variety of synthesis methods for the production of various polyhedral colloids and nanoparticles have become available,[70, 72–74, 81, 82] sparking new interest in the phase behavior of these particle shapes. While in many of these systems both the interactions and shapes of the particles will play an important role in determining the equilibrium phase behavior, a good starting point for understanding the behavior of interacting systems is the study of purely hard-core particles. For example, the hard-sphere phase behavior can be seen as a limiting zero-interaction (or high-temperature) case in the phase diagram of any interacting particle with a spherical hard core. Recently, Escobedo *et al.* used Monte Carlo (MC) simulations to study the phase behavior of six space-filling polyhedral shapes: truncated octahedra, rhombic dodecahedra, hexagonal prisms, triangular prisms, gyrobifastigiums and cubes.[77] They showed that the phase diagrams of the first three of these particles do not only contain a fluid and a crystal phase, but also an intermediate plastic crystal or rotator phase, where long-range positional order is still present, but some or all of the orientational order is lost. Conversely, for hard cubes they confirmed the presence of an intermediate cubatic phase seen in earlier work, [75] where long-range positional order is lost, but the particles are still orientationally aligned in all three directions. However, they did observe layering of the particles in the cubatic phase, indicating the presence of positional correlations over large distances in at least one direction.

In this chapter, we examine in more detail the phase behavior of colloidal hard cubes. While the stability of an isotropic fluid at low densities and a simple cubic crystal structure at high densities have already been firmly established, the existence and nature of an intermediate phase are not yet clear. We examine which phase coexists with the fluid phase and we investigate the positional and orientational order in this phase. Additionally, we perform free energy calculations to determine the coexistence densities. From the behavior of the system slightly above coexistence, we conclude that the equilibrium phase at this point is a crystal with both positional and orientational long-range order, but with a surprisingly large number of vacancies. Free energy calculations on these defect-rich crystals show that the equilibrium concentration of crystal vacancies near coexistence is as high as 6.4%.

5.2 Model and simulation methods

5.2.1 Overlap and collision detection

The model we study consists of perfectly sharp hard cubes with edge length σ . Aside from hard-core interactions, which prevent configurations with overlapping cubes, the particles do not interact. To investigate the phase behavior of these particles, we use both Monte Carlo (MC) and event-driven molecular dynamics (EDMD) simulations. In both types of simulation, overlaps are detected using an algorithm based on the separating axis theorem.[83] According to this theorem, for any two non-overlapping convex bodies there exists an axis onto which both shapes can be projected without overlapping. In other words, if both shapes are projected onto this separating axis, the resulting two intervals

on the axis are completely disjoint. No such axis exists if the particles overlap. For two convex polyhedral particles, only a finite number of possible separating axes need to be checked: in that case, the potential separating axes are either parallel to a normal of one of the faces of either of the two particles, or perpendicular to the plane spanned by one of the edges of the first particle and one of the edges of the second particle. If none of these directions correspond to a separating axis, the particles overlap.

For a cube-shaped particle a , all face normals and edges are parallel to one of three perpendicular axes $\mathbf{u}_{a,i}$ of unit length, with $i \in \{1, 2, 3\}$. Thus, the fifteen potential separating axes for two cubes are given by $\mathbf{u}_{a,i}$, $\mathbf{u}_{b,i}$, and $\mathbf{u}_{a,i} \times \mathbf{u}_{b,j}$. To calculate the projection of both particles onto a potential separating axis \mathbf{L} , it is convenient to take the center \mathbf{r}_a of particle a as the origin, placing particle b at position $\mathbf{d} = \mathbf{r}_b - \mathbf{r}_a$. Because the particles are convex, it is sufficient to project the vertices of each particles onto \mathbf{L} . For particle a , the positions of the vertices are given by: $(\pm\mathbf{u}_{a,1} \pm \mathbf{u}_{a,2} \pm \mathbf{u}_{a,3})\sigma/2$. The projections onto \mathbf{L} are thus contained in the interval $[-R_a(\mathbf{L}), R_a(\mathbf{L})]$, with

$$R_a(\mathbf{L}) = \frac{\sigma}{2} \sum_{i=1}^3 |\mathbf{u}_{a,i} \cdot \mathbf{L}|. \quad (5.1)$$

Here, we have taken the separating axis \mathbf{L} to be of unit length. Similarly, the projections of the vertices of particle b are in an interval centered around $\mathbf{d} \cdot \mathbf{L}$ with radius

$$R_b(\mathbf{L}) = \frac{\sigma}{2} \sum_{i=1}^3 |\mathbf{u}_{b,i} \cdot \mathbf{L}|. \quad (5.2)$$

If \mathbf{L} is a separating axis, these intervals are non-overlapping. In that case,

$$\mathbf{d} \cdot \mathbf{L} > R_a(\mathbf{L}) + R_b(\mathbf{L}). \quad (5.3)$$

If this inequality holds for any one of the potential separating axes, the two particles do not overlap. We can use Eq. 5.3 to design a distance function f for two particles:

$$f(a, b) = \max_{\mathbf{L}} \{ \mathbf{d} \cdot \mathbf{L} - (R_a(\mathbf{L}) + R_b(\mathbf{L})) \}, \quad (5.4)$$

where the maximum is taken over all potential choices for \mathbf{L} . The function $f(a, b)$ is negative whenever the particles a and b overlap, and positive when they do not. Additionally, the function is continuous as a function of translations and rotations of both particles. To predict collisions in the EDMD simulations, we numerically find the roots of f as a function of time, following the methods used in Ref. [20]. An Andersen thermostat was used to allow the total energy in the EDMD simulations to fluctuate: at fixed time intervals, a random selection of particles are given a new velocity and angular velocity drawn from a Boltzmann distribution.[17]

5.2.2 Free energy calculations

To determine the Helmholtz free energy of the solid and fluid phases as a function of the density, we use thermodynamic integration.[17] When the free energy of a reference

density $F(\rho_0)$ is known, the free energy as a function of number density $F(\rho)$ can be determined using the equation of state. In particular, the free energy is given by

$$\frac{\beta F(\rho)}{N} = \frac{\beta F(\rho_0)}{N} + \beta \int_{\rho_0}^{\rho} \frac{P(\rho')}{(\rho')^2} d\rho' \quad (5.5)$$

where ρ is the density and $\beta = 1/k_B T$ with k_B Boltzmann's constant and T the temperature.

To measure the chemical potential μ at a reference density ρ_0 for the fluid, we use Widom insertion.[17] The free energy of the fluid at density ρ_0 is then given by

$$\frac{\beta F_f(\rho_0)}{N} = \beta \mu(\rho_0) + \frac{\beta P(\rho_0)}{\rho} \quad (5.6)$$

To determine the free energy of a crystal without vacancies, we use a variation on the method introduced by Frenkel and Ladd,[66] where particles are tied to their lattice sites with springs, transforming the crystal into a non-interacting Einstein crystal for a sufficiently high spring constant. In our case, we add an aligning potential as well to handle the orientational degrees of freedom of the particles. Following Ref. [84], the external potential applied to the system during the Einstein integration is given by:

$$\beta U_{\text{ext}}(\lambda) = \lambda \sum_{i=1}^N \left[\frac{1}{\sigma^2} |\mathbf{r}_i - \mathbf{r}_i^0|^2 + \sin^2 \Psi_a + \sin^2 \Psi_b \right] \quad (5.7)$$

where λ is the strength of the external potential, and \mathbf{r}_i^0 is the position of the lattice site associated with particle i . The lattice sites are on a simple cubic lattice with N_L lattice sites and with the lattice vectors parallel to the x , y , and z -axes. The second term fixes the orientation of the particles. The angles Ψ_a and Ψ_b are defined as follows: let $\alpha_j = \mathbf{u}_{i,j} \cdot \hat{\mathbf{x}}$ and $\beta_k = \mathbf{u}_{i,k} \cdot \hat{\mathbf{y}}$ such that $\alpha_j^2 + \beta_k^2$ is maximized with $j \neq k$. Then $\cos(\Psi_{i,a}) = \alpha_j$ and $\cos(\Psi_{i,b}) = \beta_k$.

In the limit of high spring constants λ , this potential transforms the crystal of cubes into an Einstein crystal, where both the particle positions and orientations are bound so tightly that particles never interact. Note that the center of mass of the crystal is constrained.

For an Einstein crystal with an unconstrained center of mass, the free energy is given by:[17]

$$\frac{\beta F_{\text{ein}}(\lambda)}{N} = -\frac{3}{2} \log \frac{\pi}{\lambda} \quad (5.8)$$

while the rotational free energy is [84]

$$\frac{\beta F_{\text{rot}}(\lambda)}{N} = -\log \frac{\int \exp(-\lambda [\sin^2 \Psi_a + \sin^2 \Psi_b]) d\Omega}{\int d\Omega}. \quad (5.9)$$

Here, the integral is taken over all possible orientations of a single particle. The translational and orientational thermal de Broglie wavelength do not influence the phase behavior of the system, and are both taken to be equal to our unit length σ . We evaluated this integral using Monte Carlo integration.

The full free energy of the crystal of hard cubes without vacancies can be written as:[85]

$$\frac{\beta F}{N} = \frac{\beta F_{\text{ein}}(\lambda_{max})}{N} + \frac{\beta F_{\text{rot}}(\lambda_{max})}{N} + \frac{\beta F_{\text{int}}}{N} + \frac{3}{2N} \log \frac{\lambda_{max}}{\pi} - \frac{3}{2N} \log N + \frac{\log \rho \sigma^3}{N}, \quad (5.10)$$

where the last three terms are correction terms related to fixing the center of mass of the Einstein crystal and the interacting crystal. The free energy difference F_{int} between the Einstein crystal and the interacting crystal, both with a fixed center of mass, is given by:

$$\frac{\beta F_{\text{int}}}{N} = -\frac{\beta}{N} \int_0^{\lambda_{max}} \left\langle \sum_{i=1}^N \left(\frac{1}{\sigma^2} |\mathbf{r}_i - \mathbf{r}_i^0|^2 + \sin^2 \Psi_a + \sin^2 \Psi_b \right) \right\rangle_{\lambda} d\lambda. \quad (5.11)$$

As in Ref. [17, 85], we calculate the integral in Eq 5.11 using a Gauss-Legendre quadrature in combination with MC simulations.

To calculate the free energy of the system with vacancies, instead of fixing the particles to a specific lattice site, we attach the particles to the their nearest lattice site.[86] In this case, the external potential applied to the system during the Einstein integration is:

$$U_{\text{ext}}(\lambda) = \lambda \sum_{i=1}^N \left(\frac{1}{\sigma^2} |\mathbf{r}_i - \mathbf{r}^0(\mathbf{r}_i)|^2 + \sin^2 \Psi_{i,a} + \sin^2 \Psi_{i,b} \right) \quad (5.12)$$

where $\mathbf{r}^0(\mathbf{r}_i)$ is the position of the lattice site nearest to \mathbf{r}_i .

The free energy of the noninteracting system is

$$\frac{\beta F_{\text{ein}}^{\text{vac}}(\lambda)}{N} = \frac{\beta F_{\text{ein}}(\lambda)}{N} - \log \frac{N_L!}{N!(N_L - N)!} + \frac{\beta F_{\text{rot}}(\lambda)}{N}, \quad (5.13)$$

where the first term is the translational free energy of a normal Einstein crystal, the second term is the combinatorial entropy associated with placing N particles on N_L lattice sites, and the third term is the rotational free energy of the crystal, given by Eq. 5.9.

The full free energy of the crystal of hard cubes with vacancies is then given by:

$$\frac{\beta F}{N} = \frac{\beta F_{\text{ein}}^{\text{vac}}(\lambda_{max})}{N} + \frac{\beta F_{\text{int}}^{\text{vac}}}{N} \quad (5.14)$$

where $F_{\text{int}}^{\text{vac}}$ denotes the free energy difference between the Einstein crystal and the crystal of hard cubes, and is analogous to Eq. 5.11 where the nearest lattice site is used in place of a specific lattice site, and the center of mass of the system is unconstrained in the simulations. To equilibrate the position of the center of mass, we introduce Monte Carlo moves that collectively translate every particle in the system.[86] Additionally, moves that translate a particle by exactly one lattice vector are introduced in order to improve sampling of different distributions of vacancies over the crystal. For a system with full lattice site occupancy ($N = N_L$), we obtain good agreement between the two methods.

5.3 Order parameters and correlation functions

We investigate three types of ordering in the system: positional order, orientational order, and bond-orientational order. For each type of order, we define an order parameter

$G^{pair}(a, b)$ for a particle pair (a, b) , measuring the amount of correlation between two particles. The global order $\langle G \rangle$ in a system is then defined as:

$$\langle G \rangle^2 = \frac{1}{N^2} \sum_{a=1}^N \sum_{b=1}^N G^{pair}(a, b). \quad (5.15)$$

Additionally, we can investigate the decay of the correlation function of this order parameter as a function of distance:

$$G(r) = \langle G^{pair}(a, b) \rangle(r) = \left\langle \frac{|\sum_{a,b} G(a, b) \delta(|\mathbf{r}_{ab}| - r)|}{\sum_{a,b} \delta(|\mathbf{r}_{ab}| - r)} \right\rangle, \quad (5.16)$$

where $\delta(r)$ denotes the Kronecker delta function. In case of true long-range order, the correlation function $\langle G^{pair}(a, b) \rangle(r)$ decays to a constant in the limit of large distances. For a sufficiently large system, this constant is related to the global order $\langle G \rangle$ in the system: [76]

$$\lim_{r \rightarrow \infty} G(r) = \langle G \rangle^2 \quad (5.17)$$

If the order is only quasi-long-range, the correlation function instead decays to 0 as a power law. In the case of short-range order, the correlation function follows an exponential decay related to the correlation length in the system.

5.3.1 Positional order

For positional order, the order parameter of interest is

$$G_{pos}^{pair}(a, b) = \exp(i\mathbf{K} \cdot (\mathbf{r}_a - \mathbf{r}_b)), \quad (5.18)$$

with \mathbf{K} denoting one of the reciprocal lattice vectors of the crystal structure. The correlation function $G_{pos}(r)$ can be calculated using Eq. 5.16, and the global positional order $\langle G_{pos} \rangle$ can be written as:

$$\langle G_{pos} \rangle = \left| \frac{1}{N} \sum_a \exp(i\mathbf{K} \cdot \mathbf{r}_a) \right|. \quad (5.19)$$

Long range order is only present in the system if a reciprocal lattice vector \mathbf{K} can be found for which $G_{pos}(r)$ decays to a constant at large distances. In our simulations, the simulations start from a simple cubic crystal aligned with the cubic simulation box. The lattice vectors are of length $L/N^{1/3} = \rho^{-1/3}$, with L the length of the simulation box and $\rho = N/V$ the number density of the system. Thus, unless the orientation of the crystal changes during the simulation, the first three reciprocal lattice vectors are vectors of length $2\pi\rho^{1/3}$ along the x , y and z axes.

The order parameter used for positional order is closely related to the Fourier transform of the positions of the particles in the system. We note that this is analogous to the data obtained in light scattering experiments. In such an experiment, the intensity of the light scattered along a scattering vector \mathbf{k} depends both on the shape of the particles

and the structure in the system, expressed by the form factor and the structure factor, respectively. The structure factor $S(\mathbf{k})$ is given by:

$$S(\mathbf{k}) = \frac{1}{N} \left\langle \sum_{a=1}^N \sum_{b=1}^N e^{i\mathbf{k} \cdot (\mathbf{r}_a - \mathbf{r}_b)} \right\rangle, \quad (5.20)$$

where \mathbf{k} is the scattering vector, which corresponds to the difference between the scattered wave vector and the incident wave vector. Maxima in $S(\mathbf{k})$ (and therefore in the scattering pattern) will occur whenever

$$\mathbf{k} = a\mathbf{v}_1 + b\mathbf{v}_2 + c\mathbf{v}_3, \quad (5.21)$$

where the vectors \mathbf{v}_i correspond to the three independent reciprocal lattice vectors of the crystal, and a, b and c are integers. In a cubic lattice, the reciprocal lattice vectors are simply parallel to the basis vectors of the lattice in real space. To plot a scattering pattern, we choose our scattering vectors in a plane parallel to one of the crystal planes in the system: each \mathbf{k} was taken to be a linear combination of two of the three lattice vectors of the crystal in the simulation. Since the orientation of the lattice was seen to change during the simulation, the direction of these lattice vectors was determined from the orientations of the particles. Because the edge vectors of the particles are aligned with the lattice vectors on average, a good estimate of direction of the lattice vectors can be obtained by averaging all edge vectors aligned in approximately the same direction.

5.3.2 Bond-orientational order

The bond-orientational order describes the correlations between the directions of bonds between neighboring particles in a system. To measure the order, we use a bond-orientational order parameter based on spherical harmonics, which can also be used to find clusters of locally ordered particles in partially crystallized systems. [87] To measure the local bond-order vector $q_{l,m}$, a list of neighbors is constructed for each particle, containing all other particles within a radial distance r_c . The number of neighbors for a particle i is denoted as $N_b(i)$. We then calculate $q_{l,m}(i)$ for each particle a as

$$q_{l,m}(a) = \frac{1}{N_b(a)} \sum_{b=1}^{N_b(a)} Y_{l,m}(\theta_{a,b}, \phi_{a,b}), \quad (5.22)$$

where $Y_{l,m}(\theta, \phi)$ are the spherical harmonics, with $m \in [-l, l]$ and $\theta_{a,b}$ and $\phi_{a,b}$ are the polar and azimuthal angles of the center-of-mass distance vector $\mathbf{r}_{ab} = \mathbf{r}_b - \mathbf{r}_a$, with \mathbf{r}_a the position vector of particle a . The correlation in bond-orientational order between two particles can then be defined as the inner product between the normalized bond-order vectors $q_{l,m}$ between two particles:

$$d_l(a, b) = \frac{\sum_{m=-l}^l q_{l,m}(a) q_{l,m}^*(b)}{\left(\sum_{m=-l}^l |q_{l,m}(a)|^2 \right)^{1/2} \left(\sum_{m=-l}^l |q_{l,m}(b)|^2 \right)^{1/2}}. \quad (5.23)$$

For a simple cubic crystal structure, we expect 4-fold bond-orientational order, and therefore choose $l = 4$. Thus, as the order parameter for bond-orientational order, we use:

$$G_{bond}^{pair}(a, b) = d_4(a, b). \quad (5.24)$$

The correlation function $G_{bond}(r)$ associated with this order parameter is calculated using Eq. 5.16.

Additionally, we can use $G_{bond}^{pair}(a, b)$ to find clusters with local bond-orientational order. In order to do this, we calculate the inner product d_l of the bond orientational order parameter $q_{l,m}(i)$ for each particle with that of each of its neighbors. If the dot product for a pair of particles is larger than a cutoff value d_c , the two particles are considered to be connected. Thus, the number of connections for each particle is given by:

$$\xi(i) = \sum_{j=1}^{N_b(i)} H(d_l(i, j) - d_c), \quad (5.25)$$

where H is the Heaviside step function. Solid-like particles are defined as particles with at least ξ_c connections. All other particles are considered liquid-like. After determining the connections in the system, clusters of solid-like particles are identified as groups of connected solid-like particles.

The clusters resulting from this algorithm depend on several parameters. Firstly, the symmetry index l for the bond orientational order parameter indicates the degree of symmetry detected by the order parameter, here chosen to be $l = 4$. Secondly, the neighbor cutoff r_c should be large enough to include the nearest neighbors of each particle, but not so large that particles further away are included in the algorithm. An estimate for a reasonable value can be determined from the radial distribution function $g(r)$ of the crystal structure under consideration: r_c should be chosen between the first and second peaks of $g(r)$. In the case of hard cubes, we chose $r_c = 1.55\sigma$. Finally, the dot-product cutoff d_c and the cutoff for the number of neighbors ξ_c should be chosen such that the order parameter is able to make a clear distinction between the crystal and fluid phases. Here, we choose $d_c = 0.6$ and $\xi_c = 3$, resulting in only small clusters in the fluid phase and a large system-spanning cluster in the crystal phase.

5.3.3 Orientational order

For the orientational order in the system, the order parameter used to calculate the correlation function $G_{or}(r)$ is

$$G_{or}^{pair}(\mathbf{u}_a, \mathbf{u}_b) = \frac{1}{3} \sum_{j=1}^3 \left[35(\mathbf{u}_{a,j} \cdot \mathbf{u}_{b,j})^4 - 30(\mathbf{u}_{a,j} \cdot \mathbf{u}_{b,j})^2 + 3 \right] \quad (5.26)$$

where $\mathbf{u}_{a,j}$ denotes the j th axis of particle a . [76, 88] This order parameter will on average be equal to 1 for particles with perfect cubatic order, but may be higher if nematic order is present. In this case, nematic order would indicate that the cubes are not only aligned, but also have the same faces pointing in the same directions. As the six sides of a cube are equivalent, nematic order should not be possible in the system, but since particles

in the crystal phase are initialized with the same orientation, this can lead to artificially high values of the order parameter. To remedy this, the three axes $\mathbf{u}_{a,i}$ for each particle a are randomly reordered before performing the calculations.

Like the bond-orientational order parameter, we will also use $G_{or}^{pair}(a,b)$ for finding clusters exhibiting local orientational order. For the purpose of finding these clusters, two particles a and b are considered to be connected if their center-to-center distance $r_{ab} < r_c$ and $G_4(\mathbf{u}_a, \mathbf{u}_b) > G_c$. We use the same values for r_c and ξ_c as used in the local positional order parameter, and choose $G_c = 0.6$. This choice of parameters results in clusters that approximately match the clusters found by the positional order algorithm in size.

5.4 Results

As mentioned earlier, the phase behavior of hard cubes has been studied previously in Refs. [75, 77], using expansion and compression runs of MC simulations in the NPT -ensemble. They reported the observation of a fluid phase at low packing fractions, a coexistence region between a fluid and a cubatic phase for $0.45 < \eta < 0.52$, and a continuous transition from the cubatic phase to a simple cubic crystal structure at $\eta = 0.57$. Here, we will examine in more detail the phase behavior of hard cubes, and investigate in particular the existence of the cubatic phase.

To begin, we determine the equation of state of the system using both EDMD (at constant number of particles N , volume V and temperature T) and NPT MC simulations (at constant pressure P). The equation of state resulting from EDMD simulations is shown in Fig. 5.1. The results from MC simulations agreed very well with the EDMD simulations, but were more sensitive to statistical errors even for significantly longer simulation times. For the NPT MC simulations, the system was initialized either with random positions and orientations at low densities for the fluid branch, or in a simple cubic crystal structure for the solid branch. All EDMD simulations were started from a simple cubic lattice. While this requires the crystal to melt before fluid pressures can be measured, the phase transition between a fluid and a solid shows very little sign of hysteresis, and good agreement between the fluid branches of the two simulation methods is reached. Due to the free energy cost of creating a fluid-solid coexistence inside the simulation box, a small part of the equation of state for the metastable fluid and solid can still be measured. As the metastable extensions of both the fluid and solid branch are very short, i.e., the spinodal points are very close to the binodal ones, the transition is weakly first order, and the phase transformation proceeds either via nucleation and growth with a small nucleation barrier or via spinodal decomposition. In addition, one may argue that the surface tension of the fluid-solid interface of hard cubes should be small. From the equation of state, a single phase transition is clearly evident around $\beta P \sigma^3 = 6$. Furthermore, the equation of state shows good agreement with the one shown in Ref. [77].

The equation of state in Fig. 5.1 shows no sign of a first-order phase transition from a possible cubatic phase to a crystal, suggesting that a possible phase transition would be continuous. If no first-order phase transition exists, the free energy of the solid branch can be calculated via thermodynamic integration without taking into account the possibility of any discontinuous transitions. Performing free energy calculations on the fluid and crystal

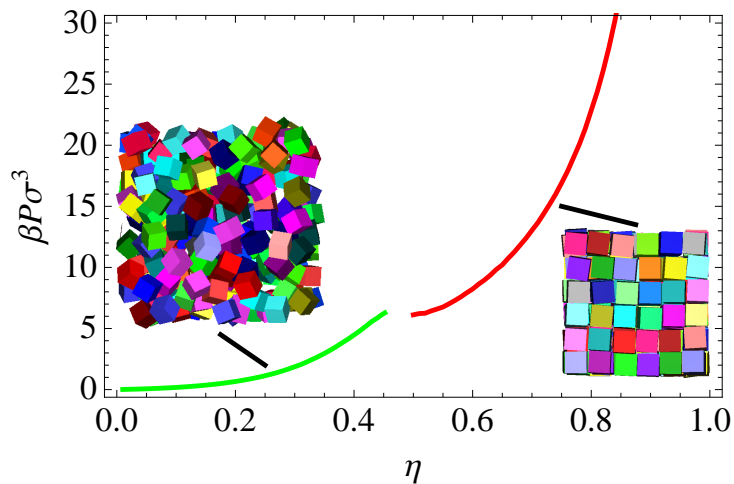


Figure 5.1: Equations of state, $\beta P \sigma^3$ versus η as determined using EDMD simulations of $N = 8000$ particles. The fluid branch is shown in red while the solid branch is shown in blue. Almost no hysteresis of the two branches is seen.

phases yielded a fluid-solid coexistence region between packing fractions $\eta_f = 0.450$ and $\eta_s = 0.517$, in excellent agreement with the approximate phase boundaries found in Ref. [77].

In order to investigate the region near the coexistence region more closely, we performed EDMD simulations on systems of $N = 64000$ particles starting from a simple cubic lattice. Coexistence between the fluid and solid phase can be observed directly for packing fractions $0.455 \leq \eta \leq 0.48$. Snapshots of the coexistence are shown in Fig. 5.1. In these snapshots, crystalline clusters were found using the local bond and orientational order parameters described in the previous section. Particles that were considered not to be part of a crystalline cluster are displayed much smaller than their actual size, in order to show what parts of the system are solid-like. We find good agreement between the located clusters based on orientational and bond order. This suggests that significant orientational order only occurs when bond order exists, and vice versa. Moreover, we find configurations with planar fluid-solid interfaces, but also fluid droplets and tubes in the solid phase and solid tubes in the fluid phase as the system tends to minimize the surface free energy. Hence, the surface tension is small, but not zero.

In Refs. [75, 77], the phase in coexistence with the fluid was identified as cubic, based on the finite diffusion present in the system up to packing fraction $\eta = 0.57$. In our simulations, part of the diffusion in the system appears to be caused by diffusion of entire rows of particles. In this way all particles in such a row are shifted to the next lattice site by using the periodic boundary conditions of the system to shift all particles in that row to the next lattice site. If this would be the main source of diffusion, larger system sizes should strongly suppress this behavior, as the free energy barrier involved in row diffusion scales with the number of particles in the row. We examined the diffusion for systems of $N = 1000, 8000$ and 64000 particles, but found no significant finite size effects in the diffusion constants, as shown in Fig. 5.2. Closer looks at trajectories of particles

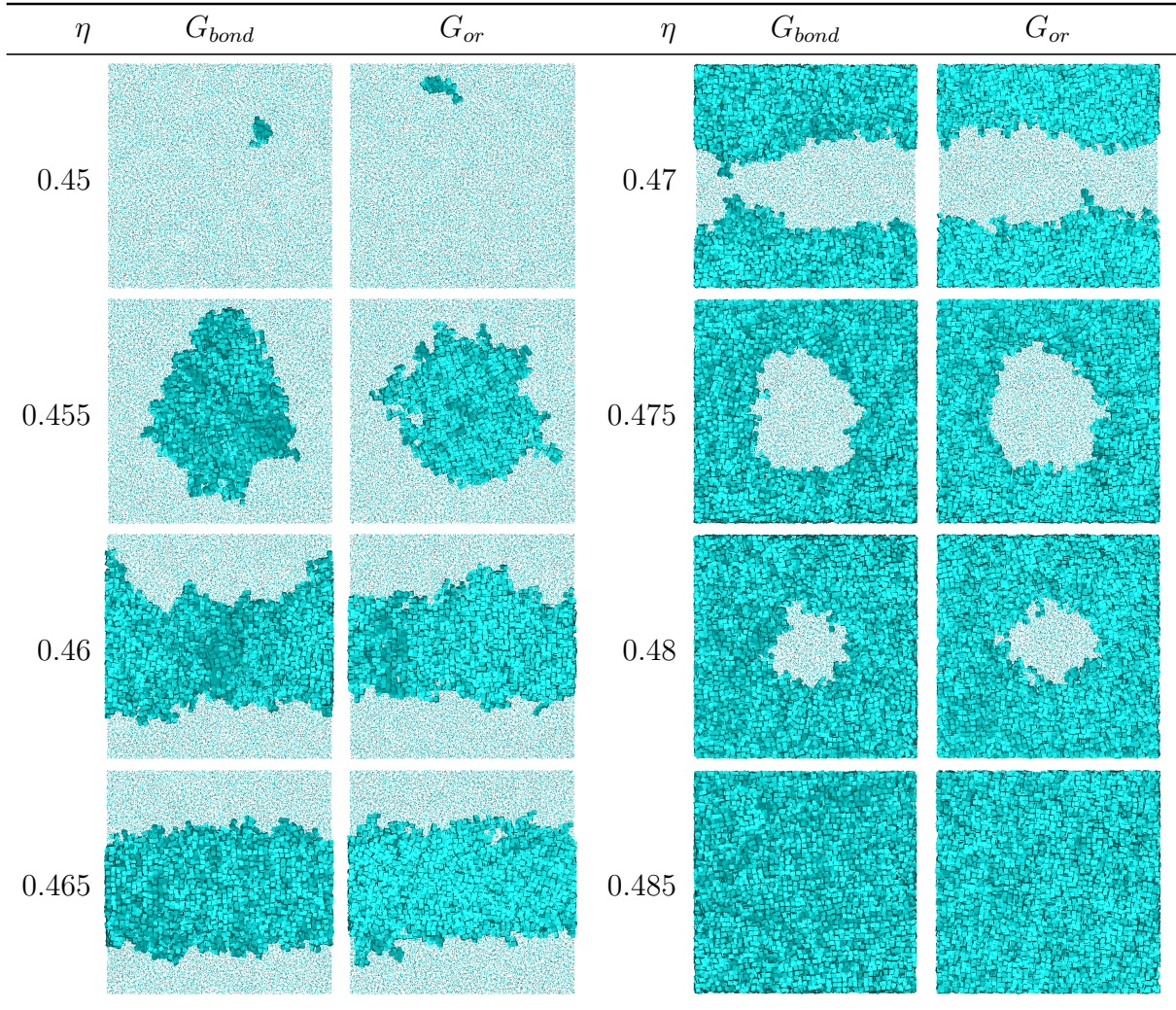


Table 5.1: Snapshots of EDMD simulations with $N = 64000$ hard cubes, at a range of packing fractions in the coexistence region. For each snapshot, clusters were determined based on q_4 for positional order and G_4 for orientational order. Particles in the largest solid cluster are shown at actual size, while all other particles are displayed much smaller.

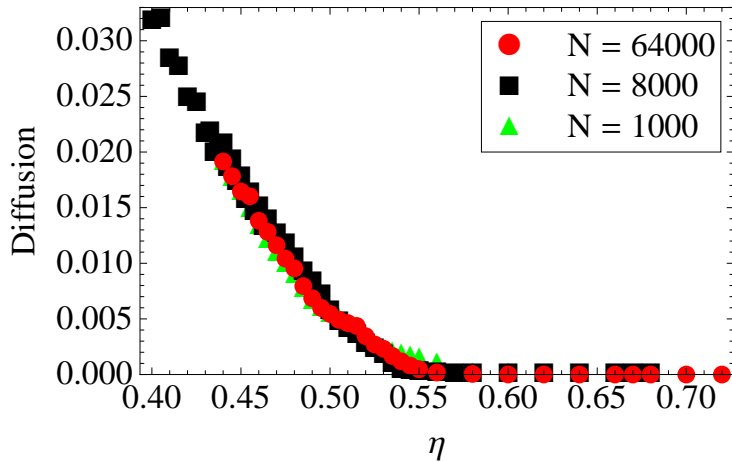


Figure 5.2: Diffusion coefficient D (in arbitrary units) as a function of the packing fraction for three different system sizes.

in the crystal suggest that the main cause of diffusion is accordeon-like motion of rows of particles, where lines of particles are compressed and stretched, allowing particles to move to a different lattice site.

Under close examination, the snapshots in Table 5.1 taken just above coexistence still exhibit a significant amount of positional order. However, the direction of the crystal is seen to change during the EDMD simulation: after a short equilibration time, the lattice vectors are no longer aligned with the simulation box. This spontaneous misalignment was observed in EDMD simulations of systems of size $N = 1000, 8000$ and 64000 , as well as in MC simulations of $N = 1000, 3375$ and 8000 particles. The rotation of the lattice only occurs at packing fractions lower than $\eta \simeq 0.57$, approximately corresponding to the region where a cubatic phase was identified in Refs. [75, 77]. However, it is not directly clear that the structures found at these densities do not exhibit long-range order. Table 5.2 shows scattering patterns for systems of $N = 8000$ particles at a range of densities near coexistence. A pattern of peaks indicating cubic crystalline order clearly starts emerging at the solid coexistence density of $\eta_s = 0.5$. In the coexistence region, pockets of fluid are present in the system, significantly reducing the crystalline order until only a ring-shaped maximum remains at packing fraction $\eta = 0.45$ and lower, where the box no longer contains crystalline clusters. While the crystalline order increases at higher densities, the pattern at $\eta = 0.5$ is already indicative of a crystalline structure.

We now study the correlation functions related to the orientational, bond-orientational and positional order in the system at packing fractions slightly above coexistence. In particular, the existence of long-range positional order would indicate the absence of a cubatic phase. Figure 5.4 shows the correlation functions for the orientational order ($G_{or}(r)$) and the bond-orientational order ($G_{bond}(r)$) at $\eta = 0.52$. These functions clearly reach a constant at large distances, and this behavior was seen to be consistent across all packing fractions above coexistence. A plot of the global positional order ($\langle G_{pos} \rangle$) as a function of η is shown on the right in Fig. 5.4. It is clear that both the bond-orientational and orientational order are long-range in nature and increase monotonically

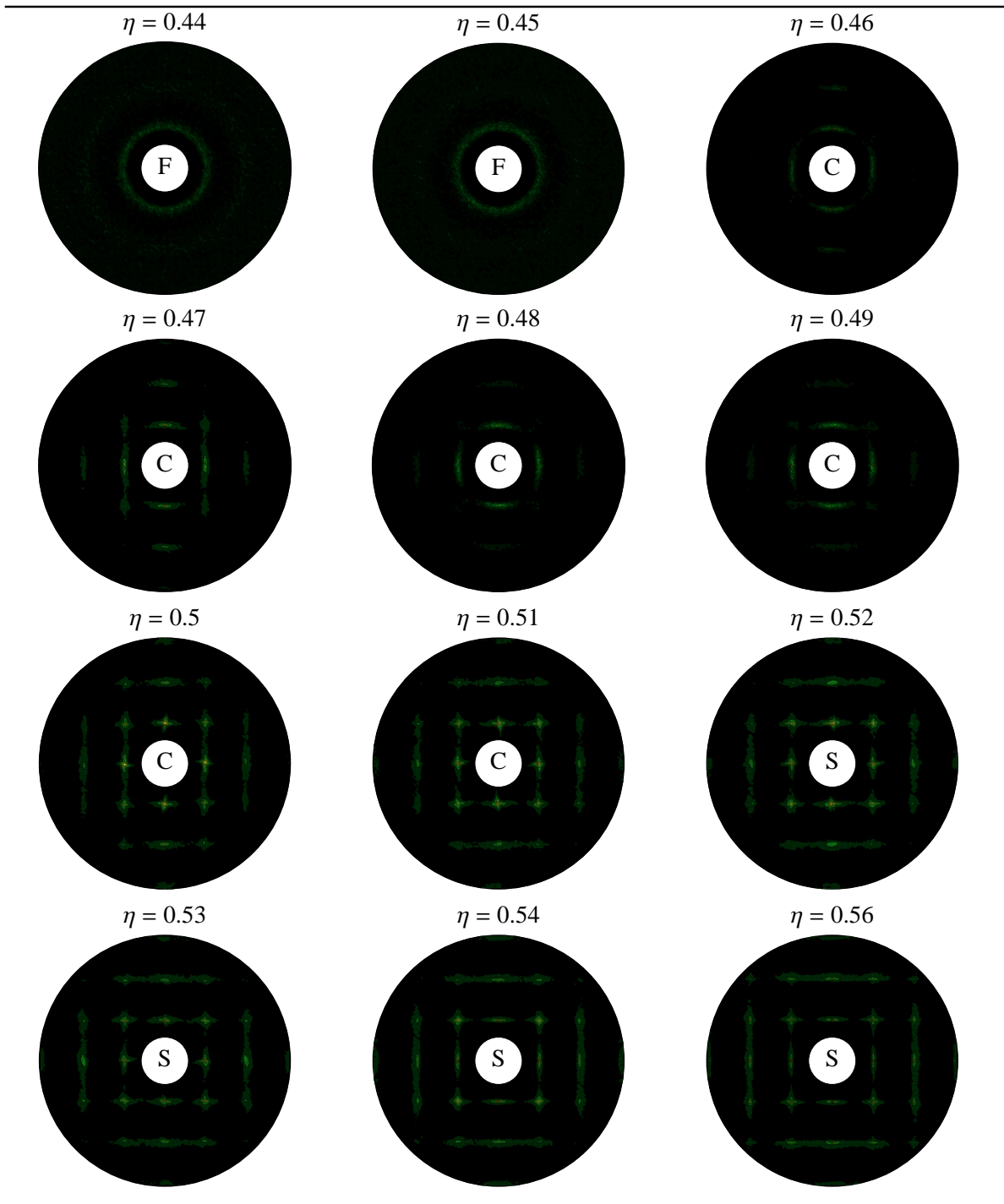


Table 5.2: Scattering patterns for a range of packing fractions η as labeled, measured in a system of $N = 8000$ particles and averaged over 50 snapshots. The letter in the middle denotes whether the sample is in the fluid phase (“F”), solid phase (“S”) or in the coexistence region (“C”), according to the phase diagram obtained from free energy calculations. For the two lowest packing fractions, the color scale has been adjusted to show the structure in the fluid more clearly.

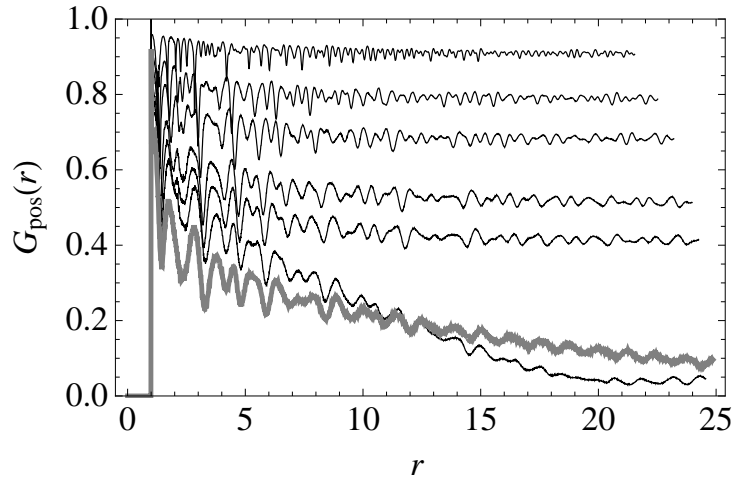


Figure 5.3: Positional correlation functions $G_{pos}(r)$ as a function of r in systems of $N = 64000$ hard cubes, for various packing fractions η . The thick line corresponds to $\eta = 0.52$, while the other lines correspond to $\eta = 0.54$ (bottom), 0.56, 0.58, 0.64, 0.7, and 0.8 (top). Note that the correlation for $\eta = 0.52$ is higher than the one for $\eta = 0.54$ at large distances.

with the packing fraction η . In Fig. 5.3, we present plots of the positional correlation function $G_{pos}(r)$ at a range of packing fractions above coexistence. At packing fractions $\eta > 0.56$, the correlation functions reach a constant value, indicating long-range positional order. However, at lower densities, the behavior is much less well defined, and different simulations at the same density can give different results. As seen from the crossing of the lines for $\eta = 0.52$ and $\eta = 0.54$, the correlation function does not necessarily decay faster at lower packing fractions. For these plots, the reciprocal lattice vector \mathbf{K} was chosen to correspond to a maximum in $S(\mathbf{K})$. While changing this vector to other maxima can change the behavior of the correlation function significantly, we did not find signs of long-range positional order at packing fractions below $\eta = 0.56$. Combined with a shorter-ranged positional order, this would correspond to a cubic phase. However, the region of packing fractions where no long-range positional order is observed is also the region where the crystal orientation is seen to change during the simulation. It is possible that the reorientation of the crystal structure in the simulation box introduces defects that break the long-range order, and since the rotation also slightly distorts the crystal, it seems unlikely that these rotated crystals correspond to the equilibrium state.

To examine the rotated lattices in detail, we projected the particle positions on a plane, averaging over a series of snapshots in a simulation of $N = 64000$ particles, at several packing fractions around $\eta = 0.54$. As before, the simulations were started in a $40 \times 40 \times 40$ simple cubic crystal state. Surprisingly, after equilibration we observed a clear lattice of 41×41 peaks in several simulations. Projecting along a different axis confirmed that the crystal sometimes formed extra layers in all three directions, increasing the total number of lattice positions. As the number of particles in the system is constant, the number of vacancies in the crystal is then approximately 7% of the number of lattice sites. In other simulations, the lattice rotated, and formed extra lattice sites in the process. This

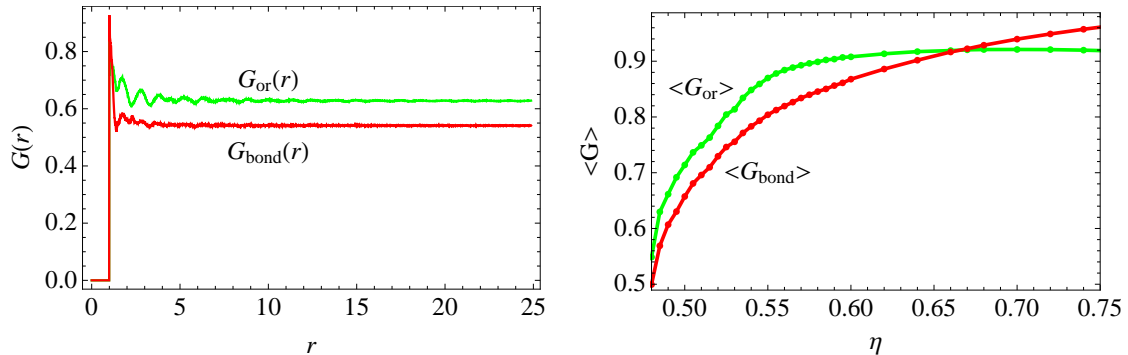


Figure 5.4: Orientational and bond-orientational order in systems of $N = 64000$ particles. **Left:** Orientational and bond-order correlation functions $G_{or}(r)$ (light) and $G_{bond}(r)$ (dark) at packing fraction $\eta = 0.52$. **Right:** Global order parameters $\langle G_{or} \rangle$ (light) and $\langle G_{bond} \rangle$ (dark), as calculated from the limiting value of the correlation functions (see Eq. 5.17).

behavior strongly suggests that the equilibrium concentration of vacancies is significantly higher in hard cubes than in e.g. hard spheres, where it is estimated to be $2.6 \cdot 10^{-4}$. [89, 90]

By performing EDMD simulations on systems with $N_L = 64000$ lattice sites, but fewer particles, we observe that the rotation of the crystal lattice in the simulation box can be prevented by a sufficiently high defect concentration. Figure 5.5 shows the global positional order $\langle G_{pos} \rangle$ as a function of the fraction of defects $\alpha = (N_L - N)/N_L$ at packing fractions $\eta = 0.52, 0.54$ and 0.56 . For $\eta = 0.52$, the positional order shows a clear peak at a defect concentration around 3%, which shift to lower numbers of vacancies as the density increases. The positional order parameter correlation functions near the peak in the order parameter clearly reach a constant at high distances, indicating long-range order. Typical plots are shown on the right in Fig. 5.5. This strongly suggests that the phase which was previously identified as cubatic is simply a metastable state, in which the system gets trapped as the number of particles does not accommodate a crystal with an equilibrium number of vacancies in the simulation box. A lower free energy for a system with a significant number of vacancies may also explain the observations of lattice reorientation in the simulation box: rotating the lattice is likely a relatively easy way for the system to create a small number of defects without adding a full extra layer to the crystal. Additionally, the number of defects in the system will strongly affect the diffusion in the crystal. Hence, the sharp decrease in the diffusion constant around $\eta = 0.56$ in Fig. 5.2 likely corresponds to the packing fraction above which the system was no longer able to form vacancies spontaneously in the finite simulation box.

We performed free energy calculations on crystals with a range of vacancy concentrations, as described in Section 5.2.2 above. Preliminary results for packing fraction $\eta = 0.52$ are shown in Fig. 5.6. As the number of vacancies increases, the free energy of the system decreases significantly. From these results, the equilibrium defect concentration seems to be on the order of 4%. Interestingly, the free energy as a function of the defect concentration is extremely flat near the equilibrium number of vacancies, indicating that significant fluctuations in the number of defects are possible without large free energy costs. To determine the equilibrium concentration of defects for higher densities,

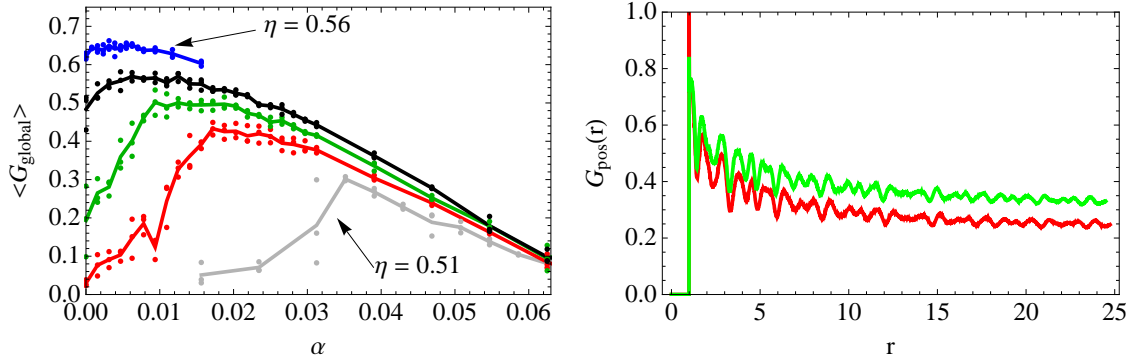


Figure 5.5: Left: Global positional order $\langle G_{\text{pos}} \rangle$ as a function of the fraction of vacancies in the lattice, at packing fractions $\eta = 0.51$ (bottom, gray), 0.52 (red), 0.53 (green), 0.54 (black) and 0.56 (top, blue). The points indicate measurements of $\langle G_{\text{pos}} \rangle$ along the x , y and z axes separately, while the lines are averaged over all three directions. Each point is averaged over 20 snapshots. **Right:** Positional order parameter correlation functions $G_{\text{pos}}(r)$ at $\eta = 0.52$ with $\alpha = (N_L - N)/N_L = 0.015$ (bottom) and at $\eta = 0.54$ with $\alpha = 0.007$ (top).

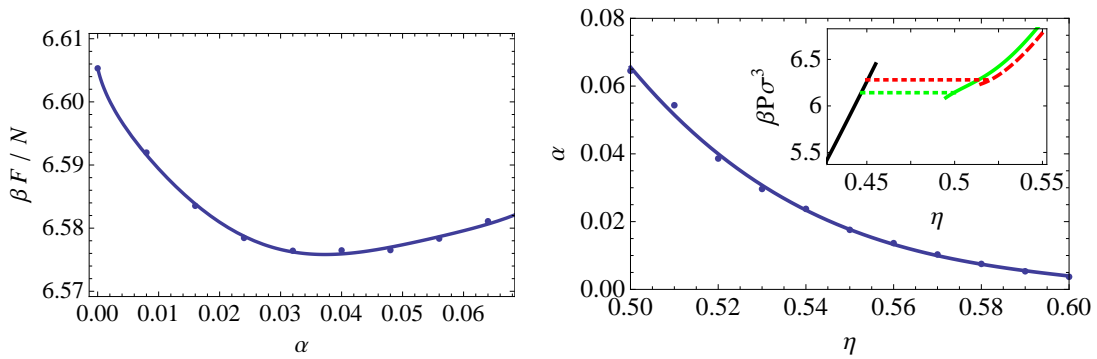


Figure 5.6: Left: Free energy as function of the defect concentration for a simple cubic crystal of hard cubes at constant packing fraction $\eta = 0.52$. The line is a fit through the points, with a minimum at $\alpha = 0.04$. **Right:** Equilibrium concentration of defects as a function of the packing fraction, as determined by free energy calculations. The line is a fit to guide the eye. The inset shows the equation of state of the fluid (black), of the solid without vacancies (red), and of the solid with an equilibrium concentration of vacancies (green). The coexistence as determined by Ref. [77] is depicted with a red dotted line, while the coexistence as determined in this Letter is shown with a green dotted line.

we performed EDMD simulations to calculate the crystal equation of state for the same range of defect concentrations, and used thermodynamic integration to calculate the free energy landscape as a function of density and defect concentration. Minimizing the free energy at densities $0.51 \leq \eta \leq 0.6$ showed that the expected defect concentration goes down monotonously as the density increases, as shown on the right in Fig. 5.6. Using the minimum in the free energy at each density, we performed a common tangent construction and calculated the coexistence densities to be $\eta_f = 0.45$ and $\eta_m = 0.50$ for the fluid and the solid, respectively. As can be expected, the decrease in free energy caused by the vacancies shifts the coexistence down compared to the defect-free crystal, as can be seen in the inset on the right-hand side in Fig. 5.6.

5.5 Conclusions and discussion

In summary, we have studied the phase behavior of colloidal hard cubes using both MC and EDMD simulations. The resulting phase diagram consists only of a fluid phase and a simple cubic crystal phase, with a coexistence region between $\eta_f = 0.45$ and $\eta_s = 0.50$. Close to the solid coexistence density, the concentration of vacancies in the crystal phase at a packing fraction just above coexistence is around 5%, which is extremely high when compared to other systems. This high equilibrium defect concentration drives the system to distortions and rotations of the crystal structure in order to form extra defects, leading to a less ordered metastable phase that was identified as a cubatic phase in earlier studies. [75, 77]

It is possible that the high vacancy concentration is related to the relatively low free energy cost of placing a particle between two (otherwise empty) lattice positions in the simple cubic crystal phase. In a hard-sphere crystal, for example, such a position would be highly unlikely as it requires a significant displacement of neighboring particles. Thus, a vacancy in hard-sphere and similar crystals will generally be localized to a single lattice site, and will occasionally hop as it is filled by a nearby particle. In contrast, the space of a vacancy in a hard-cube crystal can be smeared out over a longer row of particles, in such a way that each particle gains some extra free volume. While the particles are still significantly more likely to find themselves in one of the lattice positions, the extra entropy provided by the defect can then be significantly higher than it would be in a hard-sphere crystal. Consequently, one might also expect a finite equilibrium concentration of vacancies in crystal structures of other particles where particle movement between lattice sites is possible without significantly affecting other nearby particles. While in simulations of hard cubes the crystal was seen to spontaneously change its lattice to generate these vacancies, this effect may be less strong in other systems, which makes it harder to find whether or not the crystal phase exhibits a high equilibrium concentration of vacancies. However, for crystal structures such as the ones found for hexagonal and triangular prisms in Ref. [77], or the square lattice of hard squares 2D [91], the possibility of crystal vacancies should likely be taken into account, as these could affect the region of stability for the crystal phase.

5.6 Acknowledgements

I would like to thank Laura Filion for her collaboration on this project, and for performing the Monte Carlo simulations and free energy calculations discussed in this chapter. I would also like to thank Matthieu Marechal for useful discussions.

Phase diagrams of colloidal spheres with a constant zeta-potential

We study suspensions of colloidal spheres with a constant zeta-potential within Poisson-Boltzmann theory, quantifying the discharging of the spheres with increasing colloid density and decreasing salt concentration. We use the calculated renormalized charge of the colloids to determine their pairwise effective screened-Coulomb repulsions. We then calculate bulk phase diagrams in the colloid concentration-salt concentration representation, for various zeta-potentials, by a mapping onto published fits of phase boundaries of point-Yukawa systems. Although the resulting phase diagrams do feature face-centered cubic (fcc) and body-centered cubic (bcc) phases, they are dominated by a (re-entrant) fluid phase due to the colloidal discharging with increasing colloid concentration and decreasing salt concentration.

6.1 Introduction

Charged colloidal particles suspended in a liquid electrolyte are interesting soft-matter systems that have generated fundamental as well as industrial attention for decades. [92] Understanding the stability and phase behaviour of these systems as a function of colloid concentration and ionic strength is an important theme in many of these studies. A key role is played by the electrostatic repulsions between the colloidal spheres, which are not only capable of stabilising suspensions against irreversible aggregation due to attractive Van der Waals forces, [93] but are also the driving force for crystallisation, [94] provided the surface charge on the colloids is high enough and the range of the repulsions long enough. [92–94] The classic theory that describes the electrostatic repulsions between charged colloidal particles in suspension goes back to the 1940's, when Derjaguin, Landau, Verwey, and Overbeek (DLVO) found, within linear screening theory, that suspended spheres repel each other by screened-coulomb (Yukawa) interactions. [42, 95] The strength of these repulsions increases with the square of the colloidal charge, and they decay exponentially with particle-particle separation on the length scale of the Debye screening length of the solvent. [96] This pairwise Yukawa form is a corner stone of colloid science, and can explain a large number of observations. [92–94] For instance, the experimentally observed crystallisation of charged colloidal spheres into body-centered cubic (bcc) and face-centered cubic (fcc) phases upon increasing the colloidal packing fraction at low and high salt concentrations, [97–100] respectively, is in fair agreement with simulations of Yukawa systems. [101–104] Interestingly, in these simulation studies, as well as in many other studies, [105–109] the charge of the colloids is assumed to be independent of the colloid density and the salt concentration.

Experiments on deionized aqueous suspensions of highly charged spherical latex colloids with ionizable sulphate groups showed indeed evidence for an effective charge that is independent of volume fraction using elasticity and conductivity measurements. [110–112] Differences between the effective charge obtained from conductivity and elasticity measurements were attributed to either charge renormalization [105] or macro-ion shielding due to many-body effects. [113–115] Similar conclusions were obtained for silica particles with ionizable carboxylate groups on the surface. [116]

The constant-charge assumption was argued to break down, however, in some recent studies where the electrostatic repulsions were argued to be reduced with increasing colloid concentration. Biesheuvel, [117] for instance, argues that experimental equilibrium sedimentation-diffusion profiles of charged silica spheres in ethanol at extremely low salt concentrations [118] are better fitted by a charge-regulation model than by a constant-charge model. [119] More recent evidence for a concentration-dependent colloidal charge stems from re-entrant melting and re-entrant freezing observations of PMMA spheres in a solvent mixture of *cis*-decaline and cyclohexyl bromide, i.e. the phase sequence upon increasing the colloid concentration is fluid-crystal-fluid-crystal. [120] In addition, direct force measurements between a single pair of colloidal PMMA spheres in hexadecane, a pair that is part of a triplet, and a pair that is part of a multiplet have very recently revealed a significant reduction of the force with increasing number of neighbouring particles. [121] Interestingly, in the three experiments of Refs.[118, 120, 121] the solvent is a nonpolar medium.

In fact, the experimental findings of Ref. [121] could well be interpreted and explained in terms of constant-potential boundary conditions on the colloidal surfaces, rather than the more usual constant-charge assumption. Recently, electrophoresis experiments on PMMA spheres in a low-polar solvent that the charge per particle decreased as a function of the volume fraction, while the surface potential appeared to remain more or less constant. [122] This chapter addresses the consequence of constant-potential boundary conditions for the packing fraction-salt concentration phase diagram of Yukawa systems by calculating the colloidal charge and the effective screening length for various zeta-potentials as a function of salt- and colloid concentration. In the case of high zeta-potential this requires nonlinear screening theory, and hence the renormalized rather than the bare colloidal charge determines the effective screened-Coulomb repulsions between the colloids. [98, 105, 108, 116, 123–127] For this reason we use the renormalized charge throughout. We also compare our constant-potential calculations with those of an explicit charge-regulation model, [128–133] and conclude that their results are qualitatively similar, and even quantitatively if they are considered as a function of an effective screening length.

6.2 Model and theory

We consider N colloidal spheres of radius a in a solvent of volume V , temperature T , dielectric constant ϵ and Bjerrum length $\lambda_B = e^2/\epsilon k_B T$. Here e is the elementary charge and k_B the Boltzmann constant. The colloidal density is denoted by $n = N/V$ and the packing fraction by $\eta = (4\pi/3)na^3$. The suspension is presumed to be in osmotic contact with a 1:1 electrolyte of Debye length κ^{-1} and total salt concentration $2\rho_s$. We are interested in suspensions of charged colloids of which the surface (zeta) potential ψ_0 rather than the charge Ze is fixed. We will show that this constant-potential condition mimics charge-regulation on the colloidal surfaces fairly accurately. The first goal of this article is to calculate Z as a function of η for fixed dimensionless combinations κa , a/λ_B , and $\phi_0 \equiv e\psi_0/k_B T$. This result will then be used to quantify the effective Yukawa interactions between pairs of colloids, and hence the phase boundaries between fluid, face-centered cubic (fcc) and body-centered cubic (bcc) crystalline phases.

In the actual suspension of constant-potential colloidal spheres, the charge distribution of each of the N colloids will be distributed heterogeneously over its surface due to the proximity of other colloids in some directions. This leads to a tremendously complex many-body problem that we simplify here by *assuming* a spherically symmetric environment for each colloid, which is nevertheless expected to describe the average electrostatic properties realistically. Below we will calculate the electrostatic potential $\psi(r)$ at a radial distance r from a charged colloidal sphere at a given zeta-potential ψ_0 , i.e. at a given value $\psi(a) = \psi_0$. The colloidal charge Ze then follows from Gauss' law

$$\psi'(a) = -\frac{Ze}{\epsilon a^2}, \quad (6.1)$$

where a prime denotes a radial derivative.

We first consider a single colloid in the center of a spherical Wigner-Seitz cell of radius R , such that the cell volume equals the volume per particle, $(4\pi/3)R^3 = V/N$, which

implies $R = a\eta^{-1/3}$. The radial coordinate of the cell is called r . We write the ionic density profiles for $r \in (a, R)$ as Boltzmann distributions $\rho_{\pm}(r) = \rho_s \exp(\mp\phi(r))$, with $\phi(r) = e\psi(r)/k_B T$ the dimensionless electrostatic potential. Together with the Poisson equation $\nabla^2\phi = -4\pi\lambda_B(\rho_+(r) - \rho_-(r))$, this gives rise to the radially symmetric PB-equation and boundary conditions (BC's)

$$\phi''(r) + \frac{2}{r}\phi'(r) = \kappa^2 \sinh \phi(r), \quad r \in (a, R); \quad (6.2)$$

$$\phi(a) = \phi_0; \quad (6.3)$$

$$\phi'(R) = 0, \quad (6.4)$$

where a prime denotes a derivative with respect to r . Note that BC (6.4) implies charge neutrality of the cell. Once the solution $\phi(r)$ is found for given η , κa , and ϕ_0 , e.g. numerically on a radial grid, the colloidal charge Z follows from Eq.(6.1), which we rewrite in dimensionless form as

$$\frac{Z\lambda_B}{a} = -a\phi'(a). \quad (6.5)$$

From the numerical solutions that we will present below it turns out that Z decreases monotonically from a finite asymptotic low- η (large- R) value Z_0 to essentially 0 at $\eta \simeq 1$ (or $R \simeq a$).

Within linear-screening theory at low packing fraction, where $\sinh \phi \simeq \phi$, the potential distribution can be solved for analytically, yielding $\phi(r) = \phi_0 a \exp[-\kappa(r-a)]/r$, such that the colloidal charge takes the asymptotic low- η and low- ϕ_0 value

$$\frac{Z_0\lambda_B}{a} = (1 + \kappa a)\phi_0. \quad (6.6)$$

In the appendix we show that the discharging effect with increasing η , as found from the nonlinear screening theory discussed above, can also be approximated within linear screening theory, yielding

$$Z(\eta, \kappa a) = \frac{Z_0}{1 + \eta/\eta^*}, \quad \eta^* = \frac{(\kappa a)^2}{3(1 + \kappa a)}, \quad (6.7)$$

where η^* is a crossover packing fraction at which the colloidal charge has decayed to half its dilute-limit value Z_0 given in Eq.(6.6). For typical numbers of experimental interest, e.g. $a/\lambda_B = 100$ and $\kappa a = 0.25$, we then find $Z_0 = 125\phi_0$ and $\eta^* = 0.017$. With $\phi_0 \simeq 1 - 2$, which corresponds to a surface potential of 25-50mV, we should expect a few hundred charges in the dilute limit and a significant charge reduction for $\eta \gtrsim 10^{-2}$.

The constant-potential boundary condition that we employ here is supposed to mimic charge-regulation on the colloidal surface through an association-dissociation equilibrium of chargeable groups on the surface. Here we consider, as a typical example, the reaction $SA \Leftrightarrow S^+ + A^-$ where a neutral surface group SA dissociates into a positively charged surface group S^+ and a released anion A^- . The chemistry of such a reaction can be characterised by a reaction constant K such that $[S^+][A^-]/[SA]=K$, where the square brackets indicate concentrations in the vicinity of the surface where the reaction takes place. If we now realise that $Z \propto [S^+]$, we find for the usual case where $[S^+] \ll [SA]$ that

$Z \propto 1/[A^-]$. For the case that the released anion is of the same species as the anion in the reservoir, such that $[A^-] = \rho_s \exp[\phi(a)]$, we thus have

$$Z = z \exp(-\phi(a)), \quad (6.8)$$

where the prefactor z , which is a measure for the surface chargeability, [134] accounts for the chemistry, the surface-site areal density, and the total area of the surface between the colloidal particle and the electrolyte solution. Note that Eq.(6.8) relates the (yet unknown) colloidal charge Z to the (yet unknown) zeta-potential $\phi(a)$, for a given z . A closed set of equations for charge-regulated colloids is obtained by combining the PB equation (6.2) with BC (6.4) at the boundary of a spherical Wigner-Seitz cell of radius R , with BC (6.3) replaced by

$$a\phi'(a) = -\frac{\lambda_B z}{a} \exp(-\phi(a)), \quad (6.9)$$

for some given chargeability z . The resulting solution $\phi(r)$ gives the zeta-potential $\phi(a)$ as well as the colloidal charge Z using Eq.(6.8). When comparing the constant-potential model with the ionic association-dissociation model, we will tune the chargeability z such that the low- η results for Z coincide for both models.

It is well known that nonlinear screening effects, in particular counterion condensation in the vicinity of a highly charged colloidal surface, reduce the effective colloidal charge that dictates the screened-Coulomb interactions between the colloids. [105, 108, 123–125, 135] The so-called renormalized colloidal charge, Z^* , can be calculated from the electrostatic potential $\phi(r)$ as obtained from the nonlinear PB equation by matching the numerically obtained solution at the edge of the cell to the analytically known solution of a suitably linearized problem. By extrapolating the solution of the linearized problem to the colloidal surface at $r = a$, one obtains the effective charge by evaluating the derivative at $r = a$ using Eq.(6.5). Following Trizac *et al.*, [136] the renormalized charge Z^* can be written as

$$\frac{Z^* \lambda_B}{a} = -\frac{\tanh \phi_D}{\bar{\kappa} a} \left((\bar{\kappa}^2 a R - 1) \sinh[\bar{\kappa}(R - a)] + \bar{\kappa}(R - a) \cosh[\bar{\kappa}(R - a)] \right), \quad (6.10)$$

where the ‘Donnan’ potential is defined as $\phi_D \equiv \phi(R)$, i.e. the numerically found potential at the boundary of the cell, and where the effective inverse screening length is

$$\bar{\kappa} = \kappa \sqrt{\cosh \phi_D}. \quad (6.11)$$

Note that Z^* and $\bar{\kappa}$ can be calculated for the constant-potential as well as the association-dissociation model in a spherical cell.

6.3 Effective charge and screening length

For both the constant surface potential (CSP) and the association-dissociation (AD) model discussed above we calculated the bare colloidal charge Z , the effective (renormalized) charge Z^* , and the effective inverse screening length $\bar{\kappa}$ in the geometry of spherical

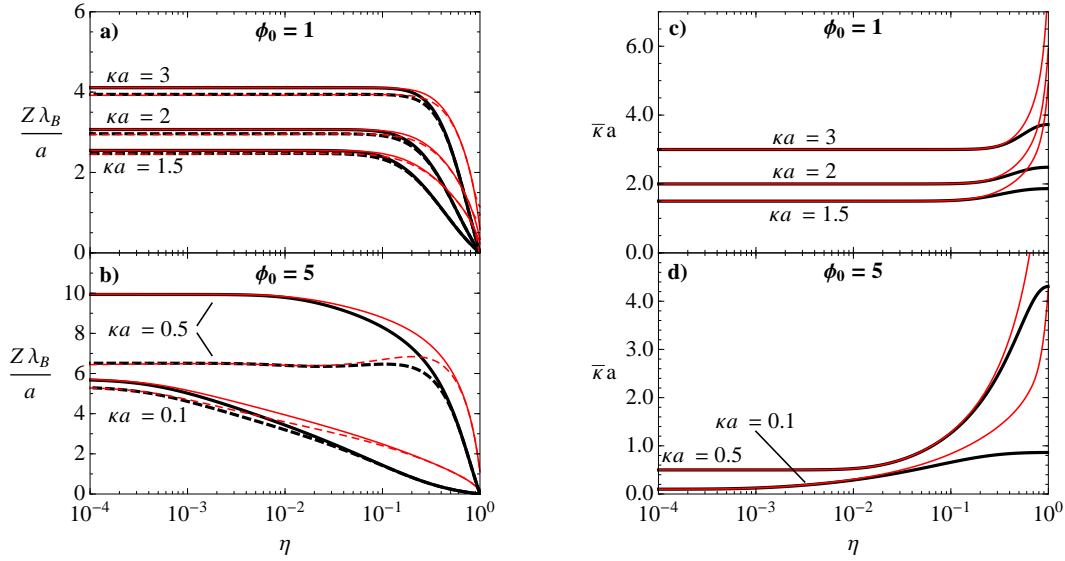


Figure 6.1: Left: The bare colloidal charge Z (continuous black curves) and the renormalized charge Z^* (dashed black curves), both in units of a/λ_B (see text), as a function of the colloidal packing fraction η for several screening parameters κa , for constant surface potentials (a) $\phi_0 = 1$ and (b) $\phi_0 = 5$. The red curves denote Z and Z^* as obtained from the association-dissociation model, with the chargeability z chosen such that the surface potential in the dilute limit $\eta \rightarrow 0$ equals ϕ_0 . **Right:** The effective inverse screening length $\bar{\kappa}$ as a function of the packing fraction η for several reservoir screening parameters κa , for constant surface potentials (c) $\phi_0 = 1$ and (d) $\phi_0 = 5$ as represented by the black curves. The red curves denote $\bar{\kappa}$ as obtained from the association-dissociation model, with the chargeability z chosen such that the surface potential in the dilute limit $\eta \rightarrow 0$ equals ϕ_0 . Note that $\bar{\kappa} = \kappa$ in all cases for $\eta \rightarrow 0$.

Wigner-Seitz cells. In Fig.6.1(a) and (b) we show $Z\lambda_B/a$ (full curves) and $Z^*\lambda_B/a$ (dashed curves) as a function of packing fraction η , for two screening constants for both the CSP model (black curves) and the AD model (red curves), in (a) for fixed zeta-potential $\phi_0 = 1$ and in (b) for $\phi_0 = 5$. In all cases the chargeability parameter z of the AD model is chosen such as to agree with the CSP model in the low-density limit $\eta \rightarrow 0$. For low packing fractions, the red and black curves show agreement for equal κa , by construction. At higher η the agreement is only qualitative, and the charges predicted by the AD model exceed those of the CSP model, which should not come as a surprise since the former interpolates between the constant-charge and the constant-potential model. The close agreement between Z and Z^* for all κa at $\phi_0 = 1$ in Fig.6.1(a) is also to be expected, since $\phi_0 = 1$ is not far into the nonlinear regime. By contrast, deep in the nonlinear regime of $\phi_0 = 5$, as shown in Fig.6.1(b), there is a significant charge renormalization effect such that $Z^* < Z$ by a factor of about 1.2 and 1.5 for $\kappa a = 0.1$ and $\kappa a = 0.5$, respectively. The merging of the red and the black curves at high- η in Fig.6.1(b) is due to the reduction of the charge into the linear-screening regime such that $Z = Z^*$. The increase of Z^* with κ , as observed in both Fig.6.1(a) and (b), is in line with well-known charge-renormalization results, [105, 108, 123–125, 136] and with Eq. 6.6.

In Fig.6.1(c) and (d) we plot, for the same zeta-potentials, the effective screening parameter $\bar{\kappa}$ as a function of η for several reservoir screening constants κ . At low enough η , where $\kappa R \gg 1$, the two screening constants are indistinguishable from each other in all cases. The reason is that the cell is then large enough for the potential to decay to essentially zero at $r = R$, such that the asymptotic decay of $\phi(r)$ is governed completely by the screening constant κ of the background (reservoir) salt concentration. At larger η , and hence smaller cells, $\phi(R)$ is no longer vanishingly small and the ion concentrations $\rho_{\pm}(R)$ at $r = R$ deviate considerably from the ionic reservoir concentration ρ_s . This larger ionic concentration at the cell boundary, which represents an enhanced ion concentration in between the colloidal particles in the true many-body system, leads to a larger effective screening constant $\bar{\kappa}$ with increasing η at a fixed κ , as is shown in Fig.6.1(c) and (d). Given that larger charges are obtained in the AD model than in the CSP model at high η , the number of counterions in the cell, and hence $\bar{\kappa}$, is also larger in the AD model.

6.4 Effective interactions and phase diagrams

Once the effective colloidal charge Z^* and the effective screening length $\bar{\kappa}^{-1}$ have been determined from the numerical solution of the PB equation in a spherical cell, either for constant-potential or association-dissociation boundary conditions, the effective interactions $u(r)$ between a pair of colloidal particles separated by a distance r follows, assuming DLVO theory, as

$$\frac{u(r)}{k_B T} = \begin{cases} \infty, & r < 2a; \\ \lambda_B \left(\frac{Z^* \exp(\bar{\kappa}a)}{1 + \bar{\kappa}a} \right)^2 \frac{\exp(-\bar{\kappa}r)}{r}, & r > 2a, \end{cases} \quad (6.12)$$

where we include a short-range hard-core repulsion for overlapping colloids and ignore Van der Waals forces (which is justified for index-matched particles). Note that the pair potential $u(r)$ depends on density-dependent parameters Z^* and $\bar{\kappa}$, and therefore contains two many-body effects, (i) charge renormalization, and (ii) colloidal discharging with increasing density. However, one could expect macro-ion shielding as another many-body effect. [98, 116, 126, 137] In states where the pair interaction $u(r)$ is so weak that a fluid phase results, we expect the macro-ion shielding to be weak; in crystalline states with strong effective pair interactions macro-ion shielding could also be significant. We expect, however, that the strongest underlying assumption in crystalline states is the spherical cell employed in our calculations. The actual Wigner-Seitz cell in face-centered-cubic and body-centered-cubic crystal phases will probably generate an anisotropic charge distribution on constant-potential colloids and hence anisotropic pair interactions. Such a problem could in principle be tackled with the numerical technique developed in Ref. [138], but due to its numerical involvement such a study is left for future work. Below, we will find a surprisingly large parameter regime, where a fluid phase is predicted, which gives an *a posteriori* justification for the use of the relatively simple pair potential $u(r)$ of Eq. (6.12).

One could use this pair interaction to simulate (or otherwise calculate) properties of the suspension in a given state-point, e.g. whether the system is in a fluid or crystalline

state. We restrict our attention here to the limiting case in which the colloidal particles are sufficiently highly charged and/or sufficiently weakly screened, that the pair-potential at contact satisfies $u(2a) \gg k_B T$, thereby effectively preventing direct particle-particle contact. In this limit the suspension can be effectively regarded as a point-Yukawa system that can be completely characterised by only *two* dimensionless parameters U and λ for the strength and the range of the interactions, respectively. They are defined as

$$U = \left(\frac{Z^* \exp(\bar{\kappa}a)}{1 + \bar{\kappa}a} \right)^2 \frac{\lambda_B}{a} \left(\frac{3\eta}{4\pi} \right)^{1/3} \quad (6.13)$$

$$\lambda = \bar{\kappa}a \left(\frac{3\eta}{4\pi} \right)^{-1/3}, \quad (6.14)$$

such that the point-Yukawa interaction potential of interest, in units of $k_B T$, reads $U \exp(-\lambda x)/x$ with $x = r(N/V)^{1/3}$ the particle separation in units of the typical particle spacing. Note that *three* dimensionless parameters would have been needed if hard-core contact was not a low Boltzmann-weight configuration, e.g. then the contact-potential $\beta u(2a)$ (i.e. the inverse temperature), the dimensionless screening parameter κa , and the packing fraction η would be a natural choice. The mapping of the phase diagram of the point-Yukawa system onto hard-core Yukawa systems has been tested and verified explicitly by computer simulation. [104]

The point-Yukawa system has been studied by simulation in great detail over the years, [101–104] and by now it is well known this model features a disordered fluid phase and two crystalline phases (face-centered cubic (fcc) and body-centered cubic (bcc)). Their first-order phase boundaries are well-documented, and can accurately be described by curves in the two-dimensional (λ, U) plane. Here, we employ the fits for the phase boundaries of point-Yukawa particles that were presented in Ref. [104], which were based on the results of Hamaguchi *et al.* [103] The melting-freezing line between the bcc crystal and the fluid is accurately fitted by

$$\begin{aligned} \ln U &= 4.670 - 0.04171\lambda + 0.1329\lambda^2 - 0.01043\lambda^3 \\ &\quad + 4.343 \cdot 10^{-4}\lambda^4 - 6.924 \cdot 10^{-6}\lambda^5, \\ &\text{for } 0 \leq \lambda \leq 12, \end{aligned} \quad (6.15)$$

and the bcc-fcc transition by

$$\begin{aligned} \ln U &= 97.65106 - 150.469699\lambda + 106.626405\lambda^2 \\ &\quad - 41.67136\lambda^3 + 9.639931\lambda^4 - 1.3150249\lambda^5 \\ &\quad + 0.09784811\lambda^6 - 0.00306396\lambda^7, \\ &\text{for } 1.85 \leq \lambda \leq 6.8. \end{aligned} \quad (6.16)$$

Here we exploit these empirical relations as follows. For given dimensionless colloid radius a/λ_B and screening constant κa , we calculate Z^* and $\bar{\kappa}a$ for various η for the CSP and

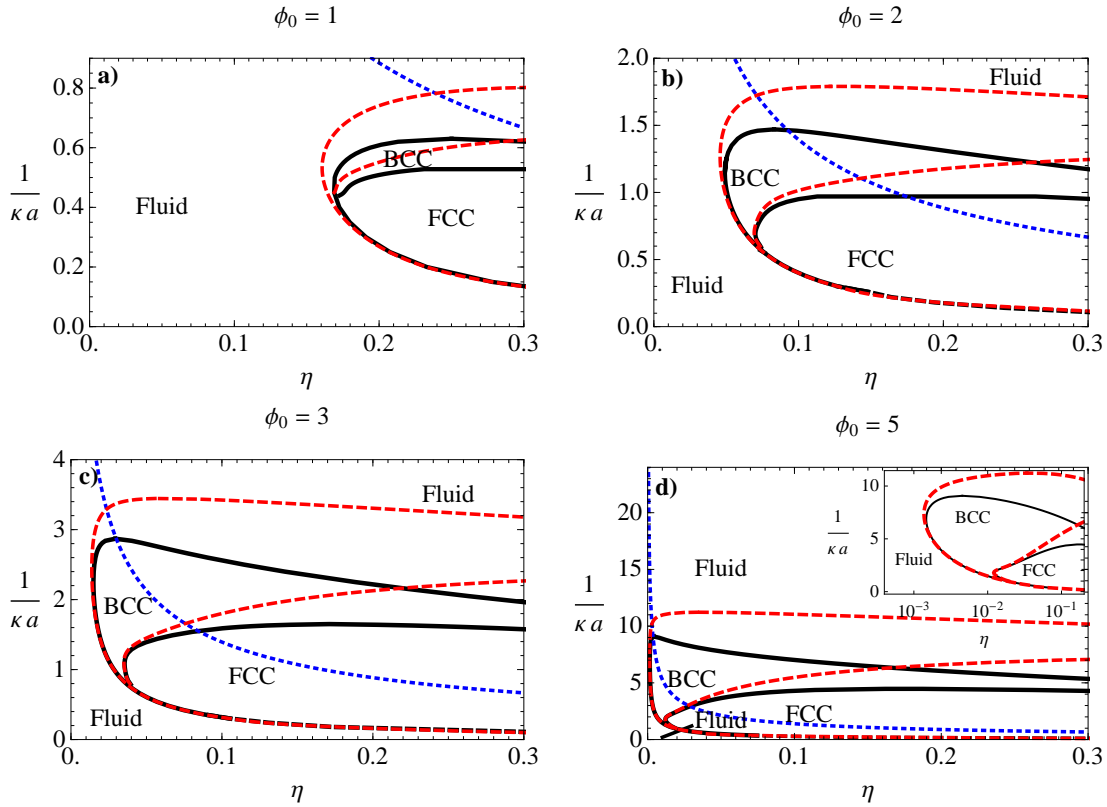


Figure 6.2: Phase diagrams in the packing fraction-screening length (η, κ^{-1}) representation for constant-potential colloids (radius $a/\lambda_B = 100$) interacting with the hard-core Yukawa potential of Eq.(6.12), for surface potentials $\phi_0 = 1, 2, 3,$ and 5 . The black lines represent phase boundaries for the constant-potential model, and the red dashed lines for the association-dissociation model with the surface potential equal to ϕ_0 in the dilute limit. The dashed black lines indicate extrapolation of Eq.(6.15) beyond its strict regime of accuracy. The inset in the phase diagram for $\phi_0 = 5$ represents η on a logarithmic scale for clarity. The labels “Fluid”, “BCC”, and “FCC” denote the stable fluid, bcc, and fcc regions. We note that the very narrow fluid-fcc, fluid-bcc, and fcc-bcc coexistence regions are just represented by single curves. The dotted blue curves represent the estimated crossover-packing fraction η^* of Eq.(6.7), beyond which $Z(\eta) < Z(0)/2$.

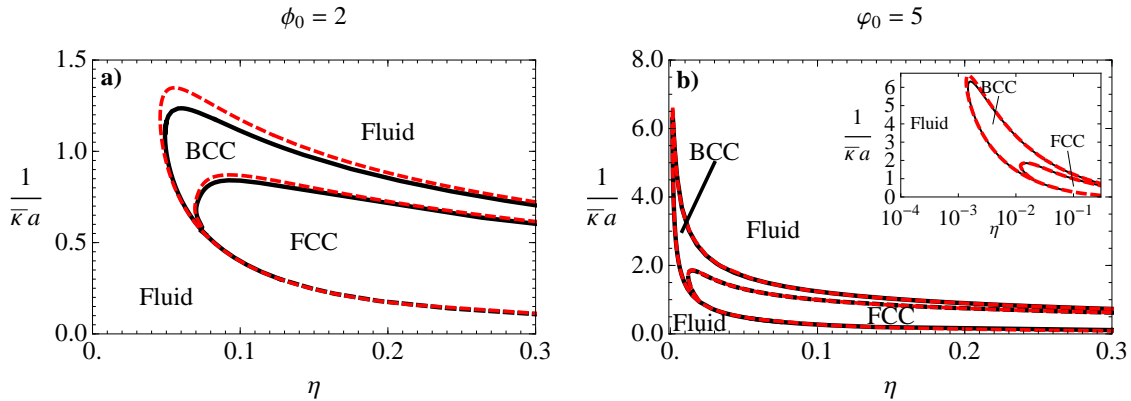


Figure 6.3: Phase diagrams in the packing fraction-*effective* screening length representation $(\eta, (\bar{\kappa}a)^{-1})$, for $a/\lambda_B = 100$, for constant-potential colloids with (a) $\phi_0 = 2$ and (b) $\phi_0 = 5$, as well as for charge-regulated colloids. Lines, symbols, and colors as in Fig.6.2.

the AD model in the spherical cell, as described in the previous section. These quantities can be used to compute the dimensionless Yukawa parameters U and λ from Eqs.(6.13) and (6.14), such that their phase and phase-boundaries are known from Eqs.(6.15) and (6.16).

For $a/\lambda_B = 100$, Fig.6.2 shows the phase diagrams that result from this point-Yukawa mapping procedure in the $(\eta, (\kappa a)^{-1})$ representation, for the CSP model (black curves) with surface potentials (a) $\phi_0 = 1$, (b) $\phi_0 = 2$, (c) $\phi_0 = 3$, (d) $\phi_0 = 5$, and for the corresponding AD model (red curves). The dashed lines represent the phase boundary fits of Eqs.(6.15) and (6.16) outside their strict λ -regime of applicability. We restrict attention to $\eta < 0.3$, as the point-Yukawa limit breaks down due to strong excluded-volume effects at higher packing fractions. An expected feature is the shift of the freezing curves to lower η for higher ϕ_0 , due to the higher (renormalized) charge and the stronger repulsions at higher ϕ_0 . Due to the higher charges in the AD model, its crystallisation regimes (red curves) extend to somewhat lower η 's and longer screening lengths than those of the CSP model (black curves). However, the most striking feature of all these phase diagrams is the huge extension of the fluid regime: at high *and* at low screening length there is *no* crystalline phase at all (for $\eta < 0.3$), while at some intermediate salt concentrations the crystal phases are sandwiched in between an ordinary low-density fluid and a re-entrant fluid phase. This re-entrant fluid regime becomes more prominent with increasing zeta-potential ϕ_0 . The underlying physics of this finite-salt and finite- η regime where bcc and fcc crystals exist is the *discharging* of the colloids with increasing η and decreasing salt concentration: (i) although at high salt (small screening length) the colloidal charge is high, the screened-Coulomb interaction is then so short-ranged that the system resembles a hard-sphere system that will only crystallize at $\eta \simeq 0.5$; (ii) at low salt (long screening length) the colloidal charge is too low to have seizable repulsions that drive crystallisation. Only at intermediate salt and intermediate colloidal packing the charge is high enough and the screening sufficiently long-ranged to drive crystallisation.

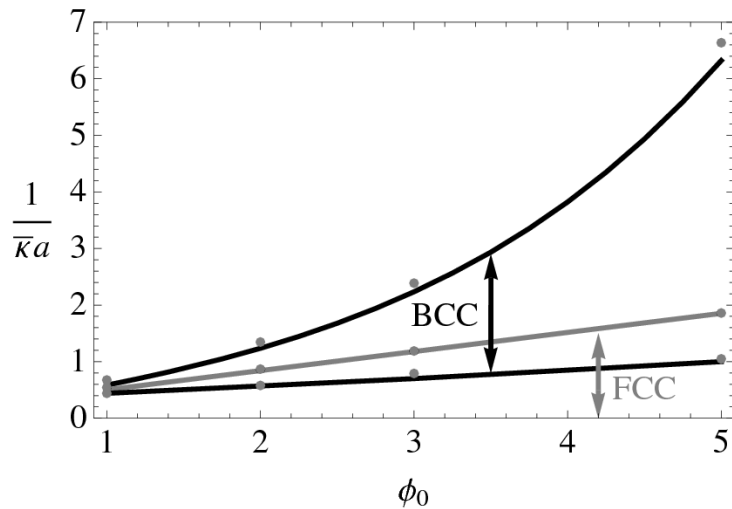


Figure 6.4: Maximum and minimum effective screening lengths where bcc and fcc can be found, as a function of the surface potential, assuming a constant surface potential for $a/\lambda_B = 100$. The bcc regime is in between the two black lines, and the fcc regime below the gray line. The gray points indicate the results from the AD model.

The dotted blue curves in Fig.6.2 represent the crossover packing fraction η^* of Eq.(6.7) beyond which the colloidal charge has been reduced to less than 50 percent of its dilute-limit value. Clearly, our expression for η^* indeed roughly coincides with the onset of the re-entrant fluid regime. Eq.(6.7) thus provides a quick guide to estimate where or whether re-entrant melting is to be expected at all. Interestingly, at $\phi_0 = 3$, there are values for κa (albeit in a very narrow range) where a phase sequence fluid-bcc-fcc-bcc is predicted here upon increasing the colloidal packing fraction, showing a re-entrant bcc phase appearing after the fcc crystal. Moreover, for $\eta > 0.5$ one expects hard-sphere freezing into an fcc (or hcp) stacking on the basis of hard-sphere interactions, so the fcc phase is then also re-entrant.

Experimentally it is not always possible or convenient to characterise the screening in terms of the Debye length κ^{-1} of the (hypothetical) reservoir with which the suspension would be in osmotic equilibrium. For instance, in conductivity measurements at finite colloid concentration one essentially measures the ionic strength of the sample, which is directly related to the effective screening constant $\bar{\kappa}$ rather than κ . Also, any measurement of effective colloidal interactions will yield $\bar{\kappa}$. Because of this accessibility of $\bar{\kappa}$, we replot in Fig.6.3 the phase diagrams for $\phi_0 = 2$ and $\phi_0 = 5$ of Fig.6.2, but now in the $(\eta, (\bar{\kappa}a)^{-1})$ representation. While the phase behavior in for example a sedimentation experiment will be easier to compare to the phase diagrams shown in Fig. 6.2, the representation of Fig. 6.3 could be useful in cases where no ion reservoir is present, while the effective screening length is known. Interestingly, the CSP and AD model are much closer together in Fig. 6.3 compared to Fig. 6.2, and the re-entrant fluid phase appears even more pronounced in this representation.

In order to quantify in which finite salt-concentration regime bcc and fcc crystals are expected in a colloidal concentration series $0 < \eta < 0.3$, we analyse the maximum and

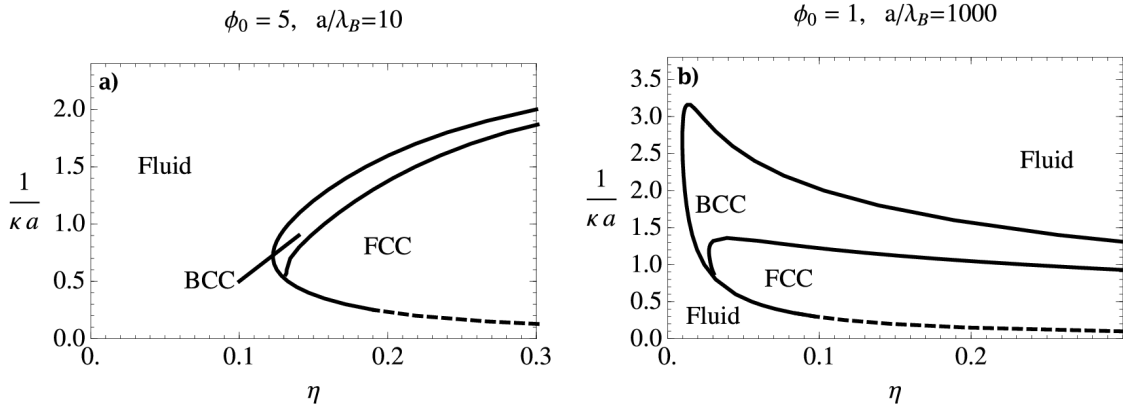


Figure 6.5: Phase diagrams in the packing fraction-screening length representation ($\eta, (\kappa a)^{-1}$), for constant-potential colloids with (a) $\phi_0 = 5$ for $a/\lambda_B = 10$ and (b) $\phi_0 = 1$ and for $a/\lambda_B = 1000$. Lines and symbols as in Fig.6.2.

minimum values of $\bar{\kappa}a$ at which these two crystal phases can exist, as a function of the zeta-potential ϕ_0 , for $a/\lambda_B = 100$. Fig. 6.4 shows the resulting screening-length regimes, both for bcc (black curves) and fcc (blue curve), where the lowest screening length for fcc crystals is set to zero because of the hard-sphere freezing into fcc at $\eta = 0.5$ even for $1/\kappa a \rightarrow 0$ —of course we only restricted attention to $\eta < 0.3$ until now so strictly speaking also the fcc phase should have had a nonvanishing lower bound. Nevertheless, despite this small inconsistency, Fig.6.4 clearly shows not only that a larger zeta-potential gives rise to a larger crystal regime, but also that for all ϕ_0 there is a limiting screening length beyond which neither fcc nor bcc crystals can exist, both for the CSP and the AD model.

So far we focussed on $a/\lambda_B = 100$, which in aqueous suspensions corresponds to a colloidal radius of about 70nm. However the colloidal size regime can easily be a factor 10 larger or smaller, and for that reason we also consider the CSP model for $a/\lambda_B = 10$ and 1000. In Fig.6.5 we show the phase diagrams for the smaller colloids with $\phi_0 = 5$ in (a), and for larger colloids with $\phi_0 = 1$ in (b). When compared to the larger colloids ($a/\lambda_B = 100$), the phase diagram for the smaller colloids comes closest to the one shown in Fig.6.2(b) for $\phi_0 = 2$, but the reentrant fluid has disappeared completely. Additionally, the smaller particles need a much higher potential to crystallize – the phase diagram for $a/\lambda_B = 10$ at $\phi_0 = 1$ does not show a crystal phase at all for $\eta < 0.3$. Similarly, the larger colloids require a much lower surface potential to resemble the phase diagram shown in Fig. 6.2(c). Additionally, the range of screening lengths where a reentrant fluid exists is much larger than for $a/\lambda_B = 100$. Given that $\phi_0 = 5$ is a rather high potential that may be difficult to achieve in reality while $\phi_0 = 1$ is frequently occurring, one concludes that re-entrant melting occurs in the largest salt-concentration regime and is hence easiest observable by tuning the salt, for larger colloids.

6.5 Summary and conclusions

Within a spherical cell model we have calculated the bare charge Z , the renormalized charge Z^* , and the effective screening length $\bar{\kappa}^{-1}$ of colloidal spheres at a constant zeta-potential ϕ_0 . We find from numerical solutions of the nonlinear Poisson-Boltzmann equation that these constant-potential colloids discharge with increasing packing fraction and ionic screening length, in fair agreement with analytical estimates for the dilute-limit charge Z_0 in Eq.(6.6) and the typical crossover packing fraction η^* given in Eq.(6.7). We also show that the constant-potential assumption is a reasonably accurate description of charge regulation by an ionic association-dissociation equilibrium on the colloidal surface. We use our nonlinear calculations of Z^* and $\bar{\kappa}$ to determine the effective screened-Coulomb interactions between the colloids at a given state point, and we calculate the phase diagram for various zeta-potentials by a mapping onto empirical fits of simulated phase diagrams of point-Yukawa fluids. This reveals a very limited regime of bcc and fcc crystals: in order to form crystals, the charge is only high enough and the repulsions only long-ranged enough in a finite intermediate regime of packing fraction and salt concentrations; at high η or low salt the spheres discharge too much, and at high salt the repulsions are too short-ranged to stabilise crystals. In the salt-regime where crystals can exist, the discharging mechanism gives rise to re-entrant phase behaviour, with phase sequences fluid-bcc-fluid and even fluid-bcc-fcc-bcc (although in an extremely small regime) upon increasing the colloid concentration from extremely dilute to $\eta = 0.3$.

The phase behaviour of constant-potential or charge-regulated colloids as reported here is quite different from that of constant-charge colloids, for which the pairwise repulsions do not weaken with increasing volume fraction or decreasing salt concentration. As a consequence constant-charge colloids have a much larger parameter-regime where crystals exist, and do not show the re-entrant behaviour. [101–104] The most direct comparison is to be made with the constant-charge phase diagrams of Fig.2 and Fig.4 of Ref.[104], where the charge is fixed such that the surface potential at infinite dilution corresponds to $\phi_0 \simeq 1$ and 2, respectively. Our theoretical findings can thus be used to gain insight into the colloidal charging mechanism by studying colloidal crystallisation regimes as a function of packing fraction and salt concentration.

6.6 Acknowledgements

I would like to thank René van Roij for his theoretical work on the cell model discussed in this chapter, and for many fruitful discussions and suggestions. I would also like to thank Niels Boon for performing the calculations on the association-dissociation model.

Appendix

Although it is numerically straightforward to solve the nonlinear PB equation (6.2) with BC's (6.3) and (6.4) in a spherical Wigner-Seitz cell of radius R , it may also be convenient to have analytic results that allow for quick estimates of the (order of) magnitude of the colloidal charge Z . A standard approach is to linearise the $\sinh \phi(r)$ term of Eq.(6.2),

e.g. with $\phi(r) - \phi(R)$ as the small expansion parameter. The resulting solution is then of the form $\phi(r) = A \exp(-\bar{\kappa}r)/r + B \exp(\bar{\kappa}r)/r + C$, with $\bar{\kappa}$ defined in Eq.(6.11), $C = \phi(R) - \tanh \phi(R)$, and with integration constants A and B fixed by the two BC's. The algebra involved is, however, not very transparent.

A considerable simplification is achieved if we consider the so-called Jellium model, in which the central colloidal sphere is no longer considered to be surrounded by only cations and anions in a finite cell, but instead by cations, anions *and* other colloids with charge Z (to be determined). [123–125] A nonlinear PB equation and BC's can then be written, for $r \geq a$,

$$\phi''(r) + \frac{2}{r}\phi'(r) = \kappa^2 \sinh \phi(r) - 4\pi\lambda_B Z n; \quad (6.17)$$

$$\phi(a) = \phi_0; \quad (6.18)$$

$$\phi'(\infty) = 0, \quad (6.19)$$

where it is assumed that the 'other' colloids are distributed homogeneously with density n . From this one derives directly that the asymptotic potential is given by

$$\sinh \phi(\infty) = \frac{4\pi\lambda_B Z n}{\kappa^2} = \frac{3\eta(Z\lambda_B/a)}{(\kappa a)^2}. \quad (6.20)$$

Now linearising $\sinh \phi(r)$ with $\phi(r) - \phi(\infty)$ as the small expansion parameter gives rise to the solution

$$\phi(r) = \phi(\infty) + (\phi_0 - \phi(\infty)) \frac{\exp(-\tilde{\kappa}(r-a))}{r/a}, \quad (6.21)$$

where the effective screening length $\tilde{\kappa}^{-1}$ is defined by

$$\tilde{\kappa} = \kappa \sqrt{\cosh \phi(\infty)}. \quad (6.22)$$

We note that the average ion concentrations in the system, within the present linearisation scheme, is given by $c_{\pm} = \rho_s \exp(\mp \phi(\infty))$, such that the corresponding screening length $\tilde{\kappa}^{-1}$ is given by $\tilde{\kappa}^2 = 4\pi\lambda_B(c_+ + c_-)$. In other words, the effective screening length $\tilde{\kappa}$ and the asymptotic potential $\phi(\infty)$ of this jellium model play exactly the same role as $\bar{\kappa}$ and $\phi(R)$ that we introduced before in the spherical cell. In particular, $\bar{\kappa}^{-1}$ and $\tilde{\kappa}^{-1}$ can be seen as the *actual* screening length in the suspension (in contrast to the screening length κ^{-1} of the ion reservoir).

From Eq.(6.21) the colloidal charge Z follows, using Eq.(6.5), as the solution of the transcendental equation

$$\frac{Z\lambda_B}{a} = (\phi_0 - \phi(\infty))(1 + \bar{\kappa}a), \quad (6.23)$$

where one should realise that both $\phi(\infty)$ and $\tilde{\kappa}$ depend on $Z\lambda_B/a$ through Eqs.(6.20) and (6.22). It is possible to solve Eq.(6.23) explicitly in the dilute limit. For $\eta = 0$ one finds $\phi(\infty) = 0$ from Eq.(6.20), and hence $Z = Z_0$ given by Eq.(6.6). For finite but low-enough η for which $\phi(\infty) \ll 1$ one can ignore $\mathcal{O}(\eta^2)$ contributions, such that $\sinh \phi(\infty) \simeq \phi(\infty)$ and $\cosh \phi(\infty) \simeq 1$, to find Eq.(6.7) from the self-consistency condition Eq.(6.23).

Crystal nucleation in binary hard-sphere mixtures: The effect of the order parameter on the cluster composition

We study crystal nucleation in a binary mixture of hard spheres and investigate the composition and size of the (non)critical clusters using Monte Carlo simulations. In order to study nucleation of a crystal phase in computer simulations, a one-dimensional order parameter is usually defined to identify the solid phase from the supersaturated fluid phase. We show that the choice of order parameter can strongly influence the composition of noncritical clusters due to the projection of the Gibbs free-energy landscape in the two-dimensional composition plane onto a one-dimensional order parameter. On the other hand, the critical cluster is independent of the choice of the order parameter, due to the geometrical properties of the saddle point in the free-energy landscape, which is invariant under coordinate transformation. We investigate the effect of the order parameter on the cluster composition for nucleation of a substitutional solid solution in a simple toy model of identical hard spheres but tagged with different colors and for nucleation of an interstitial solid solution in a binary hard-sphere mixture with a diameter ratio $q = 0.3$. In both cases, we find that the composition of noncritical clusters depends on the order parameter choice, but are well explained by the predictions from classical nucleation theory. More importantly, we find that the properties of the critical cluster do not depend on the order parameter choice.

7.1 Introduction

The process of nucleation in colloidal systems has attracted significant attention in recent years, both in experimental and simulation studies. The framework with which phenomena like these have been described traditionally is classical nucleation theory (CNT), which is based on the notion that a thermal fluctuation spontaneously generates a small droplet of the thermodynamically stable phase into the bulk of the metastable phase. In CNT as developed by Volmer [139], Becker [140], and Zeldovich [141], the free energy of formation of small nuclei of the new phase in the parent phase is described by using the “capillary approximation”, i.e., the free energy to form a cluster of the new phase relative to the homogeneous metastable phase is described by their difference in bulk free energy and a surface free-energy term that is given by that of a planar interface between the two coexisting phases at the same temperature. Thus the droplet is assumed to be separated from the metastable bulk by a sharp step-like interface in CNT. The bulk free-energy term is proportional to the volume of the droplet and represents the driving force to form the new phase, while the surface free-energy cost to create an interface is proportional to the surface area of the cluster. Hence, small droplets with a large surface-to-volume ratio have a large probability to dissolve, while droplets that exceed a critical size and cross the free-energy barrier, can grow further to form the new stable bulk phase.

CNT has successfully explained simulation results for the nucleation of spherical particles, such as the fluid-solid and gas-liquid nucleation in Lennard-Jones systems [87, 142, 143] and crystal nucleation of hard spheres [144, 145]. A modified CNT has been used to explain the nucleation of anisotropic clusters of the nematic or solid phase (also called tactoids) from a supersaturated isotropic phase of colloidal hard rods [146–148] and the nucleation of 2D assemblies of attractive rods [149, 150]. This state of affairs should be contrasted with the case of binary nucleation for which various nucleation theories have been developed that differ substantially in the way they describe the composition of the cluster [151–153]. For instance, Reiss assumed the surface tension to be independent of composition [151], while Doyle extended CNT by taking into account a surface tension that depends on the cluster composition [154]. However, more than 20 years later, it was shown by Renninger [155], Wilemski [156, 157], and Reiss [158] that Doyle’s derivation leads to thermodynamic inconsistencies. A revised thermodynamically consistent classical binary nucleation theory was developed by Wilemski in which the composition of the surface layer and the interior of the cluster could vary independently [156, 157]. However, in the case of strong surface enrichment effects, this approach can lead to unphysical negative particle numbers in the critical clusters [159, 160]. In addition, it was shown in Ref. [161] that the derivation by Wilemski starts off with the wrong equations, but the resulting equations are correct. Moreover, binary nucleation can be accompanied with huge fractionation effects, i.e., the compositions of the metastable phase and of the phase to be nucleated can differ enormously from the compositions of the two coexisting bulk phases. It is therefore unclear i) how to determine the surface free-energy term for a cluster, which is in quasi-equilibrium with a metastable parent phase with a composition that is very different from those of the two coexisting bulk phases, ii) whether the interfacial tension depends on composition, curvature, and surface enrichment effects, and finally iii) whether or not one can use the capillary approximation in the first place to describe

binary nucleation in systems where fractionation and surface activity of the species are important. To summarize, there is no straightforward generalization to multicomponent systems of classical nucleation theory that is thermodynamically consistent, does not lead to unphysical effects, and can be applied to small nuclei [153, 162].

Numerical studies may shed light on this issue, as the nucleation barrier can be determined directly in computer simulations using the umbrella sampling technique [163, 164]. In this method, an order parameter is chosen and configuration averages for sequential values of the order parameter are taken. While this makes it possible to measure properties of clusters with specific values for the order parameter, it should be noted that the results can depend on the choice of order parameter. In this chapter, we investigate whether the size and composition of (non)critical clusters can be affected by the order parameter choice employed in simulation studies of multicomponent nucleation. For simplicity, we focus here on crystal nucleation in binary hard-sphere mixtures, where surface activity of the species can be neglected, and we assume the surface tension to be composition independent. The chapter is organized as follows. In Sec. 7.2, we describe the general nucleation theorem as derived by Oxtoby and Kashchiev [153], which does not rely on the capillary approximation and can even be employed to describe small clusters. Starting from the multicomponent nucleation theorem, it is straightforward to reproduce the usual CNT for binary nucleation, which is the focus in the remainder of the chapter. In Sec. 7.3 and 7.4, we define the (Landau) free energy as a function of an order parameter, and we describe the order parameter that is employed to study crystal nucleation. Additionally, we discuss the effect of order parameter choice on the nucleation barrier in more detail. We present results for binary nucleation for a simple toy model of hard spheres in Sec. 7.5, and subsequently, we study the nucleation of an interstitial solid solution in an asymmetric binary hard-sphere mixture in Sec. 7.6.

7.2 Classical nucleation theory for multi-component systems

We study the formation of a multicomponent spherical cluster of the new phase in a supersaturated homogeneous bulk phase α consisting of species $i = 1, 2, \dots$. We note that the thermodynamic variables corresponding to the metastable phase α are denoted by the subscript α , whereas those corresponding to the new phase do not carry an extra subscript to lighten the notation. We first consider a homogeneous bulk phase α characterized by an entropy S_α^o , volume V_α^o , and particle numbers $N_{i,\alpha}^o$. Note that the superscripts denote the original bulk phase. The internal energy U_α^o of the original bulk phase reads

$$U_\alpha^o = T^o S_\alpha^o - P_\alpha^o V_\alpha^o + \sum \mu_{i,\alpha}^o N_{i,\alpha}^o \quad (7.1)$$

with T^o the temperature, P_α^o the bulk pressure, $\mu_{i,\alpha}^o$ the bulk chemical potential of species i , and the summation runs over all species.

Following the derivation in Refs. [153, 162], we now consider a spherical cluster of the new phase with a volume V separated from the original phase by an arbitrarily chosen Gibbs dividing surface. The volume of the interface is set to zero, and the particle number of species i in the cluster is given by $N_i + N_{i,s}$, where N_i is the number of particles of

species i in a volume V which is homogeneous in the new bulk phase, and $N_{i,s}$ is the surface excess number of particles of species i that corrects for the difference between a step-like interfacial density profile and the actual one. The surface excess number $N_{i,s}$ depends on the choice of dividing surface. The internal energy U of the resulting system is then given by

$$U = TS_\alpha + TS - P_\alpha V_\alpha - PV + \Psi + \sum \mu_{i,\alpha} N_{i,\alpha} + \sum \mu_i N_i + \sum \mu_{i,s} N_{i,s}, \quad (7.2)$$

where P and S denote the bulk pressure and entropy of the nucleated phase, and μ_i and $\mu_{i,s}$ are the chemical potentials of species i in the new phase and the surface phase, T is the temperature of the system with the cluster, and $\Psi = \Psi(\{N_i\}, \{N_{i,s}\}, V)$ is the total surface energy of the spherical cluster. As the volume of the surface layer is zero, the corresponding pressure is not defined. Note that we did not include the entropy associated with choosing the location of the cluster in the system. In other words, the cluster is placed at a specific location.

The difference in the appropriate thermodynamic potential as a function of cluster size depends on the quantities that are kept fixed during the nucleation process. If the nucleus is formed at constant temperature and constant total number of particles of each species i , and if we keep the pressure of the original phase fixed, then $T = T^\circ$, $N_{i,\alpha} + N_i + N_{i,s} = N_{i,\alpha}^\circ$, and $P_\alpha^\circ = P_\alpha$. The corresponding Gibbs free energy of the initial system G_α° and that of the final system G are then given by the Legendre transformation

$$\begin{aligned} G_\alpha^\circ &= U_\alpha^\circ - T^\circ S_\alpha^\circ + P_\alpha^\circ V_\alpha^\circ = \sum \mu_{i,\alpha}^\circ N_{i,\alpha}^\circ \\ G &= U - TS + P_\alpha^\circ (V_\alpha + V) \\ &= (P_\alpha^\circ - P)V + \Psi + \sum \mu_{i,\alpha} N_{i,\alpha} + \sum \mu_i N_i \\ &\quad + \sum \mu_{i,s} N_{i,s}. \end{aligned} \quad (7.3)$$

If we now assume that the composition of the metastable phase α remains unchanged and we consider the Maxwell relation

$$\left(\frac{\partial V_\alpha}{\partial N_{i,\alpha}} \right)_{T, P_\alpha, \{N_{j \neq i, \alpha}\}} = v_{i,\alpha} = \left(\frac{\partial \mu_{i,\alpha}}{\partial P_\alpha} \right)_{T, \{N_{i,\alpha}\}} \quad (7.4)$$

with $v_{i,\alpha}$ the partial particle volumes of species i in phase α , we find that at constant pressure, the chemical potential for each species i remains constant $\mu_{i,\alpha}^\circ = \mu_{i,\alpha}$. Subsequently, we obtain for the change in Gibbs free energy $\Delta G = G - G_\alpha^\circ$ when a nucleus is formed in the bulk of the original phase:

$$\begin{aligned} \Delta G &= (P_\alpha^\circ - P)V + \Psi + \sum (\mu_i(P) - \mu_{i,\alpha}^\circ(P_\alpha^\circ)) N_i + \\ &\quad \sum (\mu_{i,s} - \mu_{i,\alpha}^\circ(P_\alpha^\circ)) N_{i,s}. \end{aligned} \quad (7.5)$$

Consequently, the Gibbs free energy ΔG of a growing cluster depends on the number of particles N_i and $N_{i,s}$ in the cluster and the surface energy of the cluster. Hence, one can define a free-energy surface in the multi-dimensional composition plane with a saddle

point that corresponds to the critical nucleus [151]. The conditions for the critical cluster read

$$\begin{aligned} \left(\frac{\partial \Delta G}{\partial N_i} \right)_{V, \{N_{j \neq i}\}, \{N_{i,s}\}} &= 0, \\ \left(\frac{\partial \Delta G}{\partial N_{i,s}} \right)_{V, \{N_i\}, \{N_{j \neq i,s}\}} &= 0, \\ \left(\frac{\partial \Delta G}{\partial V} \right)_{\{N_i\}, \{N_{i,s}\}} &= 0. \end{aligned} \quad (7.6)$$

To recover the chemical and mechanical equilibrium conditions, we use the above conditions as well as the Gibbs-Duhem equation and the Gibbs adsorption equation. The Gibbs-Duhem equation at constant temperature for the nucleated bulk phase is

$$-VdP + \sum N_i d\mu_i = 0, \quad (7.7)$$

and the Gibbs adsorption equation for the surface at constant temperature is

$$Ad\gamma + \sum N_{i,s} d\mu_{i,s} = 0, \quad (7.8)$$

where we have employed $\Psi = \gamma A$. Note that γ denotes the surface free energy per unit area and A is the surface area of the cluster. The resulting equilibrium conditions for all particle species i in the critical cluster, the surface, and the metastable parent phase are then given by

$$\mu_i^*(P^*) = \mu_{i,s}^* = \mu_{i,\alpha}^o(P_\alpha^o), \quad (7.9)$$

and for the pressure difference inside and outside the droplet we find

$$P^* - P_\alpha^o = \frac{\partial \gamma^* A^*}{\partial V^*}, \quad (7.10)$$

where $*$ denotes quantities associated with a system where a critical cluster is present. Hence, the composition of the critical cluster can be determined from these saddle point conditions.

In order to obtain the usual classical nucleation theory for multicomponent systems, we assume a spherical droplet with radius R . Note that the surface area is then $A = 4\pi R^2$. In addition, we use the fact that the volume of a spherical droplet can be expressed in terms of the partial particle volumes v_i of species i :

$$V = \frac{4}{3}\pi R^3 = \sum N_i v_i. \quad (7.11)$$

Combining this with Eq. (7.10), we arrive at the generalised Laplace equation:

$$P^* - P_\alpha^o = \frac{2\gamma^*}{R^*} + \left[\frac{\partial \gamma^*}{\partial R^*} \right], \quad (7.12)$$

where the square brackets denote a derivative associated with the displacement of the dividing surface. One can now choose the dividing surface so that

$$\left[\frac{\partial \gamma^*}{\partial R^*} \right] = 0, \quad (7.13)$$

and hence one recovers the usual Laplace equation. This choice for the dividing surface, corresponding to a specific value for R^* and γ^* , is called the surface of tension. In addition, if we use the Gibbs adsorption isotherm (7.8) and the Maxwell relation (7.4) for the bulk phase of the nucleated cluster, we find for the critical cluster

$$d\mu_{i,s}^* = d\mu_i^* = v_i dP \quad (7.14)$$

and

$$\left[A \frac{\partial \gamma^*}{\partial R^*} \right] = - \sum N_{i,s} v_i \left[\frac{\partial P^*}{\partial R^*} \right] = 0, \quad (7.15)$$

which is the condition for a curvature independent surface tension. Since $\partial P^*/\partial R^* \neq 0$, Eq. (7.15) implies that the dividing surface has to be chosen such that

$$\sum N_{i,s} v_i = 0, \quad (7.16)$$

which is called the equimolar surface, as for one-component systems $N_{i,s} = 0$, i.e. the number of particles in the cluster equals the number of particles in a uniform bulk phase with the same volume. It is generally not possible in a multicomponent system to choose the dividing surface such that $N_{i,s} = 0$ for all species. Thus, as v_i is usually positive, $N_{i,s} < 0$ for at least one of the species. This may lead to (unphysical) negative particle numbers when $N_i + N_{i,s} < 0$ as noted in Refs. [159, 160]. However, as will be discussed in sections 7.5 and 7.6, there are cases in which the assumption $N_{i,s} = 0$ for all i is valid.

If the nucleated phase is assumed to be incompressible, one can integrate the Gibbs-Duhem equation (7.7) at constant temperature to arrive at

$$V(P_\alpha^o - P) = \sum (\mu_i(P_\alpha^o) - \mu_i(P)) N_i, \quad (7.17)$$

and using Eq. (7.5), we find

$$\begin{aligned} \Delta G &= \gamma A + \sum (\mu_i(P_\alpha^o) - \mu_{i,\alpha}^o(P_\alpha^o)) N_i + \\ &\quad \sum (\mu_{i,s} - \mu_{i,\alpha}^o(P_\alpha^o)) N_{i,s}. \end{aligned} \quad (7.18)$$

Again using the Gibbs-Duhem equation at constant temperature and pressure and the Gibbs adsorption isotherm, and minimizing the free energy with respect to N_i at fixed $\{N_{i,s}\}$, we recover the Gibbs-Thomson (also called Kelvin) equations for multi-component spherical critical clusters

$$\Delta \mu_i^* = - \frac{2\gamma^* v_i}{R^*}, \quad (7.19)$$

where $\Delta\mu_i^* = \mu_i^*(P_\alpha^o) - \mu_{i,\alpha}^o(P_\alpha^o)$. The radius of the critical cluster R^* and the barrier height ΔG^* read

$$R^* = \frac{2\gamma^*v_i}{|\Delta\mu_i^*|} \quad (7.20)$$

$$\Delta G^* = \frac{4\pi R^{*2}\gamma^*}{3} = \frac{16\pi\gamma^{*3}}{3(\Delta\mu_i^*/v_i)^2}. \quad (7.21)$$

Using Eq. (7.20) or the Maxwell relation (7.4), one can show:

$$v_i\Delta\mu_i = v_j\Delta\mu_j, \quad (7.22)$$

and the radius of the critical cluster R^* can be expressed in terms of the bulk composition $x_i = N_i/\sum N_i$ of the critical cluster and $v = V/\sum N_i$:

$$R^* = \frac{2\gamma^*v}{\sum x_i|\Delta\mu_i^*|}. \quad (7.23)$$

In order to study multi-component nucleation, MC simulations are often performed in the isobaric-isothermal ensemble, in which the number of particles $N_{1,\alpha}^o$ and $N_{2,\alpha}^o$, the pressure of the original bulk phase P_α^o , and the temperature T are kept fixed. One of the assumptions of classical nucleation theory is that the composition of the metastable bulk phase remains constant, while nucleating the new phase, see Eq. (7.4). In simulations this can only be achieved if the system is sufficiently large, i.e., the volume of the metastable bulk phase is much larger than that of the nucleating cluster. Especially, for binary (multicomponent) nucleation, where the composition of the stable phase is very different from that of the metastable phase, this can lead to a huge depletion of one of the components in the metastable fluid phase, and therefore a change in composition. In order to circumvent this problem, simulation studies on binary nucleation are often carried out in the semi-grand canonical ensemble [165, 166], i.e. the total number of particles $N_\alpha^o = \sum N_{i,\alpha}^o$, the chemical potential difference $\Delta\mu_{12,\alpha}^o = \mu_{2,\alpha}^o - \mu_{1,\alpha}^o$ between the two species, the pressure P_α^o , and the temperature T are kept fixed of the original bulk phase. The corresponding thermodynamic potential is obtained by a Legendre transformation

$$Y(N, \Delta\mu_{12}, P, T) = G(N, N_2, P, T) - N_2\Delta\mu_{12} \quad (7.24)$$

Combining Eq. (7.3) with the conditions that the total number of particles are fixed $N_{1,\alpha}^o + N_{2,\alpha}^o = N_1 + N_2 + N_{1,\alpha} + N_{2,\alpha}$, the chemical potential difference in the metastable phase is kept fixed $\Delta\mu_{12,\alpha}^o = \Delta\mu_{12,\alpha}$, constant pressure of the metastable phase $P_\alpha^o = P_\alpha$ and constant temperature $T = T^o$, we find for the corresponding thermodynamic potentials

$$\begin{aligned} Y_\alpha^o &= G_\alpha^o - N_{2,\alpha}^o\Delta\mu_{12,\alpha}^o = \mu_{1,\alpha}^o(N_{1,\alpha}^o + N_{2,\alpha}^o) \\ Y &= G - (N_{2,\alpha} + N_2)\Delta\mu_{12,\alpha} \\ &= (P_\alpha^o - P)V + \Phi + \mu_{1,\alpha}(N_{1,\alpha} + N_{2,\alpha}) + \\ &\quad \mu_1(N_1 + N_2) - \Delta\mu_{12}N_2 - \Delta\mu_{12,\alpha}N_{2,\alpha}, \end{aligned} \quad (7.25)$$

where we have set the surface excess numbers $N_{i,s}$ to zero. Using the Maxwell equation

$$\left(\frac{\partial\mu_1}{\partial P}\right)_{N,\Delta\mu_{12},T} = \left(\frac{\partial V}{\partial N}\right)_{\Delta\mu_{12},P,T} = v, \quad (7.26)$$

we find that due to constant pressure, the chemical potential of species 1 remains unchanged $\mu_{1,\alpha}^o = \mu_{1,\alpha}$. Hence, we find that the change in free energy due to the formation of a nucleus $\Delta Y = Y - Y_\alpha^o$ equals ΔG as given in Eq. (7.5) and the nucleation barrier can be calculated in the semi-grand canonical ensemble. Similarly, one can show that in any statistical ensemble (grand canonical, canonical, etc.), the change in the corresponding thermodynamic potential as a function of cluster size is always the same, provided that the metastable parent phase is sufficiently large. A similar result was also obtained by Oxtoby *et al.*, who showed that the nucleation free-energy barriers in the isobaric-isothermal and grand canonical ensemble are identical, i.e., $\Delta G = \Delta\Omega$ for a one-component system [167].

7.3 Free-energy barrier

While nucleation is an inherently non-equilibrium process, the assumption of local equilibrium is often made to describe the behavior of the system during the nucleation process. In essence, this assumption states that the nucleus is in quasi-equilibrium with the parent phase for every cluster size. This is approximately true if the time required to reach an equilibrium distribution of clusters is short compared to the time needed to nucleate. After the system crosses the free-energy barrier, the cluster of the new phase grows too rapidly for this assumption to be accurate, but during the nucleation process itself, local equilibrium has proven to be a useful assumption.

In order to compute the free-energy barrier that separates the metastable phase from the stable phase, an order parameter Φ (or reaction coordinate) should be defined that quantifies how much the system has transformed to the new phase. A common order parameter that is employed in nucleation studies is the size of the largest cluster in the system as defined by a certain cluster criterion. In this chapter, we restrict ourselves to binary nucleation. From Eq. (7.18), we find that the Gibbs free energy ΔG of a growing binary cluster depends on the number of particles of species 1 and 2 in the cluster, and hence, one can define a free-energy surface in the (N_1, N_2) -plane with a saddle point that corresponds to the critical nucleus [151]. By projecting the phase space of the system onto the (usually) one-dimensional order parameter, one can define the (Landau) Gibbs free energy $\Delta G(\Phi)$ as a function of this order parameter Φ

$$\beta\Delta G(\Phi) = G_c - \ln P(\Phi), \quad (7.27)$$

where $\beta = 1/k_B T$, k_B Boltzmann's constant, T the temperature, G_c is a normalization constant generally taken to correspond to the free energy of the homogeneous metastable phase, and $P(\Phi)$ is the probability of observing an order parameter of value Φ . In a system of N particles, at fixed pressure P , and constant temperature T , the probability

$P(\Phi)$ is given by:

$$P(\Phi) = \frac{\int dV \int d\mathbf{r}^N \exp[-\beta(U(\mathbf{r}^N) + PV)] \delta(\Phi - \Phi(\mathbf{r}^N))}{\int dV \int d\mathbf{r}^N \exp[-\beta(U(\mathbf{r}^N) + PV)]} \quad (7.28)$$

with V the volume of the system, U the potential energy, and δ the Kronecker delta function. The order parameter function $\Phi(\mathbf{r}^N)$ is a function that assigns to each configuration \mathbf{r}^N of the system a value for the order parameter. The probability distribution $P(\Phi)$ can be obtained from Monte Carlo (MC) simulations via the umbrella sampling technique [163, 164]. In this method, an additional external potential U_{bias} is added to the system to bias the sampling towards configurations corresponding to a certain window of order parameter values centered around Φ_o . By increasing Φ_o sequentially, the entire free-energy barrier as a function of Φ can be sampled. The typical biasing potential used in umbrella sampling simulations is given by:

$$\beta U_{bias}(\mathbf{r}^N) = k(\Phi(\mathbf{r}^N) - \Phi_o)^2, \quad (7.29)$$

where the constants k and Φ_o determine the width and location of the window, and \mathbf{r}^N are the positions of all N particles in the simulation.

7.4 Order parameter

In order to follow a phase transformation, a cluster criterion is required that is able to identify the new phase from the supersaturated phase. In this chapter, we focus on the formation of a solid cluster in a supersaturated fluid phase. In order to study crystal nucleation, the local bond-order parameter is used to differentiate between liquid-like and solid-like particles and a cluster algorithm is employed to identify the solid clusters [87]. In the calculation of the local bond order parameter a list of ‘‘neighbours’’ is determined for each particle. The neighbours of particle i include all particles within a radial distance r_c of particle i , and the total number of neighbours is denoted $N_b(i)$. A bond orientational order parameter $q_{l,m}(i)$ for each particle is then defined as

$$q_{l,m}(i) = \frac{1}{N_b(i)} \sum_{j=1}^{N_b(i)} Y_{l,m}(\theta_{i,j}, \phi_{i,j}), \quad (7.30)$$

where $Y_{l,m}(\theta, \phi)$ are the spherical harmonics, $m \in [-l, l]$ and $\theta_{i,j}$ and $\phi_{i,j}$ are the polar and azimuthal angles of the center-of-mass distance vector $\mathbf{r}_{ij} = \mathbf{r}_j - \mathbf{r}_i$ with \mathbf{r}_i the position vector of particle i . Solid-like particles are identified as particles for which the number of connections per particle $\xi(i)$ is at least ξ_c and where

$$\xi(i) = \sum_{j=1}^{N_b(i)} H(d_l(i,j) - d_c), \quad (7.31)$$

H is the Heaviside step function, d_c is the dot-product cutoff, and

$$d_i(i, j) = \frac{\sum_{m=-l}^l q_{l,m}(i)q_{l,m}^*(j)}{\left(\sum_{m=-l}^l |q_{l,m}(i)|^2\right)^{1/2} \left(\sum_{m=-l}^l |q_{l,m}(j)|^2\right)^{1/2}}. \quad (7.32)$$

A cluster contains all solid-like particles which have a solid-like neighbour in the same cluster. Thus each particle can be a member of only one cluster.

The parameters contained in this algorithm include the neighbour cutoff r_c , the dot-product cutoff d_c , the critical value for the number of solid-like neighbours ξ_c , and the symmetry index for the bond orientational order parameter l . The hard-sphere crystals considered here are expected to have random hexagonal order, thus the symmetry index is chosen to be 6 in the present study.

This choice of order parameter Φ , defined as the number of solid-like particles in the largest crystalline cluster, has been used to study crystal nucleation in various one-component systems, e.g., Lennard-Jones systems [87], hard-sphere systems [144], and Yukawa systems [168].

On the other hand, for binary systems, a variety of crystal structures can appear in the bulk phase diagram, e.g., substitutionally ordered (superlattice) crystal structures with varying stoichiometries, substitutionally disordered solid solutions, interstitial solid solutions, crystalline phases of species 1 with a dispersed fluid of species 2, etc. Nucleation of a substitutionally disordered solid solution and a crystal with the CsCl structure has been studied in a binary mixture of hard spheres using the total number of particles in the largest crystalline cluster as an order parameter, i.e. $\Phi = N_1 + N_2$ [165]. This order parameter has also been employed in a crystal nucleation study of a substitutionally disordered face-centered cubic crystal and a crystal with the CsCl structure of oppositely charged colloids [169], and nucleation of the NaCl salt crystal from its melt using the symmetry index $l = 4$ instead of $l = 6$ for the bond orientational order parameter [170]. However, one can also define other linear combinations of N_1 and N_2 as an order parameter. When the partial particle volumes of the two species are very different, one can employ the volume of the largest crystalline cluster $\Phi = V = N_1v_1 + N_2v_2$ as an order parameter. While, if the crystal structure consists of only one species, say species 1, with the other species randomly dispersed, the number of particles of species 1 in the largest crystalline cluster would be more appropriate to use as an order parameter $\Phi = N_1$. On the other hand, one can also use the stoichiometry n of the AB_n superlattice structure to define the order parameter $\Phi = N_1 + N_2/n$ in order to prevent a strong bias towards one of the species. More generally, if the cluster size is measured by the order parameter $\Phi = N_1 + \lambda N_2$, the sensitivity of the order parameter to particles of species 2 can be tuned via the parameter λ . For $\lambda = 1$, this corresponds to the total number of particles in the cluster, while for $\lambda = 0$, this corresponds to the number of particles of type 1.

As already mentioned above, the umbrella sampling technique is often employed to determine the probability distribution $P(\Phi)$ and the Gibbs free energy $\Delta G(\Phi)$. To this end, a biasing potential is introduced to sample configurations with certain values for this order parameter Φ . In this chapter, we investigate the effect of the choice of order

parameter on the properties of the clusters during nucleation in a binary mixture of hard spheres, where we assume that the surface excess numbers of species i are negligible. Using Eq. (7.18), we now write down explicitly the change in Gibbs free energy for binary nucleation

$$\Delta G = \gamma A + \Delta\mu_1 N_1 + \Delta\mu_2 N_2, \quad (7.33)$$

where $\Delta\mu_i = \mu_i(P_\alpha^o) - \mu_{i,\alpha}^o(P_\alpha^o)$. The Gibbs free energy ΔG depends on the particle numbers N_1 and N_2 and the composition of the critical cluster can be determined from the saddle point conditions for ΔG . The free-energy surface in the two-dimensional composition plane (N_1, N_2) is projected in umbrella sampling MC simulations onto a one-dimensional order parameter, e.g. $\Phi = N_1 + \lambda N_2$. Hence, the projected $\Delta G(\Phi)$ and the averaged (or projected) cluster composition of noncritical clusters both depend on the order parameter. We note that this is not an artifact of the umbrella sampling MC simulations, but merely the projection of a correctly measured equilibrium distribution. To determine the averaged composition of noncritical spherical clusters with radius R as a function of Φ , we can minimize ΔG with respect to N_2 while keeping the order parameter Φ fixed:

$$\left(\frac{\partial\Delta G}{\partial N_2}\right)_\Phi = \Delta\mu_2 - \lambda\Delta\mu_1 + \frac{2\gamma v_1}{R}(\omega - \lambda) = 0, \quad (7.34)$$

where $\omega = v_2/v_1$. If we use the umbrella sampling technique in MC simulations to determine the Gibbs free energy $\Delta G(\Phi)$ as a function of Φ , one can easily determine the slope of the barrier from the simulations, which is equal to

$$\begin{aligned} \frac{d\Delta G}{d\Phi} &= \left(\Delta\mu_2 + \frac{2\gamma v_1}{R}\omega\right) \left(\frac{\partial N_2}{\partial\Phi}\right) + \\ &\quad \left(\Delta\mu_1 + \frac{2\gamma v_1}{R}\right) \left(\frac{\partial N_1}{\partial\Phi}\right) \end{aligned} \quad (7.35)$$

with

$$\frac{\partial N_1}{\partial\Phi} = \frac{1 - x - \lambda N \frac{\partial x}{\partial\Phi}}{1 - x + \lambda x} \quad (7.36)$$

$$\frac{\partial N_2}{\partial\Phi} = \frac{x + N \frac{\partial x}{\partial\Phi}}{1 - x + \lambda x}, \quad (7.37)$$

where we define the composition $x = N_2/N$ and $N = N_1 + N_2$. Combining Eqs. (7.34) and (7.35) yields

$$\omega\Delta\mu_1 - \Delta\mu_2 = (\omega - \lambda) \frac{d\Delta G}{d\Phi}. \quad (7.38)$$

We wish to make a few remarks here. First, we recover the Gibbs-Thomson equations for the critical cluster (7.19) when we set $d\Delta G/d\Phi$ in Eq. (7.35) to zero, and we recover Eq. (7.22) from Eq. (7.38) for critical clusters. Consequently, the size and composition of the critical cluster are independent of the choice of λ . This can also be understood from the fact that the saddlepoint in the free-energy landscape is invariant under coordinate

transformations. As long as the top of the nucleation barrier corresponds to this saddle point, the average properties of the cluster will be dominated by the configurations around this saddlepoint, regardless of the chosen order parameter. While most reasonable choices of order parameter fulfill this requirement, it is possible to design order parameters that shift the top of the barrier away from the saddle point. In this case, the clusters at the top of the barrier are non-critical clusters, and rates calculated from the resulting free energy barrier are unreliable. It is important to note that a different choice of order parameter can change the height of the nucleation barrier, since the barrier height is determined by the fraction of phase space mapped to the same order parameter value at the top of the barrier. However, this effect should be small, as the probability of finding a cluster at the top of the nucleation barrier is dominated by the probability of being in the saddle point of the free-energy landscape. For noncritical clusters, we clearly find that the slope of the barrier, and hence the composition of the cluster, depends on the choice of order parameter via λ . Below, we study the effect of the choice of order parameter for a simple toy model of hard spheres and for the nucleation of an interstitial solid solution in an asymmetric binary hard-sphere mixture. It is interesting to compare this to past studies investigating one-component systems with higher-dimensional order parameters [171, 172]. For the Lennard-Jones system, Moroni *et al.*, have shown that the number of particles in the cluster alone is insufficient to provide a good prediction for the probability a cluster will grow out to a large crystal [171]. Using a two-dimensional order parameter, they observed a strong correlation between the crystallinity and the size of clusters with a 50% probability of growing out. Specifically, clusters with a large amount of face-centered-cubic (fcc) ordering require much smaller sizes to grow out than those with more body-centered-cubic (bcc) ordering. They found that this correlation was not visible in the two-dimensional free-energy landscape, and argued that the shape and structure of a nucleus could determine whether it will grow out. However, we note that the two-dimensional order parameter is still a projection from a higher-dimensional phase space. Thus, the properties of non-critical clusters likely depend on the choice of this order parameter as well.

7.5 A substitutional solid solution

In order to obtain more insight in the effect of order parameter choice on the cluster composition of noncritical clusters, we first investigate binary crystal nucleation in a toy model of hard spheres. Here, we consider a system consisting of two species of hard spheres with identical sizes, but tagged with different colors, say species 1 is red and species 2 is blue. Obviously, the stable solid phase to be nucleated is a substitutional disordered face-centered-cubic (fcc) crystal phase with the red and blue particles randomly distributed on an fcc lattice. Refs. [144, 145] showed that the nucleation barriers for pure hard spheres are well-described by the predictions from classical nucleation theory, where because of the condition of the equimolar surface, the surface excess number $N_s = 0$. It is therefore safe to neglect the surface excess numbers for the present model as well. In addition, it is clear that the partial particle volumes v_i and volume per particle v are identical, and $\omega = v_2/v_1 = 1$. Using the Gibbs-Thomson equations for a binary critical cluster (7.19),

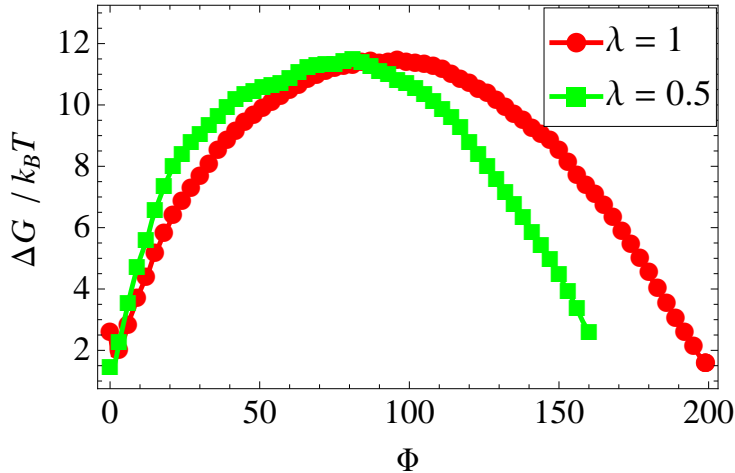


Figure 7.1: Gibbs free energy $\Delta G(\Phi)/k_B T$ as a function of order parameter $\Phi = N_1 + \lambda N_2$ for a binary mixture of red (species 1) and blue (species 2) hard spheres with equal diameter σ as obtained from umbrella sampling MC simulations at a reduced pressure of $P^* = P_\alpha^o \sigma^3 / k_B T = 17$ with $\lambda = 1$ and $\lambda = 0.5$.

we find that the supersaturation $\Delta\mu_1^* = \Delta\mu_2^* = -2\gamma^*v/R^*$, and hence the composition of the critical cluster follows straightforwardly from the bulk chemical potentials $\mu_1^*(P_\alpha^o)$ and $\mu_2^*(P_\alpha^o)$, which depends on the bulk chemical potentials of the original bulk phase and the supersaturation.

As already mentioned above, the composition of noncritical clusters depends on the choice of order parameter, i.e., the projection of the two-dimensional composition plane onto a one-dimensional order parameter Φ . Using Eq. (7.38), we find that for $\lambda = 1$, the composition of noncritical cluster is determined by the supersaturation $\Delta\mu_1 = \Delta\mu_2$ and the bulk chemical potentials of the original bulk phase. For $\lambda = 0$, we only measure the number of particles of one color, say red, in the cluster. However, a thermodynamic average of all clusters with N_1 red particles also includes all post-critical clusters with many blue particles, and as a result, the order parameter fails to work for $\lambda = 0$. For non-zero values of λ , the ensemble of clusters of each size is well-defined, and we can perform umbrella sampling MC simulations to measure the average cluster composition.

In order to keep the composition of the metastable fluid fixed, we perform Monte Carlo simulations on a binary mixture with $N = 1000$ hard spheres in the semi-grand canonical ensemble. Both species of hard spheres are identical in size with diameter σ , and are either tagged red (species 1) or blue (species 2). The simulations were carried out in a cubic box with periodic boundary conditions and the Metropolis sampling consists of particle displacements and volume changes, and attempts to switch the identity (color) of the particles. The acceptance rule for the identity swap moves is determined by the chemical potential difference $\Delta\mu_{12,\alpha}^o$ [165, 166]. We use the umbrella sampling technique to determine the nucleation barrier $\Delta Y = \Delta G$ as a function of an order parameter $\Phi = N_1 + \lambda N_2$, where $N_1(N_2)$ denotes the number of red (blue) solid-like particles in the largest crystalline cluster in the system as determined by the local bond-order parameter and cluster criterion described in Sec. 7.4 with cutoff radius $r_c = 1.3\sigma$, dot-product

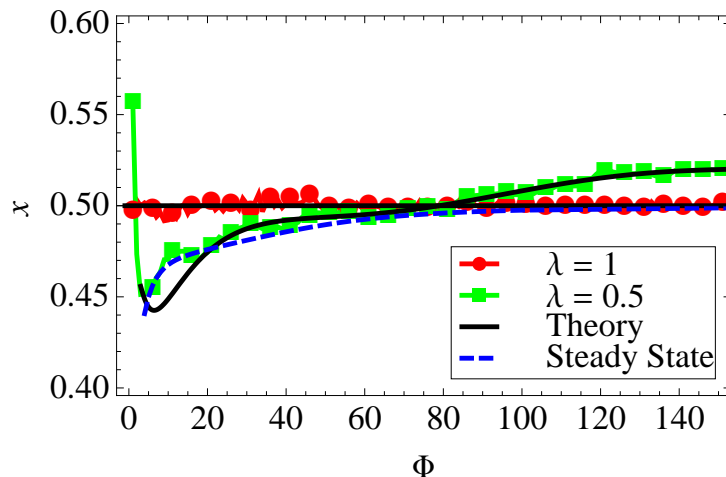


Figure 7.2: Composition $x = N_2/N$ of the largest crystalline cluster as a function of order parameter $\Phi = N_1 + \lambda N_2$ for a binary mixture of red (species 1) and blue (species 2) hard spheres with equal diameter σ as obtained from umbrella sampling simulations at pressure $P^* = P_\alpha^o \sigma^3 / k_B T = 17$ with $\lambda = 1$ (red circles) and $\lambda = 0.5$ (green squares). For comparison, we plot the theoretical prediction (7.38) using the measured nucleation barrier of Fig. 7.1 (black solid line) and the composition determined from a steady-state cluster size distribution for $\lambda = 0.5$ (blue dashed line). The critical cluster size is $\Phi \simeq 79$ and 96 for $\lambda = 0.5$ and 1 , respectively.

cutoff $d_c = 0.7$, and number of solid bonds $\xi_c \geq 6$. We first calculate the nucleation barrier for $\lambda = 1$, for which the order parameter Φ is simply the total number of solid-like particles in the largest cluster. We set the reduced pressure $P^* = P_\alpha^o \sigma^3 / k_B T = 17$, and $\Delta\mu_{12,\alpha}^o = 0$, which corresponds on average to an equimolar mixture of red and blue hard spheres for the metastable fluid phase. We plot the resulting nucleation barriers ΔG as a function of Φ in Fig. 7.1. We note that the nucleation barrier for $\lambda = 1$ is equivalent to the nucleation barrier for a pure system of hard spheres [144, 145]. In addition, we show the composition of the largest cluster as a function of Φ in Fig. 7.2. We find that the averaged composition $x = N_2/N = 0.5$ as it should be since $\Delta\mu_1 = \Delta\mu_2$ and the bulk chemical potentials of the metastable fluid are equal $\mu_{1,\alpha}^o = \mu_{2,\alpha}^o$. Using the binomial coefficients and the measured one-dimensional free-energy barrier, we determine the two-dimensional free-energy landscape $\Delta G(N_1, N_2) / k_B T = -\ln P(N_1, N_2)$ from the probability distribution function

$$P(N_1, N_2) = \exp[-\Delta G(N_1 + N_2) / k_B T] 2^N \binom{N}{N_1}. \quad (7.39)$$

Fig. 7.3 presents a contour plot of the two-dimensional free-energy landscape $\beta\Delta G(N_1, N_2)$ as a function of N_1 and N_2 . Exemplarily, we also plot isolines for the order parameter $\Phi = N_1 + \lambda N_2$ for $\lambda = 1$ and 0.5 to show the projection of the two-dimensional composition plane onto a one-dimensional order parameter.

In order to check the effect of order parameter choice in the biasing potential (7.29) on the nucleation barrier and the composition of the clusters, we also calculate the nucleation

barrier for $\lambda = 0.5$ at the same reduced pressure. We plot the nucleation barrier in Fig. 7.1 and the averaged composition of the cluster as a function of Φ in Fig. 7.2. While the barrier height is not significantly affected by the choice of order parameter in the biasing potential, in agreement with our predictions in Sec. 7.4, the critical cluster “size” as measured by Φ , i.e. $\simeq 79$ and 96 for $\lambda = 0.5$ and 1 , respectively, depends on the order parameter choice as expected. In addition, we determine the theoretical prediction for the cluster composition using Eq. (7.38). Using the measured slope of the nucleation barrier from Fig. 7.1, we obtain the chemical potential difference $\Delta\mu_{12}(\Phi)$ of species 1 and 2 in the cluster from Eq. (7.38). Using Eq. (7.39), we find

$$P(N_1, N_2) \propto 2^N \frac{N!}{N_2!(N - N_2)!} \exp[-\beta N_2 \Delta\mu_{12}(\Phi)] \quad (7.40)$$

from which we determine the most probable (or averaged) composition:

$$x = 1 - \exp[-\beta \Delta\mu_{12}(\Phi)]. \quad (7.41)$$

The theoretical prediction for the composition is plotted in Fig. 7.2. We find good agreement with the measured composition, except for very small cluster sizes, where we do not expect CNT to match our nucleation barriers. For comparison, we also plot the same predictions for the nucleation paths in Fig. 7.3. We clearly observe that the two nucleation paths cross at the saddle point yielding the same size and composition of the critical cluster for both order parameters, as expected.

Finally, we also determine the composition of the clusters from the steady-state distribution. In systems where the nucleation of the new phase is measured directly, either in experiments or simulations, the measured cluster size distribution corresponds to a steady-state distribution rather than an equilibrium distribution. The steady-state distribution observed during the nucleation process is different from the equilibrium distribution, as clusters that exceed the critical cluster size during the steady-state process will continue to grow further. The steady-state distribution depends both on the free-energy landscape and the dynamics of the system, and includes a flux across the free-energy barrier, whereas the equilibrium distribution can only be determined by preventing the system from nucleating, i.e. constraining the maximum cluster size by e.g. umbrella sampling MC simulations. While the equilibrium and steady-state distributions are in good agreement for small cluster sizes, they disagree strongly for postcritical cluster sizes, i.e., when the system crosses the free-energy barrier. In particular, the equilibrium cluster size distribution shows a minimum corresponding with the maximum in the free-energy barrier, and the steady-state distribution generally decreases continuously (even) beyond the critical cluster size.

We calculate the cluster composition from the steady-state distribution for our binary mixture of hard spheres. To this end, we determine the free energy as a function of cluster size N_1 and N_2 from Eq. (7.39) using a fit to the free-energy barrier obtained from umbrella sampling MC simulations with $\lambda = 1$. The dynamics of the cluster are described

by the following rates:

$$\begin{aligned}
k_{N_1, N_2}^{+,1} &= 1 \\
k_{N_1, N_2}^{+,2} &= 1 \\
k_{N_1, N_2}^{-,1} &= \exp[-\beta(G(N_1 - 1, N_2) - G(N_1, N_2))] \\
k_{N_1, N_2}^{-,2} &= \exp[-\beta(G(N_1, N_2 - 1) - G(N_1, N_2))].
\end{aligned}$$

Here, $k_{N_1, N_2}^{+(-),i}$ is the rate associated with adding (removing) a particle of species i to (from) the nucleus consisting of N_1 and N_2 particles. Hence, clusters can only grow or shrink by one particle at a time with a rate determined by the corresponding free-energy difference. In order to determine the steady-state cluster size distribution, we set a limit to the steady-state distribution by defining a maximum cluster size, which exceeds the critical cluster size. As a barrier crossing can be considered as a one-way event, subsequent nucleation events should start again from the metastable fluid phase. To this end, we impose that the addition of an extra particle to a nucleus with this maximum cluster size falls back to size zero. We note that this step is not reversible, and results in slightly modified rates for nuclei with the maximum cluster size and for clusters of zero size. With the exception of these steps, the dynamics obey detailed balance.

In order to determine the steady-state distribution, we set the rate at which clusters of size (N_1, N_2) are created to zero. Hence, the flux with which clusters of size (N_1, N_2) are created should balance the flux with which clusters of this size disappear:

$$\begin{aligned}
P_{ss}(N_1, N_2) \sum_i (k_{N_1, N_2}^{+,i} + k_{N_1, N_2}^{-,i}) &= \\
P_{ss}(N_1 + 1, N_2) k_{N_1+1, N_2}^{-,1} + P_{ss}(N_1 - 1, N_2) k_{N_1-1, N_2}^{+,1} &+ \\
P_{ss}(N_1, N_2 + 1) k_{N_1, N_2+1}^{-,2} + P_{ss}(N_1, N_2 - 1) k_{N_1, N_2-1}^{+,2}. &
\end{aligned}$$

Here, $P_{ss}(N_1, N_2)$ denotes the steady-state cluster size distribution. The equations for cluster size zero and the maximum cluster size are slightly different due to a flux of clusters from maximum to zero cluster size. By solving this set of linear equations numerically, we obtain the steady-state distribution. Subsequently, the average cluster composition can be obtained from the steady-state distribution by averaging over clusters with equal $\Phi = N_1 + \lambda N_2$. The resulting cluster composition is shown in Fig. 7.2 for $\lambda = 0.5$. Since the two-dimensional steady-state cluster size distribution, which is symmetric in N_1 and N_2 decreases monotonically with cluster size, the resulting projected composition is always lower than 0.5 and matches well with the cluster compositions obtained from umbrella sampling MC simulations and the theoretical prediction, except at small cluster sizes as expected. Moreover, in the limit of large (postcritical) clusters, the cluster growth rate approaches a constant for the current choice of dynamics, resulting in a nearly flat steady-state cluster size distribution and a cluster composition of 0.5.

In conclusion, we have shown using a simple model for a binary mixture of hard spheres that the composition of the critical cluster does not depend on the choice of order parameter, while the composition of noncritical clusters is affected by the order parameter. This is a direct consequence of the projection of the two-dimensional free-energy landscape onto a one-dimensional order parameter, say $\Phi = N_1 + \lambda N_2$, which

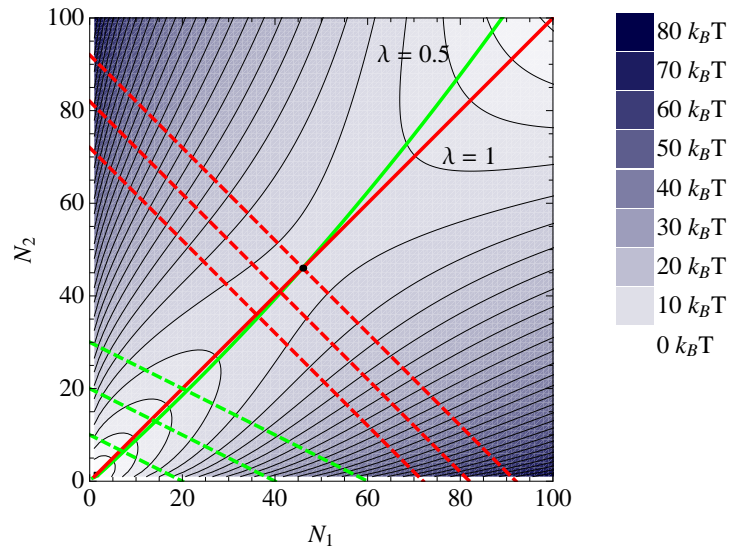


Figure 7.3: Contour plot of the two-dimensional free-energy landscape $\Delta G(N_1, N_2)/k_B T$ as a function of N_1 and N_2 . We also plot a few isolines for the order parameter $\Phi = N_1 + \lambda N_2$ for $\lambda = 0.5$ and 1 (dashed lines), and we plot the nucleation path (solid lines labeled with $\lambda = 1$ and $\lambda = 0.5$) for the two order parameters that we considered as predicted by (7.38). The two nucleation paths cross at the saddle point corresponding to the critical cluster size.

influence directly the projected (Landau) $\Delta G(\Phi)$ and the averaged (or projected) cluster composition. Moreover, as the umbrella sampling method allows us to equilibrate the system for various values of the order parameter, the system can be regarded to be in local equilibrium for each value of the order parameter. The nucleation paths that the system then follows remain close to the minimum free-energy path (see Fig. 7.3), and thus the height of the nucleation barrier is largely unaffected by the choice of order parameter.

7.6 An interstitial solid solution

We consider crystal nucleation of an interstitial solid solution in a highly asymmetric binary mixture of large and small hard spheres with size ratio $q = \sigma_2/\sigma_1 = 0.3$, where $\sigma_{1(2)}$ denotes the diameter of species 1 (large spheres) and 2 (small spheres). The interstitial solid solution consists of a face-centered-cubic crystal phase of large spheres with a random occupancy of the octahedral holes by small spheres, and hence the composition of the interstitial solid solution can vary from $x = N_2/N \in [0, 1]$ [173]. As the volume of this solid phase is not largely affected by the density of small spheres, we set the partial particle volume v_2 and $\omega = v_2/v_1$ to zero. Using Eq. (7.38), we find the following relation if the system is in local equilibrium at fixed order parameter $\Phi = N_1 + \lambda N_2$

$$\Delta\mu_2 = \lambda \frac{d\Delta G}{d\Phi}. \quad (7.42)$$

For $\lambda = 0$, the order parameter $\Phi = N_1$ measures only the large spheres in the cluster, and the cluster composition of both critical and noncritical clusters is determined by the chemical equilibrium condition for the small spheres in the cluster and the metastable fluid phase, i.e., $\Delta\mu_2 = 0$. For $\lambda = 1$, when all particles in the clusters are counted by the order parameter $\Phi = N_1 + N_2$, the composition of precritical clusters will have a higher density of small particles compared to the chemical equilibrium condition for the small particles in the cluster and the metastable fluid phase, as the slope of the nucleation barrier is positive, and similarly postcritical clusters will have a lower density of small particles. For both order parameters, we find that the critical cluster satisfies the Gibbs-Thomson equation (7.19), and thus for a partial particle volume $v_2 = 0$, we obtain chemical equilibrium for the small particles in the critical cluster and the fluid phase independent of the order parameter choice.

As the composition and size of the critical cluster are not affected by the choice of order parameter, we set $\lambda = 0$ in order to investigate whether or not we observe diffusive equilibrium for species 2 for all noncritical clusters. To keep the composition of the fluid fixed, it would be convenient to use again Monte Carlo simulations in the semi-grand canonical ($NPT - \Delta\mu_{12,\alpha}$) ensemble. However, the acceptance probability of changing small spheres into large spheres is extremely small, which makes the equilibration time of the simulation prohibitively long, even when we use the augmented semigrand ensemble presented in Ref. [165], where the diameter of the particles is changed gradually in different stages. In order to solve this problem, we determine the free-energy barrier using the umbrella sampling technique in isothermal-isobaric MC simulations, in which the pressure P_α^o , the temperature T , and the particle numbers $N_{1,\alpha}^o$ and $N_{2,\alpha}^o$ are kept fixed of the original metastable bulk phase. We perform successive simulations for each window, but in such a way that the composition $x_\alpha^o = N_{2,\alpha}^o / (N_{1,\alpha}^o + N_{2,\alpha}^o)$ of the metastable fluid phase is on average kept fixed during the growth of the nucleus. To this end, we first measure the instantaneous composition x_α of the fluid phase in the initial configuration for the successive umbrella sampling windows centered around a new order parameter value Φ . If the composition of the fluid has changed more than 0.1%, we resize random particles in the fluid phase during an equilibration run until the fluid phase reaches its original composition x_α^o . We then start the production run to measure the probability distribution function $P(\Phi)$ and the corresponding part of the free-energy barrier in a normal isobaric-isothermal MC simulation. We assume that the composition of the fluid phase during MC simulations of a single umbrella sampling window does not change significantly, since the cluster size is approximately constant. In order to determine the composition of the fluid phase, we first determine the largest crystalline cluster in the system by using the local bond-order parameter and cluster criterion as described in Sec. 7.4 with cutoff radius $r_c = 1.1\sigma_1$, dot-product cutoff $d_c = 0.7$, and number of solid bonds $\xi_c \geq 6$. The composition of the fluid is defined as $x_\alpha = (N_{2,\alpha}^o - N_2) / (N_{2,\alpha}^o + N_{1,\alpha}^o - N_2 - N_1)$ where N_1 is the number of large spheres in the cluster and N_2 is the number of small spheres which have at least 6 neighbors of large spheres in the cluster within cut-off distance $r_c = 1.1\sigma_1$. $N_{1,\alpha}^o$ and $N_{2,\alpha}^o$ denote the total number of large and small spheres in the MC simulation.

In addition, we determine the composition of the solid nucleus $x = N_2/N$. In order to avoid surface effects and defects in the crystal structure of the solid nucleus, we determine

the fraction of octahedral holes that is occupied by a small sphere in the fcc lattice of the large spheres in the solid cluster. An octahedral hole is defined as a set of 6 large particles, where each particle is a neighbour of 4 other particles in the same set, and the octahedral hole is occupied by a small particle if all 6 large particles are within a cutoff radius of $0.22\sigma_1$ of the center-of-mass of this small sphere.

We first determine the nucleation barrier in a normal $N_{1,\alpha}^o N_{2,\alpha}^o P_\alpha^o T$ MC simulation using the umbrella sampling technique for system sizes $N_\alpha^o = N_{1,\alpha}^o + N_{2,\alpha}^o = 3000, 6000,$ and 9000 particles. The initial fluid composition is set to $x_\alpha^o = 0.5$ and reduced pressure $P^* = \beta P_\alpha^o \sigma_1^3 = 25$. We plot the Gibbs free energy $\Delta G/k_B T$ as a function of the number of large spheres N_1 in the largest crystalline cluster in Fig. 7.4. We observe that the nucleation barrier height and critical cluster size decreases upon increasing system size. This can be explained by a change in the composition of the metastable fluid phase during the growth of a crystalline cluster. In Fig. 7.5, we plot the composition of the metastable fluid phase as a function of the cluster size N_1 for the various system sizes. We clearly find that the fluid composition changes significantly during the growth of a solid nucleus for smaller system sizes. In order to corroborate this result, we perform umbrella sampling MC simulations in which the composition of the metastable fluid phase is kept fixed in each successive umbrella sampling window using the method as described above. The composition of the fluid phase is indeed kept fixed by this method as shown in Fig. 7.5. The nucleation barrier as obtained by fixing the composition of the metastable fluid phase is presented in Fig. 7.4. As the nucleation barrier calculated at fixed fluid composition should correspond to an infinitely large system size, we plot the barrier heights $\Delta G^*/k_B T$ as a function of $1/N_\alpha^o$ with $N_\alpha^o = N_{1,\alpha}^o + N_{2,\alpha}^o$. We find that the barrier height depends linearly on $1/N_\alpha^o$ within errorbars. Moreover, extrapolating the barrier heights obtained from $N_{1,\alpha}^o N_{2,\alpha}^o P_\alpha^o T$ MC simulations to the thermodynamic limit, we find that the finite-size corrected barrier height agrees well within errorbars with the barrier height determined from umbrella sampling MC simulations with fixed fluid composition corresponding to an infinitely large system size. In addition, we plot the composition of the solid cluster as a function of cluster size N_1 in Fig. 7.5, and we find no strong dependence of the cluster composition on system size.

Finally, we determine the composition of (non)critical clusters for the nucleation of the interstitial solid solution for four different fluid compositions $x_\alpha^o = 0.2, 0.5, 0.7$ and 0.8 at statepoints well-inside the fluid-solid coexistence region using umbrella sampling MC simulations with fixed fluid composition and system size $N_\alpha^o = 3000$. Following Ref. [165], the ‘‘supercooling’’ was kept fixed, i.e., $P_\alpha^o/P_{coex}^* = 1.2$, where P_{coex}^* is the pressure at the bulk fluid-solid coexistence at the corresponding fluid composition. We note however that these statepoints correspond to different values for the supersaturation, and can therefore lead to significantly different barrier heights. We determine the Gibbs free-energy barrier and the cluster composition as a function of cluster size N_1 using umbrella sampling MC simulations, and plot the results in Fig. 7.6 and 7.7 for the four different fluid compositions. In Fig. 7.7, the dashed lines indicate the compositions predicted by Eq. (7.42) with $\lambda = 0$, i.e., chemical equilibrium for species 2 in the clusters and the metastable fluid phase. For comparison, we also plot the composition of the coexisting solid phase at P_α^o . We clearly observe that the measured cluster compositions obtained from umbrella sampling MC simulations are in good agreement with the predictions from

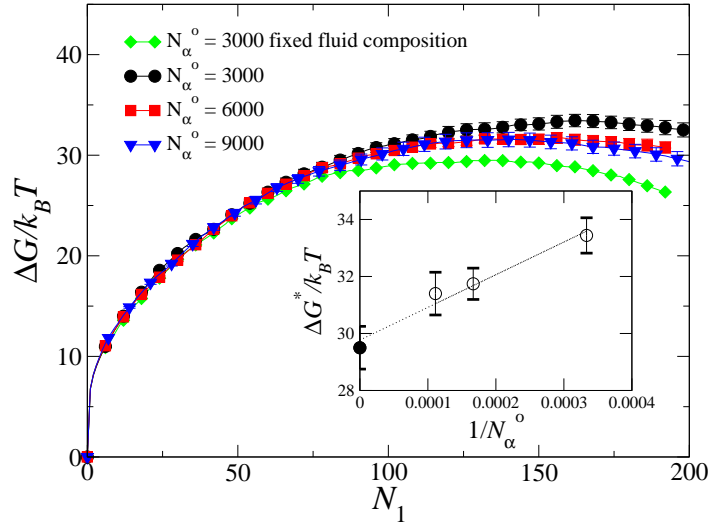


Figure 7.4: a) Gibbs free energy $\Delta G/k_B T$ as a function of number of large particles N_1 in the largest crystalline cluster using normal $N_1^o N_2^o P T$ MC simulations and isobaric-isothermal MC simulations with fixed fluid composition $x_\alpha = 0.5$, and pressure $P^* = \beta P_\alpha^o \sigma_1^3 = 25$. b) Free-energy barrier height $\Delta G^*/k_B T$ as a function of $1/N_\alpha^o$.

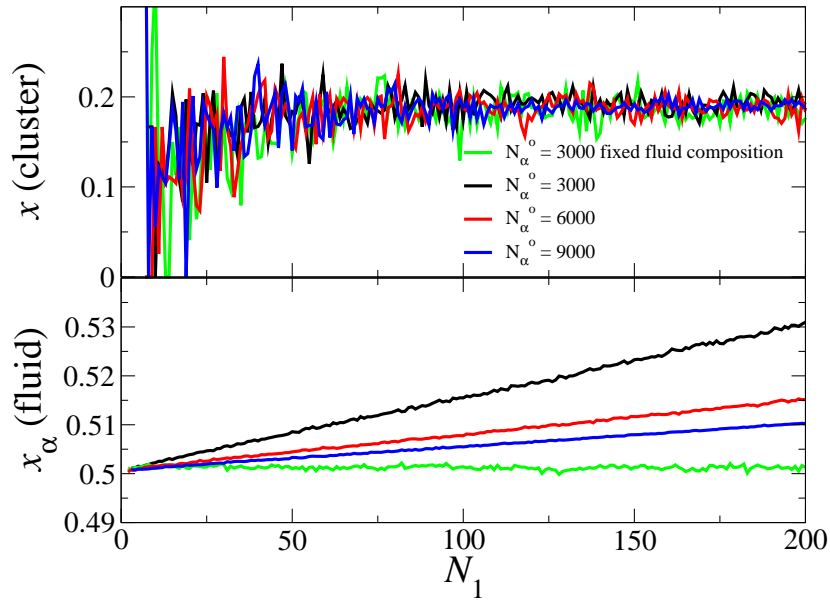


Figure 7.5: The composition of the largest crystalline cluster $x = N_2/N$ (top) and the metastable fluid phase x_α (bottom) as a function of cluster size N_1 . The green lines denote the simulation in which the composition of the fluid was reset to the original value at the start of each US window. The other lines correspond to normal $N_{1,\alpha}^o N_{2,\alpha}^o P_\alpha^o T$ MC simulations, where the overall composition of the system is kept fixed for various system sizes.

CNT for cluster sizes larger than 30, which predicts chemical equilibrium for the small spheres in the cluster and the metastable parent phase. If we now take a closer look at the statepoint defined by $x_\alpha^o = 0.2$ and $P_\alpha^o/P_{coex}^* = 1.2$ for the metastable fluid phase, we find from Ref. [173] that the composition of the coexisting fluid and solid phase after full phase separation should be $x \simeq 0.47$ and 0.15 , respectively. Interestingly, we find that the composition of the nucleating clusters is much lower ($x \simeq 0.07$) than that of the coexisting bulk crystal phase. Hence, the phase separation is mainly driven by the nucleation of large spheres while maintaining chemical equilibrium for the smaller species throughout the whole system. Only when the chemical potential of the large spheres in the metastable fluid is sufficiently low due to a depletion of large spheres as a result of crystal nucleation and crystal growth, small spheres will diffuse into the crystal phase in order to increase the composition of the solid phase. However, we note that the chemical equilibrium condition for the smaller species only holds for the present order parameter choice $\Phi = N_1$, whereas any other choice of order parameter would certainly yield different results for the cluster composition.

For highly asymmetric binary hard-sphere mixtures, where the stable solid phase corresponds to a fcc of large spheres with a dispersed fluid of small particles, one would naively expect that the small particles are always in chemical equilibrium during the nucleation process. Hence, in order to study crystal nucleation in highly asymmetric mixtures, one can employ an effective pairwise depletion potential description as described in Ref. [174–176] provided that three- and higher-body interactions are negligible and the depletion potentials are determined at fixed chemical potential of the small spheres. Such an effective pair potential approach was employed in a nucleation study in the vicinity of a critical isostructural solid-solid transition in a binary mixture of hard spheres with size ratio $q = \sigma_2/\sigma_1 = 0.1$, but this study showed according to the authors a breakdown of classical nucleation theory [177]. It would be interesting to investigate whether or not the breakdown is caused by the (false) assumption of chemical equilibrium of small spheres during the nucleation process. For less asymmetric binary hard-sphere mixtures, where the small spheres cannot diffuse freely in the solid cluster, chemical equilibrium of the smaller species is harder to maintain, especially when the nucleated crystal phase has long-range crystalline order for both species as in the case of a superlattice structure where the chemical potentials of the two species are not independent as it is determined by the stoichiometry of the crystal structure. It would be interesting to investigate at which size ratio and pressures this crossover occurs.

7.7 Conclusions

In this chapter, we have studied crystal nucleation in a binary mixture of hard spheres and we have investigated what the effect is of the choice of order parameter on the composition and size of both critical and noncritical clusters. We have studied nucleation of a substitutional solid solution in a simple toy model of identical hard spheres but tagged with different colors and we investigate the nucleation of an interstitial solid solution in a binary hard-sphere mixture with a diameter ratio $q = 0.3$. In order to study nucleation of a crystal phase in computer simulations, a one-dimensional order parameter is usually

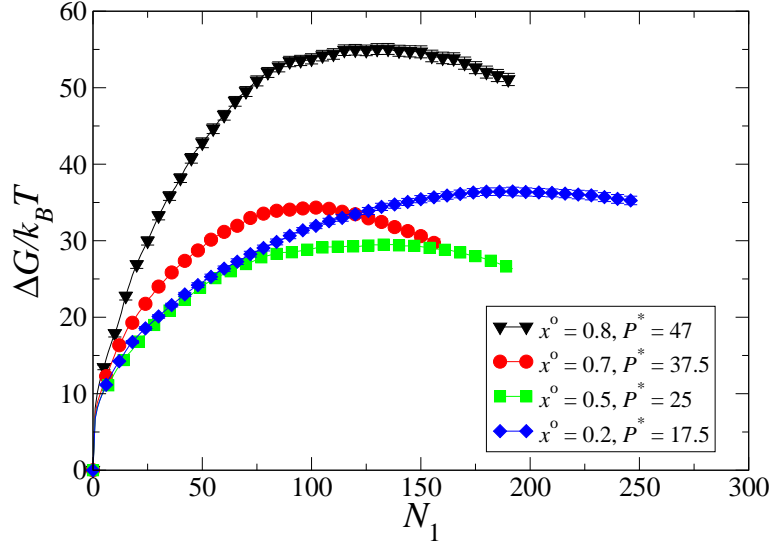


Figure 7.6: Gibbs free energy $\Delta G/k_B T$ as a function of cluster size N_1 for four different fluid compositions $x_\alpha^o = 0.2, 0.5, 0.7,$ and 0.8 for a binary mixture of hard spheres with size ratio 0.3 at 20% supercooling, i.e., $P_\alpha^o/P_{coex}^* = 1.2$ with P_{coex}^* the bulk coexistence pressure.

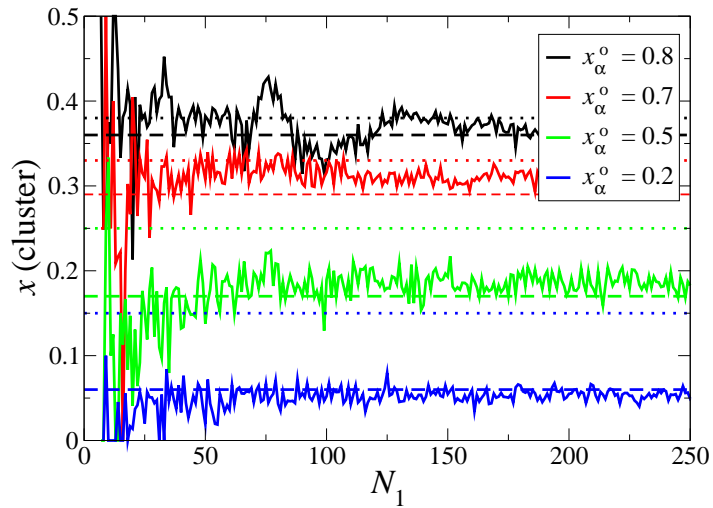


Figure 7.7: Cluster compositions $x = N_2/N$ as a function of cluster size N_1 for four different fluid compositions $x_\alpha^o = 0.2, 0.5, 0.7,$ and 0.8 for a binary mixture of hard spheres with size ratio 0.3 at supercooling $P_\alpha^o/P_{coex}^* = 1.2$. The long dashed lines denote the composition predicted by CNT, which corresponds to chemical equilibrium of species 2 in the solid clusters and the metastable fluid phase, while the dotted lines denote the composition of the coexisting bulk crystal phase.

defined to identify the solid phase from the supersaturated fluid phase. We have shown that the choice of order parameter can strongly influence the composition of noncritical clusters, as the free-energy landscape in the two-dimensional composition plane (N_1, N_2) is projected onto a one-dimensional order parameter, say $\Phi = N_1 + \lambda N_2$, in umbrella sampling MC simulations. This is supported by the good agreement that we found between our results on the composition of noncritical clusters obtained from umbrella sampling MC simulations and the predictions from CNT for the nucleation of a substitutional solid solution in a toy model. While the effect is clearly visible in the case of a binary system, it should occur more generally whenever a higher-dimensional free-energy landscape is projected onto a single order parameter. For the nucleation of an interstitial solid solution in a highly asymmetric hard-sphere system, we found that the composition of noncritical clusters is determined by the chemical equilibrium condition of the small spheres in the cluster and the fluid phase, as the partial particle volume of the small spheres in the solid phase can be neglected. We compared the composition of the noncritical clusters obtained from umbrella sampling MC simulations and the theoretical prediction from CNT, and found again good agreement. More importantly, we find that the barrier height and the composition of the critical cluster are not significantly affected by the choice of order parameter. As a result, critical clusters and the barrier height should be comparable even with different order parameters.

7.8 Acknowledgements

I would like to thank Ran Ni for calculating the free energy barriers for the nucleation of the ISS phase, Laura Filion for calculating the phase diagram of the binary hard sphere system at size ration 0.3, and both of them for many long and fruitful discussions.

Assembly of colloidal spheres and dumbbells through emulsion droplet evaporation

In this chapter, we examine the clusters formed by particles confined to emulsion droplets. By slow evaporation of the droplets, small numbers of particles can be forced together into densely packed clusters. We use Monte Carlo simulations to investigate clusters of both spheres and dumbbells, modeling the evaporation process as two separate steps: a compression step in which the particles are forced into a dense packing due to spherical confinement, and a subsequent second step that minimizes the second moment of the mass distribution of the cluster. This second step mimics the rearrangements of the cluster in the final stages of evaporation, where the shape of the emulsion droplet is strongly influenced by the particles. While only hard-core interactions are taken into account, comparisons between clusters obtained from simulations and experimental snapshots lead us to conclude that good agreement is found when using this simple model.

8.1 Introduction

As spherical colloidal particles are often considered as a model system for atoms, a logical extension would be modeling clusters of colloidal spheres as colloidal molecules.[178] Various methods have been proposed for the fabrication of colloidal molecules,[179] e.g. by geometrical confinement of colloidal spheres and capillary forces, [180] by controlled coagulation, [181, 182] or by coalescence of colloids with liquid protrusions. [183, 184] Emulsion droplet evaporation, was introduced by Manoharan *et al.* a number of years ago. [185] In this method, emulsion droplets containing small numbers of particles are suspended in a liquid. By evaporating the solvent in the emulsion droplets, the size of the droplets can be slowly reduced, causing the particles in each droplet to be compressed into densely packed clusters. For clusters of up to around 16 particles, it has been shown that this method leads to well-defined cluster shapes that are largely consistent across various systems with different particles and solvents. [186, 187] By separating these clusters based on their size, this process can yield largely monodisperse anisotropic building blocks that could be useful in engineering a range of complex structures. For example, it has been suggested that the tetrahedral clusters commonly seen in these experiments could be used to create crystals with a diamond lattice, potentially allowing for structures with useful optical properties.[188–191]

The structure of the particles in an emulsion droplet suspended in a liquid is determined not only by the interactions between the particles, but also on the droplet volume and the particle-droplet (γ_{pd}), particle-liquid (γ_{pl}) and droplet-liquid (γ_{dl}) surface tensions. The particle configuration and droplet shape can be determined from minimizing the total surface energy. [192] While the surface tensions and interaction potentials in experiments are often not exactly known, the uniqueness of the structures found in different experiments suggests that they do not depend strongly on the details of the underlying system. Indeed, Ref [192] shows that the clusters are unique over a whole range of contact angles and are mostly determined by geometrical constraints. The contact angle θ is given by Young's equation and depends on the three surface tensions:

$$\gamma_{dl} \cos \theta = \gamma_{pl} - \gamma_{pd}. \quad (8.1)$$

Interestingly, for cluster sizes $N \leq 11$, the clusters observed closely correspond to the particle configurations that minimize the second moment M_2 of the mass distribution:

$$M_2 = \sum_{i=1}^N |\mathbf{r}_i - \mathbf{r}_0|^2, \quad (8.2)$$

with \mathbf{r}_0 the center of mass of the cluster, and \mathbf{r}_i the position of the center of particle i . [185, 192, 193] For larger clusters, the clusters that minimize this second moment generally have a central particle, a feature absent in the experimentally observed structures. As the particles in experiments were seen to stick to the surface of the emulsion droplets at all times during the evaporation process, it was suggested by Manoharan *et al.* [185] that the structures were formed in two steps. The colloids first reach an optimal close packing confined to the surface of a sphere, and are then pulled towards the center by capillary forces while the particles are restricted to a continuous and smooth surface. In agreement

with the observed clusters, this last step reduces the second mass moment, but prevents any spheres from ending up on the inside of the cluster. Lauga and Brenner [192] showed that this process can be accurately modeled with simulations of particles attached to a deformable surface, yielding the experimentally observed structures for all sizes $N \leq 12$. Additionally, they argued that the uniqueness of these packings can be understood from geometrical considerations: the close-packed configurations where all particles are confined to the surface of a sphere are unique for almost all N , and in nearly all cases the force constraints in the system limit the cluster to a single mode of rearrangement, resulting in a single final configuration.

The emulsion evaporation method has been applied to a variety of systems, including nanoparticles [194–196] and colloidal spheres mixed with either smaller particles [196, 197] or polymers [198]. In this chapter, we use simulations to investigate the clusters formed by both symmetric and asymmetric colloidal dumbbells in evaporating droplets, and compare the results with experimental results. In the experiments, PMMA (poly-methyl-methacrylate) dumbbell particles were produced via an overswelling method. [199] The resulting particles were dispersed in aqueous emulsion droplets suspended in an oil phase. After evaporation of the droplets, small clusters of dumbbells remain. The structure of these clusters has been studied using Scanning Electron Microscopy (SEM), and shows a larger variety of cluster shapes than those found in clusters of spherical particles. We performed simulations on a simple model for these droplets where both the particles and interface are modeled purely as hard-core interactions. When comparing the structures resulting from the simulations with those found in the experiments, we find good agreement for the symmetric dumbbells if the dumbbell particles in the simulations are constrained to the droplet interface. For the asymmetric dumbbells, we find that the larger spheres dominate the cluster shape, and we recover the same structures seen in clusters of spheres with no specific ordering of the smaller spheres of the dumbbells.

8.2 Simulation Methods

We study the behavior of colloidal particles in an emulsion droplet during the evaporation of the solvent. In the experimental setup, the particle-particle and particle-wall interactions are difficult to determine and will probably change during the evaporation process. We assume that the particles are confined in a spherical cavity that shrinks during the evaporation of the droplets. As a first approximation, we model the particles and the droplet interface by hard interactions. As a result, no deformations of the wall from its spherical shape occur, which is justified in the first stage of the evaporation process, i.e. before packing constraints become important.

We simulate both spherical and dumbbell particles. In both cases, our unit of length is taken to be σ , the diameter of the largest sphere size. The dumbbells are modeled as two partially overlapping hard spheres with diameter ratio $q = \sigma_S/\sigma$, at a fixed distance d between the centers. For both systems, the center of mass of each sphere is confined to a spherical simulation box with hard walls. During the simulations, the pressure is slowly increased from $P^* = P\sigma^3/k_B T = 1$ to 20 to mimic the evaporation of the droplet. At $P^* = 20$, the particles no longer have enough freedom of movement to rearrange, but

still vibrate. To fix the structure, the pressure is then increased to $P^* = 100$, effectively leading to a fully jammed state.

In our simulations, we consider two different regimes for the particle wettability. In the non-wetting regime (contact angle $\cos\theta = 1$), the particles can move freely within the spherical cavity under the constraint that the particles do not overlap with each other or the droplet interface. For finite wettability ($-1 < \cos\theta < 1$), the particles are attached at the droplet interface by an adsorption free energy [200] which we model by confining the center of mass of the particles to a thin spherical shell with thickness $d_S = 0.1\sigma_S$ at the droplet surface, where σ_S is the diameter of the smallest sphere in the system. We find that the final structure of the cluster is not affected by the shell thickness d_S , provided that $d_S \ll \sigma_S$.

Manoharan *et al.* suggested [185] that after reaching this spherical packing stage, further evaporation of the droplet induces a reorganization of the particles due to the attractive Van der Waals interactions, which reduces the second moment of the mass distribution in the system. To model the second stage of the evaporation process, we use the jammed spherical clusters obtained from the spherical compression simulations, remove the spherical confinement, and use a standard Monte Carlo scheme to minimize M_2 . In this simulation, the total energy of the system is taken to be proportional to M_2 , with a dimensionless proportionality constant α that is increased slowly to anneal the cluster to a local potential energy minimum:

$$\beta U(\mathbf{r}_s^N) = \alpha \sum_{i=1}^{N_s} m_i |\mathbf{r}_i - \mathbf{r}_0|^2 / \sigma^2, \quad (8.3)$$

with $\beta = 1/k_B T$, k_B Boltzmann's constant, T the temperature, σ the sphere diameter, and N_s the number of spheres in the cluster. In the case of dumbbell particles, each sphere is counted separately in the summation. The (dimensionless) mass m_i is only important if multiple sphere sizes appear in the system, and is taken to be 1 for the largest sphere size in the system. The strength of the potential α is increased from 100 to 1000, at which point no further reorganization is observed. The system is then quenched at $\alpha = 10000$ to remove any further vibrations. For the results presented below, both the compression and annealing parts of the simulation consist of $8 \cdot 10^6$ Monte Carlo cycles. We also performed simulations with lower compression and annealing rates, but found similar results for the final clusters.

8.3 Results

8.3.1 Spheres

Several experimental studies have shown that colloidal spheres confined to emulsion droplets form unique clusters for sizes $N \leq 16$ upon slow evaporation. [185–187] As a test of our method, we first apply it to clusters of spherical particles, with cluster sizes $2 \leq N \leq 16$. We study the resulting packing of spheres in a shrinking spherical cavity for non-wettable particles and wettable particles which are adsorbed at the interface. Subsequently, we employ the resulting spherical packings in MC simulations to minimize M_2 ,

thereby mimicking the final stage of the evaporation process. We present the results of the packing before and after minimizing M_2 for both wettable and non-wettable particles in Table 8.1. We find that the cluster configuration for cluster size $N = 4$ and 6 , are a tetrahedron and an octahedron respectively, independent of the particle wettability or M_2 minimization. For $N = 5, 7, 8, 9$ and 10 , we find that the configurations are independent of the particle wettability, but different structures are observed before and after the M_2 minimization. The final configurations are the triangular dipyramid ($N = 5$), pentagonal dipyramid ($N = 7$), snub disphenoid ($N = 8$), triaugmented triangular prism ($N = 9$), and the gyroelongated square dipyramid ($N = 10$). The configurations for $N = 11, 13, 14, 15$ and 16 are all different and depend on the particle wettability and the M_2 minimization. For $N = 12$, we find that the configurations depend on the particle wettability, but not on the M_2 minimization.

We now compare the resulting structures with the experiments on polystyrene, silica and PMMA spheres in toluene or hexane droplets suspended in water by Manoharan [185] and the experiments on water-borne polystyrene and silica spheres in water-in-oil emulsions by Cho.[187] During the evaporation process, the polystyrene, silica and PMMA spheres in Ref. [185, 186] are attached at the droplet interface and as expected the observed clusters with $N \leq 12$ match with our predictions for wettable particles after M_2 minimization, with one exception: for cluster size $N = 11$, the non-convex structure seen by Manoharan only appears for non-wettable particles.

In the experiments by Cho, [187] the water-borne particles form the same clusters as observed in Ref. [185, 186], but additional isomeric structures were found for $N = 7, 8$, and 11 . As the isomeric clusters correspond to the optimal sphere packings for particles interacting with a Coulomb potential, it was argued by Cho that the electrostatic repulsion between the polystyrene and silica spheres caused the formation of these Coulomb clusters: the stronger electrostatic repulsion between the particles prevents the reorganization of the cluster in the second stage of the evaporation process. [187] The isomeric clusters for $N = 7$ and 8 agree well with our predictions before the M_2 minimization which are independent of the wettability of the particles. For $N = 11$, the two isomeric structures found correspond to those we found for wettable particles before and after M_2 minimization (for silica and polystyrene spheres, respectively).

For larger clusters ($N > 12$), no clear match between simulations and experiments can be found. Nonetheless, it is clear that for sufficiently small clusters, our method provides a good indication of the types of structures that can be expected in clusters formed by evaporation of emulsion droplets with spherical particles.

8.3.2 Symmetric dumbbells

While spheres already provide a variety of cluster shapes depending on the number of particles per cluster, new structures can be obtained by replacing the spheres with anisotropic particles. As a simple example, we consider colloidal dumbbells.

In the experiments by Peng *et al.*,[201] both symmetric and asymmetric colloidal dumbbells were synthesized and dispersed in emulsion droplets. After evaporating the emulsion droplets, the resulting clusters were observed via Scanning Electron Microscopy (SEM). The symmetric dumbbells consisted of two spheres, each with a diameter $\sigma =$

N	Non-wettable		Wettable		Mano- haran	Cho	
	before	after	before	after		Polyst.	Silica
4	a	a	a	a	a		
5	a	b	a	b	b		
6	a	a	a	a	a		
7	a	b	a	b	b		a
8	a	b	a	b	b	a	a
9	a	b	a	b	b		
10	a	b	a	b	b		
11	a	b	c	d	b	d	c
12	a	a	b	b	b		
13	a	b	c	d	e		
14	a	b	c	d	e		
15	a	b	c	d	e		
16	a	b	c	d			

Table 8.1: Structures found from simulations of spherical particles in evaporating droplets, and experimental results. The first column shows the number of particles N . The next two columns show the results if the particles are not confined to the droplet interface, both before and after minimizing M_2 . The fourth and fifth column show the configurations resulting from fixing the particles to the droplet interface. The last columns show the experimental results by Manoharan *et al.*[185] and the additional structures seen by Cho *et al.* [187]. The letters denote structures that are (almost) the same for the same cluster size.

1.42 μm , and a distance $d = 0.5\sigma$ between the two centers. In the experiments, the dumbbells formed a series of structures different from those found when using spherical particles, often with several different configurations per cluster size.

We performed simulations of hard dumbbells with sizes corresponding to the experimental system using the same methods as we used for spheres. In contrast to clusters of spherical particles, but in agreement with the experimental snapshots, these simulations result in multiple isomeric configurations. Even with slow compression speeds, the system can reach several distinct states. Interestingly, for cluster sizes $N = 3$ and 6 , two mirrored structures appear with a different chirality, a property that is absent in the clusters of spherical particles.

In the experimental setup, the particles were seen to stick to the oil-water interface before the evaporation of the emulsion droplets. In our simulations, we indeed find better agreement with the experimental snapshots in the case of particles with finite wettability: for small cluster sizes ($N < 5$) wettability does not affect the structures formed, but for all larger cluster sizes $N \geq 5$ good agreement was only found for wettable particles. Table 8.2 shows the configurations obtained from simulations of wettable particles, matched with experimental snapshots where possible. For cluster sizes $N = 2$ and 4 , only one cluster shape is found, with no significant changes after M_2 minimization. Cluster sizes $N = 3$ and 6 both show a single structure as well, but each has an isomer that is its mirror image. Both structures show rotational symmetry over a 120° angle. For $N = 6$, the cluster deforms slightly during M_2 minimization, but stays qualitatively the same. For cluster size $N = 5$, only a single (highly asymmetric) structure is found, with some reorganization during the final minimization step. For all clusters up to size $N = 6$, almost all experimental snapshots agree well with the structures found before M_2 minimization, and the small changes during the minimization step do not break this agreement. For larger clusters ($N \geq 7$), we still find good agreement between the spherical packings and experiments, although a number of different isomeric structures can also result from the same simulations. While one of the experimental snapshots for $N = 8$ was best matched by a configuration after M_2 minimization, this minimization step generally reduced the agreement between simulation and experiment. Moreover, the final configurations often showed a clearly visible central particle in the cluster (such as the one shown for $N = 10$ in Table 8.2), which was absent in the experimental snapshots.

Apart from cluster sizes $N = 2, 3, 4$ and 6 , the clusters obtained from symmetric dumbbells do not appear symmetric themselves. While it seems likely the larger cluster sizes would behave more or less as spherical particles with some degree of surface roughness when used as colloidal building blocks, these smaller clusters sizes could well provide a more interesting phase behavior.

8.3.3 Asymmetric dumbbells

The same experiment was applied to asymmetric colloidal dumbbells, where one of the two spheres in each dumbbell is smaller than the other. In this case, the diameters of the smaller and larger spheres were $\sigma_S = 1.03\mu\text{m}$ and $\sigma = 1.42\mu\text{m}$, respectively, corresponding to a size ratio of $q = 0.73$. The centers of the two spheres are $d = 0.37\sigma$ apart. For these particles, an even larger variety was observed in the resulting clusters, particularly in the

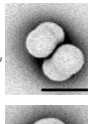
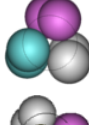
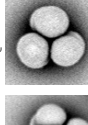
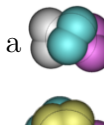
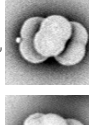
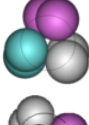
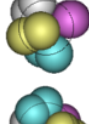
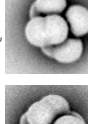
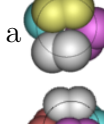
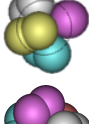
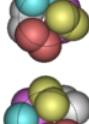
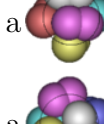
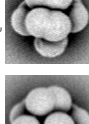
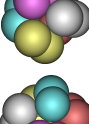
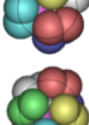
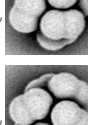
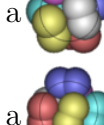
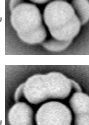
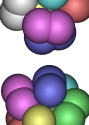
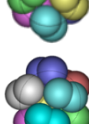
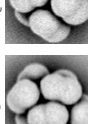
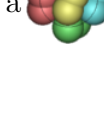
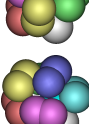
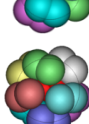
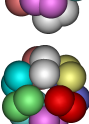
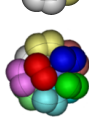
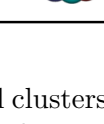
N	Sim.	Exp.	Sim.	Exp.	M_2	Exp.
2	a 	a 			a 	
3	a 	a 	a 	a 	a 	
4	a 	a 	a 	a 	a 	
5	a 	a 	a 	a 	a 	
6	a 	a 	a 	a 	a 	
7	a 	a 	a 	a 	b 	
8	a 	b 			c 	c 
9	a 	a 			b 	
10	a 				b 	
11	a 	a 	b 	b 	c 	

Table 8.2: Comparison of experimental clusters of symmetric dumbbells with simulation results of wettable particles. The first column shows the number of dumbbells N in the cluster. The second and fourth columns show configurations resulting from simulations, next to similar configurations observed in experiments in the third and fifth column (where available). The fourth column shows the results after minimizing M_2 from a typical spherically packed configuration, compared with a matching experimental cluster in the last column cluster size $N = 8$. The letters indicate clusters with (almost) the same structure.

positioning of the small spheres. Table 8.3 shows two experimental snapshots for each cluster size $2 \leq N \leq 12$. Apparently, the locations of the smaller parts of the dumbbells are not strongly determined by the forces that form the cluster. In fact, regardless of the positions of the small spheres, the configurations of large spheres closely resemble the structures found in clusters of spherical particles, as shown by the last column in Table 8.3.

When applying the same simulation method to this system, the configurations found after the compression step do not agree with the experimental snapshots for either wettable or non-wettable particles. Clear differences in the positions of the large spheres can be seen, and the small spheres generally still have limited freedom of movement before M_2 minimization, rather than being mechanically arrested due to contacts with other spheres as seen in the experimental snapshots. When minimizing the second moment of the mass distribution, the resulting configuration is influenced by the mass ratio m_S/m_L of the small and large spheres. Of course, as the minimization of M_2 is only an empirical model for the final stages of droplet evaporation, the “mass” in this context is not physically linked to the real mass of the sphere. Simply letting the mass of each sphere scale with its volume, such that $m_S/m_L = \sigma_S^3/\sigma^3$, generally leads to configurations with the smaller spheres preferentially residing in the center of the cluster, which deviates from the experimental observations. Reducing the effect of the positions of small spheres on M_2 yields much better agreement with the experimental observations. The resulting clusters are independent of the exact mass ratio, as long as $0 < m_S/m_L \ll \sigma_S^3/\sigma^3$: all that appears to be required is a strong preference for large spheres to be near the center of the cluster, and a weak contribution of the small spheres to prevent any freedom of movement in the final configuration. In Table 8.3, the simulation results for wettable particles with $m_S/m_L = 0.1\sigma_S^3/\sigma^3$ are shown both before and after M_2 minimization. For all cluster sizes shown, the structure of the large spheres in the final configuration agrees with those seen in experiments, with the positions of the small particles varying between different simulation runs and experimental snapshots.

The effect of particle wettability is largely the same as in the case of spherical particles: for all cluster sizes $N \leq 10$, the large spheres end up in the same configuration after M_2 minimization. For cluster size $N = 11$, we now see both the convex and non-convex configurations appear, regardless of particle wettability. However, at cluster size $N = 12$ non-wettable particles show a central particle that is absent in the experimental snapshots, resulting in slightly better overall agreement if the particles are assumed to be wettable.

In short, asymmetric dumbbells at this size ratio do not seem to meaningfully affect the configuration of large spheres in the resulting clusters when compared to spherical particles. However, for small clusters, the presence of the small spheres could still significantly affect the phase behavior of the newly formed colloidal building blocks. For example, the small spheres will likely have a strong influence on the densest packing crystal phases for these cluster sizes.

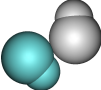
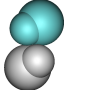
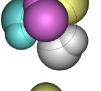
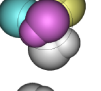
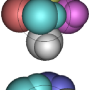
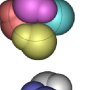
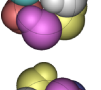
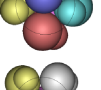
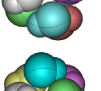
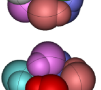
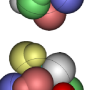
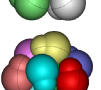
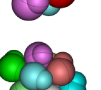
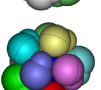
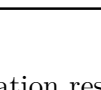
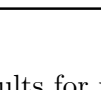
N	Sim.	M_2	Exp.	Exp.	Sph.
2					
3					
4					
5					
6					
7					
8					
9					
10					
11					
12					

Table 8.3: Comparison simulation results for wettable asymmetric dumbbells (size ratio 0.73) with experimental snapshots. The first column shows the number of dumbbells N in the cluster. The second column shows a typical configuration after the compression step, and the third column the resulting configuration after minimizing M_2 , using a mass ratio $m_S/m_L = 0.1\sigma_S^3\sigma^3$. The next two columns show experimental snapshots of two different clusters. Note that in both simulations and experiments, there are variations in the positions of the small spheres. The last column shows the packing of spherical particles that corresponds to the configuration of large spheres in the observed clusters.

8.4 Conclusions

In summary, we have investigated the effect of a shrinking spherical confinement on systems of both wettable and non-wettable colloidal particles, as a simple model for particles trapped in evaporating emulsion droplets. After compression, the second moment of the mass distribution M_2 of the obtained spherical packing was minimized. For spherical particles, this technique results in clusters that show good agreement with those found in earlier experimental studies. When applying the same method to symmetric colloidal dumbbells, we obtained clusters very similar to those in an experimental setup even before the M_2 minimization step, particularly for wettable particles. This suggests that the structures found for this system are mainly determined by the densest packing of dumbbells on a spherical surface.

For asymmetric dumbbells with size ratio $q = 0.73$, the larger spheres strongly dominates the process that shapes the cluster: in the resulting configurations the large spheres form the same structures as observed in clusters of spherical particles, while the small spheres can be found in a variety of configurations. To model this, a relatively small effective mass $m_S \ll m_L \sigma_S^3 / \sigma^3$ has to be assigned to the small spheres in the M_2 minimization step.

For almost all clusters considered, fixing the particles to the droplet interface during the compression step yields either the same results or a configuration in closer agreement with experimental snapshots. From the available experimental data, the model used appears to be able to give good qualitative predictions for possible structures of clusters formed in emulsion droplet evaporation experiments for particles consisting of one or more spheres.

8.5 Acknowledgements

I would like to thank Bo Peng for performing all of the experimental work on colloidal dumbbells discussed in this chapter.

Crystallization of colloidal spheres in evaporating emulsion droplets

The slow evaporation of emulsion droplets containing colloids or nanoparticles provides a straightforward method of producing compact clusters. The structure of the clusters resulting from this process is determined both by the bulk phase behavior of the particles and the confining effects of the droplet interface. In this chapter, we study crystallization of hard spheres in an evaporating droplet, modeled as a slowly shrinking spherical wall confining the cluster, and compare our results with experimental observations of clusters of nanoparticles. The orientation of the crystalline domains that appear in the cluster is strongly influenced by the presence of the confining wall, leading to frustrations between multiple domains that grow inward from the droplet interface to the center of the cluster. Suppressing surface ordering on the droplet interface by adding a long-range repulsive wall-particle potential limits cluster growth on the surface of the cluster and leads to much larger continuous crystal domains. Additionally, we investigate the effect of system size and square-shoulder repulsions between the particles on the crystallization process, but find no qualitative differences in the resulting crystal domains.

9.1 Introduction

Emulsion droplet evaporation has proven to be a useful experimental method for producing compact clusters of either colloids or nanoparticles. [185, 194–196] In the previous chapter, we investigated the structures formed by colloidal spheres and dumbbells on the surface of small evaporating emulsion droplets. The small number of particles ($N < 16$) on these droplets lead to largely monodisperse clusters for each cluster size with a well-defined shape. In this case, the behavior of the particles is dominated by the presence of the spherical confinement. In larger clusters, the bulk phase behavior of the particles starts to play an important role. In the limit of sufficiently large droplets, the influence of the droplet interface is negligible, and the behavior of the particles is determined by the slowly increasing density of the system. Assuming the evaporation rate is low enough to allow the particles to reach equilibrium during the evaporation of the droplet, the system will follow the bulk phase behavior of the particles. For example, if the colloids inside the droplets can be effectively described as hard spheres, we expect a face-centered-cubic (FCC) structure to appear at high densities, with possible stacking errors leading to random hexagonally close-packed (RHCP) structures. In a bulk system, these crystals would nucleate at random locations, but the presence of an interface can significantly affect the nucleation of crystals. In particular, it is well known that flat interfaces assist crystal formation, strongly increasing nucleation rates.[202] The same effect has been demonstrated for both concave and convex spherical surfaces with a sufficiently large radius of curvature compared to the particle diameter.[203] As a result, the presence of spherical confinement is expected to increase the rate of crystal nucleation at the edge of the droplet, potentially leading to multiple domains aligned with the droplet interface at different locations.

In this chapter, we investigate the crystallization of hard spheres confined in evaporating emulsion droplets modeled as a shrinking spherical confinement, using Event-Driven Molecular Dynamics (EDMD) simulations. We compare our results with experimental findings in systems of nanoparticles in droplets of cyclohexane suspended in an aqueous solution. In particular, we study the shape and size of the crystalline domains formed during the evaporation process, and investigate the effect of the number of particles on the resulting crystallinity. Additionally, we investigate the effect of a repulsive potential between the particles, and study the ordering of the spheres at the surface of the cluster.

9.2 Methods

We study the behavior of colloidal hard spheres with diameter σ in a shrinking spherical confinement, for system sizes in the range of 2000 to 64000 particles. The pair interaction of the particles is given by

$$\beta U^{HS}(r_{ij}) = \begin{cases} \infty, & r_{ij} < \sigma \\ 0, & r_{ij} \geq \sigma \end{cases}, \quad (9.1)$$

with r_{ij} the center-of-mass distance between particles i and j . In addition, we examine the effect of a square-shoulder repulsion potential U^{rep} added to the hard-sphere potential:

$$\beta U^{rep}(r) = \begin{cases} \epsilon, & r < q \\ 0, & r \geq q \end{cases}, \quad (9.2)$$

where q is the interaction range, ϵ denotes the height of the repulsive shoulder, and $\beta = 1/k_B T$ with k_B Boltzmann's constant and T the temperature of the system.

We employ Event-Driven Molecular Dynamics simulations, as described in Chapter 1. The diameter σ of the spheres is taken as our unit of length, and the mass m of the particles as the unit of mass. The time unit is $\tau = \sqrt{m\sigma^2/k_B T}$. The emulsion droplet interface is implemented as a hard spherical wall with a radius R that linearly decreases in time at rate v_R . The center of mass of each particle is confined to the spherical cavity by a wall-particle potential

$$\beta U^{wall}(r) = \begin{cases} \infty, & r \geq R \\ 0, & r < R \end{cases}, \quad (9.3)$$

with r the distance of the center of mass of the particle to the center of the cavity.

Simulations are started in a homogeneous random configuration at a low packing fraction $\eta = N\sigma^3/8R^3 \simeq 0.3$. Since crystallization is only expected to begin at significantly higher packing fractions, the system is first compressed relatively quickly to a higher packing fraction $\eta = 0.45$, well below the hard-sphere crystallization point at $\eta = 0.492$. [17] Snapshots of the system at this packing fraction did not show any sign of crystallization.

To keep the temperature of the system constant during compression, we use an Andersen thermostat: at regular intervals during the simulation, a random selection of particles are selected and given new velocities taken from a Boltzmann distribution. As the system approaches a jammed state, both the pressure and the amount of energy added to the system per time unit due to compression increase more and more rapidly. As a result, at some point the increase in temperature is faster than can be controlled by the thermostat, and the number of collisions per time unit diverges due to the faster movement of the particles, slowing down the speed of the simulation until it has effectively stopped. At this point, the simulation is ended, and we compare the final snapshots with experimental results.

To introduce wall-particle interaction in the system, spherical interfaces corresponding to steps in potential energy can be added to the system. In our simulations, we approximate several continuous wall-particle interaction potentials using 30 concentric spherical interfaces at distance R_i from the center of the cavity, with $i = 1, \dots, 30$. The interfaces are evenly spaced between the outermost shell at distance $R_{30} = R$ from the center, and the innermost shell at $R_1 = R - 4\sigma$. The outer interface still functions as a hard confinement, while the potential energy of a particle at a distance r from the center of the cavity is given by

$$\beta U^{wall}(r) = \begin{cases} \infty, & r \geq R \\ \epsilon_i^{wall}, & R_i < r < R_{i+1} \\ 0, & r < R_1 \end{cases}. \quad (9.4)$$

The values of ϵ_i^{wall} are based on a continuous particle-wall potential $V^{wall}(r)$, such that

$$\epsilon_i^{wall} = \beta V^{wall}(R_i) \quad (9.5)$$

We investigate the crystalline domains inside the cluster using the orientational bond-order parameter q_6 , as described in Chapter 7. The bond length cutoff was chosen to be $r_c = 1.4\sigma$, the bond order cutoff $d_c = 0.6$, and the minimum number of neighbors required

for a particle to be considered crystalline was $\xi_c = 7$. Additionally, crystalline domains are distinguished by the requirement that the dot product between the q -vectors of two particles in the same domain is at least $d_{dom} = 0.9$.

We compare our results to an experimental system of nanoparticles consisting of an iron oxide (FeO) core surrounded by a shell of iron cobalt oxide (CoFe_2O_4), which in turn is coated with a layer of surfactant (oleic acid). The surfactant layer functions like a soft shell preventing aggregation. These particles are synthesized according to the method described in Ref. [204]. The particles have a core diameter of 6.5 nm and a polydispersity of 2% (not including the soft shell, which makes them more monodisperse). Measurements in 2D images of crystalline domains give a typical interparticle distance of 9.5 nm. This would imply that the thickness of the soft shell is on the order of 1.5 nm, not taking into account the effects of compression. Additionally, we investigated larger particles with a core diameter of 18 nm.

To form clusters, we suspend 7 mg of nanoparticles in 2 ml of cyclohexane. This suspension is added to a mixture of 10 ml of purified water, 400 mg of Dextran (2M) and 70 mg of sodium dodecyl sulphate. The prepared solution is sheared at 7500 rpm at a radius of 2.5 cm with a space of 0.1 mm resulting in a nearly monodisperse emulsion. The emulsion is heated to 80°C for 4 hours to evaporate the cyclohexane and the remaining clusters are washed three times by centrifuging and redispersing in ultrapure water. Analysis was performed using a Tecnai20 electron microscope. The sample was deposited on a TEM-grid together with 18 nm gold markers, and cooled to -180°C using liquid nitrogen. The sample was then heated to -85°C under high vacuum in order to sublime the water and freeze dry the clusters. This was done to preserve the shape and structure of the clusters and to prevent capillary forces during drying. The images were taken after cooling the sample down again to a temperature of -180°C.

To analyze the crystal structure of the resulting clusters, we determined the 3D coordinates of the nanoparticles using electron tomography. Crystalline clusters are then detected using the same method as applied to the simulated clusters. To account for errors in the measurement of the particle positions, the cluster criterion is chosen to be less strict, using $\xi_c = 4$ and $d_{dom} = 0.85$.

9.3 Results

9.3.1 Colloidal hard spheres in a hard spherical cavity

To investigate the effects of the rate of compression on the cluster, we simulate systems of $N = 4000$ hard spheres inside a spherical shell, for a range of compression speeds v_R . Typical snapshots for a low compression speed $v_R = 10^{-5}\sigma/\tau$ are shown in Fig. 9.1. Different crystalline domains are indicated with different colors, with light blue denoting particles in a fluid environment. For compression speeds higher than $10^{-3}\sigma/\tau$, the amount of crystalline order is significantly less, as the system has less time to arrange into an ordered configuration during the compression. Varying the compression speed below $v_R = 10^{-4}\sigma/\tau$ does not significantly affect the resulting configuration.

When observing the crystallization of the cluster during the simulation, crystalline clusters are always seen to appear at the edge of the droplet, aided by the presence of

the confining interface. At packing fractions near the fluid coexistence density ($\eta_f = 0.492$ [17]), several crystalline layers are already observed at the edge, forming a basis for further crystal growth as the density of the system increases. As a result, crystals grow out more or less continuously with increasing density: no real nucleation effect is required for further crystallization, and the crystal grows inwards from multiple direction at once, resulting in several wedge-shaped crystalline domains with different orientations pointing towards the center of the cluster.

While the wedge-shaped domains are locally aligned with the wall, the curvature of the spherical surface frustrates the first two crystalline layers, causing these to become less ordered. Thus, in Fig. 9.1, the crystalline domains start several layers away from the droplet surface. This can be compared with a similar effect seen in nucleation of hard spheres at the interface of a convex spherical seed particle, where the resulting crystal nucleus was even seen to detach from the surface after a sufficiently large cluster size was reached. [203] We observed similar wedge-shaped domains in the experimental system, as shown on the left in Fig. 9.2. A typical electron microscopy snapshot is also shown.

In some of the clusters in both the experiments and simulations, the wedge-shaped clusters show signs of icosahedral symmetry. Figure 9.3 shows both a snapshot of a cluster of $N = 4000$ hard spheres and an experimental cluster. In both clusters, five-fold symmetry of the crystalline domains can clearly be seen from multiple directions. While not all domains are perfectly tetrahedral, they can be seen to form 20 roughly equal clusters arranged into an icosahedron.

While the interparticle and particle-wall interactions in the experimental system are not likely to be strictly hard-core, the qualitative agreement between experiments and simulations suggests that the structures formed in clusters produced via emulsion droplet evaporation can be modeled effectively by a simple hard-sphere approximation in at least some cases. As a result, we can use this model to study the effects of system size and wall-particle interactions on the structure of the cluster, and to study the ordering of particles on the cluster surface in more detail.

In clusters containing more particles, the larger radius of curvature of the droplet surface allows the orientation of the crystal to change direction more or less continuously around almost the entire crystal surface, as shown in Fig. 9.4 for clusters of $N = 10000$ and 64000 particles. This effect appears to be stronger for larger clusters. In addition, the number of crystalline layers formed near the droplet edge before the crystal domains extend further inwards is larger than in smaller clusters. However, the frustrations caused by the surface curvature still lead to disordered areas within the cluster. During compression, the crystallization progresses slowly from the droplet interface towards the middle as the packing fraction increases. For these larger clusters, no icosahedral symmetry was observed.

We investigated the ordering of particles on the surface of the cluster by performing Delaunay triangulation to determine the number of nearest neighbors of each particles.[205] In this analysis, a particle was considered to be on the droplet surface if its center of mass was less than half of the particle diameter away from the surface ($r > R - \sigma/2$). In Fig.9.5, we show snapshots of clusters where the surface particles are colored based on the number of nearest neighbors. Most particles have 6 neighbors (purple), but defects of particles with 4 (yellow), 5 (pink) or 7 (red) neighbors can be seen as well. For

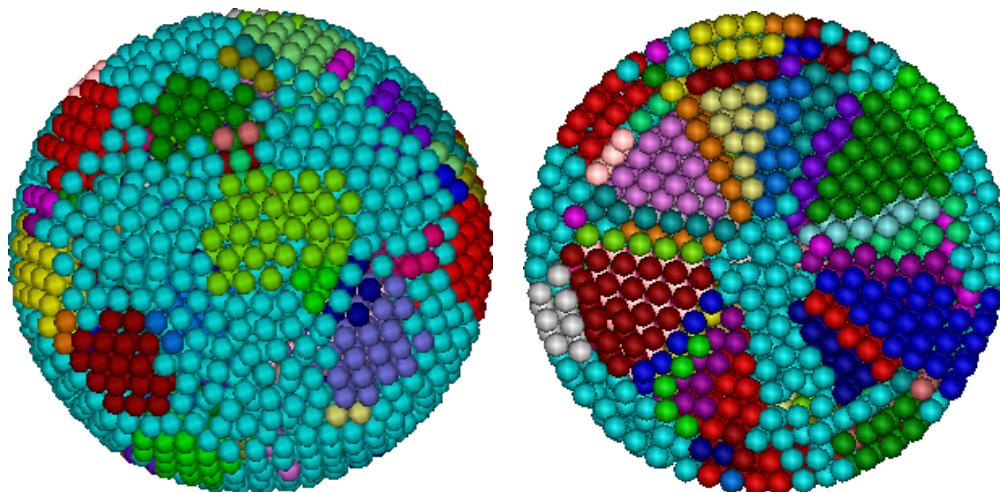


Figure 9.1: Typical configurations of $N = 4000$ hard spheres compressed in a hard spherical cavity at a compression rate $v_R = 10^{-5}\sigma/\tau$ obtained from EDMD simulations. The picture on the left shows the outside of the cluster, while the picture on the right shows a cut through the middle of the cluster, with the different colors showing different wedge-shaped crystalline domains. Particles identified as fluid-like are colored light blue.

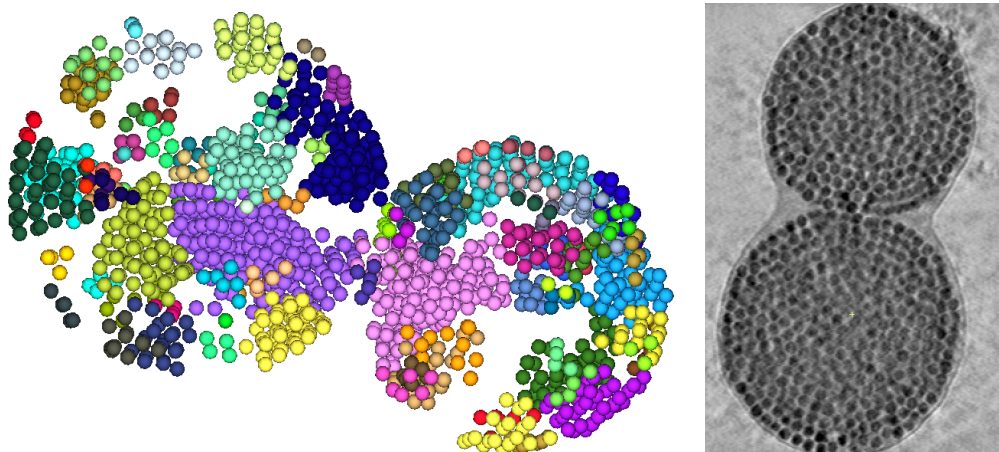


Figure 9.2: Left: Crystalline domains found experimentally in two clusters of nanoparticles with a core diameter of 18 nm, after evaporating the emulsion droplet. Only the particles that are part of a crystalline domains are shown. **Right:** Typical electron microscopy image of two clusters of nanoparticles. The clusters are around 320 nm in diameter.

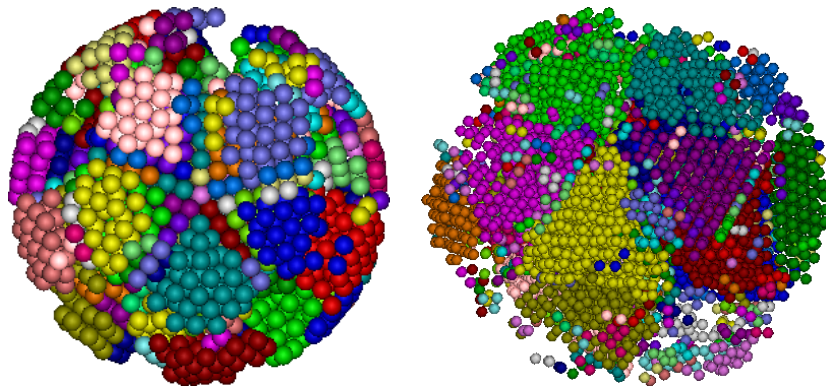


Figure 9.3: Icosahedral symmetry in a cluster of $N = 4000$ hard spheres compressed in spherical confinement (left) and an experimental cluster of nanoparticles with a core diameter of 7 nm (right). The five-fold symmetry is visible from many directions. Only particles that are part of a crystalline cluster are shown.

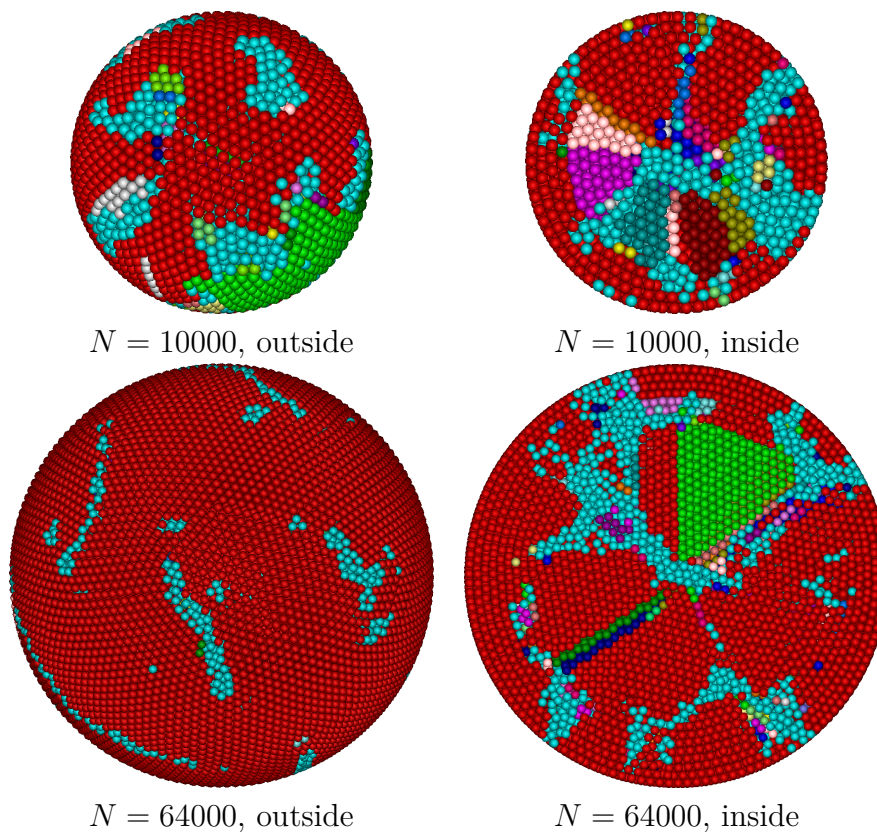


Figure 9.4: Left: Typical configurations in a system of $N = 10000$ (top) and $N = 64000$ (bottom) hard spheres compressed in a hard spherical cavity at a compression rate $v_R = 10^{-3}\sigma/\tau$, obtained from EDMD simulations. In this case, a large crystalline domain (red) changes orientation continuously over the entire surface of the cluster, and grows inward at multiple locations with different orientations. The pictures on the left show the outside of the clusters, while the pictures on the right show a cut through the middle of the clusters, with the different colors showing different crystal domains.

larger clusters ($N = 10000$ and 64000), these defects are clustered in 12 roughly evenly spaced locations over the spherical surface. For comparison, the bottom right picture shows the surface ordering on a hollow spherical shell, where the particles were confined to the droplet surface by a strong wall-particle square well attraction with a well width of 0.1σ . In this case, long scars of particles with alternately 5 or 7 neighbors can be seen at several points on the sphere. Both the formation of these scars and the necessity of forming at least 12 surface defects are well-known behavior for spherical packings of spheres [206]. It is interesting to note that a cluster with icosahedral symmetry would also lead to at least 12 evenly spaced defects, as an icosahedron has 12 points where five domains touch.

Depending on the system, strong attractions between the particles and the droplet interface can occur in experiments. In some cases, the droplet evaporation can even result in hollow shells of particles, indicating that the particles are firmly adsorbed to the interface between the two solvents. If we introduce a sufficiently strong, short-ranged attractive potential between the wall and the particles in our simulations, the same behavior can be observed. Here, the attractive force is modeled by a square well attraction with width of 0.1σ and a well depth that is sufficiently large to prevent particles from escaping. Particles form a single layer at the interface, resulting in an ordered hexagonal pattern after compression.

9.3.2 Colloidal hard spheres in a spherical cavity with a repulsive wall-particle interaction

In some experimentally observed droplets of nanoparticles, we also observe domains that span a much larger part of the cluster. While it is not clear why the experimental system is more ordered in these cases, it is important to note that neither the particle-wall nor the particle-particle interactions are perfectly hard in the experimental system. To investigate the effects of this, we performed simulations where the particles were repelled from the droplet interface. When the continuous wall-particle repulsion is short-ranged ($V^{wall}(r) \propto \sigma^n / (R - r)^n$, with $n \geq 2$), the resulting clusters are not significantly affected, and contain the same wedge-shaped crystal domains. However, in the case of a long-range interaction ($\beta V^{wall}(r) = 32\sigma / (R - r)$), the effects of the interface on nucleation are suppressed and wedge-shaped domains no longer form. Instead, the orientation of the crystalline order is often constant throughout the cluster, although cases with two or three domains are seen as well. An example is shown in Fig. 9.6. In this case, nucleation at the droplet interface is suppressed sufficiently to allow a single nucleus to grow to the size of the droplet before more crystal domains can form.

9.3.3 Colloidal hard spheres in a hard spherical cavity with repulsive particle-particle interactions

To investigate the possible effects of steric repulsions between the spheres, we performed EDMD simulations on hard particles interacting with a square-shoulder interaction potential, as described above. Figure 9.7 shows the resulting configurations of a cluster of $N = 4000$ particles, with a shoulder width of $q = 0.05\sigma$. No qualitative differences in

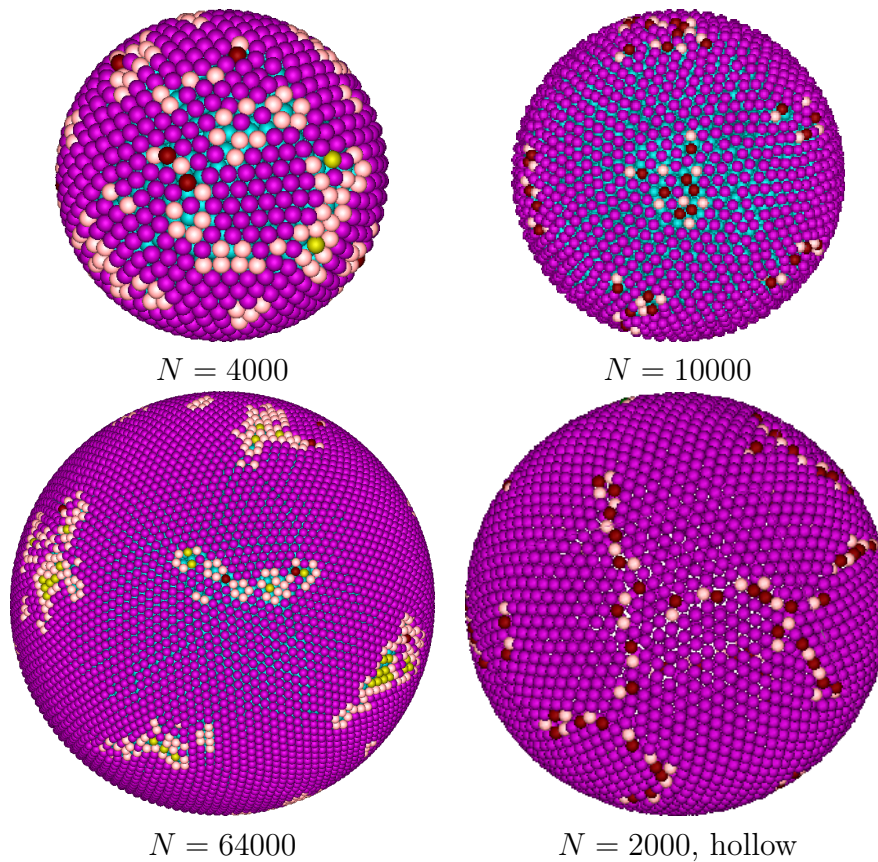


Figure 9.5: Surface order in clusters of hard spheres in compressed in hard spherical confinement, with $N = 4000, 10000,$ and 64000 particles. For comparison, a hollow cluster of $N = 2000$ particles with strongly attractive wall-particle interactions is also shown. The colors denote the number of neighbors in the Delaunay triangulation. Purple particles have 6 nearest neighbors on the surface, while defects most commonly lead to particles with 4 (yellow), 5 (pink) and 7 (red) neighbors.

the resulting domains was observed for a range of shoulder heights $0.5 < \epsilon < 5$, and for shoulder widths $q/\sigma = 0.02, 0.05$ and 0.1 . While it is possible that smoother potentials significantly affect the crystallization process in the cluster, the formation of wedge-shaped domains appears to be at least insensitive to the pair potentials tried here.

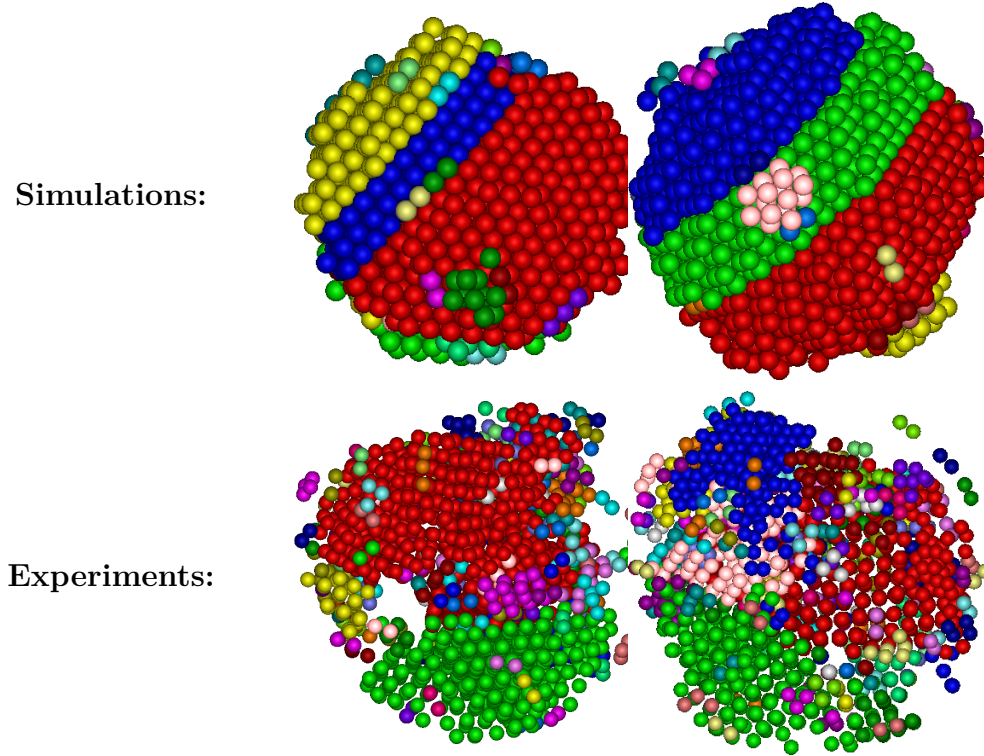


Figure 9.6: Crystalline domains in clusters obtained from simulations (top two pictures) and experiments (bottom two pictures). For the simulations, $N = 4000$ hard spheres were compressed with a long-range repulsive wall-particle interaction $\beta V^{wall} \propto 1/r$ and compression rates $v_R = 10^{-4}\sigma/\tau$ (left) and $10^{-5}\sigma/\tau$ (right). In all snapshots, different colors denote different crystalline domains, and only the particles identified as solid-like are shown. The experimental clusters consisted of nanoparticles with a core diameter of 7 nm.

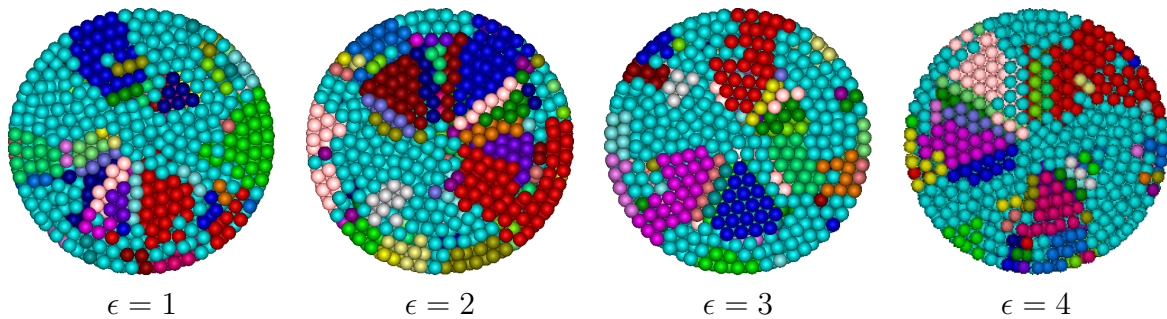


Figure 9.7: Crystalline domains in systems of $N = 4000$ hard spheres interacting with a square shoulder repulsion in a hard spherical cavity, with $\epsilon = 1$ (left), 2, 3, and 4 (right). No qualitative differences in the domains was observed.

9.4 Conclusions

In summary, we have investigated the effect of shrinking spherical confinement on systems of colloidal hard spheres, as a simple model for particles trapped in evaporating emulsion droplets. In the presence of a hard confining interface, crystallization in the clusters always starts at the surface of the cluster, leading to crystalline order with different orientations along the droplet edge. In sufficiently small systems ($N \simeq 4000$), the domains change orientation discontinuously, leading to wedge-shaped crystalline domains growing inward from the surface. These domains show good qualitative agreement with those seen in experiments on droplets containing nanoparticles. In both experiments and simulations, icosahedral ordering of tetragonal domains was observed. In simulations of clusters containing more particles ($N = 10000$ or larger), the larger spherical confinement allows the hard-sphere crystal to change orientation continuously, leading to a large crystalline domain in the shape of a spherical shell, which grows inwards at several points with different orientations. Even in this case, the internal part of the cluster shows a large degree of disorder, and icosahedral ordering of the crystalline domains was not observed for these larger clusters. Larger clusters do show a more ordered surface, with defects in the surface ordering often largely restricted to twelve evenly spaced clusters. In small clusters, this surface order is destroyed by the domain boundaries of the underlying crystalline structure.

If a long-range repulsion between the droplet interface and the particles is implemented in the simulations, the internal order of the generated clusters increases significantly. This soft potential almost completely prevents ordering of particles on the surface during compression, making crystallization along the surface much more difficult than in the case of a hard wall or short-ranged repulsion. As a result, crystallization occurs at only a single location in the cluster, leading to a much larger degree of crystalline order in the resulting crystal. In the experiments these more ordered clusters appear to be more common in systems with smaller nanoparticles. It is likely that any interactions with the droplet interface are also relatively longer ranged in this case: in the case of smaller particles both the size of the surfactants in the system and the range of any electrostatic interactions are larger compared to the size of a single nanoparticle.

Finally, we investigated the effects of square shoulder repulsions between the spheres, but found no significant differences in the resulting crystalline domains for the parameter range we studied. While more complex interactions could influence domain formation, our simulations suggest that the most direct route of influencing crystallization in clusters formed via emulsion droplet evaporation involves changing the interactions between the particles and the droplet surface.

9.5 Acknowledgements

I would like to thank Bart de Nijs for performing the experiments on nanoparticles discussed in this chapter.

Colloidal micelles from asymmetric hard dumbbells

In colloidal systems, effective depletion attractions between particles can be induced by the addition of depletants to the suspension. These interactions can be suppressed by a rough surface coating of smaller particles. In the case of colloidal dumbbells consisting of one smooth sphere and one coated sphere, the depletion attractions are effectively limited to the uncoated spheres. The resulting interactions can induce the formation of clusters, but the aggregation is hindered by the presence of the non-interacting spheres. This causes the dumbbells to self-assemble into micelle-like clusters, with the attractive parts in the center and the rough spheres on the edges. Hence, the particles can act as a simple model system for surfactants. In this chapter, we study cluster size distributions in these systems using both Monte Carlo simulations and free-energy calculations, and compare the results to distributions measured in an experimental system. Direct Monte Carlo simulations starting from a homogeneous state give rise to cluster distributions that are in good agreement with those found in experiments. However, it is clear that these simulations do not reach full equilibrium, as the slow exchange of particles between clusters gives rise to extremely long equilibration times. Our free-energy calculations demonstrate that the equilibrium size distribution shows a strong preference for specific cluster sizes larger than those that readily form via self-assembly, suggesting strong non-equilibrium effects on the clusters arising in these systems.

10.1 Introduction

Due to recent advances in colloidal synthesis techniques, the variety of colloidal particles with anisotropic interactions has increased considerably. [4] These new colloids can be used as the colloidal building blocks for a wide range of structures. In particular, colloidal particles with site-specific interactions, so-called 'patchy particles' have received a large amount of attention over the last few years. [15, 207] Patchy particles have already been shown to give rise to interesting phase behavior, leading to both clusters and crystals with structures that can be tuned by modifying the number and positions of the patches on each colloid, [16, 49, 208, 209] as well as equilibrium gel-like structures. [210] A special case of these patchy particles is formed by particles with only a single attractive patch.

Spherical colloids of this type, often referred to as Janus particles, have already been shown to form both micelle-like and vesicle-like structures. [211, 212]

In this chapter, we investigate asymmetric colloidal dumbbells where the smaller sphere in each particle acts as a single attractive patch as a result of depletion interactions. By giving the surface of the larger spheres a rough coating, all depletion interactions aside from those between the smaller spheres are strongly suppressed, effectively leaving only specific attractions between the smaller smooth spheres. As a result, these particles form clusters that resemble micelles formed by surfactant molecules: the smooth spheres are positioned on the inside of the cluster and surrounded by a layer of the larger rough spheres. The size of these clusters is strongly determined by the geometry of the dumbbells: in the absence of rough spheres, clusters could grow without limit, and any attractions sufficiently strong to cause significant cluster formation would lead to a phase separation in the system. In the case of dumbbells, however, adding more particles to the cluster also increases the number of purely repulsive rough spheres on the outside of the cluster. These rough spheres in turn limit the number of bonds that a smooth particle can form and reduce the freedom of movement of the other large spheres in the cluster, making larger clusters less favorable. As this effect is stronger for relatively larger rough spheres, more asymmetric dumbbells tend to form smaller clusters.

We study the cluster sizes and shapes formed in systems of these dumbbells using free-energy calculations, and compare them with those seen in experiments, as well as with direct simulations starting from a homogeneous initial configuration. In particular, we investigate the effect of colloidal number density, interaction range, interaction strength, and dumbbell size ratio on the clusters formed in equilibrium, and the effects of the dynamics of the system on the formation of these clusters.

10.2 Theory

10.2.1 Free-energy calculations

We consider a system of N dumbbells in a volume V at temperature T . These dumbbells interact with hard-core interactions and depletion attractions and tend to form micelles under the constraint that the total number of dumbbells satisfies

$$N = \sum_{n=1}^{\infty} N_n, \quad (10.1)$$

where N_n is the number of micelles consisting of n dumbbells. For sufficiently dilute micelle fluids the system can be modeled as an ideal gas of clusters, non-interacting but capable of exchanging particles. This allows us to write the canonical partition function $Z(N, V, T)$, as:

$$Z(N, V, T) = \prod_{n=1}^{\infty} \frac{Q_n^{N_n}}{N_n!} \quad (10.2)$$

$$Q_n = \frac{1}{(4\pi)^n \Lambda^{3n}} \int_V d\mathbf{r}^n \int d\omega^n \exp(-\beta U(\mathbf{r}^n, \omega^n)) c(\mathbf{r}^n), \quad (10.3)$$

where Q_n is the internal configurational integral of a cluster of n dumbbells, $\beta = 1/k_B T$ with k_B Boltzmann's constant, Λ^3 is the thermal volume of a dumbbell particle, \mathbf{r}^n denotes the positions of the attractive spheres of the dumbbells in the cluster, and ω^n the orientations of the dumbbell particles. The function $c(\mathbf{r}^n)$ equals 1 if the smooth spheres at positions \mathbf{r}^n form a single cluster and is 0 otherwise. We consider two particles to be part of the same cluster if their smooth spheres are close enough to attract each other. Since the partition function for a monomer is $Q_1 = V/\Lambda^3$, we can rewrite Eq. 10.3 as:

$$Q = \prod_{n=1}^{\infty} \frac{(V/\Lambda^3)^{N_n}}{N_n!} \left(\frac{Q_n}{Q_1} \right)^{N_n} \quad (10.4)$$

Here, Q_n/Q_1 is the ratio of the partition function of a cluster of n particles to that of a cluster of a single particle. Due to the restriction that the cluster be connected, this no longer depends on the volume of the box, as long as V is large enough to accommodate any cluster. The Helmholtz free energy reads:

$$F(N, V, T, \{N_1, \dots, N_n\}) = -k_B T \log Z(N, V, T) \quad (10.5)$$

$$= \sum_{n=1}^{\infty} N_n k_B T \left[\log \left(\frac{N_n}{V} \Lambda^3 \frac{Q_1}{Q_n} \right) - 1 \right] \quad (10.6)$$

For an ideal gas of these particles, with only clusters of size 1, the Helmholtz free energy reduces to that of an ideal gas of monomers $\beta F/N = \log(\rho \Lambda^3) - 1$, with $\rho = N/V$ the particle density.

The ratio Q_n/Q_1 can be measured using a grand-canonical (μVT) Monte Carlo simulation (GCMC).[213] By imposing the constraint of having only a single cluster in a GCMC simulation, the probability $P(n)$ of observing a cluster of size n reads:

$$\frac{P(n)}{P(1)} = \frac{Q_n}{Q_1} \exp[\beta \mu (n - 1)], \quad (10.7)$$

Hence, the ratio Q_n/Q_1 can be directly obtained for all n from the GCMC simulation. In principle, Q_n/Q_1 is independent of μ , although simulations at different values of μ can be used to sample all cluster sizes. We can now minimize the Helmholtz free energy functional $F(N, V, T, \{N_1, \dots, N_n\})$ of the cluster gas with respect to the distribution N_n , while satisfying the normalization constraint 10.1:

$$\frac{\partial}{\partial N_n} \left(F - \mu \sum_{n=1}^{\infty} n N_n \right) = \mu_n - \mu_0, \quad (10.8)$$

with $\mu = \mu_1$ a Lagrange multiplier. This yields:

$$\mu_n = \left(\frac{\partial F}{\partial N_n} \right)_{V, T, N_1, \dots, N_{n-1}, N_{n+1}, \dots} = k_B T \log \left(\frac{N_n}{V} \Lambda^3 \frac{Q_1}{Q_n} \right) \quad (10.9)$$

Combining Eqs. 10.8 and 10.1 gives

$$\rho_n \Lambda^3 = (\rho_1 \Lambda^3)^n \frac{Q_n}{Q_1} \quad (10.10)$$

with ρ the overall particle density in the system and ρ_n is the number density of clusters of size n . The resulting polynomial equation in $\rho_1 \Lambda^3$ has only one solution for $\rho_1 \geq 0$, which depends continuously on ρ . In other words, no phase transitions will occur.

10.2.2 Critical micelle concentration

As is generally the case for adsorption equilibria and micelle-like systems, the monomer density ρ_1 as a function of the particle density crosses over from a linear regime to a nearly constant value as the density increases. As an example, consider a system where only one cluster size appears consisting of n particles. Inserting Eq. 10.10 into 10.1 gives:

$$\rho_1 \Lambda^3 + n \rho_1^n \Lambda^{3n} \frac{Q_n}{Q_1} = \rho \Lambda^3. \quad (10.11)$$

This can be rewritten as:

$$\frac{\rho_1}{\rho_0} + n \left(\frac{\rho_1}{\rho_0} \right)^n = \frac{\rho}{\rho_0}, \quad (10.12)$$

where

$$\rho_0 \equiv \left(\frac{Q_n}{Q_1} \right)^{1/(n-1)} \Lambda^{-3}. \quad (10.13)$$

When the density of the system is low, i.e. $\rho \ll \rho_0$, the density of monomers is approximately equal to the system density, as the second term in Eq. 10.12 is negligible compared to the first one. In this regime, the entropy the particles lose by bonding is much larger than the potential energy difference gained by forming a cluster. However, for larger densities clusters appear, and the density of monomers will be more or less constant. The crossover density between these regimes is often referred to as the critical micelle concentration (cmc). For sufficiently large micelles ($n \gg 1$), the density of monomers is approximately equal to the cmc when $\rho \gg \rho_{cmc}$. While the density ρ_0 defined here is a good indication of the critical micelle concentration, calculation of the cmc becomes more difficult in systems with an equilibrium between multiple cluster sizes, such as the one studied here. In addition, due to the relatively small cluster sizes ($n < 30$) considered here the density of monomers continues to increase slowly as a function of density even if the majority of the system consists of dumbbells, without reaching a clear limiting value that could be used as a cmc.

In this chapter, we use a commonly used definition of the cmc that corresponds to the point where exactly half of the particles in the system are part of a cluster. Thus, at $\rho = \rho_{cmc}$, $\rho_1 = \rho/2$. As an additional clustering criterion, we also determine the heat capacity as a function of the interaction strength ϵ . The heat capacity at constant volume $c_V = (dU/dT)_V$ corresponds to the change in energy if the temperature increases by a small amount. In the regime where the number of clusters increases strongly with decreasing temperature, the heat capacity is maximal. In our system, a decrease in the temperature is equivalent to an increase in the interaction strength ϵ , as ϵ is measured in units of $k_B T$. Thus, $c_V \propto - \left(\frac{dU}{d\epsilon} \right)_V$, and a maximum in the heat capacity corresponds to a minimum in $(dU/d\epsilon)_V$. By combining measurements of the average potential energy per cluster size from GCMC simulations with the cluster size distribution, we can calculate the total potential energy per particle for different values of ϵ , and find the maximum in the heat capacity.

10.3 Model and methods

10.3.1 Interactions

The particles are modeled by hard-core asymmetric dumbbells with only depletion attractions between the smooth sides. Any remaining depletion interaction between the rough spheres, and any charges on the particles are neglected. For the hard-core interactions, the rough and smooth spheres have diameters σ_R and σ , respectively, and are a distance d apart. The rough spheres only interact with other spheres (smooth or rough) via hard-core interactions. The depletion potential between the smooth spheres is given by [214, 215]

$$\beta U_{depl}(r) = \begin{cases} \infty, & r \leq \sigma \\ -\epsilon \frac{\frac{r^3}{2q^3} - \frac{3r}{2q} + 1}{\frac{\sigma^3}{2q^3} - \frac{3\sigma}{2q} + 1}, & \sigma < r \leq q \\ 0, & r > q \end{cases}, \quad (10.14)$$

where r is the distance between the small spheres of two dumbbells. The interaction potential is described by two parameters, an interaction range q and interaction strength ϵ . The range of attraction is $q = \sigma + \sigma_{pol}$, with σ_{pol} the diameter of the polymer responsible for the depletion interactions. For two smooth spheres in contact, the potential well depth is $\epsilon k_B T$, with ϵ given by

$$\epsilon = \phi_p \frac{\frac{\sigma^3}{2q^3} - \frac{3\sigma}{2q} + 1}{(q - \sigma)^3} q^3. \quad (10.15)$$

Here, $\phi_p = \pi \sigma_{pol}^3 N_{pol} / 6V$ is the packing fraction of polymers in a reservoir in chemical equilibrium with the system and N_{pol} is the number of polymers.

10.3.2 Direct simulations

We study this model using both direct Monte Carlo simulations and free-energy calculations. In the direct Monte Carlo simulations, we simulate a system of $N = 1000$ particles at constant density ρ and temperature T . We directly measure the cluster size distribution during the simulation. The initial configuration consists of particles with random orientations and positions, effectively leading to a system of monomers. The simulation is then equilibrated for at least 10^7 MC cycles. To improve mobility of clusters with more than one particle, cluster moves are introduced which collectively move all particles that are part of the same cluster. Particles are considered to be part of the same cluster if the center-of-mass distance between their smooth spheres is less than the attraction range q .

10.3.3 Grand-canonical Monte Carlo

To measure the cluster free energies f_n , we simulate single clusters at constant chemical potential μ and temperature T , allowing only moves that result in a single cluster. In addition to performing normal translation and rotation moves, we insert and remove particles according to a standard GCMC scheme, but restrict the system to single clusters. The box volume has no influence on the outcome of the simulation, as insertions are only

accepted near the cluster. To prevent insertions too far away from the cluster, the trial insertion moves can in principle be restricted to a small region around the cluster, as long as no valid insertions (that would not result in more than one cluster) are excluded. While this could be done by restricting the insertions to a sufficiently large spherical volume around the center of mass of the cluster, a better solution is to only insert particles inside the attractive wells of particles already in the cluster.

Ideally, we would like to attempt insertions such that the center of the smooth sphere of the new particle is restricted to a volume v_w , corresponding to the union of all attractive wells in the cluster. The attractive well for each particle is the spherical shell where the distance r to the center of the smooth sphere satisfies $\sigma < r < q$. Any insertions outside this volume would be rejected due to the single-cluster constraint, and are therefore not useful.

To generate a uniformly random position in v_w , we proceed as follows: when inserting a particle, we first randomly select a particle already present in the cluster. Subsequently, we choose a random location inside the attractive well of this particle for the center of the smooth sphere of the particle. However, as the attractive wells of multiple particles can overlap, the probability of attempting a particle insertion at a position where k wells overlap is biased by this method. To correct for this bias, an insertion move into k overlapping wells is only attempted with a probability $1/k$, and is otherwise rejected. Using this method, the probability of selecting a position for the trial particle that satisfies the single-cluster criterion is v_w/vn , where $v = \frac{4\pi}{3}(q^3 - \sigma^3)$ is the volume of the attractive well around one particle. Compared to inserting into a fixed volume of size V , this improves the acceptance of insertion moves by a factor V/nv . The position of the rough sphere is simply chosen by generating a random orientation for the particle.

To maintain detailed balance, the acceptance rules for insertion and deletion moves have to be modified slightly. We require that

$$P(n)\alpha(n \rightarrow n+1)\text{acc}(n \rightarrow n+1) = P(n+1)\alpha(n+1 \rightarrow n)\text{acc}(n+1 \rightarrow n), \quad (10.16)$$

where $P(n)$ is the probability of finding exactly n particles in the system, $\alpha(i \rightarrow j)$ is the probability of attempting a move that changes the number of particles from i to j , and $\text{acc}(i \rightarrow j)$ is the acceptance probability of such a move. In our simulation, the number of insertion and deletion moves in our simulations is the same. However, since the probability of choosing a valid location for a particle insertion is now larger by a factor V/nv , this is equivalent to increasing the number of particle insertions attempted by the same factor. Thus,

$$\alpha(n \rightarrow n+1) = \frac{V}{nv}\alpha(n+1 \rightarrow n). \quad (10.17)$$

In the grand-canonical ensemble, the probability density function $P(\mathbf{r}^n, \omega^n; n)$ for finding the system in a state with n particles at positions \mathbf{r}^n and with orientations ω^n is given by

$$P(\mathbf{r}^n, \omega^n; n) \propto \frac{\exp(\beta\mu n)V^n}{\Lambda^{3n}n!} \exp(-\beta U(\mathbf{r}^n, \omega^n))c(\mathbf{r}^n), \quad (10.18)$$

As a result, the acceptance probabilities for inserting and removing particles should obey

$$\frac{\text{acc}(n \rightarrow n+1)}{\text{acc}(n+1 \rightarrow n)} = \frac{vn \exp(\beta\mu)V}{V \Lambda^3(n+1)} \exp(-\beta[U(\mathbf{r}^{n+1}, \omega^{n+1}) - U(\mathbf{r}^n, \omega^n)]), \quad (10.19)$$

with the additional constraint that the particles should still form a single cluster after the insertion or deletion. This leads to the following acceptance rules for particle insertion and deletion:

$$\begin{aligned} \text{acc}(n \rightarrow n+1) &= \min \left[1, \frac{nv}{\Lambda^3(n+1)} \exp(\beta[\mu - U(\mathbf{r}^{n+1}, \omega^{n+1}) + U(\mathbf{r}^n, \omega^n)]) \right] \\ \text{acc}(n+1 \rightarrow n) &= \min \left[1, \frac{\Lambda^3 n}{nv} \exp(-\beta[\mu - U(\mathbf{r}^n, \omega^n) + U(\mathbf{r}^{n+1}, \omega^{n+1})]) \right] c(\mathbf{r}^n). \end{aligned} \quad (10.20)$$

Here, we have left out the constraint $c(\mathbf{r}^{n+1})$ in the case of particle insertion, as insertions are only performed on valid location. Note that the rejection of insertions into overlapping potential wells are not included in this acceptance rule.

In principle, the choice of μ in the GCMC simulations does not matter for the resulting probability distribution. However, in order to sample clusters of all relevant sizes properly, one can perform simulations at different values of μ . In practice, it is not straightforward to determine the value of μ that allows a good sampling of cluster sizes, and it turns out to be more practical to set μ to 0 and to use an Umbrella Sampling scheme to sample the cluster distribution.[17] An extra energy term $U_{US}(n) = k(n - n_0)^2$ is added to the potential energy function, which biases the cluster size n towards a target value n_0 . The probabilities $P_{bias}(n)$ measured in these simulations have to be corrected to obtain the unbiased probabilities:

$$P(n) \propto \exp(k(n - n_0)^2) P_{bias}(n), \quad (10.21)$$

with a proportionality constant depending on the target cluster size n_0 . From simulations with different values of n_0 the full probability distribution $P(n)$ can be calculated.

At high interaction strengths, reorganization of the cluster is a slow process, due to the number of bonds that have to be broken to reach a new configuration. To speed up equilibration and sampling, we employ the parallel tempering method.[17] In one simulation, we simulate a number of separate clusters at different interaction strengths ϵ . The different clusters do not interact in any way, but a new Monte Carlo move is introduced that swaps configurations of two different interaction strengths. The acceptance probability of such a move is only based on the difference in total energy, including the US potential. To maximize the acceptance of these swap moves, the centers of the US windows are tuned (during equilibration) such that all clusters contain roughly the same average number of particles.

10.3.4 Effective density

In our assumption that a fluid of micelles can be treated as an ideal gas of clusters, we slightly underestimate the density of larger clusters. Analogous to Wertheim theory, we can estimate a first-order correction by using the radial distribution function $g(r)$ of a of a system with only hard-core interactions (i.e. $\epsilon = 0$) at the same density. To do this, we assume that the system mainly consists of free dumbbells and calculate the effective

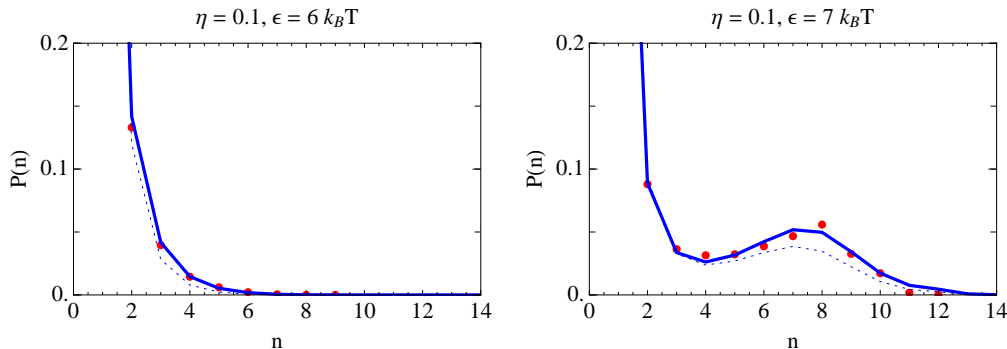


Figure 10.1: Comparison of cluster distributions calculated using free energy calculations (blue lines) with distributions from direct simulations (red points) at a packing fraction $\eta = 0.1$, interaction range $q = 1.1\sigma$ and interaction strength $\epsilon = 6 k_B T$ and $7 k_B T$. The solid lines show the calculated distributions after rescaling the density using Eq. 10.23. For the dashed lines the density has not been rescaled.

density ρ_{eff} of particles inside the potential well:

$$\rho_{eff} = \frac{\rho \int_{\sigma}^q dr r^2 g(r)}{\int_{\sigma}^q dr r^2} \quad (10.22)$$

$$\simeq \rho g(\sigma), \quad (10.23)$$

where in the second step we have assumed that $g(r)$ is approximately constant over the (short-ranged) attractive well. Hence, the excluded-volume effects in the system lead to a slightly higher effective density near the particles, and we expect that at least for systems dominated by monomers using the effective density ρ_{eff} rather than ρ should lead to better predictions of the cluster size distributions. In the limit of low densities, $\rho_{eff} \rightarrow \rho$.

We performed single-cluster simulations on rough-smooth dumbbells with size ratio $\sigma/\sigma_R = 0.5$, and compared the cluster distributions resulting from the calculated free energies to those found in direct simulations. The distance between the two spheres of each dumbbell was chosen such that the spheres touch and do not overlap, i.e. $d = (\sigma + \sigma_R)/2$. Figure 10.1 compares distributions from direct simulations (red points) with those from free-energy calculations both before rescaling (dashed blue lines) and after (solid blue lines), for interaction range $q = 1.1\sigma$ and packing fraction $\eta = 0.1$. For the interaction strengths shown, the rescaled version clearly results in a better prediction. At lower densities, the difference between the two lines decreases significantly. At higher interaction strength, equilibration issues in the direct simulations make comparisons more difficult.

10.3.5 Experimental system

We compare our results to the experiments performed by Kraft *et al.*[216] The experimental system consisted of polystyrene dumbbell particles synthesized following a modified method of Kim *et al.* [217] Spherical colloids with a diameter of $2.41 \mu\text{m}$ were synthesized, washed, and redispersed in an aqueous solvent. During this step, small polystyrene particles (0.18 nm in diameter) were adsorbed onto the colloid surface, forming a rough

coating. A spherical protrusion with a diameter of $1.11\mu\text{m}$ was then created on each particle using an overswelling method, leading to asymmetric dumbbell particles with a rough sphere diameter of $\sigma_R = 2.92\ \mu\text{m}$, a dumbbell size ratio of $\sigma/\sigma_R = 0.76$, and a total particle length of $4.9\ \mu\text{m}$, corresponding to a distance $d = 0.79\sigma$ between the spheres. To induce depletion interactions, dextran polymers were added at several concentrations. While NaCl was added to the system to screen the electrostatic interactions, some of the charge repulsion remains between the particles. As a result, it is difficult to calculate the effective interaction strength from the concentration of polymers. However, the size of the polymer ($\sigma_p = 38\ \text{nm}$) and the packing fraction of the system ($\eta = 0.003$) are known, and we expect that the electrostatic repulsions will mainly affect the effective strength of the interaction, without strongly influencing the behavior of the system. Thus, the interaction strength ϵ will be our only fitting parameter when comparing distributions from simulations or free-energy calculations to the experimental results.

10.4 Results

10.4.1 Size ratio 0.76

In order to compare with experimental results, we choose the size ratio between the smooth and rough spheres to be $\sigma/\sigma_R = 0.76$, at a distance $d = 0.79\sigma$ between the spheres. We performed single-cluster simulations to calculate cluster distributions for a range of interaction strengths ϵ and interaction ranges q . We measured the average cluster size as a function of these two parameters, at a fixed packing fraction $\eta = 0.003$ (corresponding to the packing fraction used in the experimental setup). As an illustration of the clusters formed, Fig. 10.2 shows both experimental and simulation snapshots of clusters up to size $n = 15$. Figure 10.3 shows the average cluster size as a function of interaction range q and interaction strength ϵ , as well as the most common cluster size in the distribution calculated from the free energy calculations. The points corresponding to the cmc (defined as the point where exactly half of all particles are part of a cluster) and the maximum in the heat capacity are denoted by a white and blue line, respectively. Despite small differences, both criteria provide good estimates of the interaction strength where clustering becomes significant. At this point, we observe a sharp crossover between a system consisting of only small clusters and systems dominated by large clusters with cluster size $n \simeq 20$. This is in sharp contrast with the distributions found in direct simulations, where the cluster distribution peaks around $n = 13$. We note that the direct simulations are in closer agreement with the experimental results at this size ratio. The left side of Figure 10.4 shows a comparison between cluster size distributions from experimental results (bars), direct simulations (black circles), and free-energy calculations (colored lines). In both types of simulations, the interaction range $q = 1.02\sigma$ and packing fraction $\eta = 0.003$ were chosen to match the experimental parameters. For the direct simulation, the interaction strength $\epsilon = 10\ k_B T$ was tuned to approximately match the first peak in the distribution function. The free-energy calculations are shown for a range of interaction strengths. While reasonable agreement between direct simulations and experiments can be seen, the free-energy calculations clearly predict either much larger clusters or no clusters at all. While the distribution is influenced by the interaction

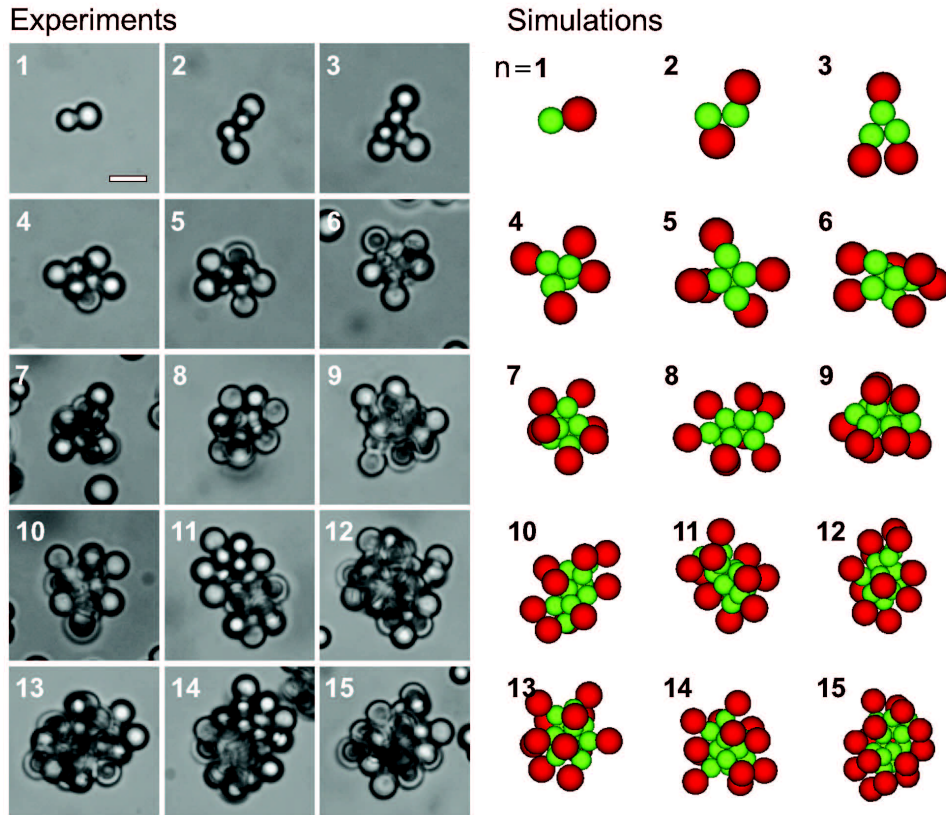


Figure 10.2: Comparison between experimental snapshots of clusters (left) and clusters seen in the direct Monte Carlo simulations (right).

strength, clusters around size 10 never appear in significant quantities. On the right, Fig. 10.4 shows the effect of the number density on the distribution. While the number of clusters formed strongly depends on the packing fraction, the peaks in the distribution do not shift. As Fig. 10.3 already suggests, varying the interaction range does not strongly influence the cluster size either.

While the MC simulation used to generate the distribution shown in Fig. 10.4 was allowed to equilibrate for 10^8 MC cycles, the potential energy of the system was still seen to decrease slowly over time. Clearly, the equilibration of cluster sizes in the system happens on timescales much longer than those that can reasonably be simulated directly. This also explains the marked difference between the direct simulations and free-energy calculations: the direct simulations have not yet reached equilibrium. While we do not have such clear indications of change over time in the experimental setup, the match between experiments and direct simulations strongly suggests that the experimental system is likely far out of equilibrium as well.

The reason for this slow equilibration can be found in the rate at which particles attach and detach from the clusters. The free-energy barrier between a monomer and larger clusters is shown in Fig. 10.5. While the free-energy barrier is $15 k_B T$ in height, making the growth from cluster size 1 to 20 a rare event, it is important to note that

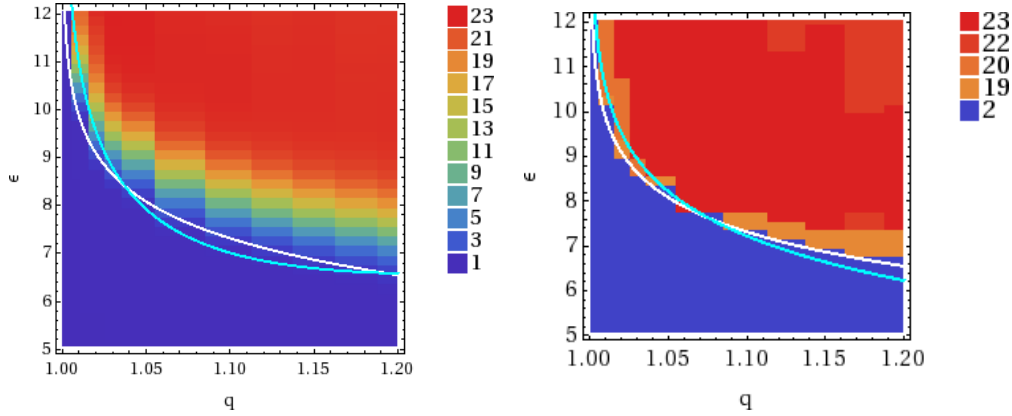


Figure 10.3: **Left:** Average cluster size as a function of the interaction range q and interaction strength ϵ , for size ratio $\sigma/\sigma_R = 0.76$, and packing fraction $\eta = 0.003$. **Right:** Most common cluster size (ignoring monomers) as a function of the q and ϵ for the same system. In both plots, the white and blue lines (here nearly on top of each other) show the cmc and the maximum of the heat capacity, respectively.

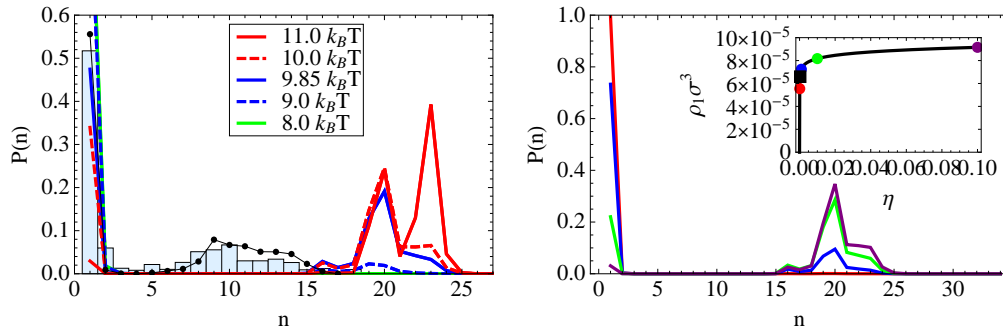


Figure 10.4: **Left:** Comparison of experimental results (bars) and direct simulations (\bullet) with equilibrium cluster size distributions of dumbbells consisting of a rough and a smooth sphere with size ratio $\sigma/\sigma_R = 0.76$, packing fraction $\eta = 0.003$ and polymer size $\sigma_p/\sigma = 0.02$. In the direct simulations, $\epsilon = 10 k_B T$, and for the free-energy calculations ϵ varies from $\epsilon = 8$ to $11 k_B T$, denoted by the colored lines. **Right:** Cluster size distribution for the same system, with the interaction strength fixed at $\epsilon = 9.85 k_B T$, at four different packing fractions $\eta = 0.0001, 0.001, 0.01$, and 0.1 . The inset shows the monomer concentration as a function of the packing fraction, with the colored dots indicating the points corresponding to the distributions in the main figure. The black square denotes the cmc, where exactly half of the dumbbells are part of a cluster.

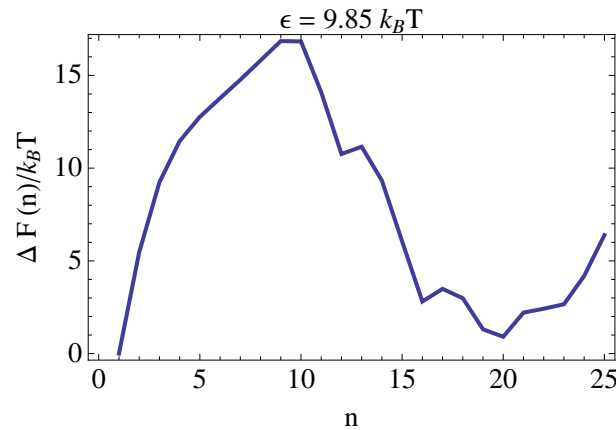


Figure 10.5: Free-energy barrier between small and large clusters, at $\epsilon = 9.85$ and $q = 1.02\sigma$. For this interaction strength, the chemical potential corresponds to the experimental packing fraction $\eta = 0.003$.

the diffusion of even a single dumbbell in or out of a cluster is a slow process as well. To attach to a cluster, the smooth part of a dumbbell has to come within a very short distance of the attractive core of that cluster, which is surrounded by repulsive rough spheres. Since moving the new dumbbell into this outer shell restricts the movement of all nearby particles, the accompanying entropy loss effectively forms an additional free-energy barrier between two consecutive cluster sizes, which becomes higher for increasing cluster size. Conversely, to remove a particle from a cluster, a large potential energy barrier has to be overcome due to the breaking of one or more bonds. For larger clusters, removing a particle from a cluster requires the breaking of at least three bonds, if not more. As this corresponds to a potential energy barrier on the order of $30 k_B T$, this is an extremely rare event. The slow process of adding or removing a particle from a cluster is likely responsible for the slow equilibration of the direct simulations: while small clusters up to size 10 are quickly formed, the timescale required to reach a cluster of 20 particles is simply prohibitively long.

Snapshots of clusters of the most common sizes in the equilibrium distributions are shown in Fig. 10.6. Cluster size 22 corresponds to a very low potential energy due to the large number of bonds per particle. However, as the rough spheres have very little freedom of movement the entropy of such a cluster is low as well. As a result, this type of cluster only appears at very high interaction strength ϵ . The structure of these larger clusters is generally based on one or more tetrahedral structures of smooth spheres, with three spheres at each edge of the tetrahedron. These are shown in pink in the figure. In principle, this type of structure can be extended indefinitely, with each smooth sphere in contact with on average 7.5 other smooth spheres. The shape of such a structure is shown in Fig. 10.7. By reducing the number of tetrahedrons in the structure, and removing the edge particles with only 3 neighbours, the resulting clusters match the lowest-energy clusters observed for sizes 16, 20, 24, and 28. However, particularly for larger clusters, these structures are extremely difficult to form both in experiments and direct simulations.

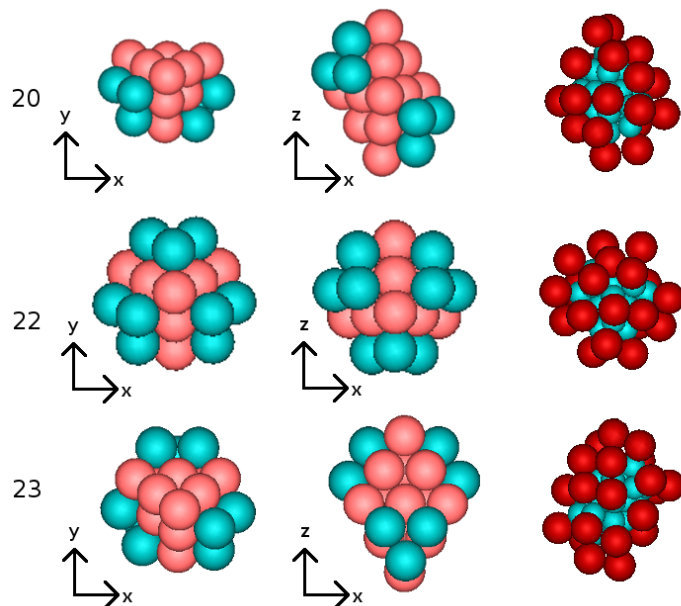


Figure 10.6: Snapshots of the most commonly seen configurations of micelles of size $n = 20$, 22, and 23, in a system of dumbbells with size ratio $\sigma/\sigma_R = 0.76$. The two first columns show the clusters from two angles, with the rough spheres hidden. In the column on the right, the red spheres are the rough spheres, and the blue spheres are smooth.



Figure 10.7: Candidate for the shape of lowest potential energy clusters as the cluster size increases. Discounting boundary effects, each sphere has 7.5 neighbours on average.

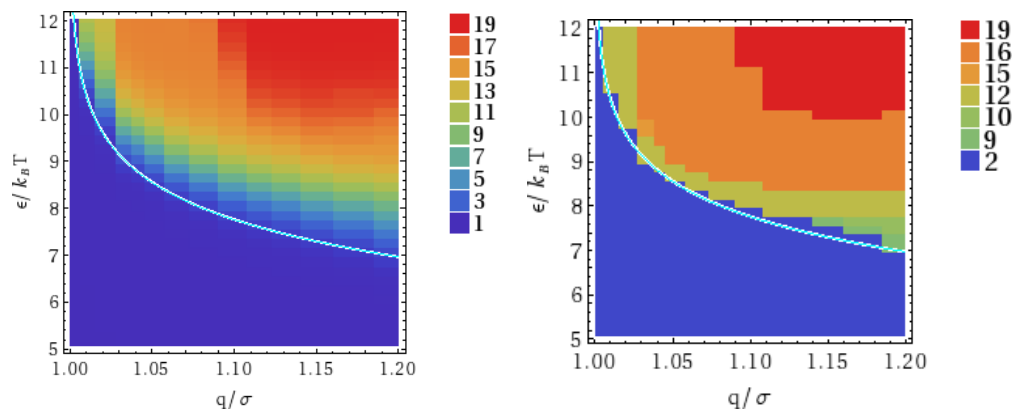


Figure 10.8: **Left:** Average cluster size as a function of the interaction range q and interaction strength ϵ , for size ratio $\sigma/\sigma_R = 0.5$, and a packing fraction of $\eta = 0.01$. **Right:** The most common cluster size in the same system, ignoring monomers. In both plots, the white and blue lines (now nearly on top of each other) show the cmc and the maximum of the heat capacity, respectively.

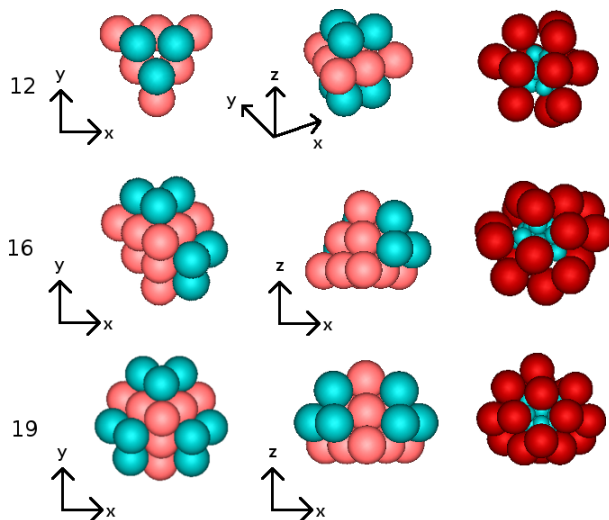


Figure 10.9: Snapshots of the most common configurations of micelles of size $n = 12, 16,$ and 19 , in a system of dumbbells with size ratio $\sigma/\sigma_R = 0.5$. The two first columns show the clusters from two angles, without the rough spheres. In the column on the right, the rough spheres are denoted by the red spheres and the smooth spheres by the blue ones.

10.4.2 Size ratio 0.5

As seen in the previous section, changes to either the interaction details or the dumbbell density can be used to influence the amount of clustering in the system, while the cluster sizes that appear are largely unaffected by these parameters. However, as we will demonstrate in the remainder of this chapter, the geometry of the dumbbell particles does have a strong influence on the cluster size distribution, by changing the preferred curvature of the micelle surface. A similar effect was seen in the study of clusters of cone-shaped particles, where larger cone angles were shown to lead to smaller cluster sizes.[218] Similarly, for the dumbbells investigated in this chapter, larger rough spheres will stabilize smaller micelles. In this section, we study the clusters formed in systems of dumbbells with a size ratio of $\sigma/\sigma_R = 0.5$. The distance between the two spheres was chosen to be $d = (\sigma + \sigma_R)/2$. Figure 10.8 shows the average and most common cluster sizes as a function of the interaction range q and interaction strength ϵ , for a fixed packing fraction $\eta = 0.01$. In this case, the system clearly favors clusters of sizes $n = 12, 16$ and 19 . The most common configurations are shown in Fig. 10.8, both with and without the rough spheres. The interior of the clusters shows crystalline order, increasing the number of bonded pairs of spheres in the cluster. The rough spheres still have a large amount of freedom of movement for most clusters, although some order is seen in the cluster of size $n = 19$.

10.4.3 Size ratio 0.3

For size ratio $\sigma/\sigma_R = 0.3$, the rough spheres severely limit the number of particles in a cluster, and clusters larger than size $n = 8$ are rare. Figure 10.10 shows the average cluster size as a function of the interaction range q and interaction strength ϵ , as well as the most common cluster sizes. For this size ratio, the particles mainly formed clusters of size $n = 6$ or 7 , with structures typically corresponding to those also seen in small clusters of attractive spherical particles. In particular, the smooth spheres in the clusters shown in Fig. 10.11 are in a configuration that minimizes the potential energy for spherical particles with short-ranged interactions. [219]

10.5 Discussion

Using Monte Carlo simulations, we have studied the cluster size distribution for a system consisting of dumbbells. The dumbbell particle consists of a smooth sphere with diameter σ and a surface-coated rough sphere with a diameter σ_R . The distance between the rough and the smooth sphere is equal to $d = (\sigma + \sigma_R)/2$, i. e. the spheres are at contact. We assume hard-sphere interactions between the rough and smooth spheres and the smooth spheres interact with with an attractive Asakura-Oosawa depletion interaction. By tuning the size ratio of the dumbbells, the size of the clusters can be tuned, assuming equilibrium can be reached. At least up to a size ratio of $\sigma/\sigma_R = 0.76$, the general behavior of the system does not seem to change qualitatively, although this should happen at larger size ratios, where lamellar structures and wide phase coexistences would be likely. In particular, in systems of purely spherical particles ($\sigma/\sigma_R \rightarrow \infty$), a gas-liquid

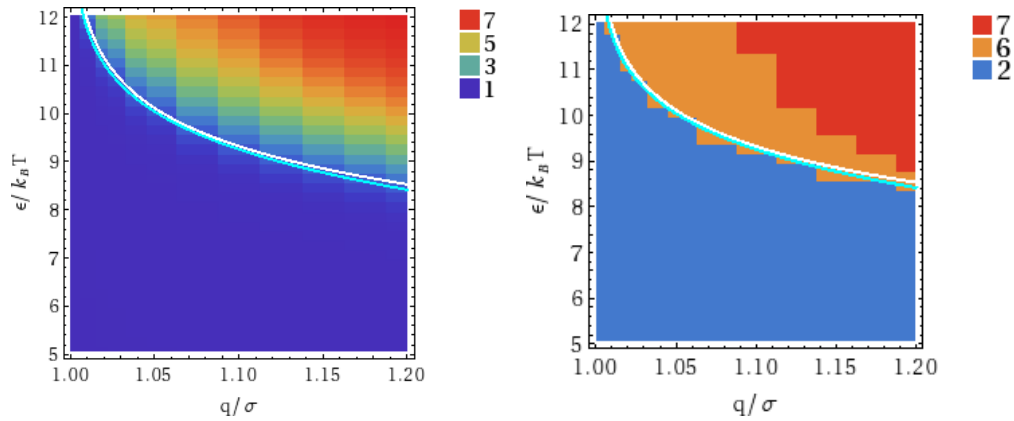


Figure 10.10: Left: Average cluster size as a function of the interaction range q and interaction strength ϵ , for size ratio $\sigma/\sigma_R = 0.3$, and a packing fraction of $\eta = 0.01$. The white and blue lines show the cmc and the maximum of the heat capacity, respectively. **Right:** The most common cluster size $n > 1$ in the same system.

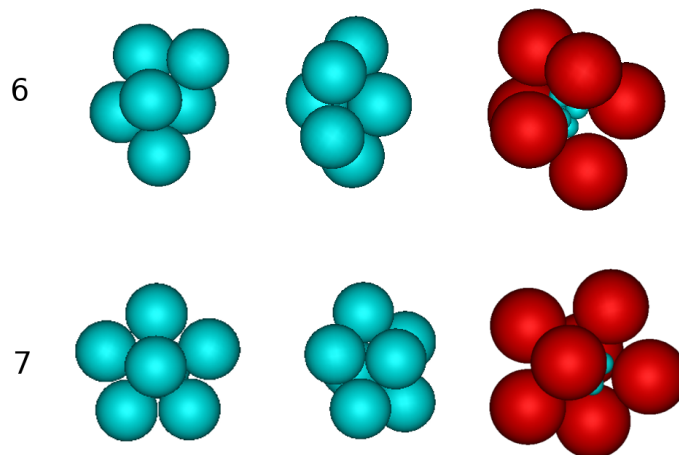


Figure 10.11: Typical clusters of size $n = 6$ and 7 for size ratio $\sigma/\sigma_R = 0.3$. For each size, the rough spheres in the two pictures on the left are hidden to show the structure of the smooth spheres.

coexistence appears in the phase diagram for sufficiently long interaction ranges (around $q/\sigma \simeq 1.5$ [220]). For colloidal dumbbells with size ratio $\sigma/\sigma_R = 0.76$, this coexistence appears to be strongly suppressed: no noticeable gas-liquid coexistence was observed up to $q/\sigma = 3$ (much longer than physically reasonable for depletion interactions) at any density or interaction strength over a wide range in Gibbs ensemble Monte Carlo simulations. Instead, either crystalline or fluid-like droplets form with a layer of rough spheres on the outside. While it is possible that it is simply very difficult to equilibrate these simulations, it appears that the wide coexistence region is suppressed by the formation of micelles. In sufficiently dense systems, a transition to another fluid phase (possibly similar to the vesicle phase found in spherical Janus particles [211]) could still occur, but further study of the system would be required to map out the full phase behavior.

The structure of the clusters formed shows similarities between all studied size ratios. For small cluster sizes (up to around 10), the smooth spheres form structures similar to those that minimize the potential energy of spherical particles with short-ranged attractions.[221] However, for larger cluster sizes, the rough spheres prevent configurations where a smooth sphere is not on the surface of the cluster. Additionally, the presence of the rough spheres increases the attraction strength needed to form clusters, since the colloids lose rotational as well as translational freedom by joining a cluster. Higher interaction strengths cause a preference for more compact clusters, with as many bonds as possible, although this effect is somewhat diminished by the fact that these compact clusters further inhibit the rotational entropy of the particles. For the range of interaction strengths studied in this chapter, a variety of cluster shapes was observed for each cluster size. While the most commonly observed structure often corresponds to the lowest-energy state for that particular cluster size, higher energy configurations are still common, and the most common cluster size does not always correspond to the largest number of bonds. Clearly, entropic effects still play an important role in determining the structure of the clusters.

To prevent the prohibitively long equilibration times involved in forming the larger clusters in these systems, the best strategy would be to focus on reducing the large energy barriers involved in cluster reorganization and breakup. This can be done by simply reducing the volume fraction of depletants in the system (i.e. lowering the interaction strength ϵ), and compensating for the reduced cluster formation by either increasing the colloidal packing fraction η or the interaction range q . Another option would be to reduce the cluster size by tuning the size ratio, leading to a smaller number of bonds per particle.

10.6 Conclusions

We investigated the distribution of cluster sizes in systems of hard-core asymmetric dumbbells, with depletion interactions between the smaller spheres in each dumbbell. We find that the number of clusters depends strongly on the packing fraction, but the cluster size is largely independent of the packing fraction, interaction range and interaction strength. Instead, changing the size ratio of the dumbbells imposes a preferred curvature on the micelle surface and therefore allows for tuning of the cluster size: more asymmetric dumbbells lead to smaller clusters. We compared our results with both Monte Carlo simulations

starting from a homogeneous initial configuration, and experimental observations. We observed a strong discrepancy between the predicted equilibrium cluster size distribution and those in both the direct MC simulations and experiments. We conclude that both the direct simulations and experiments are far out of equilibrium, due to the prohibitively long time scales involved in the breaking of bonds once they are formed.

10.7 Acknowledgements

I would like to thank Daniela Kraft and Willem Kegel for their experimental work on this system, and Ran Ni for performing the direct Monte Carlo simulations discussed in this chapter.

References

- [1] R. Brown, *A brief account of microscopical observations made in the months of june, july and august, 1827, on the particles contained in the pollen of plants, and on the general existence of active molecules in organic and inorganic bodies*, Phil. Mag. **4**, 181 (1828).
- [2] W. Sutherland, *A dynamical theory of diffusion for non-electrolytes and the molecular mass of albumin*, Phil. Mag. **9**, 781 (1905).
- [3] A. Einstein, *Über die von der molekularkinetischen theorie der wärme geforderte bewegung von in ruhenden flüssigkeiten suspendierten teilchen*, Ann. Phys. (Leipz.) **322**, 549 (1905).
- [4] S. C. Glotzer and M. J. Solomon, *Anisotropy of building blocks and their assembly into complex structures*, Nature Materials **6**, 557 (2007).
- [5] A.-P. Hynninen, J. H. J. Thijssen, E. C. M. Vermolen, M. Dijkstra, and A. Van Blaaderen, *Self-assembly route for photonic crystals with a bandgap in the visible region*, Nature Materials **6**, 202 (2007).
- [6] E. A. Kamenetzky, L. G. Magliocco, and H. P. Panzer, *Structure of solidified colloidal array laser filters studied by cryogenic transmission electron microscopy*, Science **263**, 207 (1994).
- [7] Y. A. Vlasov, X.-Z. Bo, J. C. Sturm, and D. J. Norris, *On-chip natural assembly of silicon photonic bandgap crystals*, Nature **414**, 289 (2001).
- [8] J. G. C. Veinot, H. Yan, S. M. Smith, J. Cui, Q. Huang, and T. J. Marks, *Fabrication and properties of organic light-emitting “nanodiode” arrays*, Nano Letters **2**, 333 (2002).
- [9] J. H. Holtz and S. A. Asher, *Polymerized colloidal crystal hydrogel films as intelligent chemical sensing materials*, Nature **389**, 829 (1997).
- [10] J. V. Sanders, *Close-packed structures of spheres of two different sizes i. observations on natural opal*, Philosophical Magazine, Part A **42**, 705 (1980).
- [11] W. W. Wood and J. D. Jacobson, *Preliminary results from a recalculation of the Monte Carlo equation of state of hard spheres*, J. Chem. Phys. **27**, 1207 (1957).
- [12] B. J. Alder and T. E. Wainwright, *Phase transition for a hard sphere system*, J. Chem. Phys. **27**, 1208 (1957).
- [13] P. Pusey and W. Van Meegen, *Phase behaviour of concentrated suspensions of nearly hard colloidal spheres*, Nature **320**, 340 (1986).
- [14] L. Fillion and M. Dijkstra, *Prediction of binary hard-sphere crystal structures*, Phys. Rev. E **79**, 046714 (2009).
- [15] A. B. Pawar and I. Kretzschmar, *Fabrication, assembly, and application of patchy particles*, Macromolecular Rapid Communications **31**, 150 (2010).
- [16] Z. Zhang and S. C. Glotzer, *Self-assembly of patchy particles*, Nano Letters **4**, 1407 (2004).
- [17] D. Frenkel and B. Smit, *Understanding Molecular Simulations: From Algorithms to Applications* (Academic Press, 2002).
- [18] D. C. Rapaport, *The event-driven approach to n-body simulation*, Progress of Theoretical Physics Supplement **178**, 5 (2009).

- [19] A. Donev, S. Torquato, and F. H. Stillinger, *Neighbor list collision-driven molecular dynamics simulation for nonspherical hard particles. I. Algorithmic details*, Journal of Computational Physics **202**, 737 (2005).
- [20] L. H. de la Peña, R. van Zon, J. Schofield, and S. B. Opps, *Discontinuous molecular dynamics for semiflexible and rigid bodies*, J. Chem. Phys **126**, 074105 (2007).
- [21] A. Donev, S. Torquato, and F. H. Stillinger, *Neighbor list collision-driven molecular dynamics simulation for nonspherical hard particles. II. Applications to ellipses and ellipsoids*, Journal of Computational Physics **202**, 765 (2005).
- [22] T. B. Jones, R. D. Miller, K. S. Robinson, and W. Y. Fowlkes, *Multipolar interactions of dielectric spheres*, Journal of Electrostatics **22**, 231 (1989).
- [23] P. P. Ewald, *Die Berechnung optischer und elektrostatischer Gitterpotentiale*, Annalen der Physik **369**, 253 (1921).
- [24] A. Yethiraj and A. Van Blaaderen, *A colloidal model system with an interaction tunable from hard sphere to soft and dipolar*, Nature **421**, 513 (2003).
- [25] A. Yethiraj, J. H. J. Thijssen, A. Wouterse, and A. van Blaaderen, *Large-Area Electric-Field-Induced Colloidal Single Crystals for Photonic Applications*, Advanced materials **16**, 596 (2004).
- [26] A.-P. Hynninen and M. Dijkstra, *Phase diagram of dipolar hard and soft spheres: Manipulation of colloidal crystal structures by an external field*, Phys. Rev. Lett. **94**, 138303 (2005).
- [27] M. Parthasarathy and D. J. Klingenberg, *Electrorheology: mechanisms and models*, Materials Science and Engineering: R: Reports **17**, 57 (1996).
- [28] R. Tao, *Super-strong magnetorheological fluids*, Journal of Physics: Condensed Matter **13**, R979 (2001).
- [29] W. Wen, C. Weisbuch, D. M. Phuong, G. Lu, W. Ge, C. T. Chan, and P. Sheng, *Neutral nanoparticle-based display*, Nanotechnology **16**, 598 (2005).
- [30] T.-J. Chen, R. N. Zitter, and R. Tao, *Laser diffraction determination of the crystalline structure of an electrorheological fluid*, Phys. Rev. Lett. **68**, 2555 (1992).
- [31] U. Dassanayake, S. Fraden, and A. van Blaaderen, *Structure of electrorheological fluids*, J. Chem. Phys **112**, 3851 (2000).
- [32] C. Holm, A. Ivanov, S. Kantorovich, E. Pyanzina, and E. Reznikov, *Equilibrium properties of a bidisperse ferrofluid with chain aggregates: theory and computer simulations*, Journal of Physics Condensed Matter **18**, 2737 (2006).
- [33] J. P. Huang, Z. W. Wang, and C. Holm, *Structure and magnetic properties of mono- and bi-dispersed ferrofluids as revealed by simulations*, Journal of Magnetism and Magnetic Materials **289**, 234 (2005).
- [34] M. Klokkenburg, R. P. A. Dullens, W. K. Kegel, B. H. Ern e, and A. P. Philipse, *Quantitative real-space analysis of self-assembled structures of magnetic dipolar colloids*, Phys. Rev. Lett. **96**, 037203 (2006).
- [35] P. J. Camp and G. N. Patey, *Structure and scattering in colloidal ferrofluids*, Phys. Rev. E **62**, 5403 (2000).
- [36] A. O. Ivanov and S. S. Kantorovich, *Structure of chain aggregates in ferrocolloids*, Colloid Journal **65**, 166 (March 2003).

- [37] Z. Wang and C. Holm, *Structure and magnetic properties of polydisperse ferrofluids: A molecular dynamics study*, Phys. Rev. E **68**, 041401 (2003).
- [38] H. See, A. Kawai, and F. Ikazaki, *The effect of mixing particles of different size on the electrorheological response under steady shear flow*, Rheologica Acta **41**, 55 (2002).
- [39] D. Zerrouki, J. Baudry, D. Pine, P. Chaikin, and J. Bibette, *Chiral colloidal clusters.*, Nature **455**, 380 (2008).
- [40] D. Chakrabarti, S. N. Fejer, and D. J. Wales, *Rational design of helical architectures*, Proceedings of the National Academy of Sciences **106**, 20164 (2009).
- [41] H. R. Vutukuri, A. F. Demirörs, B. Peng, P. D. J. van Oostrum, A. Imhof, and A. van Blaaderen, *Colloidal analogues of charged and uncharged polymer chains with tunable stiffness*, Submitted (2011).
- [42] E. J. W. Verwey and J. T. G. Overbeek, *Theory of the Stability of Lyotropic Colloids* (Elsevier, 1948).
- [43] G. M. Bell, S. Levine, and L. N. McCartney, *Approximate methods of determining the double-layer free energy of interaction between two charged colloidal spheres*, Journal of Colloid and Interface Science **33**, 335 (1970).
- [44] A. Satoh, R. W. Chantrell, S.-I. Kamiyama, and G. N. Coverdale, *Three dimensional Monte Carlo simulations of thick chainlike clusters composed of ferromagnetic fine particles*, Journal of Colloid and Interface Science **181**, 422 (1996).
- [45] U. Dassanayake, S. Fraden, and A. van Blaaderen, *Structure of electrorheological fluids*, J. Chem. Phys. **112**, 3851 (2000).
- [46] M. S. Wertheim, *Fluids with highly directional attractive forces. i. statistical thermodynamics*, Journal of Statistical Physics **35**, 19 (1984).
- [47] M. S. Wertheim, *Fluids with highly directional attractive forces. ii. thermodynamic perturbation theory and integral equations*, Journal of Statistical Physics **35**, 35 (1984).
- [48] M. S. Wertheim, *Fluids with highly directional attractive forces. III. multiple attraction sites*, Journal of Statistical Physics **42**, 459 (1986).
- [49] F. Sciortino, E. Bianchi, J. F. Douglas, and P. Tartaglia, *Self-assembly of patchy particles into polymer chains: A parameter-free comparison between wertheim theory and Monte Carlo simulation*, J. Chem. Phys. **126**, 194903 (2007).
- [50] G. Bosma, C. Pathmanoharan, E. H. A. de Hoog, W. K. Kegel, A. van Blaaderen, and H. N. W. Lekkerkerker, *Preparation of monodisperse, fluorescent pmma-latex colloids by dispersion polymerization*, J. Colloid Interf. Sci. **245**, 292 (2002).
- [51] B. Groh and S. Dietrich, *Crystal structures and freezing of dipolar fluids*, Phys. Rev. E **63**, 021203 (2001).
- [52] S. Klapp and F. Forstmann, *Phase behavior of aligned dipolar hard spheres: Integral equations and density functional results*, Phys. Rev. E **60**, 3183 (1999).
- [53] J. Jordanovic and S. H. L. Klapp, *Field-induced layer formation in dipolar nanofilms*, Phys. Rev. Lett. **101**, 038302 (2008).
- [54] G. M. Range and S. H. L. Klapp, *Density-functional study of model bidisperse ferrocolloids in an external magnetic field*, J. Chem. Phys **122**, 224902 (2005).
- [55] S. H. L. Klapp, *Dipolar fluids under external perturbations*, Journal of Physics: Condensed Matter **17**, R525 (2005).

- [56] S. H. L. Klapp and M. Schoen, *Spontaneous orientational order in confined dipolar fluid films*, J. Chem. Phys **117**, 8050 (2002).
- [57] S. Klapp and M. Schoen, *Ferroelectric states of a dipolar fluid confined to a slit-pore*, Journal of molecular liquids **109**, 55 (2004).
- [58] J. E. Martin, R. A. Anderson, and C. P. Tigges, *Simulation of the athermal coarsening of composites structured by a uniaxial field*, J. Chem. Phys **108**, 3765 (1998).
- [59] J. E. Martin, R. A. Anderson, and C. P. Tigges, *Simulation of the athermal coarsening of composites structured by a biaxial field*, J. Chem. Phys **108**, 7887 (1998).
- [60] J. E. Martin, R. A. Anderson, and C. P. Tigges, *Thermal coarsening of uniaxial and biaxial field-structured composites*, J. Chem. Phys **110**, 4854 (1999).
- [61] J. E. Martin, R. A. Anderson, and R. L. Williamson, *Generating strange magnetic and dielectric interactions: Classical molecules and particle foams*, J. Chem. Phys **118**, 1557 (2003).
- [62] J. E. Martin, E. Venturini, J. Odinek, and R. A. Anderson, *Anisotropic magnetism in field-structured composites*, Phys. Rev. E **61**, 2818 (2000).
- [63] V. V. Murashov and G. N. Patey, *Structure formation in dipolar fluids driven by rotating fields*, J. Chem. Phys **112**, 9828 (2000).
- [64] M. E. Leunissen, H. R. Vutukuri, and A. van Blaaderen, *Directing Colloidal Self-Assembly with Biaxial Electric Fields*, Advanced Materials **21**, 3116 (2009).
- [65] N. Elsner, C. P. Royall, B. Vincent, and D. R. E. Snoswell, *Simple models for two-dimensional tunable colloidal crystals in rotating ac electric fields*, J. Chem. Phys **130**, 154901 (2009).
- [66] D. Frenkel and A. J. C. Ladd, *New Monte Carlo method to compute the free energy of arbitrary solids. Application to the fcc and hcp phases of hard spheres*, J. Chem. Phys **81**, 3188 (1984).
- [67] P. G. Bolhuis, D. Frenkel, S. C. Mau, and D. A. Huse, *Entropy difference between crystal phases*, Nature **388**, 235 (1997).
- [68] R. J. Speedy, *Pressure of the metastable hard-sphere fluid*, Journal of Physics: Condensed Matter **9**, 8591 (1997).
- [69] P. Bolhuis and D. Frenkel, *Tracing the phase boundaries of hard spherocylinders*, J. Chem. Phys **106**, 666 (1997).
- [70] T. Sugimoto and K. Sakata, *Preparation of monodisperse pseudocubic $[\alpha]$ - Fe_2O_3 particles from condensed ferric hydroxide gel*, Journal of Colloid and Interface Science **152**, 587 (1992).
- [71] L. Rossi, S. Sacanna, W. T. M. Irvine, P. M. Chaikin, D. J. Pine, and A. P. Philipse, *Cubic crystals from cubic colloids*, Soft Matter **7**, 4139 (2011).
- [72] C. J. Murphy, T. K. Sau, A. M. Gole, C. J. Orendorff, J. Gao, L. Gou, S. E. Hunyadi, and T. Li, *Anisotropic metal nanoparticles: Synthesis, assembly, and optical applications*, The Journal of Physical Chemistry B **109**, 13857 (2005). PMID: 16852739.
- [73] Z. Pu, M. Cao, J. Yang, K. Huang, and C. Hu, *Controlled synthesis and growth mechanism of hematite nanorhomboheda, nanorods and nanocubes*, Nanotechnology **17**, 799 (2006).
- [74] C. Su, H. Wang, and X. Liu, *Controllable fabrication and growth mechanism of hematite cubes*, Crystal Research and Technology **46**, 209 (2011).

- [75] B. S. John, C. Juhlin, and F. A. Escobedo, *Phase behavior of colloidal hard perfect tetragonal parallelepipeds*, J. Chem. Phys **128**, 044909 (2008).
- [76] R. D. Batten, F. H. Stillinger, and S. Torquato, *Phase behavior of colloidal superballs: Shape interpolation from spheres to cubes*, Phys. Rev. E **81**, 061105 (2010).
- [77] U. Agarwal and F. A. Escobedo, *Mesophase behaviour of polyhedral particles*, Nature Materials (2011).
- [78] X. Zhang, Z. Zhang, and S. C. Glotzer, *Simulation study of dipole-induced self-assembly of nanocubes*, The Journal of Physical Chemistry C **111**, 4132 (2007).
- [79] J. de Graaf, R. van Roij, and M. Dijkstra, *Dense regular packings of irregular nonconvex particles*, Phys. Rev. Lett. **107**, 155501 (2011).
- [80] H. R. Vutukuri, *et al.*, To be published (2011).
- [81] H. R. Vutukuri, *Complex colloidal structures by self-assembly in electric fields* (PhD Thesis, 2012).
- [82] Y. Sun and Y. Xia, *Shape-controlled synthesis of gold and silver nanoparticles*, Science **298**, 2176 (2002).
- [83] E. G. Golshtein and N. V. Tretyakov, *Modified Lagrangians and Monotone Maps in Optimization* (Wiley, 1996).
- [84] E. G. Noya, C. Vega, J. P. K. Doye, and A. A. Louis, *Phase diagram of model anisotropic particles with octahedral symmetry*, J. Chem. Phys. **127**, 054501 (2007).
- [85] J. M. Polson, E. Trizac, S. Pronk, and D. Frenkel, *Finite-size corrections to the free energies of crystalline solids*, J. Chem. Phys. **112**, 5339 (2000).
- [86] B. M. Mladek, P. Charbonneau, C. N. Likos, D. Frenkel, and G. Kahl, *Multiple occupancy crystals formed by purely repulsive soft particles*, J. of Phys.: Cond. Matt. **20**, 494245 (2008).
- [87] P. R. ten Wolde, M. J. Ruiz-Montero, and D. Frenkel, *Numerical calculation of the rate of crystal nucleation in a lennard-jones system at moderate undercooling*, J. Chem. Phys. **104**, 9932 (1996).
- [88] J. A. C. Veerman and D. Frenkel, *Phase behavior of disklike hard-core mesogens*, Phys. Rev. A **45**, 5632 (1992).
- [89] C. H. Bennett and B. J. Alder, *Studies in molecular dynamics. ix. vacancies in hard sphere crystals*, J. Chem. Phys. **54**, 4796 (1971).
- [90] R. Speedy and H. Reiss, *Cavities in the hard sphere fluid and crystal and the equation of state*, Molecular Physics **72**, 999 (1991).
- [91] K. W. Wojciechowski and D. Frenkel, *Tetratic phase in the planar hard square system?*, Computational Methods in Science and Technology **10**, 235 (2004).
- [92] R. J. Hunter, *Foundations of colloid science, second edition* (Oxford University Press, 2001).
- [93] J. Israelachvili, *Intermolecular and surface forces, second edition* (Academic Press, 1991).
- [94] J. L. Barrat and J. P. Hansen, *Basic concepts for simple and complex fluids* (Cambridge University Press, 2003).
- [95] B. Derjaguin and L. Landau, *Acta Physicochim. USSR* **14**, 633 (1941).

- [96] J. C. Crocker and D. G. Grier, *Microscopic measurement of the pair interaction potential of charge-stabilized colloid*, Phys. Rev. Lett. **73**, 352 (1994).
- [97] E. B. Sirota, H. D. Ou-Yang, S. K. Sinha, P. M. Chaikin, J. D. Axe, and Y. Fujii, *Complete phase diagram of a charged colloidal system: A synchrotron x-ray scattering study*, Phys. Rev. Lett. **62**, 1524 (1989).
- [98] Y. Monovoukas and A. P. Gast, *The experimental phase diagram of charged colloidal suspensions*, Journal of Colloid and Interface Science **128**, 533 (1989).
- [99] T. Okubo, *Phase transition between liquid-like and crystal-like structures of deionized colloidal suspensions*, J. Chem. Soc., Faraday Trans. **86**, 2871 (1990).
- [100] T. Okubo, *Melting temperature of colloidal crystals of polystyrene spheres*, J. Chem. Phys **95**, 3690 (1991).
- [101] M. O. Robbins, K. Kremer, and G. S. Grest, *Phase diagram and dynamics of Yukawa systems*, J. Chem. Phys **88**, 3286 (1988).
- [102] E. J. Meijer and D. Frenkel, *Melting line of Yukawa system by computer simulation*, J. Chem. Phys **94**, 2269 (1991).
- [103] S. Hamaguchi, R. T. Farouki, and D. H. E. Dubin, *Triple point of Yukawa systems*, Phys. Rev. E **56**, 4671 (1997).
- [104] A.-P. Hynninen and M. Dijkstra, *Phase diagrams of hard-core repulsive Yukawa particles*, Phys. Rev. E **68**, 021407 (2003).
- [105] S. Alexander, P. M. Chaikin, P. Grant, G. J. Morales, P. Pincus, and D. Hone, *Charge renormalization, osmotic pressure, and bulk modulus of colloidal crystals: Theory*, J. Chem. Phys **80**, 5776 (1984).
- [106] M. E. Leunissen, C. G. Christova, A. Hynninen, C. P. Royall, A. I. Campbell, A. Imhof, M. Dijkstra, R. van Roij, and A. van Blaaderen, *Ionic colloidal crystals of oppositely charged particles*, Nature **437**, 235 (2005).
- [107] J. Dobnikar, Y. Chen, R. Rzehak, and H. H. von Grünberg, *Many-body interactions and the melting of colloidal crystals*, J. Chem. Phys **119**, 4971 (2003).
- [108] B. Zoetekouw and R. van Roij, *Nonlinear screening and gas-liquid separation in suspensions of charged colloids*, Phys. Rev. Lett. **97**, 258302 (2006).
- [109] Y. Levin, *Electrostatic correlations: from plasma to biology*, Reports on Progress in Physics **65**, 1577 (2002).
- [110] P. Wette, H. J. Schöpe, and T. Palberg, *Experimental determination of effective charges in aqueous suspensions of colloidal spheres*, Colloids Surf., A **222**, 311 (2003).
- [111] P. Wette, H. J. Schöpe, and T. Palberg, *Comparison of colloidal effective charges from different experiments*, J. Chem. Phys **116**, 10981 (2002).
- [112] D. Hessinger, M. Evers, and T. Palberg, *Independent ion migration in suspensions of strongly interacting charged colloidal spheres*, Phys. Rev. E **61**, 5493 (2000).
- [113] M. Brunner, C. Bechinger, W. Strepp, V. Lobaskin, and H. H. von GrÄijnberg, *Density-dependent pair interactions in 2d*, EPL (Europhysics Letters) **58**, 926 (2002).
- [114] C. Russ, H. H. von Grünberg, M. Dijkstra, and R. van Roij, *Three-body forces between charged colloidal particles*, Phys. Rev. E **66**, 011402 (2002).

- [115] R. Klein, H. H. von Grünberg, C. Bechinger, M. Brunner, and V. Lobaskin, *Macroion shielding and state-dependent pair potentials in colloidal suspensions*, Journal of Physics: Condensed Matter **14**, 7631 (2002).
- [116] P. Wette, I. Klassen, D. Holland-Moritz, D. M. Herlach, H. J. Schöpe, N. Lorenz, H. Reiber, T. Palberg, and S. V. Roth, *Communications: Complete description of re-entrant phase behavior in a charge variable colloidal model system*, J. Chem. Phys **132**, 131102 (2010).
- [117] P. M. Biesheuvel, *Evidence for charge regulation in the sedimentation of charged colloids*, Journal of Physics: Condensed Matter **16**, L499 (2004).
- [118] M. Rasa, B. H. ErnÅI, B. Zoetekouw, R. van Roij, and A. P. Philipse, *Macroscopic electric field and osmotic pressure in ultracentrifugal sedimentation*—diffusion equilibria of charged colloids, Journal of Physics: Condensed Matter **17**, 2293 (2005).
- [119] R. van Roij, *Defying gravity with entropy and electrostatics: sedimentation of charged colloids*, Journal of Physics: Condensed Matter **15**, S3569 (2003).
- [120] C. P. Royall, M. E. Leunissen, A.-P. Hynninen, M. Dijkstra, and A. van Blaaderen, *Re-entrant melting and freezing in a model system of charged colloids*, J. Chem. Phys **124**, 244706 (2006).
- [121] J. W. Merrill, S. K. Sainis, and E. R. Dufresne, *Many-body electrostatic forces between colloidal particles at vanishing ionic strength*, Phys. Rev. Lett. **103**, 138301 (2009).
- [122] T. Vissers, A. Imhof, F. Carrique, Á. Delgado, and A. van Blaaderen, *Electrophoresis of concentrated colloidal dispersions in low-polar solvents*, Journal of colloid and interface science (2011).
- [123] E. Trizac, L. Bocquet, and M. Aubouy, *Simple approach for charge renormalization in highly charged macroions*, Phys. Rev. Lett. **89**, 248301 (2002).
- [124] E. Trizac and Y. Levin, *Renormalized jellium model for charge-stabilized colloidal suspensions*, Phys. Rev. E **69**, 031403 (2004).
- [125] T. E. Colla, Y. Levin, and E. Trizac, *A self-consistent renormalized jellium approach for calculating structural and thermodynamic properties of charge stabilized colloidal suspensions*, J. Chem. Phys **131**, 074115 (2009).
- [126] A. Toyotama, T. Sawada, J. Yamanaka, and K. Kitamura, *Reentrant behavior in the order-disorder phase transition of a charged monodisperse latex*, Langmuir **19**, 3236 (2003).
- [127] L. F. Rojas-Ochoa, R. Castañeda Priego, V. Lobaskin, A. Stradner, F. Scheffold, and P. Schurtenberger, *Density dependent interactions and structure of charged colloidal dispersions in the weak screening regime*, Phys. Rev. Lett. **100**, 178304 (2008).
- [128] B. W. Ninham and V. A. Parsegian, *Electrostatic potential between surfaces bearing ionizable groups in ionic equilibrium with physiologic saline solution*, Journal of Theoretical Biology **31**, 405 (1971).
- [129] D. Y. C. Chan and D. J. Mitchell, *The free energy of an electrical double layer*, Journal of Colloid and Interface Science **95**, 193 (1983).
- [130] S. H. Behrens and M. Borkovec, *Electric double layer interaction of ionizable surfaces: Charge regulation for arbitrary potentials*, J. Chem. Phys **111**, 382 (1999).
- [131] T. Gisler, S. F. Schulz, M. Borkovec, H. Sticher, P. Schurtenberger, B. D’Aguanno, and R. Klein, *Understanding colloidal charge renormalization from surface chemistry: Experiment and theory*, J. Chem. Phys **101**, 9924 (1994).

- [132] H. H. von Grünberg, *Chemical charge regulation and charge renormalization in concentrated colloidal suspensions*, Journal of Colloid and Interface Science **219**, 339 (1999).
- [133] I. Popa, P. Sinha, M. Finessi, P. Maroni, G. Papastavrou, and M. Borkovec, *Importance of charge regulation in attractive double-layer forces between dissimilar surfaces*, Phys. Rev. Lett. **104**, 228301 (2010).
- [134] N. Boon and R. van Roij, *Charge regulation and ionic screening of patchy surfaces*, J. Chem. Phys **134**, 054706 (2011).
- [135] T. Palberg, W. Mönch, F. Bitzer, R. Piazza, and T. Bellini, *Freezing transition for colloids with adjustable charge: A test of charge renormalization*, Phys. Rev. Lett. **74**, 4555 (1995).
- [136] E. Trizac, L. Bocquet, M. Aubouy, and H. H. von Grünberg, *Alexander's prescription for colloidal charge renormalization*, Langmuir **19**, 4027 (2003).
- [137] M. Dijkstra and R. van Roij, *Vapour-liquid coexistence for purely repulsive point-Yukawa fluids*, Journal of Physics: Condensed Matter **10**, 1219 (1998).
- [138] N. Boon, E. C. Gallardo, S. Zheng, E. Eggen, M. Dijkstra, and R. van Roij, *Screening of heterogeneous surfaces: charge renormalization of janus particles*, Journal of Physics: Condensed Matter **22**, 104104 (2010).
- [139] M. Volmer and A. Weber, *Keimbildung in übersättigten gebilden*, Z. Phys. Chem. **119**, 277 (1926).
- [140] R. Becker and W. Döring, *Kinetische behandlung der keimbildung in übersättigten dämpfern.*, Ann. Phys. **24**, 719 (1935).
- [141] Y. B. Zeldovich, *Theory of new-phase formation: cavitation*, Zh. Eksp. Teor. Fiz. **12**, 525 (1942).
- [142] P. R. ten Wolde, M. J. Ruiz-Montero, and D. Frenkel, *Numerical evidence for bcc ordering at the surface of a critical fcc nucleus*, Phys. Rev. Lett. **75**, 2714 (1995).
- [143] P. R. ten Wolde and D. Frenkel, *Computer simulation study of gas-liquid nucleation in a lennard-jones system*, J. Chem. Phys. **109**, 9901 (1998).
- [144] S. Auer and D. Frenkel, *Prediction of absolute crystal-nucleation rate in hard-sphere colloids*, Nature **409**, 1020 (2001).
- [145] L. Fillion, M. Hermes, R. Ni, and M. Dijkstra, *Crystal nucleation of hard spheres using molecular dynamics, umbrella sampling, and forward flux sampling: A comparison of simulation techniques*, J. Chem. Phys. **133**, 244115 (2010).
- [146] A. Cuetos and M. Dijkstra, *Kinetic pathways for the isotropic-nematic phase transition in a system of colloidal hard rods: A simulation study*, Phys. Rev. Lett. **98**, 095701 (2007).
- [147] A. Cuetos, R. van Roij, and M. Dijkstra, *Isotropic-to-nematic nucleation in suspensions of colloidal rods*, Soft Matter **4**, 757 (2008).
- [148] R. Ni, S. Belli, R. van Roij, and M. Dijkstra, *Glassy dynamics, spinodal fluctuations, and the kinetic limit of nucleation in suspensions of colloidal hard rods*, Phys. Rev. Lett. **105**, 088302 (2010).
- [149] D. Frenkel and T. Schilling, *Smectic filaments in colloidal suspensions of rods*, Phys. Rev. E **66**, 041606 (2002).
- [150] A. Patti and M. Dijkstra, *Do multilayer crystals nucleate in suspensions of colloidal rods?*, Phys. Rev. Lett. **102**, 128301 (2009).

- [151] H. Reiss, *The kinetics of phase transitions in binary systems*, J. Chem. Phys. **18**, 840 (1950).
- [152] J. W. Cahn and J. E. Hilliard, *Free energy of a nonuniform system. III. nucleation in a two-component incompressible fluid*, J. Chem. Phys. **31**, 688 (1959).
- [153] D. W. Oxtoby and D. Kashchiev, *A general relation between the nucleation work and the size of the nucleus in multicomponent nucleation*, J. Chem. Phys. **100**, 7665 (1994).
- [154] G. J. Doyle, *Self-nucleation in the sulfuric acid-water system*, J. Chem. Phys. **35**, 795 (1961).
- [155] R. G. Renninger, F. C. Hiller, and R. C. Bone, *Comment on "Self-nucleation in the sulfuric acid-water system"*, J. Chem. Phys. **75**, 1584 (1981).
- [156] G. Wilemski, *Composition of the critical nucleus in multicomponent vapor nucleation*, J. Chem. Phys. **80**, 1370 (1984).
- [157] G. Wilemski, *Revised classical binary nucleation theory for aqueous alcohol and acetone vapors*, J. of Phys. Chem. **91**, 2492 (1987).
- [158] P. Mirabel and H. Reiss, *Resolution of the "Renninger-Wilemski problem" concerning the identification of heteromolecular nuclei*, Langmuir **3**, 228 (1987).
- [159] Y. Viisanen, R. Strey, A. Laaksonen, and M. Kulmala, *Measurement of the molecular content of binary nuclei. II. use of the nucleation rate surface for water-ethanol*, J. Chem. Phys. **100**, 6062 (1994).
- [160] A. Laaksonen, M. Kulmala, and P. E. Wagner, *On the cluster compositions in the classical binary nucleation theory*, J. Chem. Phys. **99**, 6832 (1993).
- [161] P. G. Debenedetti and H. Reiss, *Reversible work of formation of an embryo of a new phase within a uniform macroscopic mother phase*, J. Chem. Phys. **108**, 5498 (1998).
- [162] A. Laaksonen, R. McGraw, and H. Vehkamäki, *Liquid-drop formalism and free-energy surfaces in binary homogeneous nucleation theory*, J. Chem. Phys. **111**, 2019 (1999).
- [163] G. M. Torrie and J. P. Valleau, *Monte Carlo free energy estimates using non-boltzmann sampling: Application to the sub-critical lennard-jones fluid*, Chemical Physics Letters **28**, 578 (1974).
- [164] J. S. van Duijneveldt and D. Frenkel, *Computer simulation study of free energy barriers in crystal nucleation*, J. Chem. Phys. **96**, 4655 (1992).
- [165] S. Punnathanam and P. A. Monson, *Crystal nucleation in binary hard sphere mixtures: A Monte Carlo simulation study*, J. Chem. Phys. **125**, 024508 (2006).
- [166] P. R. ten Wolde and D. Frenkel, *Numerical study of gas-liquid nucleation in partially miscible binary mixtures*, J. Chem. Phys. **109**, 9919 (1998).
- [167] D. W. Oxtoby and R. Evans, *Nonclassical nucleation theory for the gas-liquid transition*, J. Chem. Phys. **89**, 7521 (1988).
- [168] S. Auer and D. Frenkel, *Crystallization of weakly charged colloidal spheres: a numerical study*, Journal of Physics: Condensed Matter **14**, 7667 (2002).
- [169] E. Sanz, C. Valeriani, D. Frenkel, and M. Dijkstra, *Evidence for out-of-equilibrium crystal nucleation in suspensions of oppositely charged colloids*, Phys. Rev. Lett. **99**, 055501 (2007).

- [170] C. Valeriani, E. Sanz, and D. Frenkel, *Rate of homogeneous crystal nucleation in molten nacl*, J. Chem. Phys. **122**, 194501 (2005).
- [171] D. Moroni, P. R. ten Wolde, and P. G. Bolhuis, *Interplay between structure and size in a critical crystal nucleus*, Phys. Rev. Lett. **94**, 235703 (2005).
- [172] P. R. Wolde and D. Frenkel, *Enhancement of protein crystal nucleation by critical density fluctuations*, Science **277**, 1975 (1997).
- [173] L. Filion, M. Hermes, R. Ni, E. C. M. Vermolen, A. Kuijk, C. G. Christova, J. C. P. Stiefelhagen, T. Vissers, A. van Blaaderen, and M. Dijkstra, *Self-assembly of a colloidal interstitial solid solution with tunable sublattice doping*, Phys. Rev. Lett. **107**, 168302 (2011).
- [174] M. Dijkstra, R. van Roij, and R. Evans, *Phase behavior and structure of binary hard-sphere mixtures*, Phys. Rev. Lett. **81**, 2268 (1998).
- [175] M. Dijkstra, R. van Roij, and R. Evans, *Direct simulation of the phase behavior of binary hard-sphere mixtures: Test of the depletion potential description*, Phys. Rev. Lett. **82**, 117 (1999).
- [176] M. Dijkstra, R. van Roij, and R. Evans, *Phase diagram of highly asymmetric binary hard-sphere mixtures*, Phys. Rev. E **59**, 5744 (1999).
- [177] A. Cacciuto, S. Auer, and D. Frenkel, *Breakdown of classical nucleation theory near isostructural phase transitions*, Phys. Rev. Lett. **93**, 166105 (2004).
- [178] A. van Blaaderen, *Colloidal molecules and beyond*, Science **301**, 470 (2003).
- [179] E. Duguet, A. Désert, A. Perrozab, and S. Ravaine, *Design and elaboration of colloidal molecules: an overview*, Chem. Soc. Rev. **40**, 941 (2011).
- [180] Y. Yin and Y. Xia, *Self-assembly of monodispersed spherical colloids into complex aggregates with well-defined sizes, shapes, and structures*, Adv. Mater. **13**, 267 (2001).
- [181] C. M. Liddell and C. J. Summers, *Nonspherical zns colloidal building blocks for three-dimensional photonic crystals*, J. Coll. Int. Sci. **274**, 103 (2004).
- [182] P. Johnson, C. van Kats, and A. van Blaaderen, *Synthesis of colloidal silica dumbbells*, Langmuir **21**, 11510 (2005).
- [183] D. Kraft, W. Vlug, C. Van Kats, A. Van Blaaderen, A. Imhof, and W. Kegel, *Self-assembly of colloids with liquid protrusions*, J. Am. Chem. Soc. **131**, 1182 (2008).
- [184] D. J. Kraft, J. Groenewold, and W. K. Kegel, *Colloidal molecules with well-controlled bond angles*, Soft Matter **5**, 3823 (2009).
- [185] V. N. Manoharan, M. T. Elsesser, and D. J. Pine, *Dense packing and symmetry in small clusters of microspheres*, Science **301**, 483 (2003).
- [186] G.-R. Yi, V. Manoharan, E. Michel, M. Elsesser, S.-M. Yang, and D. Pine, *Colloidal clusters of silica or polymer microspheres*, Adv. Mater. **16**, 1204 (2004).
- [187] Y.-S. Cho, G.-R. Yi, S.-H. Kim, D. J. Pine, and S.-M. Yang, *Colloidal clusters of microspheres from water-in-oil emulsions*, Chem. Mater. **17**, 5006 (2005).
- [188] Y. Yin and Y. Xia, *Self-assembly of monodispersed spherical colloids into complex aggregates with well-defined sizes, shapes, and structures*, Adv. Mater. **13**, 267 (2001).
- [189] Y. Lu, Y. Yin, and Y. Xia, *Three-dimensional photonic crystals with non-spherical colloids as building blocks*, Adv. Mater. **13**, 415 (2001).

- [190] V. N. Manoharan, M. T. Elsesser, and D. J. Pine, *Dense packing and symmetry in small clusters of microspheres*, *Science* **301**, 483 (2003).
- [191] G. R. Yi, T. Thorsen, V. N. Manoharan, M. J. Hwang, S. J. Jeon, D. J. Pine, S. R. Quake, and S. M. Yang, *Generation of uniform colloidal assemblies in soft microfluidic devices*, *Advanced Materials* **15**, 1300 (2003).
- [192] E. Lauga and M. P. Brenner, *Evaporation-driven assembly of colloidal particles*, *Phys. Rev. Lett.* **93**, 238301 (2004).
- [193] V. N. Manoharan, *Colloidal spheres confined by liquid droplets: Geometry, physics, and physical chemistry*, *Solid State Comm.* **139**, 557 (2006).
- [194] F. Bai, D. Wang, Z. Huo, W. Chen, L. Liu, X. Liang, C. Chen, X. Wang, Q. Peng, and Y. Li, *A versatile bottom-up assembly approach to colloidal spheres from nanocrystals*, *Angewandte Chemie International Edition* **46**, 6650 (2007).
- [195] S.-H. Kim, Y.-S. Cho, S.-J. Jeon, T. H. Eun, G.-R. Yi, and S.-M. Yang, *Microspheres with tunable refractive index by controlled assembly of nanoparticle*, *Adv. Mater.* **20**, 3268 (2008).
- [196] Y.-S. Cho, G.-R. Yi, S.-H. Kim, M. T. Elsesser, D. R. Breed, and S.-M. Yang, *Homogeneous and heterogeneous binary colloidal clusters formed by evaporation-induced self-assembly inside droplets*, *J. Coll. Int. Sci.* **318**, 124 (2008).
- [197] Y.-S. Cho, G.-R. Yi, J.-M. Lim, S.-H. Kim, V. N. Manoharan, D. J. Pine, and S.-M. Yang, *Self-organization of bidisperse colloids in water droplets*, *J. Am. Chem. Soc.* **127**, 15968 (2005).
- [198] K. Lin, C.-C. C. L. Lai, and H. Chen, *Assembly of microspheres with polymers by evaporating emulsion droplets*, *Phys. Rev. E* **78**, 041408 (2008).
- [199] B. Peng, A. van Blaaderen, and A. Imhof, *Synthesis of non-spherical PMMA colloids with anisotropic protrusions*, To be published (2012).
- [200] P. Pieranski, *Two-dimensional interfacial colloidal crystals*, *Phys. Rev. Lett.* **45**, 569 (1980).
- [201] B. Peng, F. Smallenburg, M. Dijkstra, A. van Blaaderen, and A. Imhof, To be published (2012).
- [202] S. Auer and D. Frenkel, *Line tension controls wall-induced crystal nucleation in hard-sphere colloids*, *Phys. Rev. Lett.* **91**, 015703 (2003).
- [203] A. Cacciuto, S. Auer, and D. Frenkel, *Onset of heterogeneous crystal nucleation in colloidal suspensions*, *Nature* **428**, 404 (2004).
- [204] M. I. Bodnarchuk, M. V. Kovalenko, H. Groiss, R. Resel, M. Reissner, G. Hesser, R. T. Lechner, W. Steiner, F. SchÄdfler, and W. Heiss, *Exchange-coupled bimagnetic wüstite/metal ferrite core/shell nanocrystals: Size, shape, and compositional control*, *Small* **5**, 2247 (2009).
- [205] R. J. Renka, *Algorithm 772: Stripack: Delaunay triangulation and voronoi diagram on the surface of a sphere*, *ACM Trans. Math. Softw.* **23**, 416 (1997).
- [206] A. R. Bausch, M. J. Bowick, A. Cacciuto, A. D. Dinsmore, M. F. Hsu, D. R. Nelson, M. G. Nikolaidis, A. Travesset, and D. A. Weitz, *Grain boundary scars and spherical crystallography*, *Science* **299**, 1716 (2003).
- [207] S. C. Glotzer, *Some assembly required*, *Science* **306**, 419 (2004).

- [208] E. Bianchi, P. Tartaglia, E. L. Nave, and F. Sciortino, *Fully solvable equilibrium self-assembly process: Fine-tuning the clusters size and the connectivity in patchy particle systems*, J. Phys. Chem. B **111**, 11765 (2007).
- [209] A. W. Wilber and J. P. K. Doyle, *Reversible self-assembly of patchy particles into monodisperse icosahedral clusters*, J. Chem. Phys. **127**, 085106 (2007).
- [210] E. Bianchi, J. Largo, P. Tartaglia, E. Zaccarelli, and F. Sciortino, *Phase diagram of patchy colloids: Towards empty liquids*, Phys. Rev. Lett. **97**, 168301 (2006).
- [211] F. Sciortino, A. Giacometti, and G. Pastore, *Phase diagram of janus particles*, Phys. Rev. Lett. **103**, 237801 (2009).
- [212] R. Erhardt, A. Boker, H. Zettl, H. Kaya, W. Pyckhout-Hintzen, G. Krausch, V. Abetz, and A. H. E. Müller, *Janus micelles*, Macromolecules **34**, 1069 (2001).
- [213] R. Pool and P. G. Bolhuis, *Accurate free energies of micelle formation*, The Journal of Physical Chemistry B **109**, 6650 (2005).
- [214] S. Asakura and F. Oosawa, *On interaction between two bodies immersed in a solution of macromolecules*, Journal of Chemical Physics **22**, 1255 (1954).
- [215] S. Asakura and F. Oosawa, *Interaction between particles suspended in solutions of macromolecules*, Journal of Polymer Science **33**, 183 (1958).
- [216] D. J. Kraft, R. Ni, F. Smalenburg, M. Hermes, K. Yoon, D. A. Weitz, A. van Blaaderen, J. Groenewold, M. Dijkstra, and W. K. Kegel, *Surface roughness directed self-assembly of colloidal micelles*, To be published (2011).
- [217] J. Kim, R. J. Larsen, and D. A. Weitz, *Synthesis of nonspherical colloidal particles with anisotropic properties*, J. Am. Chem. Soc. **128**, 14374 (2006).
- [218] T. Chen, Z. Zhang, and S. C. Glotzer, *A precise packing sequence for self-assembled convex structures*, Proc. Natl. Acad. Sci. U.S.A. **104**, 717 (2007).
- [219] N. Arkus, V. N. Manoharan, and M. P. Brenner, *Minimal energy clusters of hard spheres with short range attractions*, Phys. Rev. Lett. **103**, 118303 (2009).
- [220] M. Dijkstra, J. M. Brader, and R. Evans, *Phase behaviour and structure of model colloid-polymer mixtures*, Journal of Physics: Condensed Matter **11**, 10079 (1999).
- [221] G. Meng, N. Arkus, M. P. Brenner, and V. N. Manoharan, *The free-energy landscape of clusters of attractive hard spheres*, Science **327**, 560 (2010).

Summary

A colloidal dispersion consists of small particles called colloids, typically tens of nanometers to a few micrometers in size, suspended in a solvent. Collisions with the much smaller particles in the solvent cause colloids to perform Brownian motion: randomly directed movements that cause the particles to diffuse through the system. In principle, this motion allows the system of particles to explore all configurations available to them, sampling all of phase space according to the Boltzmann distribution. Analogous to molecular and atomic systems, colloidal systems can form disordered gas and liquid phases, as well as more ordered phases such as crystals, liquid crystals, or finite-sized aggregates. Since the particles form these phases based purely on their own interaction and the Brownian motion that results from thermal fluctuations in their solvent, the process of forming these ordered structures is called self-assembly. In this thesis, we study the self-assembly of a variety of colloidal systems. We attempt to determine what structures can be expected to form, investigate the order and stability of these phases, and examine the nucleation of self-assembled crystals. To do this, we make use of computers to simulate the behavior of colloidal particles in suspension. Depending on the system under consideration, we perform either Monte Carlo simulations or event-driven molecular dynamics.

In the first few chapters of this thesis, we looked at the behavior of colloidal particles in an external electric or magnetic field. Typically, colloidal particles have a dielectric constant that is different from that of the solvent material. If such a solution is placed in a homogeneous electric field, each particle obtains a dipole moment parallel to the field, leading to dipole-dipole interactions between the particles. Additionally, the field affects the orientation of most anisotropic particles, typically causing them to align their longest axis parallel to the electric field. Similarly, if a contrast in the magnetic susceptibility exists between the colloids and their solvent, magnetic fields can be used to induce these dipolar interactions instead. Since the induced dipole moments have the same direction for each colloid in the system, the system favors configurations where particles are assembled into string-like clusters along the field direction.

In Chapter 2, we study the shape and length of these strings in several systems. For monodisperse spheres, we measure the length of the strings observed at low packing fractions, and show that the results can be accurately predicted using Wertheim's perturbation theory. If two sizes of spheres are used, the structure of the clusters depends strongly on the size ratio: for highly asymmetric mixtures (size ratio < 0.33 or smaller), small particles cluster in ring-like and flame-like formations around strings of larger colloids, while spheres of nearly equal size can form strings that consist of both species. Around a size ratio of 0.8, strings consisting of regularly alternating large and small particles have been observed in experiments. We are able to see these in our simulations as well, but only if a charge repulsion between the particles is included in the model. While neither types of bidisperse strings studied in Chapter 2 are likely to be thermodynamically stable, both experiments and simulations show that particles can be trapped in such strings for long periods of time. Recently developed techniques for making such strings permanent could thus allow for the production of novel composite particles out of these clusters. Finally, we

examine the strings formed by asymmetric dumbbells in an external field. In this case, we investigate the effects of the size difference between the particles as well as the difference in dipole strength. For sufficiently strong interactions between the smaller spheres in each dumbbell, various chiral clusters can be formed.

Chapter 3 discusses the phase behavior of colloidal spheres in a biaxial electric or magnetic field: a field with a direction that is constantly and rapidly rotating within a fixed plane. Due to the rapid oscillations of the field, the dipole-dipole interactions between the particles at each instant average out to what is effectively an inverted dipolar interaction: particles attract each other in the plane of the field, but repel in the direction perpendicular to that. As a result, sheet-like rather than string-like clusters are formed, and the phase behavior of the system changes significantly. Using free energy calculations, we map out the phase diagram of both charged and uncharged spheres in a biaxial field. Both phase diagrams include a gas-liquid coexistence, and stretched face-centered-cubic (fcc) and hexagonally-close-packed (hcp) crystal structures. In addition, the charged spheres in a biaxial field exhibit a strongly layered fluid phase.

As already shown in Chapter 2, applying external fields to non-spherical particles can lead to interesting new structures. In Chapter 4, we investigate the phase behavior of colloidal cubes in an external electric field, again observing the formation of string-like clusters, as well as a columnar phase of hexagonally ordered strings of particles, and a body-centered-tetragonal (bct) crystal phase, where all particles are aligned, and the strings are arranged on a square lattice. Colloidal cubes have also recently been synthesized experimentally, and both hexagonal and square order were observed in a system of these cubes in an external electric field.

In Chapter 5, we continue our investigation of colloidal cubes, this time without an external field. This seemingly simple system of purely hard cubes has been the subject of several studies, and its phase behavior was reported to contain a cubatic phase, where the orientations of the particles show long-range order, but the positions are not correlated over large distances. Using molecular dynamics simulations, we investigate the regime where this cubatic phase was observed more closely, and observe the spontaneous formation of crystal vacancies in simulations started in the (simple cubic) crystal face. Free energy calculations show the stability of a crystal phase with a strikingly high vacancy concentration, which near the fluid-solid coexistence is orders of magnitude larger than that found in e.g. hard-sphere systems.

In several of the chapters involving dipolar interactions, we have made use of screened Coulomb potentials to describe the interactions of charged particles in solution. In a colloidal solution, particles often obtain a charge as a result of ions either attaching to the colloids out of the solvent, or detaching from the colloid surface. In either case, the total charge of the suspension should still be zero: the solvent contains ions of the opposite charge compensating for the charge of the particles. Due to electrostatic attractions, these particles are attracted to the colloids, and form a layer around each colloid that decreases (“screens”) the repulsion between the like-charged colloids. If the surface potentials of the colloids are sufficiently weak, and the double layers of different particles do not strongly affect each other, the screened Coulomb potential provides a good model for the resulting interactions between the colloids. However, in denser or more strongly interacting systems, the effective charge and screening length may depend on the presence of other nearby

particles. In Chapter 6, we use a simple cell model to estimate these parameters for colloidal particles with a constant surface potential, and calculate phase diagrams based on the resulting interactions. Depending on the surface potentials, the phase diagrams show a reentrant fluid phase: for increasing density, the system returns to a fluid state after crystallizing due to a decrease in the effective charge.

In Chapter 7, we study the nucleation of crystals in binary systems of hard spheres. The way small fluctuations in a metastable fluid can lead to the nucleation of a more stable phase is traditionally described by classical nucleation theory, which describes the free energy of a cluster as a function of its size. Determining the size of a cluster in simulations requires the definition of an order parameter that distinguishes the nucleus from the surrounding fluid. Even for monodisperse fluids, the choice of order parameter has some influence on the structure of the observed clusters. For example, if the order parameter is strict, only well-ordered clusters will be seen, with the outer layers of disordered particles excluded from the cluster. This is not an artifact in the simulations, but rather the result of the way the same clusters are described. We study the effect of the choice of order parameter in binary systems, and compare the resulting theoretical predictions with simulations done on two model systems, one where the two species were the same size, and only artificially labeled as two different species, and one with two different sizes of hard spheres.

Chapters 8 and 9 investigate the behavior of particles in evaporating emulsion droplets. Experimentally, the evaporation of droplets can be used to force colloidal particles suspended inside the droplets to form roughly spherical clusters. If this technique is used on small numbers of spheres (up to around 16), there is generally one specific shape for clusters of each size, readily reproducible even in significantly different experimental systems. For a few cluster sizes, two or three options exist for the resulting shape. In Chapter 8, we model the formation of these clusters with a very simple model, where hard spheres are compressed in spherical confinement. Additionally, we investigate the clusters formed by small numbers of symmetric or asymmetric dumbbells, and compare the results to experiments. Chapter 9 investigates the evaporation of droplets containing more particles, yielding clusters consisting of thousands of spheres. In this case, multiple crystal domains nucleate and grow inwards from the confining walls. We compare the shape of these wedge-shaped domains with crystal domains observed in recent experiments on clusters of nanoparticles, and find good agreement. Additionally, we investigate the effects of wall-particle and particle-particle repulsions.

Finally, Chapter 10 describes the use of asymmetric dumbbells as a colloidal model system for micelles. In surfactant systems, micelles are formed by large molecules with one hydrophilic side and one hydrophobic side. When placed in water, these surfactants cluster together into micelles, where the hydrophobic parts are surrounded by a shell of hydrophilic material. Similar clusters can be formed by asymmetric dumbbells, where only the smaller spheres in each dumbbell attract each other. Such a system can be realized experimentally using depletion interactions: by applying a rough coating to the larger sphere in each dumbbell, it is possible to ensure that only the smaller spheres attract. We study the cluster size distribution in such systems, and examine the shape of the resulting clusters. Comparisons between free energy calculations, direct Monte Carlo simulations, and experiments suggest that the short interaction range required in this approach leads

to very slow equilibration of the system, with non-equilibrium effects strongly limiting the cluster size.

Samenvatting

Colloïden zijn microscopisch kleine deeltjes (normaal gesproken tussen enkele tientallen nanometers en een paar micrometer in grootte), beduidend groter dan atomen en de meeste moleculen, maar te klein om met het blote oog te zien. Een colloïdale suspensie bestaat uit een oplosmiddel waarin dit soort deeltjes zijn opgelost. In veel gevallen gaat het hier om vaste deeltjes in een vloeistof (denk bijvoorbeeld aan pigmentdeeltjes in verf of inkt), maar de deeltjes kunnen ook gevormd worden door kleine gasbelletjes (scheerschuim) of druppeltjes van een andere vloeistof (mayonaise). Een van de belangrijkste redenen dat colloïdale systemen interessant zijn is de chaotische beweging van de colloïden: als je zulke deeltjes onder een microscoop bekijkt, zie je dat ze continu in beweging zijn en willekeurig van richting veranderen. Deze zogenaamde Brownse bewegingen, genoemd naar Robert Brown, die dit gedrag bestudeerde in 1827, zijn het gevolg van de beweging van de moleculen in het oplosmiddel, die voortdurend van alle kanten tegen het deeltje botsen. Hoewel de botsingen van verschillende kanten elkaar tegenwerken, en elke botsing op zich maar weinig energie overdraagt op het deeltje, zijn colloïdale deeltjes licht genoeg om door dit bombardement van moleculen voortdurend in beweging te blijven. Hoewel dit effect ook plaats vindt voor grotere deeltjes (mensen worden immers ook voortdurend van alle kanten geraakt door moleculen in de lucht), zijn de verplaatsingen voor deeltjes groter dan een paar micrometer in het algemeen verwaarloosbaar klein.

Brownse beweging heeft belangrijke gevolgen voor de structuur van een colloïdale suspensie. Denk bijvoorbeeld aan een enkel deeltje, iets zwaarder dan de omringende vloeistof. Zwaartekracht zal dit deeltje naar beneden trekken, en zonder Brownse beweging zou het uiteindelijk op de bodem blijven liggen. Een deeltje dat licht genoeg is kan echter door Brownse beweging alsnog omhoog geduwd worden, en in principe de hele met vloeistof gevulde ruimte verkennen. De zwaartekracht zal er nog steeds voor zorgen dat het deeltje vaker bij de bodem te vinden is dan ver ervandaan, al kan dit effect teniet worden gedaan door deeltjes te maken uit een materiaal met dezelfde dichtheid als het oplosmiddel. De kansverdeling voor de hoogte van het systeem kan eenvoudig bepaald worden uit de potentiële energie van het deeltje op elke hoogte: hoe hoger de energie, hoe onwaarschijnlijker het is om het deeltje op die hoogte te vinden. In de praktijk bevatten colloïdale systemen grote aantallen deeltjes, en het aantal mogelijke configuraties in een systeem is dan enorm groot. In dit geval wordt het gedrag van de deeltjes sterk beïnvloed door de interacties tussen de deeltjes: deeltjes met dezelfde lading stoten elkaar bijvoorbeeld af, en zullen dus het liefst ver uit elkaar blijven om de energie van het systeem te minimaliseren. Zulke afstotende (of aantrekkende) krachten kunnen leiden tot de vorming van kristalstructuren, waarin de afstand tussen naburige deeltjes zo groot (of juist zo klein) mogelijk is. Zelfs zonder dit soort interacties kunnen kristallen gevormd worden: een systeem van harde bollen kan bijvoorbeeld kristalliseren omdat, bij voldoende hoge dichtheden, er maar weinig ongeordende configuraties bestaan waarin de deeltjes niet overlappen, vergeleken met configuraties waarin de deeltjes (ongeveer) op een kristalrooster zijn geordend. Met andere woorden, het is makkelijker bollen dicht op elkaar te pakken als ze netjes zijn opgestapeld. Niet alleen de energie van configuraties is dus van belang,

maar ook het aantal manieren waarop een toestand gevormd kan worden. De entropie van het systeem in een bepaalde toestand is een maat voor dit aantal mogelijkheden.

Dit samenspel tussen energie en entropie kan leiden tot een rijk fasegedrag in colloïdale systemen: niet alleen kunnen colloïden kristallen vormen, maar ook vloeistoffen en gassen. Daarnaast kunnen anisotrope colloïden (die dus niet bolvormig zijn) zich in verschillende toestanden bevinden waarin ze niet geordend op een kristalrooster zijn geplaatst, maar bijvoorbeeld wel allemaal dezelfde kant op wijzen: zogenaamde vloeibare kristallen. Het omgekeerde is ook mogelijk: een kristal van colloïden die vrij rond kunnen draaien wordt wel een plastisch kristal genoemd.

Om te voorspellen in welke toestand een colloïdaal systeem zich onder bepaalde omstandigheden waarschijnlijk zal bevinden moet in principe rekening gehouden worden met alle mogelijke configuraties van een systeem. In de praktijk maakt het grote aantal mogelijkheden exacte berekeningen meestal onmogelijk voor systemen van meer dan een paar deeltjes. In plaats daarvan gebruiken we vaak computersimulaties om configuraties te genereren die voorkomen met dezelfde kansverdeling als waarin ze in werkelijkheid voor zouden komen. In dit proefschrift wordt daarbij gebruik gemaakt van twee simulatiemethoden: Monte Carlo simulaties en moleculaire dynamica. In Monte Carlo simulaties worden een reeks configuraties gemaakt door telkens de vorige configuratie een klein beetje te veranderen door bijvoorbeeld een deeltje willekeurig te verplaatsen, en de wijziging af te wijzen of te accepteren op basis van het energieverval tussen de oude en de nieuwe configuratie. Simulaties die gebruik maken van moleculaire dynamica berekenen de bewegingen van de deeltjes in het systeem op basis van de krachten tussen de deeltjes en de wetten van Newton. Hoewel voor geen van beide simulatiemethoden de dynamica van de deeltjes precies overeenkomt met die in een colloïdaal systeem, kan aangetoond worden dat het fasegedrag van een systeem onafhankelijk is van de manier waarop de deeltjes bewegen, aangenomen dat het systeem zich in een evenwichtstoestand bevindt. Hierdoor kunnen computersimulaties gebruikt worden om het gedrag van colloïdale systemen te voorspellen en te verklaren, aangenomen dat we op de hoogte zijn van de interacties tussen de deeltjes, en van eventuele externe factoren die het systeem beïnvloeden. In sommige gevallen kunnen zulke simulaties gebruikt worden om directe waarnemingen in het systeem te doen, maar in veel gevallen is het nauwkeuriger om simulaties toe te passen voor metingen die gebruikt worden in het berekenen van de vrije energie van de verschillende fasen: een maat voor de relatieve waarschijnlijkheid om een systeem in een bepaalde toestand aan te treffen.

In de eerste paar hoofdstukken van dit proefschrift bestuderen we het gedrag van colloïden in externe elektrische of magnetische velden. Beide velden hebben ongeveer dezelfde werken op de colloïdale deeltjes: ze wekken een dipoolmoment op in elk deeltje, dat er voor zorgt dat de deeltjes zich gaan gedragen als kleine parallele magneetjes. Bij een verticaal veld trekken twee deeltjes elkaar dus aan als ze boven elkaar liggen, maar stoten elkaar af als ze zich naast elkaar bevinden. Dit heeft als gevolg dat de deeltjes zichzelf ordenen in kettingvormige clusters parallel aan de veldrichting, die zich bij hoge dichtheden weer ordenen in een kristalstructuur. In hoofdstuk 2 bekijken we de structuur en lengte van deze kettingen in systemen van bolvormige deeltjes, en bestuderen we het effecten van het mengen van deeltjes van twee verschillende grootten. In hoofdstuk 3 modelleren we een iets ander extern veld, waarvan de richting met hoge snelheid ronddraait. Hierdoor

worden de interacties tussen de deeltjes precies omgedraaid, zodat ze hexagonale vlakken van deeltjes vormen in plaats van kettingen. We berekenen het fasegedrag van dit systeem zowel voor geladen als ongeladen deeltjes. In hoofdstuk 4 bekijken we weer een elektrisch veld in een constante richting, maar ditmaal met kubusvormige deeltjes. De meeste van de colloïdale systemen in deze hoofdstukken zijn recentelijk ook experimenteel gerealiseerd, en we vergelijken onze resultaten met de structuren die zijn waargenomen in experimentele observaties.

Hoofdstuk 5 kijkt in meer detail naar het fasegedrag van kubussen, ditmaal zonder lading en externe velden. Zonder de aanwezigheid van interacties speelt alleen de entropie een rol voor het fasegedrag. Eerder onderzoek aan dit systeem gaf het vermoeden dat het een zogenaamde kubatische fase zou vertonen (waarin de deeltjes niet op een kristalrooster zitten, maar wel allemaal ongeveer dezelfde oriëntatie hebben). Onze simulaties en berekeningen wijzen hier niet op, maar tonen de stabiliteit aan van een kristalfase waarin een verrassend hoog aantal lege plekken op het kristalrooster zitten. Hoewel bekend was dat kristallen in evenwicht vrijwel altijd een kleine hoeveelheid van zulke defecten bevatten, kan de concentratie in dit systeem ruim 100 keer groter zijn dan in bijvoorbeeld kristallen van harde bollen. Daarnaast bleek dat het toevoegen van defecten aan een kristal, tegengesteld aan wat je zou verwachten, de mate van orde in het systeem kan verhogen.

In hoofdstuk 6 bekijken we hoe de interactie tussen geladen bollen verandert als de dichtheid van het systeem toeneemt, en berekenen we de effecten daarvan op het fasegedrag. Omdat de effectieve lading van dit soort deeltjes vermindert als de dichtheid toeneemt, kan het voorkomen dat een systeem als functie van een toenemende dichtheid eerst een vloeibare fase, dan een kristal, dan weer een vloeibare fase, en uiteindelijk weer een kristalfase vertoont.

Hoofdstuk 7 behandelt de vorming van kristallen in mengsels van harde bollen met twee verschillende diameters. Kristallisatie begint in veel gevallen met een proces dat nucleatie wordt genoemd: ergens in de vloeistof ontstaat als gevolg van Brownse beweging een gebiedje waar de deeltjes meer geordend zijn dan in hun omgeving. Een erg kleine kristalvormige nucleus is in principe niet stabiel als gevolg van de oppervlaktespanning, waardoor grenslagen tussen kristal en vloeistof in het systeem de entropie van een systeem verminderen. Als zo'n nucleus echter groter wordt dan een zekere kritieke grootte, dan kan hij uitgroeien tot een groot kristal. Omdat zulke gevallen van nucleatie meestal vrij zeldzaam zijn in een systeem dat klein genoeg is om op een computer te kunnen simuleren, zijn er speciale methoden nodig om nucleatie in simulaties te bekijken. Een methode daarvoor is Umbrella Sampling, waarbij simulaties uitgevoerd worden met de restrictie dat de grootste kristalcluster in het systeem (ongeveer) een specifiek aantal deeltjes moet bevatten. Door zulke simulaties te combineren kan dan berekend worden hoe groot een kritieke cluster is, en hoe vaak zo'n cluster voorkomt. Hoe je de grootte van een cluster bepaalt is hierbij erg belangrijk, en in dit hoofdstuk bekeken we hoe de keuze van een methode daarvoor de gemeten resultaten kan beïnvloeden.

In hoofdstuk 8 en 9 bestuderen we het gedrag van bollen en dumbbells (deeltjes die bestaan uit twee bollen die aan elkaar vastzitten) in verdampende druppels. In recent onderzoek worden verdampende druppels regelmatig gebruikt kleine deeltjes samen te persen tot al dan niet geordende clusters. De structuur van de clusters wordt bepaald

door onder andere de vorm van de deeltjes, en de interacties tussen de wand en de deeltjes. We bekeken verschillende simpele modellen om de structuur van de resulterende clusters te voorspellen, en vergeleken onze resultaten met observaties in experimentele systemen. Voor grote aantallen (duizenden) bollen kan dit leiden tot interessant gevormde kristaldomeinen, die als taartpunten in elkaar passen. Voor kleinere aantallen bollen en dumbbells zijn de gevormde clusters vaak zeer reproduceerbaar, en komen de experimentele en gesimuleerde structuren goed overeen.

Het laatste hoofdstuk kijkt opnieuw naar clusters van dumbbells, ditmaal gevormd door aantrekkende krachten tussen de deeltjes: elke dumbbell bestaat uit een grote en een klein bol, en de kleinere bollen trekken elkaar op korte afstand aan. Hierdoor ontstaan zogenaamde colloïdale micellen: clusters waarin de kleine bollen in het midden zitten, terwijl de grotere de buitenkant afschermen. Door deze afscherming is het lastig om nieuwe deeltjes aan een bestaande cluster toe te voegen, en het berekenen van de vrije energie van clusters van verschillende formaten tonen dan ook aan dat in veel gevallen het voor directe simulaties aan dergelijke systemen vrijwel onmogelijk is om een evenwichtstoestand te bereiken. De uitwisseling van deeltjes tussen clusters wordt uiteindelijk zo traag dat de clusters nooit de grootte bereiken die ze in een evenwichtstoestand zouden hebben. Vergelijkingen met een experimenteel systeem waarin dezelfde clusters werden geproduceerd suggereren dat daar hetzelfde gebeurt.

In het kort hebben we dus een reeks colloïdale systemen bestudeerd die nu of in de nabije toekomst ook experimenteel gerealiseerd kunnen worden, en geprobeerd te voorspellen welke structuren deze systemen zullen vormen. Hoewel directe praktische toepassingen van dit onderzoek niet makkelijk te vinden zullen zijn, wordt er in het dagelijks leven op genoeg plaatsen van colloïden gebruik gemaakt om ervoor te zorgen dat een beter begrip van het gedrag van zulke deeltjes nuttig kan zijn. Daarnaast is er grote interesse in het gebruik van colloïdale structuren voor de manipulatie van licht, bijvoorbeeld in zogenaamde optische schakelingen. Doordat de deeltjesafstand in een colloïdaal kristal dezelfde orde van grootte hebben als de golflengte van zichtbaar licht, kunnen dit soort kristallen in principe gebruikt worden om lichtsignalen met grote nauwkeurigheid te manipuleren, afhankelijk van de kristalstructuur. Ook voor het maken van deze fotonische kristallen zijn voorspellingen over de manieren waarop colloïdale deeltjes zichzelf kunnen ordenen van groot belang.

Acknowledgements

Finally, I would like to extend my thanks to all the people who have helped me bring this thesis into being. Four years of research is a long time, and it would not have been nearly as interesting, fun, and satisfying without the support and company of those around me. First of all, the Soft Condensed Matter group in Utrecht is, by any measure, a wonderful group to work in. Marjolein, of course this thesis could not have been made without you: thank you for your excellent supervision. Your great interest in my work, your swift responses, the door to your office that was always open, and our many interesting discussions made doing research in Utrecht into the highly interesting, educational, and fun experience that it has been for me. Additionally, I should thank you, Alfons, Arnout and René for bringing together a great group of researchers that combine theory, experiments and simulations into many collaborations. I may have learned as much from our combined workdiscussions as from my own research!

Next, I would like to thank my officemates over the last years. Laura, Emmanuela, Ran, Anjan: thank you all for many lively discussions, debates, and arguments, on a wide variety of subjects. Statistical physics, nucleation, weird bugs in our codes, detailed balance, the politics in various countries, cultural differences between the Dutch and others, and many other topics... I could not wish for a nicer or more interesting office!

Both inside and outside the Soft Condensed Matter group there are many people who deserve my thanks for their collaboration and help with many things. Michiel, not the least for his work on the visualization program that has been incredibly useful to me and many others. Matthieu, for all his helpful advice on free energy calculations, simulation methods, and many other things. Laura, for all her work on hard cubes, for more discussions in the office than I can count, and her help in improving the language in many of my writings. Ran, for his work on nucleation, and for all the times we filled the whiteboard during our useful discussions. Chantal, whose tips and code for Ewald summations helped me get started four years ago. Bart, for his collaboration on nanoparticles in emulsion droplets. Bo, for the fabrication of the small clusters of spheres and dumbbells in similar droplets. Bing, whose droplets are filled with rods instead, and inspired some of my simulations not shown in this thesis. Rao, whose experimental work was the main inspiration for simulations on particles in external fields, and who even managed to drag me into the lab on a few occasions! Peter and Djamel, trying to figure out the interactions between charged particles with both of you was a lot of fun. Johan and Ahmet, our work on clusters of oppositely charged colloids has not quite made it onto paper yet, but hopefully it still will. Teun, thanks for many interesting chats both on oppositely charged colloids and your simulations of patchy particles. Joost, thank you for supplying me with a Monte Carlo code for cubes, and for all your work that made the group run more smoothly. Niels, for your calculations and help on particles with a constant surface potential. René I would like to thank for his help on this project as well, for organizing the theory workdiscussions, and for giving several of the best scientific talks I've seen so far. Alfons, for several fruitful collaborations, as well as many helpful tips and discussions on many occasions. Both Andrei Petoukhov and Arnout for helpful

tips on scattering patterns. Willem Kegel and Daniela for their beautiful experiments on colloidal micelles. Gerard Barkema, for supervising my Master's research, which showed me how interesting and enjoyable physics research can be. Henk Mos and his colleagues, for keeping our simulation cluster running. And everyone else who I've come in touch with while working, who contributed to the work discussions, and who showed me a bit of their views on the world of soft matter... thank you all!

Of course, work is not the only thing in life, and I would also like to thank those that have helped me take my mind away from it in the past years. For this, too, the group has been great. Any trips with (part of) the group, large and small, were always pleasant: not only Wadlopen, which was definitely a great experience, but also biking at the Veluwe, playing minigolf, a visit to the Efteling, or a museum in Rotterdam, skating trips, dinner in a park, or along the Lek... My thanks to those who helped organize these trips and those who came along! I also greatly enjoyed many of the (sometimes bizarre) coffee table discussions in our group, and the many cakes and cookies that have come by during these over the years. My thanks to anyone who contributed to either of these, and especially to the baking skills of Joost and Johan! Laura, Anjan, Ran, Joost, Helene, and many others, thank you for the enjoyable dinners and lunches we shared. And Teun, Anjan and Helene, my thanks for getting me into the climbing hall on a not-quite-regular basis!

Uiteindelijk nog maar een alinea in het Nederlands. Ten eerste, voor al mijn vrienden die me de afgelopen jaren hebben vermaakt met spelletjes en uitjes, hartelijk dank! Tim, bedankt voor het ruimschoots verbreden van mijn ervaringen met muziek, en vele bekeken series en films (ondanks af en toe een 'cheap cop-out'...). Laura, ook jij nogmaals hartelijk bedankt voor meer dan ik hier kan noemen. Zowel Tim als Laura wil ik natuurlijk ook graag bedanken voor het komen opdraven als paranimfen! En ten slotte, mijn dank aan Joke en Ed, mijn ouders. Zonder jullie was ik nooit zo ver gekomen.

List of publications

This thesis is based on the following publications:

- F. Smallenburg, L. Filion, M. Marechal and M. Dijkstra, *Vacancy-stabilized crystalline order in hard cubes*, arXiv: 1111.3466, submitted (Chapter 5)
- D. J. Kraft, R. Ni, F. Smallenburg, M. Hermes, K. Yoon, D. A. Weitz, A. van Blaaderen, J. Groenewold, M. Dijkstra and W. K. Kegel, *Surface Roughness directed Self-Assembly of Patchy Particles into Colloidal Micelles*, under review (Chapter 10)
- R. Ni, F. Smallenburg, L. Filion and M. Dijkstra, *Crystal nucleation in binary hard-sphere mixtures: the effect of order parameter on the cluster composition*, Mol. Phys. **109**, 1213 (2011) (Chapter 7)
- F. Smallenburg, N. Boon, M. Kater, M. Dijkstra and R. van Roij, *Phase diagrams of colloidal spheres with a constant zeta-potential*, J. Chem. Phys. **134**, 074505 (2011) (Chapter 6)
- F. Smallenburg and M. Dijkstra, *Phase diagram of colloidal spheres in a biaxial electric or magnetic field*, J. Chem. Phys. **132**, 204508 (2010) (Chapter 3)

Other publications:

- D. El Masri, P. van Oostrum, F. Smallenburg, T. Vissers, A. Imhof, M. Dijkstra and A. van Blaaderen, *Phase diagrams of colloidal spheres with a constant zeta-potential*, Soft Matter **7**, 3462 (2011)
- L. Filion, M. Marechal, B. van Oorschot, D. Pelt, F. Smallenburg, and M. Dijkstra, *Efficient Method for Predicting Crystal Structures at Finite Temperature: Variable Box Shape Simulations*, Phys. Rev. Lett. **103**, 188302 (2009)
- F. Smallenburg and G. T. Barkema, *Universality class of the pair contact process with diffusion*, Phys. Rev. E **78**, 031129 (2008)